PSFC/RR-03-4

THE GRIDDED ELECTROMAGNET PROBE

SHADMAN, K.

June 2003

Plasma Science and Fusion Center

Massachusetts Institute of Technology

Cambridge MA 02139 USA

This work was supported by the U.S. Department of Energy, Grant No. DE-FG02-91ER54109.

THE GRIDDED ELECTROMAGNET PROBE

by

KHASHAYAR SHADMAN

B.S. Nuclear & Electrical Engineering — University California Berkeley, 1994
M.S. Nuclear Engineering — Massachusetts Institute of Technology, 1998

SUBMITTED TO THE DEPARTMENT OF NUCLEAR ENGINEERING FOR THE PARTIAL

FULFILLMENT OF THE REQUIREMENTS FOR THE DEGREE OF

DOCTOR OF PHILOSOPHY IN NUCLEAR ENGINEERING

AT THE

MASSACHUSETTS INSTITUTE OF TECHNOLOGY

JUNE 2003

Signature of Author:_____
Department of Nuclear Engineering
April 23, 2003

Certified by:_____
Jeffrey P. Freidberg, Thesis Supervisor
Professor of Nuclear Engineering, Head of Department

Certified by:_____
Ian H. Hutchinson, Thesis Reader
Professor of Nuclear Engineering

Certified by:_____
Doctor Peter Catto, Thesis Reader
Head of Theory and Assistant Director at the PSFC

Accepted by:_____
Jeff Coderre
Professor of Nuclear Engineering
Chairman, Committee for Graduate Students

THE GRIDDED ELECTROMAGNET PROBE

by

KHASHAYAR SHADMAN

Submitted to the Department of Nuclear Engineering on *April 23, 2003* for the partial fulfillment of the requirements for the Degree of Doctor of Philosophy in Nuclear Engineering

ABSTRACT

We attempted to measure the anisotropy in the electron distribution function in magnetized plasma by exploiting the adiabatic invariance of the electron's magnetic moment with a probe comprising a grid, a collector, and an inertially cooled electromagnet. The electric mirror force of the grid, which is located at the electromagnet throat, reduces the demand on the magnetic mirror force and thereby on the electromagnet current, which then allows for the construction of a compact probe that can be inserted inside the plasma chamber.

An analysis of the effects of space charge inside the grid-collector cavity revealed that the size of the probe's entrance aperture, b, which gives the size of the plasma beam inside the probe, should be chosen to be within a factor of *ten* of the electron Debye-length λ_{De}. In addition, an analysis of the discrete structure of the grid showed that the mesh wire spacing d should be chosen to be much less than λ_{De}. Also, the wire thickness t should be chosen to be much less than d.

We built a probe with a grid of tungsten wires with dimensions, $t = 5\mu m$ and $d = 200\mu m$. We then tested this probe in a hydrogen plasma immersed in a background magnetic field of $B \sim 1kG$. The plasma was heated by microwaves via the electron cyclotron resonance. It was characterized by a density and temperature equal to $n_e \sim 10^{10} cm^{-3}$ and $T_e \sim 10eV$, respectively, which gave $\lambda_{De} \sim 300\mu m$. The collector's current-voltage characteristic demonstrated the interaction between the electric barrier at the collector and the hybrid electric-magnetic barrier at the grid, thereby establishing the basic principles of the probe. The characteristic also revealed the non-ideal behaviors associated with the electric hole in the mesh and the effects of space charge. These effects in conjunction with the poor signal-to-noise level of the data prevented the measurement of the distribution function. Still, we were able to extract the temperature anisotropy for an assumed two-temperature Maxwellian distribution. The value for this ratio was found to be greater than *one* (greater temperature for the perpendicular gyro-motion), which is plausible given the way in which the plasma is heated.

Thesis Supervisor: Jeffrey Freidberg
Title: Professor of Nuclear Engineering, Department Head

ACHNOWLEDGEMENTS

My family and friends will be thanked personally.

My Advisor, Professor Jeffrey Freidberg

Without his emotional support, I might have left the institute six years ago.

Taking courses and passing exams defined my life before I entered MIT, forcing me to re-invent myself to survive the Ph.D. program. I never felt secure in my quest to obtain this degree; I could not guarantee myself the ability to realize a novel idea, and I had no desire to implement somebody else's. Even though, he had the right to force me to choose a project with existing funds, Jeff helped me find one of my own. Once I stumbled onto the idea that led to this dissertation, Jeff encouraged me to carry the idea through even though my project had no source of funds.

A father figure and a mentor, whose support over the years has been directly responsible for the devotion that will keep me in the world of physics for the rest of my life.

My Secondary Advisor, Professor Ian Hutchinson

Without the feedback that I received from his teaching style as well as from our personal interactions, I would not have developed an artistic approach to understanding physics.

I never felt comfortable with the way Ian explained physical phenomena; I felt that the explanations lacked the rigor associated with lots of equations. During the years, I found that these insecurities were symptoms of my own misconceptions of the meaning of comprehension. My grasp of physics was meager, based on equations whose origins I did not understand. Ian (perhaps unintentionally via his intolerance for extraneous mathematics) compelled me to argue my case using physical insight instead.

He has helped me to become a more creative thinker, thereby allowing me to experience some level of spirituality in a medium that is seemingly void of such a thing.

Mr. Bob Childs

His expertise and the countless hours he spent with me brought to life the diagnostic machine, whose picture was not even concrete in my own head. Without him, I would have been limited to a drawing of what the diagnostic might have looked like. The "Childs" Probe, with all of its intricate connections, remained flawless during its operation. Thanks Bob.

Dr. Jan Egedal

A friend, a colleague, and a teacher who spent weekends away from his fiancée to help me get data with the Childs-probe. He showed me how to implement the probe as well as the nuances of the electronics used for data acquisition. He allowed me to use his power supplies, wrote codes for data interpretation to guide the course of my experiment, lend me his lab-top so that I could analyze the data, … Thanks Jan

Dr. Peter Catto

Last, but not least, I like to thank Dr. Catto for sacrificing five months of his life to help turn this Thesis into something that is readable.

OUTLINE

CHAPTER 1

INTRODUCTION TO THE THESIS

[1.0] The application of low temperature and density plasmas

[1.1] The purpose of the thesis

[1.1.1] Measuring the distribution function in a magnetized plasma

[1.2] The gridded-electromagnet probe (the GEM probe)

[1.2.1] Drawbacks of employing a grid

[1.3] Experimental results of the GEM probe

[1.3.1] The future of this probe

CHAPTER 2

MEASURING THE DISTRIBUTION FUNCTION WITH A PROBE

(a review of Langmuir probe theory, leading up to the measurement of the distribution function in a magnetized plasma)

[2.0] Introduction

[2.0.1] The $I-V$ characteristic of the Langmuir probe

[2.0.2] The probe's intrusive nature

[2.0.3] The principles for the measurement of the distribution function

[2.0.4] The electric perturbation

[2.1] The Langmuir probe in a plasma *without* a background magnetic field

[2.1.1] The extent of the electric perturbation for $B_\infty = 0$

CHAPTER 3

MEASURING THE ANISOTROPY IN THE ELECTRON VELOCITY DISTRIBUTION IN A MAGNETIZED PLASMA

(a review of the methods used to extract information about the distribution of the electrons' perpendicular-gyration speeds, leading up to the ideal behavior of the *gridded electromagnet* probe)

CHAPTER 7

THE FUTURE OF THE GEM PROBE

APPENDIX TO CHAPTER 2

[2.2x] The pre-sheath potential profile in magnetized plasmas

APPENDIX TO CHAPTER 4

[4.1x] The general expression for the densities inside the housing

[4.2x] The *potential energy* for the electrostatic potential

[4.2x.1] The *potential energy* at locations of interest

APPENDIX TO CHAPTER 5

[5.1x] Constructing the vacuum potential profile about a mesh

[5.1x.1] The Fourier coefficients of the charge per unit length

[5.1x.2] The *exact* solution for a 1-D array of wires with no *depth*

[5.3x] The exchange of kinetic energy with the perturbation

APPENDIX TO CHAPTER 6

[6.1x] The Joule-heating of the electromagnet

[6.2x] The dependence of the collection area on the magnetic geometry

[6.2x.1] The overlap area between the entrance, the grid, and the collector

CHAPTER 1

INTRODUCTION TO THE THESIS

[1.0] The application of low temperature and density plasmas

The study of low density and temperature plasmas ($n_e \leq 10^{12} cm^{-3}$, $T_e < 100eV$) has applications in many fields. One example is the physics of the ionosphere[i], whose understanding is essential for satellite communication. Another example involves the diagnosis and control of the various species comprising plasmas, which enables the production of, for example, equipment that can monitor hazardous gas emissions[ii] from power plants. A third example involves the diagnosis of plasmas as applied to the field of microelectronics[iii iv], which employs plasma sources for many of the steps involved in the production of microelectronics hardware. Here, the plasma is used for the production of reactive molecular species that govern the etching of sub-micron dielectric features for the electronic connections of microchips. The plasma is also used for the ionization of metal atoms for their deposition into the dielectric features to form the metal interconnections.

The physics of such plasmas involves electromagnetic wave propagation and absorption within a plasma medium, energy transport by and redistribution among the plasma constituents, and reaction rates for the ionization and excitation of atoms as well as for the chemical reactions of the molecular species. An understanding of these phenomena requires knowledge of the spatial and temporal variations in the electron velocity distribution. The electrons, being the much more mobile species, tend to be the

ones that absorb the input power and the ones that provide the speed that governs the cross sections for the aforementioned reactions.

The electron distribution function f is the density in phase space $d^3v d^3x$. It is, in general, an-isotropic in velocity space because of the presence of a background magnetic field, which is either employed to "contain" the plasma in the plane normal to the magnetic field lines or is naturally present, as it is in the ionosphere. In the next chapter, we will treat the issues that arise when measuring f as the ambient magnetic field inside the plasma increases from zero. Here, we focus on the measurement of interest; that of f for the case of *magnetized* plasmas, where the electron Larmor radius ρ_e is comparable to the electron Debye-length λ_{De}.

[1.1] The purpose of the thesis

This thesis describes the theoretical foundations, the design, the construction, and the operation of a novel diagnostic probe that, in principle, can measure the speed distribution associated with the electrons' gyro-motion in addition to the distribution of speeds for the motion along the magnetic field line in magnetized plasmas. In other words, this probe measures the perpendicular speed distribution in addition to the parallel speed distribution. It thus represents an important generalization of the well-known Langmuir probe, which can only measure the parallel speed distribution via the relation[v] $f_{//} \propto dI/dV_C$; an operation that restricts the contribution to the current I to electrons with $U_{//}^* = e(\Phi_\infty - V_C)$, where Φ_∞ is the plasma potential, V_C is collector voltage, and $U_{//}^*$ is the upstream energy associated with the motion along the field.

[1.1.1] Measuring the distribution function in a magnetized plasma

The concept of our probe is described with the aid of figure **1.1-1** as follows. The constancy of the electron's magnetic moment forces its perpendicular-gyration kinetic energy to change in direct proportion to the magnetic field strength; that is, $U_{\perp} = \mu B$. Therefore, if a probe is housed inside an electromagnet, as shown in the figure, and current is provided to the electromagnet to locally increase the magnetic field, the electron will gain perpendicular energy as it moves into the housing. To keep the total energy (kinetic plus electrostatic, $U_{//} + U_{\perp} - e\Phi$) constant, the increase in $U_{\perp}$ generates a retarding force in the parallel direction, which decreases $U_{//}$. The *mirror* force associated with the increasing magnetic field then reflects electrons with large pitch-angle; that is, electrons with a large ratio of $U_{\perp}/U_{//}$. Hence, the amount by which the electron current to the probe is reduced with increasing electromagnet current is a function of the anisotropy in the distribution function.

This concept was first exploited by Hayes[vi] *et. al*. The group[vii] built and tested an early version of this diagnostic. Their probe, however, was bulky because they needed an electromagnet with active cooling (with liquid nitrogen) in order to produce the required mirror force to distinguish electrons with small pitch angle. Hence, their probe could only be implemented as an end-analyzer. It could not be placed inside the plasma chamber in order to reveal local information about the distribution function. Even so, their probe measured the distribution function near the chamber boundary; and it did this over a large portion of the velocity space, thereby establishing the basic principles.

[1.2] The gridded electromagnet probe (the GEM probe)

To alleviate the burden of requiring a large local variation in the magnetic field, we suggest a new configuration that represents one novel feature of this thesis. A schematic drawing of this configuration is shown in figure **1.2-1**. The new probe configuration introduces a grid at the electromagnet throat in addition to a second electrode, the collector, at its exterior. The new probe employs three principle knobs: the grid voltage, the collector voltage, and the electromagnet current, which we operate by sweeping the grid and the collector voltages while pulsing the electromagnet current on and off.

The grid aids the mirror force by providing an electric "racquet", which can consume the excess parallel energy that the magnetic mirror force cannot. Hence, mirroring of the electrons at the throat is no longer a purely magnetic effect but a combination of magnetic and electric repulsion: $\vec{F} = -\nabla(\mu B - e\Phi)$. This feature enables the hybrid barrier at the grid to discriminate electrons with small pitch-angle without requiring a large local variation in the magnetic field.

In chapter **3**, we demonstrate how the interaction between the electric barrier at the collector and the hybrid barrier at the grid yields the distribution of parallel and perpendicular-gyration speeds. In essence, these barriers are able to restrict the contribution to the current to a local region in the space spanned by the parallel and the perpendicular energies. They isolate the contribution via a second partial derivative of the collector's $I-V$ characteristic with respect to the electrode voltages:

$$f \propto \frac{B_{em}}{B_{\infty}} \frac{\partial^2 I}{\partial V_G \partial V_C}, \qquad \{1.0-1\}$$

with the distribution function evaluated at the energies

$$\begin{pmatrix} U_{//}^{*} \\ U_{\perp}^{*} \end{pmatrix} = \begin{pmatrix} e\left(\Phi_{\infty} - V_C\right) \\ \dfrac{B_{\infty}}{B_{em}} e\left(V_G - V_C\right) \end{pmatrix},$$

where B_{∞} is the background magnetic field, B_{em} is additional magnetic field produced by the electromagnet (at the throat), and V_G and V_C are the voltages on the grid and on the collector, respectively. The upstream energies $U_{//}^{*}$ and $U_{\perp}^{*}$ describe an electron that is able to just barely overcome the hybrid and the electric barriers.

The relaxed requirement on the electromagnet's performance allows for the construction of a more compact diagnostic package, which can be inserted inside the plasma chamber, not only because of its small size, but also because of its relatively benign impact on the background magnetic field topology.

[1.2.1] Drawbacks of employing a grid

The probe has inherent problems, which are all associated with the presence of the grid. Firstly, the reflection of a healthy fraction of the electrons by the grid barrier produces space charge effects in the region between the grid and the collector. These effects are addressed in chapter **4**. The main result of the analysis is the following. As the grid voltage is ramped towards the plasma potential, the increasing electron space charge eventually produces a barrier to the electron flow. This barrier has a complicated dependence on the electrode voltages and on the local magnetic field; and this dependence invalidates the aforementioned relation between the probe current and the

distribution function. In order to prevent the formation of this barrier, we have to limit the operation of the probe to the regime estimated by the following relation:

$$V_G < \Phi_\infty - \frac{T_{//}}{e}\left[1 + 2\ln\frac{b}{10\lambda_{De}}\right],$$

where b is the radius of the beam inside the housing and $T_{//}$ is the *parallel* electron temperature, and λ_{De} is the electron Debye-length.

Secondly, the discrete structure of the grid produces an electric *hole* in the mesh; a difference between the applied voltage and the effective voltage "felt" by the electrons as they reach the grid-plane. In addition, the perturbation introduces an uncertainty in the barrier felt by the electrons, and it scatters their energies as they pass through the mesh. The analysis of chapter **5** demonstrates that the size of the electric hole (as measured in units of $1eV$) for a fine mesh, $r_w << d$, where r_w is the wire radius and d is the wire spacing, is of the order

$$\Delta_0 \sim \left(\frac{1}{2\pi}\ln\frac{d}{2\pi r_w}\right)\frac{d}{\lambda_{De}}T_{//},$$

where we have assumed the practical regime, $d/\lambda_{De} << 1$. In addition, the analysis shows that the smear in the barrier and the diffusion of the electron energies are of the order

$$\delta_0 \sim \frac{1}{2\pi}\frac{d}{\lambda_{De}}T_{//}.$$

Chapter **5** also treats another problem, which is associated with the *thickness* of the wires of the mesh, t; that is, the depth of the wires *normal* to the mesh surface. The wires preferentially absorb electrons with large pitch angle because these electrons gyrate

a larger distance across the field lines before passing through the mesh. The analysis shows that the preferential absorption of these electrons produces a correction to equation **1.0-1**, which involves the contribution of the distribution function over a finite range of perpendicular energies:

$$\Delta f \cong \frac{4t}{\pi d}\sqrt{\frac{B_\infty + B_{em}}{B_{em}}}\int_0^1 \frac{du}{\sqrt{1-u}}\frac{\partial}{\partial u}\left[\sqrt{u}\, f\left(U_{//}^*, U_\perp^* u\right)\right].$$

For $t/d << 1$, this correction can be evaluated recursively.

[1.3] Experimental results of the GEM probe

We designed, built, and inserted a gridded electromagnet probe in the Versatile Toroidal Facility at M.I.T.'s Plasma Science and Fusion Center. The toroidal plasma chamber employed microwaves launched at the electron cyclotron frequency ($2.45GHz \rightarrow B_\infty = 875G$) in order to heat a hydrogen plasma ($n_{gas} \approx 10^{11} cm^{-3}$). The housing for the probe had an entrance aperture radius of $a_E = 3mm$ and a length of $l = 80mm$. The probe employed an inertially cooled electromagnet, which produced a modest field of $B_{em} \cong 100G$, and a mesh composed of tungsten wires. We chose the minimum wire thickness available $t = 5\mu m$ and to keep $t/d << 1$, we chose a wire spacing of $d = 200\mu m$ in the hopes of creating a plasma with $\lambda_{De} \sim 1mm$. However, in order to obtain an appreciable amount of signal, we had to work with a plasma characterized by an electron density and temperature comparable to $10^{10} cm^{-3}$ and $10eV$, respectively. These parameters gave $\lambda_{De} \cong 300\mu m$ and $\rho_e \cong 100\mu m$.

Overall the probe worked reasonably well, although a number of practical problems arose. Firstly, the curvature of the background magnetic field lines in conjunction with the housing's large aspect ratio rendered the alignment with the field lines a practical challenge. Secondly, the fields emanating from the electrically floating structures inside the housing modified the flow area for the low-energy electrons, thereby contaminating their signal. Even so, for larger electron energies, the $I-V$ characteristics demonstrated the basic principles of the probe. They established the interaction between the hybrid barrier at the electromagnet throat and the electric barrier at the collector as predicted by the theory of section **3.3**. The size of the electric hole in the mesh as determined by the characteristics, however, was more than a factor of two greater than our prediction. The discrepancy is attributed to the poor value for the ratio of d/λ_{De}. The characteristics also illustrated the effects of space charge described in chapter **4**, one of which being that the electron flow to the collector becomes space charge limited as the grid voltage is ramped towards the plasma potential.

The non-ideal effects of the mesh and the moderate signal-to-noise level in the data prevented the measurement of the distribution of the perpendicular energies. However, we were able to measure the *parallel* speed distribution with the electrode at the entrance of the housing (a ring) via the aforementioned relation $f_{//} \propto dI/dV$. This distribution was to a good approximation Maxwellian with $T_{//} \cong 7.5eV \pm 10\%$. In addition, we were able to measure the temperature anisotropy for an assumed two-temperature Maxwellian distribution function. As described in section **3.1**, the temperature anisotropy can be determined from the relative change in the current with the field of the electromagnet: $T_{\perp}/T_{//} \propto d\ln I/dI_{em}$, where I_{em} is the current to the

electromagnet. The temperature of the perpendicular-gyration speed distribution was found to be $T_{\perp} \cong 10eV \pm 20\%$.

[1.3.1] The future of this probe

The non-ideal effects associated with the presence of the mesh produce stringent criteria on the parameters characterizing the probe. In particular, to eliminate the effects of space charge, we have to maintain the ratio of b/λ_{De} at a value less than *ten*. Also, to minimize the non-ideal behaviors associated with the discrete structure of the mesh, we should have $d/\lambda_{De} < 0.1$ and $t/d < 0.1$, respectively. With Debye-lengths characterizing lab-plasmas of the order $\lambda_{De} \sim 100\mu m$, we would need a mesh with $d \sim 10\mu m$ and $t \leq 1\mu m$.

We can also alleviate the difficulties of the alignment with the field lines if we reduce the probe's aspect ratio by placing the collector at the electromagnet throat and the grid at the entrance to the housing. The new configuration would help to eliminate the anomalous effects associated with the varying magnetic geometry inside the probe.

---

[i] The Propagation of Electromagnetic Waves in Plasmas, V. L. Ginzburg chapter **6** (1964)
[ii] "Microwave plasma continuous emissions monitor for trace-metals in furnace exhaust", P. P. Woskov, D. Y. Rhee, P. Thomas, & D. R. Cohn, Rev. Sci. Instrum. 67 (10), October 1996
[iii] Thin Film Processes, J. L. Vossen, W. Kern, (1978)
[iv] Principles of Plasma Discharges & Material Processing, M. Lieberman, A. J. Lichtenburg (1994)
[v] Principles of Plasma Diagnostics, I. H. Hutchinson, chapter **3** (1986)
[vi] M .A. Hayes, M. R. Brown, M. A. Kasevich, and R. B. McCowan, Rev. Sci. Instrum. **55**, 928 (1984)
[vii] M.R. Brown, T.E. Sheridan, and M.A. Hayes, J. Appl. Phys. **70**, pp. 5306-5313 (1991)

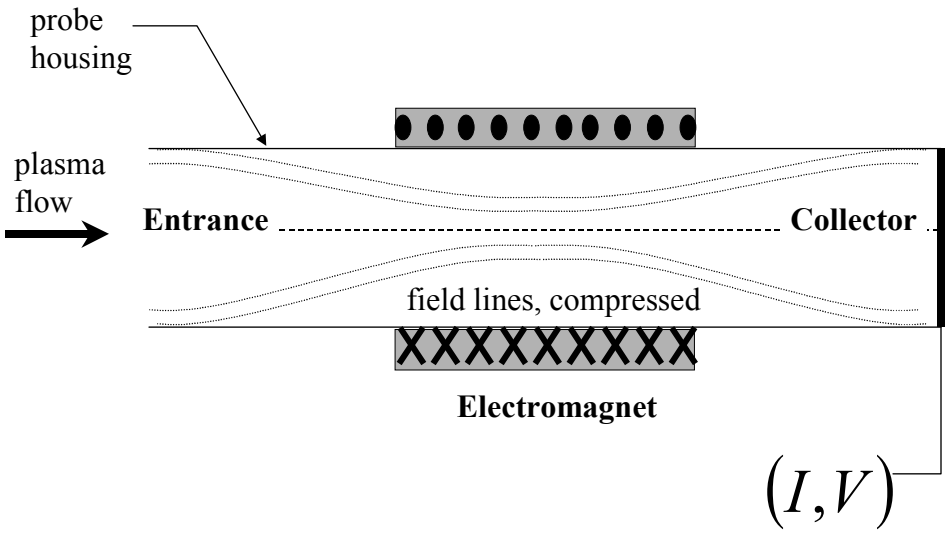

FIGURE 1.1-1: A probe that employs a local variation in the magnetic field

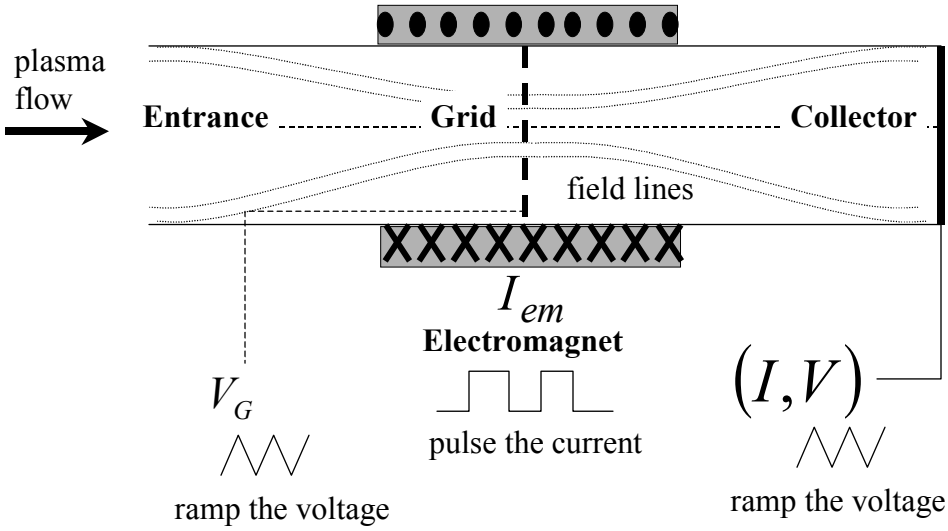

FIGURE 1.2-1: A schematic drawing of the GEM probe

CHAPTER 2

MEASURING THE DISTRIBUTION FUNCTION WITH A PROBE

[2.0] Introduction

In this chapter, we give an overview of the traditional methods for extracting information about the electron distribution function with a probe. Information about the velocity distribution function is obtained primarily with a Langmuir probe[i ii iii]. This probe is in essence a metal collector connected to a voltage source. The probe measures, via a resistor, the variation in the current collected with the applied voltage, also known as the collector's $I-V$ characteristic. A schematic drawing of a Langmuir probe is shown in figure **2.0-1**. The figure also includes a schematic drawing of a typical potential profile in the vicinity of the collector in the regime of practical interest, in which the characteristic size of the collector, a, is much larger than the electron Debye-length λ_{De}. The size of a typically ranges from *millimeters* to *centimeters*; whereas, λ_{De} is typically of the order $100\mu m$.

[2.0.1] The $I-V$ characteristic of the Langmuir probe

A schematic drawing of the collector's $I-V$ characteristic is shown in figure **2.0-2**. The ion contribution to the current is equated to the detected current at a large repulsive bias to the electrons. This current is small and, for $a >> \lambda_{De}$, virtually constant; therefore, its contribution can often be subtracted out. The remaining current drawn comprises electrons that can overcome the electric barrier provided by the collector

voltage. Therefore, the variation in the $I-V$ characteristic should, in principle, give information about the kinetic energy distribution of the electrons.

As the applied voltage approaches the ambient space potential, the barrier to the electrons diminishes. The collector, in theory, absorbs all of the available electron flux, and the current saturates; however, in practice, the large electron sink strongly overheats the probe, thereby raising its temperature to its melting point. The collector then begins to emit electrons thermionically, and its surface begins to recede. These effects produce extraneous variations in the measured current. Moreover, the large electron sink modifies the plasma in its vicinity. This is the nature of the Langmuir probe.

[2.0.2] The probe's intrusive nature

The probe is intrusive because it occupies space inside the plasma region. There is an unintrusive method for measuring the distribution function: Incoherent Thompson scattering[iv]. However, because of the combination of a small cross section for the reaction and the technological limitations on the output power of lasers, the method is impractical for the aforementioned densities (not to mention costly).

The occupation of space by the Langmuir probe creates another surface boundary for the plasma. In order to preserve the dynamics that exists in the absence of the probe, we must maintain the sink of particles to the collector much less than the sink to the plasma boundary. For a plasma in steady state, the net current to the plasma boundary is *zero*; therefore, the electron sink to the boundary is limited by the mobility of the much heavier species, the ions. Hence, we not only need to minimize the collector's surface area, but, in general, we must also maintain the collector voltage well below the ambient

space potential (the plasma potential). By doing so, we can maintain the electron sink comparable to or less than the ion sink. Otherwise, we effectively amplify the probe's collection area, which would significantly deplete the plasma of electrons (the species that ionize the gas), and thereby modify the plasma all together.

Even if we meet the aforementioned criteria, however, the probe will still perturb the plasma in its vicinity with its voltage. In other words, the electron current that is measured is the current provided by a distribution of electrons whose energies have been altered by the probe-induced electric field. Hence, the measurement of the velocity distribution not only requires the preservation of a region that is outside of the realm of the probe's electric perturbation, it also requires the preservation of information about the velocity distribution as the electrons travel from this quiescent region to the collector.

[2.0.3] The principles for the measurement of the distribution function

To retrieve information about f from the collector's $I-V$ characteristic, we need to understand the way in which the probe perturbs what it intends to measure. In the following sections, we review the theory of this perturbation as described by Hutchinson [ref. 1]. Here, we give the basic principles behind the measurement of the electron distribution function.

The electron current *leaving* the collector can be expressed as an integral of the electron distribution function over the collector surface area; that is,

$$I_e = e\int dA_C \int_{\hat{n}\cdot\vec{v}_C<0} d^3v_C \hat{n}\cdot\vec{v}_C f_C \,, \qquad \{2.0-1\}$$

where $\hat{n}$ is the unit vector normal to the collector surface and the subscript, C, denotes the value at the collector. To obtain information about the distribution function in the ambient, f_∞, we must relate f_C to f_∞.

The evolution of the velocity distribution function from the ambient to the collector is governed by Liouville's theorem. The theorem, which is discussed by Landau[v], states that the differential volume in phase space [$d^3x d^3v$] following a group of particles remains constant. Therefore, the number density in phase space, f, along the path of this group remains constant as well; that is,

$$df/dt = 0,$$

where the derivative is taken along the particle orbit.

To connect the distribution functions in the ambient and at the collector then, we need to connect the electron paths in phase space. This procedure requires that the electrons suffer no collisions; otherwise their paths will change in ways that cannot be accounted for deterministically. For the plasmas of interest, $T_e > 1eV$ and the ionization fraction is less than 10%. These parameters render the electron mean-free-path governed mainly by collisions[a] with neutral atoms as described by $\lambda_{mfp} \approx 5cm/P_{gas}$, where the gas pressure is in units of $1mtorr$ ($\cong 10^{13} cm^{-3}$). The gas pressure is typically less than $1mtorr$ (for our plasma, $P_{gas} \cong 10\mu torr$). Consequently, as long as the probe's electric perturbation remains of the order of the probe size, the electron flow from the ambient to the collector will remain collisionless; that is, $\lambda_{mfp} >> a$. This collisionless behavior

[a] NRL Plasma Formulary, revised 1994, p.39

allows us to exploit the Vlasov equation to connect the electron distribution functions in the ambient and at the collector.

The Vlasov equation is described by $df/dt = 0$ with the background electric and magnetic fields governing the force that guides the electrons. For an ambient distribution function that is homogeneous in space and time and fields that are static, the Vlasov equation readily yields the distribution function in the vicinity of the collector. The result can be expressed formally as

$$f(\vec{r},\vec{v}) = f_\infty(\vec{v}_\infty), \qquad \{2.0-2\}$$

with the relation between the arguments determined by the constants of motion. *If* the electrons suffer no collisions during their journey from the ambient to the collector, then equation **2.0-2** gives an excellent approximation for f because (aside from the fluctuations, which average to zero), the fields and the distribution function vary insignificantly during the period of the journey.

[2.0.4] The electric perturbation

To validate the use of the Vlasov equation for connecting f_C to f_∞ in equation **2.0-1**, we need to gauge the extent of the electric perturbation. The perturbation is produced in the following manner. The electrons, being much more mobile, contribute most of the initial current to the collector surface. The influx of the electrons produces a negative surface charge on the collector, and the induced electric field reduces the subsequent electron flow and accelerates the ions to the surface. The electric field profile is governed by the spatial profile of the electron and ion densities via Poisson's equation:

$$\nabla^2\Phi = -e(n_i - n_e),$$

where Φ is the electric potential (we have assumed that the ions are singly charged). These densities are, in turn, determined by the evolution of their velocity distribution functions because

$$n = \int d^3v f(\vec{r}, \vec{v}). \qquad \{2.0-3\}$$

Therefore, to calculate the potential profile, we need to know the distribution functions in the ambient; knowledge we don't have. However, because the densities are functions of the first moment of f, they are not too sensitive to the details of the distribution, which allows us to use generic (sensible) models for f_e and f_i.

In the next section, we estimate the extent of the perturbation in a plasma without a background magnetic field to validate the use of the Vlasov equation. We then show how to extract the electron density and temperature of an assumed Maxwellian electron distribution function when the signal-to-noise level in the data is too low for the measurement of f_e. Lastly, we discuss the methods for measuring f_e, itself. In section **2.2**, we repeat the analysis for a plasma *with* a background magnetic field. In particular, we conclude that for the case where the electrons are magnetized ($\rho_e \sim \lambda_{De}$), the Langmuir probe *cannot* inform us about the electrons' perpendicular-gyration speed distribution, which then leads us to the next chapter, where we discuss a series of electromagnet probes.

[2.1] The Langmuir probe in a plasma *without* a background magnetic field

In this section, we discuss the utility of the Langmuir probe in a plasma without a background magnetic field. In particular, we show how the probe extracts the density and the temperature of an assumed Maxwellian electron distribution function as well as

the speed distribution of an f_e that is isotropic in velocity space. We then suggest that the existence of an isotropic velocity distribution is unlikely for a plasma immersed in a background magnetic field and discuss our options for extracting a generic velocity distribution.

[2.1.1] The extent of the electric perturbation for $B_\infty = 0$

To solve Poisson's equation for the extent of the perturbation, we model the electron distribution function in the ambient to be Maxwellian with temperature, T_e:

$$f_\infty(U_\infty) \cong \frac{n_\infty}{\pi^{3/2} v_{te}^3} \exp(-U_\infty / T_e)$$

with $v_{te} \equiv \sqrt{2T_e/m_e}$ and with the subscript, ∞, signifying the quiescent region. This model is adequate because the electron density obtains most of its contribution from its low-energy population. This population is generally thermal, and it is mirrored by the field of the collector in the practical range $e(\Phi_\infty - V_C) > T_e$.

We then note that the electron path in phase space is governed by the conservation of total energy: $U + q\Phi = \text{constant}$, where $U \equiv m v^2/2$ is the particle's kinetic energy and q is its charge. The isotropy in the distribution function enables us to use this single constant of motion in the Vlasov equation to find $f_C(U_C) = f_\infty(U_\infty)$, where $U_\infty = U_C + e(\Phi_\infty - V_C)$. These relations then give the following generic formula for the electron density in the probe's vicinity:

$$n_e = \int d^3v f \cong 4\pi \int_0^\infty dv v^2 f_\infty(U + e[\Phi_\infty - \Phi]), \qquad \{2.1-1\}$$

where Φ_∞ is the plasma potential. For the specific case of a Maxwellian distribution, equation **2.1-1** becomes

$$n_e \cong n_\infty \exp(-\chi) \qquad \{2.1-2\}$$

with $\chi = e(\Phi_\infty - \Phi)/T_e$.

If the geometry of the perturbation is one-dimensional, then the ion density profile can be approximated from the equations for the conservation of current and of energy for a *cold* fluid; a fluid without thermal energy: $f_\infty = n_\infty \delta(\vec{v}_\infty)$, where δ denotes a *delta* function. This model is more or less valid in the entire region of the perturbation, where $T_i << e(\Phi_\infty - \Phi)$. The ion temperature in our plasma is approximately $T_i \cong 0.2eV$.

Using the definition for the fluid velocity, $\vec{u}_i \equiv (1/n_i)\int d^3v\vec{v}f$, we obtain

$$n_i = \Gamma_i / u_i \qquad \{2.1-3\}$$

with

$$u_i = \sqrt{2e(\Phi_\infty - \Phi)/m_i} \qquad \{2.1-3a\}$$

and

$$\Gamma_i = I_i / eA, \qquad \{2.1-3b\}$$

where I_i is the ion current and A is the ion collection area.

The densities produce the following approximation to Poisson's equation in the collector's vicinity, where the potential contours are essentially one-dimensional:

$$\chi'' = \delta n / \lambda_{De}^2 \qquad \{2.1-4\}$$

with

$$\delta n = k(2\chi)^{-1/2} - \exp(-\chi), \qquad \{2.1-4a\}$$

$$k = \frac{I_i}{en_\infty \sqrt{T_e / m_i}\, A}, \qquad \{2.1-4b\}$$

and $\chi'' \equiv d^2\chi / dz^2$.

The equation reveals that any departure from quasi-neutrality would have to occur in the vicinity of the collector surface on the scale of λ_{De}. If the electric field that emanates from the collector vanishes within a distance comparable to λ_{De}, then the ion collection area, A, would remain more or less equal to A_C, the area of the collector. However, this simple 1-D picture cannot be satisfied.

Firstly, in the practical regime where the probe is biased to mirror the electrons, the probe modifies the ion distribution function in its vicinity from that in the ambient because it absorbs all incoming ions. The component of the ion population in the ambient that is moving away from the collector surface (which generates half of the density) would have to be replenished somehow. Secondly, even if the aforementioned ions were replenished, the ion density would still fall below that of the electrons as the attractive electric field accelerates the ions towards the collector. The disparity in the densities would produce the *wrong* sign for χ'', which would prevent the potential from decreasing from its ambient value to the voltage at the collector.

To avoid these difficulties, the solution to the potential profile requires that the ion collection area expand with distance from the collector. Such a configuration would compress the ion density as the ions travel from the ambient to the collector. The compression would then counter the expansion effect of the acceleration, thereby maintaining the ion density comparable to the density of the electrons and allowing a *quasi-neutral solution* up to within a few Debye lengths from the collector surface.

For the planar collector that is depicted in figure **2.0-1**, the expansion in the collection area renders the geometry for the perturbation multi-dimensional. This area expansion generally complicates the variation in the ion density. To circumvent this complexity, we model the collector surface as a hemisphere, which produces a 1-D geometry for the ion flow to the collector as depicted in figure **2.1-1**. In this configuration, k is a function of the distance r. It is described by equation **2.1-4b** with $A = 2\pi r^2$. The incoming ion current, I_i, is set equal to that associated with a half-Maxwellian:

$$I_i = eA_\infty n_\infty \sqrt{T_i/(2\pi m_i)}, \qquad \{2.1-5a\}$$

where $A_\infty = 2\pi r_\infty^2$ is the collection area in the ambient. The determination of this area then gives the extent of the electric field, r_∞.

The area A_∞ is governed by the drive for quasi-neutrality, $n_e \cong n_i$, which by using equation **5.1-4a** can be expressed as $k(r) = \sqrt{2\chi}\exp(-\chi)$ with $Ak = A_C k_C$. In our spherical geometry, the solution is given by $r^2 = a^2 \exp(\chi - \chi_C)\sqrt{\chi_C/\chi}$, where $\chi_C = e(\Phi_\infty - V_C)/T_e$. The potential profile is plotted in figure **2.1-2** for various collector voltages. The plots show that as V_C decreases below Φ_∞, the perturbation extends into the plasma. This effect increases the ambient collection area, A_∞, which, in turn, increases the ion current to the collector:

$$I_i = en_\infty \sqrt{T_e/m_i}\, A_C k_C. \qquad \{2.1-5b\}$$

The ion current continues to increase with the drop in the collector voltage until $V_C = \Phi_s$, where $\Phi_s \equiv \Phi_\infty - T_e/2e$. As illustrated in figure **2.1-3**, quasi-neutrality can no longer

hold up to the collector surface for $V_C < \Phi_s$, and a sheath forms to carry the potential from Φ_s to V_C over a distance comparable to λ_{De}. The breakdown of quasi-neutrality virtually pins the value of k_C to the value at the sheath because the ion collection area does not vary significantly inside the sheath. The value of k at the sheath boundary is given by $k_s = k(\chi_s) = \exp(-0.5)$.

Hence, for $V_C < \Phi_s$, the ion current to the collector remains fixed, thereby fixing the ion collection area and the extent of the electric perturbation. Setting equations **2.1-5a** and **2.1-5b** equal for $V_C = \Phi_s$ gives

$$r_\infty \sim \left[2\pi(T_e/T_i)\exp(-1)\right]^{1/4} a\,.$$

The value of r_∞ for our plasma is about $3a$, which then validates the assumption of a collisionless regime.

[2.1.2] Extracting n_e and T_e from the $I-V$ characteristic

The electron density and temperature for an assumed Maxwellian distribution function are obtained from the ion and the electron currents. The ion current to the collector in the practical range, $V_C < \Phi_\infty - T_e/2$, is found by evaluating equation **2.1-5b** with $k_C = k_s$:

$$I_i = I_{si} \equiv en_\infty A_C \sqrt{T_e/m_i}\,\exp(-1/2). \qquad \{2.1-6\}$$

The electron current *leaving* the collector is found by first inserting the relation $f_C(U_C) = f_\infty(U_\infty)$ in equation **2.0-1** to find

$$I_e = A_C \frac{2\pi e}{m_e^2} \int_{e(\Phi_\infty - V_C)}^{\infty} dU_\infty \left[U_\infty - e\left(\Phi_\infty - V_C\right)\right] f_\infty\left(U_\infty\right), \qquad \{2.1-7\}$$

where we have used $dU_C = dU_\infty$ and $\int d^3 v_C \hat{n} \cdot \vec{v}_C = -dv_C v_C^3 \int d\phi d\theta \sin\theta \cos\theta$, which equals $-\pi dv_C v_C^3$. For a Maxwellian distribution function then, equation **2.1-7** gives

$$I_e = I_{se} \exp\left[-e\left(\Phi_\infty - V_C\right)/T_e\right] \qquad \{2.1-7a\}$$

with

$$I_{se} \equiv e n_\infty A_C \sqrt{T_e/\left(2\pi m_e\right)} \qquad \{2.1-7b\}$$

equal to the electron saturation current (for $V_C \geq \Phi_\infty$). The net current *leaving* the collector is then $I = I_e - I_i$.

In practice, the electron temperature is obtained from an exponential fit to the current near $V_C \cong V_f$, where V_f is the collector voltage at which the net current to the collector is *zero*. The density is then obtained by inserting the value of the temperature into the robust relation for the *ion* saturation current. We will apply these results in the next section, where we discuss the operation of the Langmuir probe in a magnetized plasma.

[2.1.3] Extracting an *isotropic* electron distribution function

The planar collector has no angular resolution because it absorbs electrons from all directions (in a hemisphere) as shown schematically in figure **2.1-4**. Moreover, the field that emanates from the collector surface does not, in general, remain normal to this surface in the pre-sheath. Therefore, the collector neither limits the collection of electrons to one direction nor impacts the electron energies in one direction. As a result,

the Langmuir probe's $I_e - V$ characteristic can only inform us about a velocity distribution function that is isotropic; a plausible distribution for a plasma without a background magnetic field. In such a case, the speed distribution is extracted[vi] from equation **2.1-7** via the operation

$$f_\infty\left(U^*\right) = \frac{m_e^2}{2\pi e^3 A_C}\frac{d^2 I_e}{dV_C^2} \qquad \{2.1-8\}$$

with $U^* = e\left(\Phi_\infty - V_C\right)$.

[2.1.4] Extracting an *an-isotropic* distribution function for a *weak* B_∞

As the background magnetic field in the plasma increases, the electrons become magnetized with a gyro-radius less than the characteristic size of the plasma. For such plasmas, the likelihood of an electron distribution function that is isotropic in velocity space diminishes.

The measurement of a generic velocity distribution requires a directional analyzer. Stenzel[vii] *et al*. developed such an analyzer composed of micro-channels. A schematic drawing of a channel is shown in figure **2.1-5**. The large aspect ratio of the channel localizes the contribution to the direction normal to the electrode surface. If we can neglect the curvature in the electron orbits, then equation **2.1-8** readily yields the speed distribution in this direction if we replace the factor of 2π with the solid angle of the *view*, $\pi\left(a/l\right)^2$, where a and l are the radius and the length of the channel, respectively.

However, the curvature in the electron orbits renders the available solid angle for passage through the channel dependent on the channel's orientation with respect to $\vec{B}_\infty$,

thereby complicating the relation between f_∞ and the collector current. Moreover, the measurement of the velocity distribution in the plane normal to $\vec{B}_\infty$ is limited to electrons that can reach the end of the channel; that is, to electrons with $\rho_e \equiv v_{te}/(eB_\infty/m_e) > l^2/16a$, where $v_{te} = \sqrt{2T_e/m_e}$. Therefore, the channel dimension must satisfy the following criteria: $a < 2(\Delta\Omega/4\pi)\sqrt{T_e}/B_0$ and $l = 0.5\,a/\sqrt{\Delta\Omega/4\pi}$, where a is in units of $1mm$, B_∞ is in units of $1kG$, T_e is in units of eV, and $\Delta\Omega/4\pi$ is equal to the angular resolution. The bound on the channel radius practically limits the use of the analyzer to plasmas with weak magnetic fields (Stenzel's group used the analyzer in a plasma with $B_\infty < 20G$).

For plasmas that employ *strong* magnetic fields, we may use the planar Langmuir probe by aligning its collector surface normal to the magnetic field vector for the measurement of the distribution of speeds parallel to the magnetic field line. We can do this because the strong magnetic field decouples this distribution from the one for the electrons' perpendicular gyro-motion. This limit is the topic of the next section.

[2.2] The Langmuir probe in a plasma *with* a *strong* background magnetic field

In this section, we discuss the utility of the Langmuir probe in a plasma immersed in a background magnetic field. We demonstrate that the probe can inform us about the distribution of electron speeds *parallel* to the field line when the electron gyro-radius is much smaller than the radius of the collector; the situation of interest. In particular, we show how the probe extracts the density and the *parallel* temperature for an assumed Maxwellian parallel distribution function. Furthermore, we demonstrate that the probe

can extract the *parallel* speed distribution as well. We begin the section by analyzing the probe's electric perturbation.

[2.2.1] The extent of the electric perturbation for a strong B_∞

As the background magnetic field increases from *zero*, it first impacts the electron flow to the collector because the magnitude of the electric force on the two species is the same, whereas the magnitude of the magnetic force on the electrons is stronger by the factor $\sqrt{m_i/m_e}$. The ratio of the magnetic to the electric forces on the electrons is approximately equal to the ratio of the electron Debye-length to the electron Larmor radius:

$$\lambda_{De}/\rho_e \approx B/\sqrt{10^{-11} n_e},$$

where B is in units of $1kG$ and n_e is in units of $1cm^{-3}$. For our plasma, where $n_e \approx 10^{10}\, cm^{-3}$, the magnetic force on the electrons becomes significant for $B > 100G$.

For the collector surface oriented normal to the field lines, the electric and the magnetic forces on the electrons are uncoupled. In this case, the magnetic force serves to effectively limit the flow of the electrons to the direction along the field line, which, in turn, limits the electric field that emanates from the collector to the magnetic flux tube that intersects the collector surface. A schematic drawing of the potential contours for this case is shown in figure **2.2-1**.

As demonstrated in section **2.1**, the ambient ion flux is minuscule as compared to the ion flux at the sheath, demanded by quasi-neutrality. Therefore, the pre-sheath has to extend along the field line to collect ions from the edge of the flux tube (to effectively

amplify the collection area). For $\rho_i > a$, the ions are essentially swept into the flux tube by the attractive electric field, as was the case for $B = 0$. On the other hand, for $\rho_i << a$, the ions are strongly magnetized. Hence, they would have to diffuse across the field lines to enter the flux tube. If the rate of diffusion is weak, then the pre-sheath will extend to great lengths to attract the ions to the collector. We would like to estimate this length so that we can establish the criterion for the collionless regime.

The analysis of the pre-sheath for $\rho_e << a$ is described by Hutchinson[viii]; and it is shown in some detail in appendix **2.2x**. The calculation yields an implicit relation for the pre-sheath potential profile:

$$\hat{z} \equiv \int_{-\infty}^{z} dz'/L \cong \exp(-2\chi/3)\sqrt{8\chi}/\pi \qquad \{2.2-1\}$$

with $\chi = e(\Phi_\infty - \Phi)/T_{//}$ and $\hat{z}$ equal to the distance to the collector, *normalized* to the characteristic length of the pre-sheath,

$$L \equiv \frac{A_C}{p}\frac{n_\infty\sqrt{T_{//}/m_i}}{\Gamma_i}. \qquad \{2.2-2\}$$

Here, Γ_i is the cross field ion flux entering the magnetic flux tube, p is the perimeter of the flux tube (normally the circumference of the collector), and $T_{//}$ is the electron parallel temperature.

The potential profile is illustrated in figure **2.2-2**. The figure shows that the electric field becomes infinite for $V_C = \Phi_s$, where now $\Phi_s \cong \Phi_\infty - 0.85T_{//}/e$ (see equation **2.2x-5**). Hence, for $V_C \le \Phi_s$, a sheath forms, thereby pinning the length of the pre-sheath to about $L/2$ (if we assume a constant ion source rate). This length was found by setting $\chi = \chi_s$ in equation **2.2-1**, which gives $\hat{z}_s \cong 0.5$.

For $\rho_i \sim a$, we can estimate L by setting Γ_i in equation **2.2-2** equal to the ion flux from a half-Maxwellian:

$$L/2 = \frac{a}{4}\frac{n_\infty \sqrt{T_{//}/m_i}}{\Gamma_i} \sim 0.6a\sqrt{T_{//}/T_i} \cong 4a\,,$$

where we have assumed that the collector is a circle with radius a.

In the opposite regime, $\rho_i << a$, the source is estimated by the flux from cross-field diffusion via ion-neutral collisions: $\Gamma_i \approx D\,n/a$ with $D = \left(v_{ti}/\lambda_{mfp}\right)\rho_i^2$, where $v_{ti} = \sqrt{2T_i/m_i}$ and λ_{mfp} is the mean-free-path for ion collisions with neutrals. This flux is weak relative to the flux from the ions' thermal energy, which implies that we would have to rely on turbulence to maintain $L \sim a$ (the contribution from the ionization[b] of the neutral gas within the flux tube is negligible). Hence, to guarantee that $L \sim a$ without the aid of anomalous diffusion, the ion Larmor radius must be of the order or greater than a; a relation that is marginally satisfied by our probe: $\rho_i \sim 1mm$, whereas $a \cong 5mm$.

[2.2.2] Extracting n_e and $T_{//}$ from the $I-V$ characteristic

The electron density and parallel temperature are obtained from the ion and the electron currents to the collector. The ion current in the practical regime where a sheath has formed is equal to

$$I_{si} \cong 0.5eA_C n_\infty \sqrt{T_{//}/m_i}\,. \qquad \{2.2-3\}$$

[b] NRL Plasma Formulary, revised 1994, p.54

Equation **2.2-3** is a consequence of inserting $\hat{z}_s \cong 0.5$ into equation **2.2x-6**. The expression in equation **2.2-3** is the same as the one in equation **2.1-6**, with $T_e \to T_{//}$ and with $\exp(-0.5) \to 0.5$.

The electron current *leaving* the collector is determined by equation **2.0-1** (with the collector surface oriented normal to $\vec{B}_\infty$):

$$I_e = e\int dA_C \int\limits_{v_{//}^C>0} d^3v_C v_{//}^C f_C$$

with $d^3v_C = dv_{//}^C d^2v_\perp^C$ and with the subscripts denoting the directions parallel and perpendicular to the magnetic field vector. For $\rho_e << a$, the electric field essentially impacts the motion along the field line. The electric field normal to $\vec{B}$ induces drifts in the electron motion, but the magnitude of the drift speed is of the order ρ_e/a relative to the speed of the gyro-motion, and thereby minuscule. With the perpendicular energy a virtual constant of the motion, the Vlasov equation in conjunction with the constant of motion, $U_{//} - e\Phi$, gives

$$I_e = \frac{2\pi e}{m_e^2} A_C \int\limits_{U_{//}^\infty > e(\Phi_\infty - V_C)} dU_{//}^\infty dU_\perp^\infty f_\infty , \qquad \{2.2-4\}$$

where we have gyro-averaged the distribution function,

$$\int d^2v_\perp f = \int dv_\perp v_\perp \oint d\phi f \to \int dv_\perp v_\perp 2\pi f .$$

Equation **2.2-4** assumes that the contribution to the current from cross-field diffusion is negligible. This assumption is necessary because the electrons that diffuse into the pre-sheath do so via collisions or via the aid of transient fields. The assumption

is valid in practice because the electron and ion flux (which determines the length of the pre-sheath) from cross-field diffusion tend to be comparable.

For a separable electron distribution function, $f_\infty = f_{//} f_\perp$, where the parallel distribution function $f_{//}$ is Maxwellian,

$$f_{//M} = n_\infty \left(2\pi T_{//}/m_e\right)^{-1/2} \exp\left(-U_{//}^\infty/T_{//}\right)$$

and $2\pi \int dv_\perp^\infty v_\perp^\infty f_\perp = \left(2\pi/m_e\right)\int dU_\perp^\infty f_\perp \equiv 1$, equation **2.2-4** yields the same expression for the electron current as equation **2.1-7a**, but with T_e replaced by $T_{//}$. The parallel temperature is obtained via a fit of a straight line to $\ln\left(I_e\right) - V$. The value of the temperature is then used in equation **2.2-3** to obtain the density. This observation is shown graphically in figures **2.2-3a** and **2.2-3b** for an $I - V$ characteristic obtained in our plasma (where the electrode area was $22mm^2$). The fit gives $T_{//} \cong 7.5eV$ and $n_e \cong 5 \cdot 10^9 cm^{-3}$.

Ideally, we would obtain the plasma potential by observing the voltage at which the electron current saturates (as described by equation **2.1-7b**). However, as V_C approaches Φ_∞, the large electron sink to the collector generally depletes the flux tube of electrons (this affects the rate of ionization of the neutral gas). As a result, the electron current decreases below what is predicted by equation **2.1-7a** as illustrated by a comparison of the current and the exponential fit in figure **2.2-3b**. Moreover, the current does not quite saturate because the probe modifies the dynamics in the plasma.

Therefore, in practice, the plasma potential is estimated by the cross-point of the fit to $\ln\left(I_e\right) - V$ and the line that is tangent to the slope for the remnant variation in the

electron current, as shown in figure **2.2-3b**. This estimate gives $\Phi_\infty \cong 25V$. This value is then corroborated by a second estimate, which is derived from the voltage at which the fit to $\ln(I_e) - V$ corresponds to $\ln(I_{s//})$, where $I_{s//} = en_\infty A_C \sqrt{T_{//}/2\pi m_e}$. This current is estimated from the product of $I_{si} \cong 200\mu A$ and the theoretical ratio of the electron-to-ion saturation currents as determined by equations **2.1-7b** and **2.2-3**. For a Hydrogen plasma, $I_{s//} \cong I_{si}\sqrt{2m_i/\pi m_e} \cong 7mA$, which corresponds to a voltage of $30V$. Therefore, we conclude that $25V \le \Phi_\infty \le 30V$. Notice that the fit to the characteristic yields the product $I_{s//} \exp(e\Phi_\infty / T_{//})$. Therefore, if we choose $\Phi_\infty = 25V$, the corresponding electron saturation current would be $I_{s//} \cong 3.5mA$.

[2.2.3] Extracting the *parallel* distribution function

Taking the derivative of equation **2.2-4** with respect to the collector voltage relates the differential in the current to a general electron distribution function f_∞ at the parallel energy $U_{//}^* = e(\Phi_\infty - V_C)$. If the parallel and perpendicular energy distributions are separable, then

$$f_{//}\left[U_{//}^*\right] = \frac{m_e}{e^2 A_C}\frac{dI_e}{dV_C}. \qquad \{2.2-5\}$$

Equation **2.2-5** is a manifestation of the equivalence (to within a constant factor) between the parallel energy distribution and the distribution of the electron current. In fact, we find that working with the latter distribution is more convenient. Using the definition,

$$dI_e = eA_C dv_{//} v_{//} f_{//} \equiv dU_{//} F_{//},$$

produces the simple relations $I_e = \int_{e(\Phi_\infty - V_C)}^{\infty} dU_{//}^\infty F_{//}$ and

$$F_{//}\left[U_{//}^{*}\right]=\frac{1}{e}\frac{dI_e}{dV_C}. \qquad \{2.2-6\}$$

The distribution of current is plotted in figure **2.2-4** along with its Maxwellian counterpart.

[2.3] Conclusion

In this chapter, we have demonstrated the utility of the Langmuir probe. We have shown that for a plasma without a background magnetic field, the probe can measure the density and the temperature of an assumed Maxwellian electron distribution function as well as the speed distribution of a generic isotropic velocity distribution function. We then discussed the limitations imposed by a background magnetic field. We demonstrated that for the case where the electrons are magnetized with respect to the size of the collector, the probe is able to extract information about the distribution of speeds parallel to the field line.

In particular, if this distribution is Maxwellian, then the electron current *leaving* the collector is equal to

$$I_e = I_{s//}\exp\left[-e\left(\Phi_\infty - V_C\right)/T_{//}\right],$$

with $I_{s//} = en_\infty A_C\sqrt{T_{//}/2\pi m_e}$. Notice that the parallel temperature is obtained experimentally from the following operation:

$$T_{//} = e\,dV_C/d\ln I_e.$$

We also found that the drive for quasi-neutrality produces a robust relation for the ion current to the collector for the practical regime where a sheath has formed:

$$I_{si} \cong 0.5en_\infty A_C\sqrt{T_{//}/m_i},$$

which together with the parallel temperature gives the electron density n_∞.

Moreover, for a generic distribution function whose parallel and perpendicular speed distributions are uncoupled, we found that the differential in the electron current yields the parallel speed distribution, which is to within a constant factor equal to the *distribution of electron current* along the field line in the space of the parallel energies:

$$F_{//}\left[e\left(\Phi_\infty - V_C\right)\right] = \frac{1}{e}\frac{dI_e}{dV_C},$$

where $F_{//} \equiv \left(eA_C / m_e\right) f_{//}$.

In order to extract information about the electrons' perpendicular energy distribution, the probe must provide a barrier to the electrons that involves $U_\perp$. In the next chapter, we discuss how to provide such a barrier by exploiting the adiabatic invariance of the electron's magnetic moment.

---

[i] Principles of Plasma Diagnostics, I. H. Hutchinson, chapter **3** (1986)
[ii] Plasma Diagnostics Vol. (1), O. Auciello, D. L. Flamm, chapter **3** (1989)
[iii] Plasma Diagnostic Techniques, R. H. Huddlestone, S. L. Leonard, chapter **4** (1965)
[iv] Principles of Plasma Diagnostics, I. H. Hutchinson, chapter **7** (1986)
[v] Mechanics 3rd edition, L.D. Landau and E.M. Lifshitz , pp. 146-147
[vi] F. F. Chen, Plasma Diagnostic Techniques (1965)
[vii] R.L. Stenzel, W. Gekelman, N. Wild, J.M. Urrutia, and D. Whelan, Rev. Sci. Instrum. **54**, 1302 (1983)
[viii] I. H. Hutchinson, Principles of Plasma Diagnostics, pp. 67-71

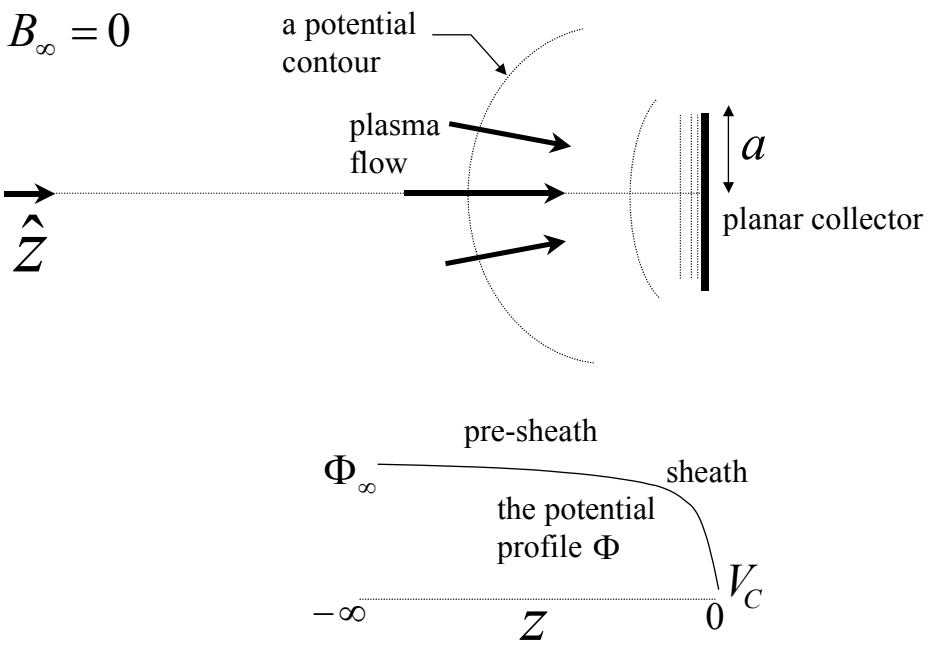

FIGURE 2.0-1: A schematic drawing of a planar Langmuir probe

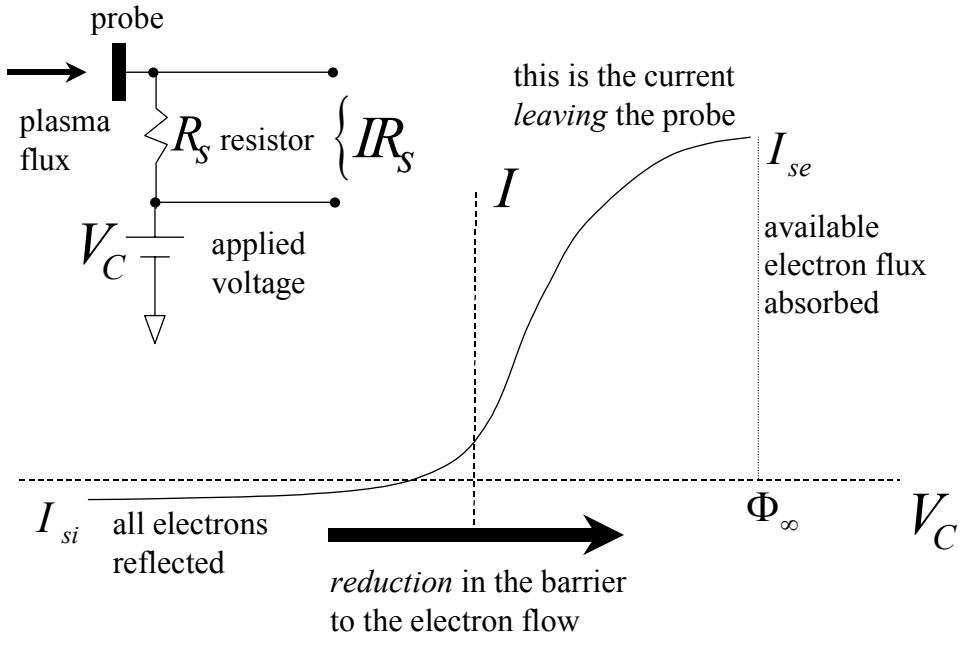

FIGURE 2.0-2: The current-voltage characteristic of a Langmuir probe.

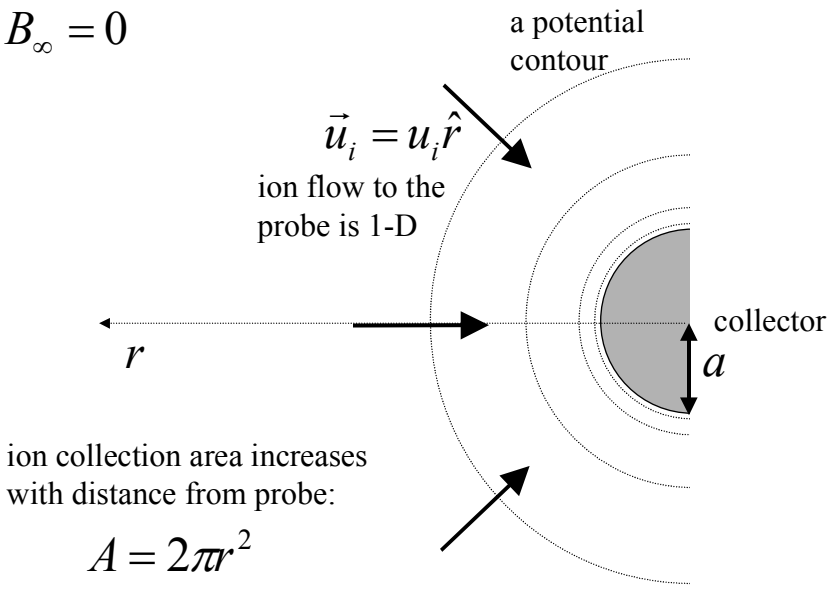

FIGURE 2.1-1: A schematic drawing of the model hemispherical probe

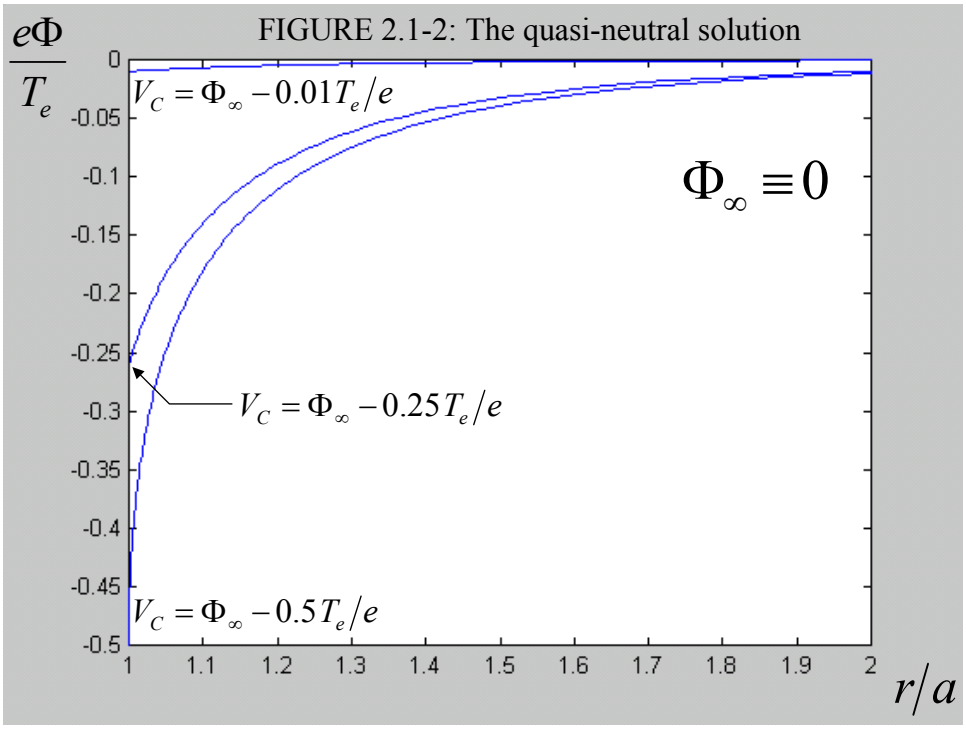

FIGURE 2.1-2: The quasi-neutral solution

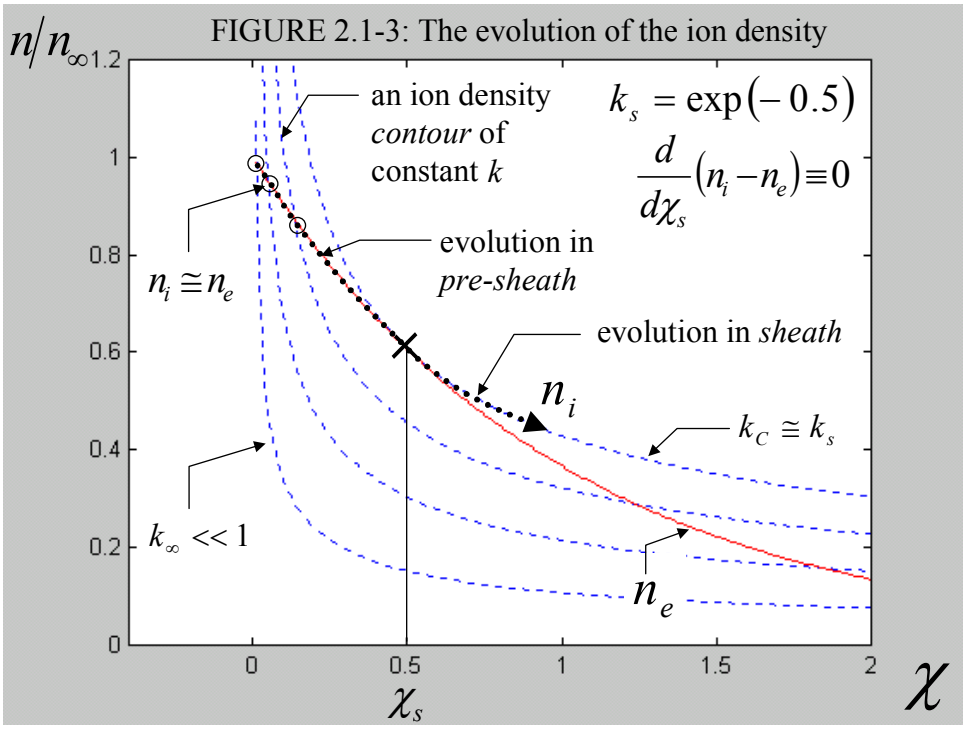

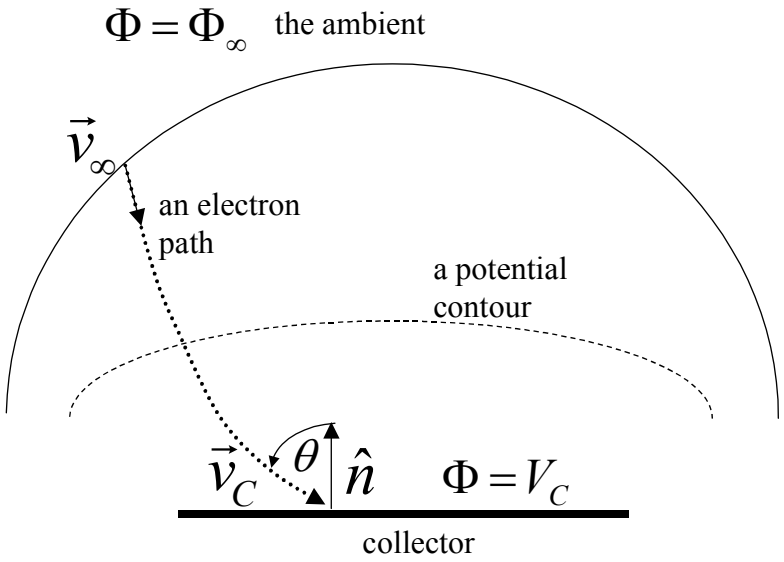

FIGURE 2.1-4: The geometry for the measurement of the electron *speed* distribution with a planar collector

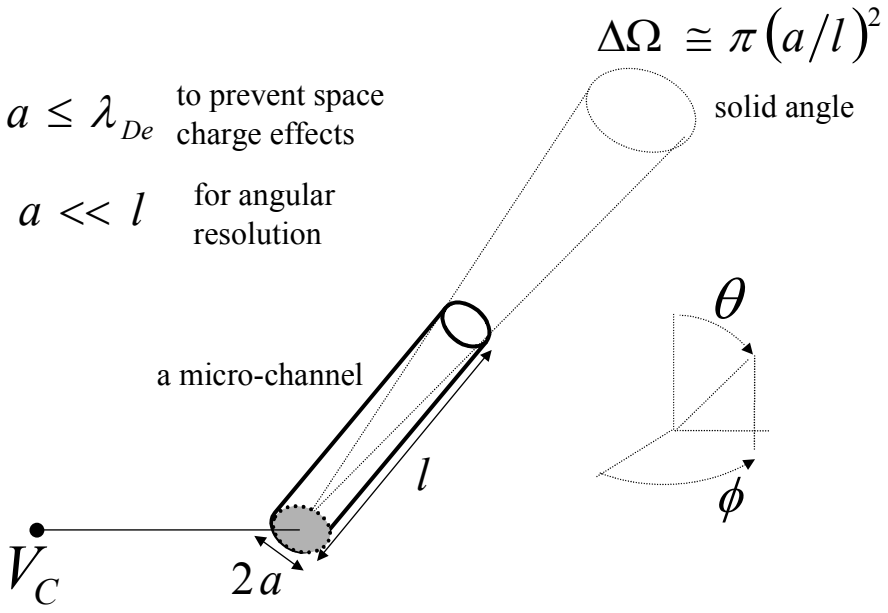

FIGURE 2.1-5: The geometry of a directional analyzer

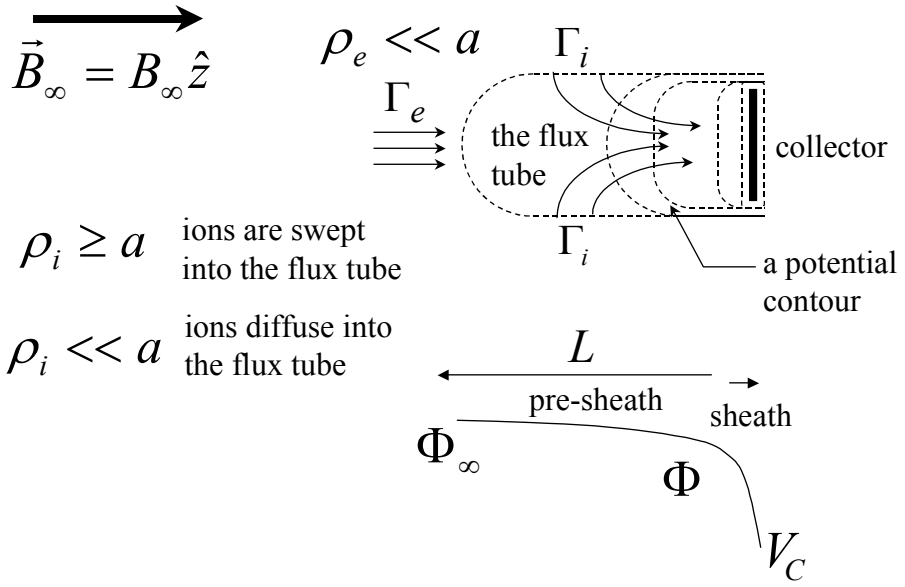

FIGURE 2.2-1: The geometry for the potential contours and the plasma flow to the collector for *magnetized* electrons

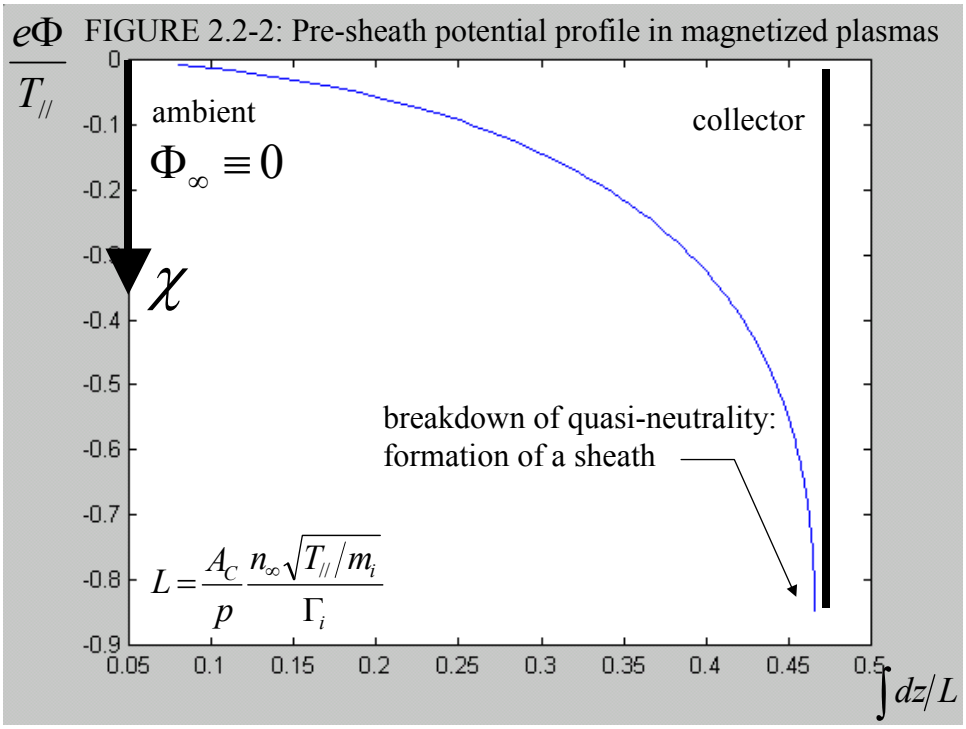
$\frac{e\Phi}{T_{//}}$
FIGURE 2.2-2: Pre-sheath potential profile in magnetized plasmas
ambient
$\Phi_\infty \equiv 0$
collector
χ
breakdown of quasi-neutrality:
formation of a sheath
$L = \frac{A_C}{p} \frac{n_\infty \sqrt{T_{//}/m_i}}{\Gamma_i}$
$\int dz/L$

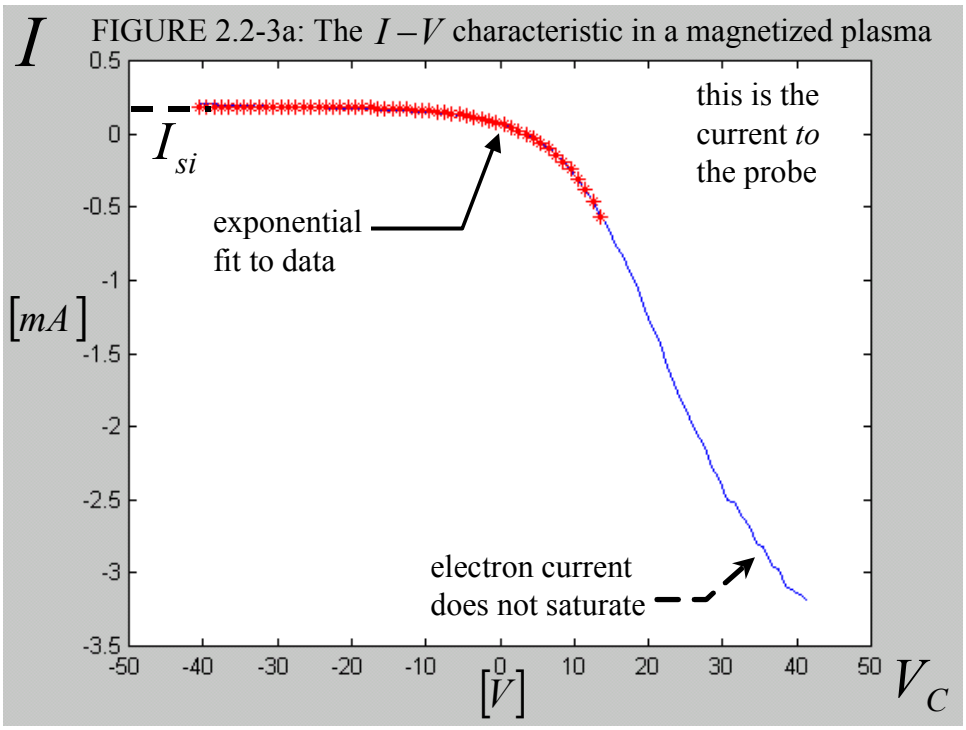
I
FIGURE 2.2-3a: The $I-V$ characteristic in a magnetized plasma
I_{si}
this is the
current *to*
the probe
exponential
fit to data
electron current
does not saturate
$[mA]$
$[V]$
V_C

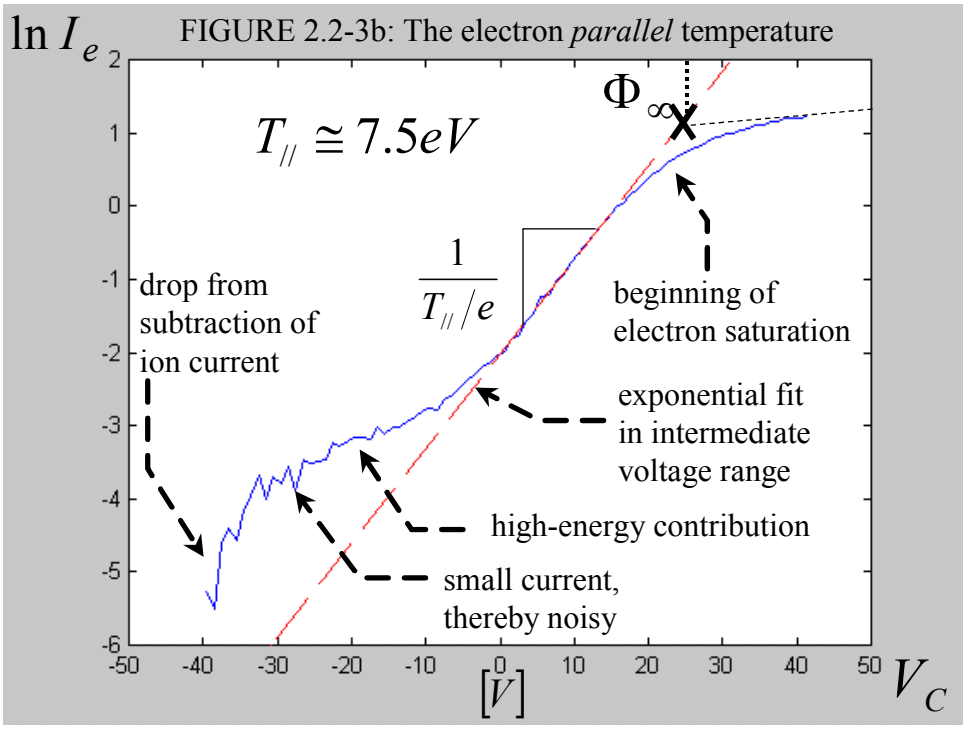

FIGURE 2.2-3b: The electron *parallel* temperature

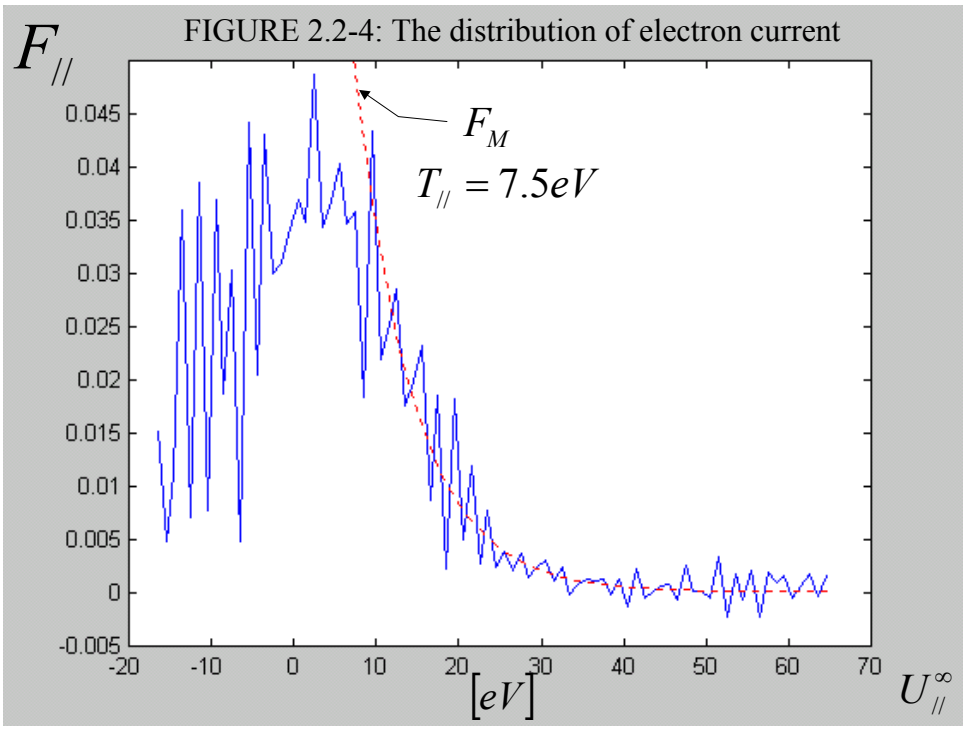

FIGURE 2.2-4: The distribution of electron current

CHAPTER 3

MEASURING THE ANISOTROPY IN THE ELECTRON VELOCITY DISTRIBUTION IN A MAGNETIZED PLASMA

[3.0] Introduction

In the previous chapter, we concluded that the Langmuir probe, as it stands, cannot extract any information about the electrons' perpendicular-gyration speed distribution for the case where ρ_e and λ_{De} are comparable; the case for our plasma. The reason is that the electric field that emanates from the probe essentially impacts the speed along the field line. In order to extract information about $f(v_{//}, v_{\perp})$, the barrier that the probe provides to the electrons must involve their perpendicular-gyration speeds as well. In other words, the electron's $v_{\perp}$ must impact $v_{//}$, its speed towards the probe. In this chapter, we discuss a series of probes that exploit the adiabatic invariance of the magnetic moment in order to couple the two speeds.

The magnetic moment,

$$\mu \equiv U_{\perp} / B ,$$

is equal to the ratio of the perpendicular-gyration energy to the magnetic field strength experienced by the particle. It is also proportional to the magnetic flux trapped by the gyro-orbit. Its invariance arises from the periodicity[i] of the particle's gyro-motion in phase space.

The conservation of μ produces a force (called the magnetic mirror force) on the particle's motion along the field line as the particle travels through a region with a spatially inhomogeneous magnetic field. The magnetic field cannot exchange energy

with the particle so the mirror force is necessary to conserve the particle's total energy (kinetic plus electrostatic).

The result is that the electron's path in phase space is constrained by the following "constants" of motion: μ and $\mathrm{K} \equiv U_{//} + U_{\perp} - e\Phi$. Using the definition of μ, the total energy can be represented as

$$\mathrm{K} = U_{//}^{\infty} + \mu B_{\infty} - e\Phi_{\infty}.$$

The term, *constant*, is placed in quotes because the magnetic moment is not an exact invariant, as we will address shortly.

The conservation of the magnetic moment and of the total energy produces an effective potential energy for the motion along the field line, which we define as

$$P \equiv \mu\left(B - B_{\infty}\right) - e\left(\Phi - \Phi_{\infty}\right), \qquad \{3.0-1\}$$

where the potential energy is measured relative to its ambient value. The effective potential is a sum of an electric and a magnetic component. In order for the electrons to reach the probe, their ambient parallel energy must overcome the resulting potential *hill* along their journey to the probe. If the maximum potential energy that is gained by the electron does not vary from one field line to another, then the electron current to the probe can be represented as

$$I_e = \int_0^{\infty} dU_{\perp}^{\infty} \int_{\max[P]}^{\infty} dU_{//}^{\infty} F_{\infty} \qquad \{3.0-2\}$$

with

$$F_{\infty} \equiv \frac{2\pi e A_C}{m_e^2} f_{\infty}. \qquad \{3.0-2a\}$$

[3.0.1] The adiabatic invariance of the magnetic moment

The quantity μ exhibits oscillations[ii] about its ambient value μ_∞ since it is an adiabatic invariant rather than a constant of the motion. These oscillations are dependent on the gradients in the electric potential and in the magnetic field. The magnitude of these oscillations scale as ρ_e/L relative to μ_∞, where L is the scale length for the aforementioned gradients; and they vanish only when both $\vec{E}\times\vec{B}=0$ and $d\vec{B}/dt=0$, where the derivative is taken along the electron's path. The ratio of ρ_e/L is of the order $100\mu m/1cm = 0.01$ for our experimental conditions.

The oscillations in the magnetic moment will have no net impact on the current to the probe because they average to zero. However, μ also exhibits a *secular* variation; that is, it exhibits a finite *jump*[iii] as the electron travels through a region with $\vec{B} \neq const$. This jump, however, is practically insignificant because its logarithm scales as

$$\ln(\delta\mu/\mu) \approx -L/\rho .$$

Therefore, in practice, we can treat μ as a constant of the motion.

[3.0.2] The addition of an electromagnet to the Langmuir probe

The probes that we address in the subsequent sections use an electromagnet to locally vary the magnetic field. The on-axis profile of the field produced by the electromagnet is shown in figure **3.0-1**. The collector for the probes is placed away from the regions with large gradients in the magnetic field: $z=\pm L_{em}$; otherwise, the field lines would be skewed with respect to the probe surface-normal [$B_r \cong -(r/2)dB_z/dz$, where r represents the distance from the electromagnet axis]. This would couple the electric and

the magnetic force, thereby invalidating the assumption that $d\mu/dt = 0$ because ρ_e/L would become of the order $\rho_e/\lambda_{De} \sim 1$.

In addition, in practice, the field is *increased* inside the electromagnet to maintain the electron collection area independent of the local changes in the magnetic topology. The variation in this area with the local magnetic field is shown schematically in figure **3.0-2**.

[3.0.3] The *barrier* to the electron current

Different probe geometries provide different potential hills for the electrons. The shape of the hill varies with the placement of the collector relative to the electromagnet throat. The *top* of the hill is no longer located, in general, at the collector surface; the location of maximum electric potential energy gained by the electrons. The location and the magnitude of the peak now vary with the electron's ambient perpendicular gyration energy.

The spatial evolution of the potential energy can be represented as

$$P = \alpha(z)U_{\perp}^{\infty} + \Theta(z), \qquad \{3.0-3\}$$

where we have defined

$$\alpha \equiv B/B_{\infty} - 1 \qquad \{3.0-3a\}$$

and

$$\Theta \equiv e(\Phi_{\infty} - \Phi). \qquad \{3.0-3b\}$$

Then, the line described by $U_{//}^{\infty} = P(z)$ describes the electrons that come to rest at the location z (and are subsequently reflected). The parametric relation between $\Theta(z)$ and

$\alpha(z)$ is responsible for the translation and rotation of the line, and it dictates the ultimate shape of the *barrier*, or equivalently the boundary for current contribution. That is, it dictates whether it will be a multi-segmented polygon or even a curve in energy space.

In the following sections, we determine the *barrier* for a sequence of increasingly complex probe configurations, leading up to the configuration that renders this thesis novel: the *GEM* probe. For each configuration, we derive a relation among the current, the applied fields, and the temperature anisotropy for a two-temperature Maxwellian distribution function:

$$F_M \equiv \frac{I_{s//}}{T_\perp T_{//}} \cdot \exp\left[-\frac{1}{T_{//}} \left(U_{//}^{\infty} + U_\perp^{\infty} / \beta \right) \right], \qquad \{3.0-4\}$$

where $I_{s//} = eA_C n_\infty \sqrt{T_{//} / 2\pi m_e}$ and

$$\beta \equiv T_\perp / T_{//} \qquad \{3.0-4a\}$$

is the *temperature anisotropy*. We then demonstrate how each configuration is able to extract information about a general electron distribution function.

[3.1] Placing a collector inside the electromagnet (the M probe)

The first arrangement is discussed by Boyd[iv] *et.al* and is depicted in figure **3.1-1**. It is the placement of a collector at the throat of the electromagnet where the magnetic field is a maximum ($\alpha > 0$). Then, the electric and the magnetic components of the potential energy both increase to their maximum value at the collector. This arrangement renders the barrier indifferent to the profiles of the electric and the magnetic field leading up to the collector.

[3.1.1] The formation of a single, hybrid barrier

In this case, the barrier is a straight line, given by $U_{//}^{\infty} = \Theta_C + \alpha_0 U_{\perp}^{\infty}$ with $\Theta_C = e\left(\Phi_{\infty} - V_C\right)$ and $\alpha_0 = \left(B_0 - B_{\infty}\right)/B_{\infty} = B_{em}/B_{\infty}$, where the subscripts C and 0 denote the values at the collector and at the throat, respectively. In this configuration, the two subscripts happen to denote the same location. This barrier specifies the relation described by equation **3.0-2** as follows:

$$I_M = \int_{\Theta_C}^{\infty} dU_{//}^{\infty} \int_0^{\frac{\Theta_C - U_{//}^{\infty}}{\alpha_0}} dU_{\perp}^{\infty} F_{\infty} \; . \qquad \{3.1-1\}$$

[3.1.2] The $I-V$ characteristic for a bi-Maxwellian distribution

For a bi-Maxwellian distribution, equations **3.0-4** and **3.1-1** yield the following relation between the collector current and the applied fields:

$$I_M = I_{s//} \frac{\exp\left(-\chi_C\right)}{1+\alpha_0 \beta} \qquad \{3.1-2\}$$

where

$$\chi \equiv \Theta / T_{//} \; . \qquad \{3.1-3a\}$$

The current of equation **3.1-2** is equal to the exponential drop, $I_{s//} \exp\left(-\chi_C\right)$, reduced by the current removed by the magnetic mirror force, $\Delta I_M = \gamma_0 I_{s//} \exp\left(-\chi_C\right)$, where

$$\gamma_0 \equiv \frac{\alpha_0 \beta}{1+\alpha_0 \beta} \; . \qquad \{3.1-3b\}$$

The quantity $\Delta I_M \equiv I_M\big|_{\alpha=0} - I_M$ is the contribution that is removed from the *triangle* that is depicted in figure **3.1-1**; and the quantity γ_0 is a measure of the *efficiency* with which the compression in the magnetic field reflects the electrons. This quantity

increases with the temperature anisotropy because the magnetic component of the barrier is more effective for electrons with large *pitch angle*: electrons with large $U_{\perp}^{\infty}/U_{//}^{\infty}$.

[3.1.3] Extracting the temperature anisotropy

The temperature anisotropy β is obtained from the relative change in the current with the local increase in the magnetic field since

$$\beta = \frac{1}{\alpha_0}\frac{\Delta I_M}{I_M}. \qquad \{3.1-4\}$$

This method does not require a significant modification to the ambient magnetic field. Hence, it places little stress on the electromagnet's capability. Therefore, even though it yields only *global* information (in energy space), we believe that this method is the most useful because it significantly extends the diagnostic capability of the Langmuir probe in magnetized plasmas without much engineering effort. In other words, the *M* probe is *the* diagnostic configuration to be employed for the measurement of the temperature anisotropy in magnetized plasmas.

[3.1.4] Extracting information about a general distribution function

In fact, the *M* probe can also deliver local information about a generic distribution function. In general, equation **3.1-1** produces the following relations for the variations in the electron current with α and Θ :

$$\frac{dI_M}{d\alpha_0} = -\int_0^{\infty} dU_{\perp}^{\infty} U_{\perp}^{\infty} \breve{F}_{\infty}, \qquad \{3.1-5a\}$$

$$\frac{dI_M}{d\Theta_C} = -\int_0^{\infty} dU_{\perp}^{\infty} \breve{F}_{\infty}, \qquad \{3.1-5b\}$$

where the distribution inside the integral, $\breve{F}_{\infty}$, is evaluated along the line $U_{//}^{\infty} = \Theta_C + \alpha_0 U_{\perp}^{\infty}$. In the limit $\alpha \to 0$, the ratio of these two expressions yields the average perpendicular energy of the electrons within a narrow parallel energy band, $U_{//}^{\infty} = \Theta_C$; that is,

$$\left\langle U_{\perp}^{\infty} \right\rangle = \left. \frac{dI_M / d\alpha_0}{dI_M / d\Theta_C} \right|_{\alpha_0 = 0} . \qquad \{3.1-6\}$$

The integral described by equation **3.1-5b** can, in principle, yield the distribution function, itself, via an Abel-inversion technique[v] mentioned by Boyd. The philosophy of this method can be understood by regarding $dI_M / d\Theta_C$ as a chord average of photon intensities emanating from a plasma with F_{∞} representing the emissivity. The method, however, is somewhat impractical because it requires a relatively complicated inversion procedure in addition to a large increase in the local magnetic field for measurements at large "viewing" angles: $\arctan(\alpha_0) > 45^{\circ}$. The latter requirement burdens the electromagnet's heat removal capability, thereby driving the production of a bulky diagnostic package. In the next section, we discuss a configuration that eliminates the former difficulty by producing a relatively simple inversion technique.

[3.2] Placing a collector outside the electromagnet (the EM probe)

In this section, we demonstrate how the removal of the collector from the electromagnet throat simplifies the inversion technique for determining F_{∞}. In essence, the removal of the collector from the mid-plane separates the locations of maximum electric and magnetic potential energies gained by the electron. The separation segments

the barrier in two and provides independent motion to each segment. The independent control then allows the barrier to locally dissect the energy space to yield the distribution function.

[3.2.1] The formation of two pure barriers

Figure **3.2-1** shows a schematic drawing of the *EM* probe. This probe was first exploited by Hayes *et. al.*[vi]. The barrier that is shown in the figure for this probe is *ideal*. The actual barrier is, in general, dependent on the parametric relations, $[\Theta(z),\alpha(z)]$. We address this problem at the end of the section.

In order to understand the resulting shape of the ideal barrier, we follow the evolution of the *line* described by $U_{//}^{\infty} = P(z)$ in figure **3.2-1**. First, the *line* rotates clockwise as the magnetic field increases to its maximum value at the throat. This movement sweeps out the electrons with large pitch angle. The *line* subsequently rotates counter-clockwise as the magnetic field decreases to its ambient value at the collector. In this region, the ideal evolution neglects any potential drop inside the pre-sheath as well as any remnant magnetic field associated with the electromagnet. Lastly, the electric field in the sheath translates the *line* to the value of the electrostatic energy at the collector. This movement removes electrons with small parallel energies.

The resulting barrier has two segments: one that is electric, controlled by the collector voltage; and one that is magnetic, controlled by the electromagnet current. The barrier in conjunction with equation **3.0-2** then gives the following expression for the collector current:

$$I_{EM} = \int_{\Theta_C}^{\infty} dU_{//}^{\infty} \int_0^{U_{//}^{\infty}/\alpha_0} dU_{\perp}^{\infty} F_{\infty} \,. \qquad \{3.2-1\}$$

[3.2.2] The $I-V$ characteristic for a bi-Maxwellian distribution

For a bi-Maxwellian distribution, we obtain the following for the relation between the current and the applied fields:

$$I_{EM} = I_{s//} \exp(-\chi_C) - \Delta I_{EM} \qquad \{3.2-2\}$$

with

$$\Delta I_{EM} = I_{s//} \gamma_0 \exp(-\chi_C/\gamma_0). \qquad \{3.2-2a\}$$

The exponential dependence of ΔI_{EM} is different from the one associated with the *M* probe. This difference can be understood via a graphic comparison of the current in the (triangular) area removed by the local increase in the magnetic field. The value of ΔI_{EM} is smaller because the electric component of the barrier would have removed most of the electrons that are being removed by the magnetic component. Therefore, the contribution to ΔI_{EM} is limited to electrons with large perpendicular and parallel energies.

In addition, ΔI_{EM}'s exponential dependence on γ renders this configuration a poor choice for the measurement of the temperature anisotropy because it subjects the derived value to the uncertainties in the value of χ_C. On the other hand, this configuration has the ability to dissect the energy space in order to obtain the distribution function itself.

[3.2.3] Extracting a general distribution function

Figure **3.2-2** demonstrates the *EM* barrier's ability to localize the contribution to the current in energy space. An incremental change in the electric barrier removes the

contribution within a band comprising electrons that have a narrow range of parallel energies. For a larger magnetic field, however, the removal of current from this band is lessened by electrons within a narrow range of parallel and perpendicular energies. The result is that the distribution function is equal to

$$F_{\infty}^{*} = \frac{\alpha_0^2}{\Theta_C} \frac{\partial^2 I_{EM}}{\partial \alpha_0 \partial \Theta_C}, \qquad \{3.2-3\}$$

where the *star* denotes the evaluation of the energies at the joint of the two segments; that is, where

$$\begin{pmatrix} U_{//}^{*} \\ U_{\perp}^{*} \end{pmatrix} = \begin{pmatrix} \Theta_C \\ \Theta_C / \alpha_0 \end{pmatrix}. \qquad \{3.2-3a\}$$

[3.2.4] The non-ideal behavior and practical difficulties

As already mentioned, the ideal barrier neglects the electrostatic energy associated with the pre-sheath as well the remnant magnetic field at the collector, associated with the electromagnet. The remnant magnetic field (through its variation with α_0) will prevent the second partial derivative from localizing the contribution to the current. This field, however, can be reduced arbitrarily by increasing the electromagnet aspect ratio or by increasing the distance between the collector and the electromagnet throat. In fact, it can be eliminated all together by using another current carrying coil to cancel the field produced by the electromagnet.

However, we do not have the same control over the electric potential inside the electromagnet. The analysis of the potential profile in magnetized plasmas in section **2.2** demonstrated that the sheath condition demands a pre-sheath potential drop of $0.85 T_{//}/e$

(for $B = const$). This drop must occur before the entrance to the probe housing because the source of the electric field in the pre-sheath is the ion source rate, and this rate vanishes inside the housing. Therefore, for $\alpha = 0$, the potential inside the electromagnet is constant, either equal to the probe voltage for $V_C > \Phi_s$ or pinned to Φ_s for $V_C \le \Phi_s$.

If the densities inside the housing were not influenced by the local increase in the magnetic field, then the pre-sheath potential drop would impart just a translation, equal to $\Theta_s = 0.85 T_{//}$, to the magnetic component of the barrier. In other words, the pivot for the magnetic arm would no longer be at the origin. Instead, it would be located at $\left(U_{//}^{\infty}, U_{\perp}^{\infty}\right) = \left(\Theta_s, 0\right)$. The finite Θ_s would modify equation **3.2-3** by transforming Θ_C to $\Theta_C - \Theta_s$; and it would alter the value of $U_{\perp}^{*}$ to $\left(\Theta_C - \Theta_s\right)/\alpha_0$. An implication of these modifications would be that the *EM* probe could not measure the distribution function for $U_{//}^{\infty} < \Theta_s$ because the two components of the barrier would not be able to form a cross-point in this region.

However, these are not the only modifications. The local variation in the magnetic field will impact the densities inside the housing (*space charge effects*), which, in turn, modifies Θ_s. The variation in Θ_s will not prevent the second partial derivative from localizing the contribution to the current, but it will modify the area in gray in figure **3.2-2**. The net result is that in addition to the aforementioned modifications, the coefficient to the second partial derivative in equation **3.2-3** will acquire the factor, $\left[1 + \alpha_0 \, \partial\Theta_s / \partial\alpha_0 / \left(\Theta_C - \Theta_s\right)\right]^{-1}$.

Aside from the uncertainties that plague the magnetic arm of the barrier, the *EM* probe requires a large electromagnet current in order to distinguish electrons with small

pitch angle. This difficulty is depicted graphically in figure **3.2-3**, which illustrates the region of accessibility in energy space for the measurement of the distribution function.

[3.2.5] The experimental results with the EM probe

Hayes[vii] *et.al*. employed this configuration as an end-analyzer (the probe outside the plasma region) to determine the distribution function in a low density and temperature ($n_e < 10^{10} cm^{-3}$, $T_e < 10eV$) plasma powered by microwaves at the electron cyclotron frequency of $1.5Ghz$ ($B_\infty = 540G$). The active cooling of the electro-magnet coil (with liquid nitrogen) enabled them to increase the field at the electro-magnet throat to four times the ambient value. This increase produced a $\max(\alpha_0) = 3$, which enabled them to access about 80% of the energy-space.

Their analysis, however, did not account for the pre-sheath potential drop and its variation with the magnetic field for the large values of α employed. In addition, their bulky diagnostic package did not allow them to place the probe inside the plasma for a (spatially) local determination of the distribution function. In fact, they had to employ "zeroing" coils to eliminate the field produced by the electromagnet inside the plasma as well as at the collector. In the next section, we describe our probe, which alleviates the burden on the electro-magnet's performance.

[3.3] The addition of a grid electrode inside the electromagnet (the GEM probe)

In this section, we analyze a probe configuration that produces a barrier, which is able to distinguish electrons, regardless of their pitch angle. This probe enlists the aid of a *grid* electrode at the electromagnet throat in addition to a *collector* placed at the exterior

of the electromagnet. The addition of the grid electrode produces a hybrid barrier at the throat, which relieves the electromagnet current of producing all of the mirror force needed to reflect the electrons on the basis of their perpendicular energies.

[3.3.1] The formation of two barriers, one of which is a hybrid

The schematic diagram of the gridded electromagnet (GEM) probe and the ideal barrier that it provides are depicted in figure **3.3-1**. The figure illustrates the ideal evolution of the *line* described by $U_{//}^{\infty} = P(z)$. First, the *line* rotates clockwise as the magnetic field increases to its maximum at the grid. During this motion, the *line* also translates as the electrostatic energy increases to Θ_G (where the subscript, G, denotes the value at the grid). The end result of this motion is independent of the parametric relations, $\left[\Theta(z,)\alpha(z)\right]$. However, for the evolution of the *line* to remain ideal, its electric component *cannot* increase beyond Θ_G *before* the magnetic field has reached its ambient value at the collector. Otherwise, the barrier will have additional structure and can no longer be represented by the two segments shown in the figure. The condition for the ideal evolution will be met as long as the potential profile inside the region sandwiched by the grid and the collector remains in the *vacuum* regime. This regime is described in chapter **4**.

The ideal boundary is composed of two segments, as was the case for the *EM* probe. The difference is the definite translation in the pivot of the "magnetic" segment, which we now refer to as the hybrid segment. The hybrid component of the barrier is able to mirror electrons with small pitch angle as well, thereby enabling the measurement of the distribution function in the entire energy space.

The two-segmented barrier in conjunction with equation **3.0-2** yields the following expression for the electrode current:

$$I_C = \int_{\max[\Theta_C,\Theta_G]}^{\infty} dU_{//}^{\infty} \int_0^{\left(U_{//}^{\infty}-\Theta_G\right)/\alpha_0} dU_{\perp}^{\infty} F_{\infty} \ . \qquad \{3.3-1\}$$

[3.3.2] The $I-V$ characteristic for a bi-Maxwellian distribution

For a bi-Maxwellian distribution, we obtain the following relation between the current and the applied fields:

$$I_C = I_{s//} \exp\left(-\max\left[\chi_C, \chi_G\right]\right) - \Delta I_C \qquad \{3.3-2\}$$

with

$$\Delta I_C = I_{s//}\gamma_0 \exp\left(-\chi_G\right)\exp\left(-\frac{\max\left[\chi_C,\chi_G\right]-\chi_G}{\gamma_0}\right). \qquad \{3.3-2a\}$$

For $\Theta_C < \Theta_G$, the potential energy at the grid provides the barrier regardless of the electron's energies, and all of the current that passes through the grid (the *first* pass, which we define as I_+) contributes to the collector. In other words, the collector voltage is superfluous. In this regime, the GEM probe is equivalent to the M probe. As expected, equation **3.3-2** reduces to the expression described by equation **3.1-2**. Therefore, this probe has the ability to measure the temperature anisotropy in the M-regime: $\Theta_C < \Theta_G$.

On the other hand, for $\Theta_G = 0$, the GEM probe mimics the EM probe. Then, equation **3.3-2** becomes the expression described by equation **3.2-2**. Therefore, the probe also has the ability to measure the distribution function in the EM-regime: $\Theta_C > \Theta_G$.

[3.3.3] Extracting a general distribution function

In addition to the method used in section **3.2** to dissect the energy space for the determination of the distribution function, the *knob* associated with the grid voltage allows for another method as shown in figure **3.3-2**. This method is similar to the one depicted in figure **3.2-2** for the EM probe. The difference is that the dissection is being performed by the electrode voltages with α_0 maintained finite, but constant.

The result is that the second partial derivative with respect to the applied voltages yields the distribution function:

$$F_\infty^* = \alpha_0 \frac{\partial^2 I_C}{\partial\Theta_G \partial\Theta_C}. \qquad \{3.3-3\}$$

The *star* denotes the evaluation of the energies at the joint of the hybrid and the electric segments of the barrier; that is, where

$$\begin{pmatrix} U_{//}^* \\ U_\perp^* \end{pmatrix} = \begin{pmatrix} \Theta_C \\ (\Theta_C - \Theta_G)/\alpha_0 \end{pmatrix}. \qquad \{3.3-3a\}$$

Here, we have assumed that we are in the applicable regime: $\Theta_C > \Theta_G$.

[3.3.4] The benefits of employing a grid

The grid enables the barrier to distinguish electrons with small pitch angle *without* the need for a large electromagnet current. This identification is done simply by reducing the difference between the electrode voltages, as illustrated in figure **3.3-3**. Hence, the barrier provided by the *GEM* probe allows for the measurement of the distribution function over the entire energy space with a value for α that is practical. The reduced demand on the electromagnet current allows for the production of a compact diagnostic

package with an inertially cooled electromagnet. The small size, in turn, enables the insertion of the probe inside the plasma chamber for a spatially localized measurement of the distribution function.

In addition, the grid voltage pins the electrostatic energy at the throat, thereby rendering the barrier free of the uncertainties that plague the previous configuration. Furthermore, the inversion technique for this configuration does not require that the magnetic field return to its ambient value at the collector because the second partial derivative is with respect to the electrode voltages. A finite difference between the magnetic field at the collector and B_∞ would introduce a tilt in the electric component of the barrier. This tilt would simply modify the relations described by equations **3.3-3** and equations **3.3-3a** as follows: $\alpha_0 \to \alpha_0 - \alpha_C$,

$$U_\perp^* \to (\Theta_C - \Theta_G)/(\alpha_0 - \alpha_C),$$

and

$$U_{//}^* \to (\alpha_0\Theta_C - \alpha_C\Theta_G)/(\alpha_0 - \alpha_C),$$

where α_C is the increase in the field at the collector due to the electromagnet, normalized to the ambient magnetic field. The above transformations can be understood by carrying out the analysis in the coordinate $U_{//}^\infty - \alpha_C U_\perp^\infty$ as opposed to $U_{//}^\infty$.

[3.3.5] The duality between the grid and the collector currents

The grid current provides yet another benefit. In principle, the duality between the grid and the collector currents enables I_G to inform us about the distribution function as well. This duality stems from the following fact: the grid receives a *second* pass

contribution, which we label as I_-, from the current that is reflected by the collector, as shown in figure **3.3-4**. That is,

$$I_G = I_+ + I_-, \qquad \{3.3-4a\}$$

whereas

$$I_C = I_+ - I_-, \qquad \{3.3-4b\}$$

where I_C is given by equation **3.3-1**. In fact, the component, I_-, is the one that yields the distribution function because the collector voltage does not impact I_+ ($d_{\Theta_C} I_+ = 0$). Notice that I_+ can be obtained from equation **3.1-1** by setting Θ_C equal to Θ_G. The indifference of I_+ to Θ_C produces the following relation: $\partial_{\Theta_C} I_G = -\partial_{\Theta_C} I_C$, which by using equation **3.3-3** gives

$$F_\infty^* = -\alpha_0 \frac{\partial^2 I_G}{\partial\Theta_G \partial\Theta_C}. \qquad \{3.3-5\}$$

[3.3.6] A remark about the grid's non-ideal behavior

This ideal hybrid configuration seems superior to the other two. However, the mesh of wires comprising the grid behaves neither as a transparent medium for the electron flow nor as a planar (opaque) electrode. As we demonstrate in chapter **5**, the mesh produces an electric field with a spatial perturbation, which stem from the discrete structure of the mesh. This perturbation has a component that impacts the electrons' perpendicular energies. Therefore, only a fraction of the applied field at the grid impacts the electrons' momentum along the field lines, and this fraction is path dependent. The mesh is also a medium that preferentially absorbs electrons with large pitch angle. The

variable mesh opacity modifies the distribution function downstream from the grid-plane, which complicates the inversion process for obtaining F_∞.

Lastly, the removal of a healthy fraction of the electrons by the grid barrier produces space charge inside the grid-collector cavity. As we demonstrate in the next chapter, the effects of space charge eventually produce an unwanted barrier to the electron flow as the grid voltage is increased to the plasma potential. The prevention of this regime then places an upper bound on the grid voltage, thereby restricting the operation of the probe.

[3.4] Conclusion

In chapter **2**, we demonstrated that by discriminating electrons with the electric force, we can obtain information about the electron parallel distribution function in magnetized plasmas. In particular, for a Maxwellian parallel distribution, we obtained the following relation for the collector's $I-V$ characteristic:

$$I = I_{s//} \exp\left(-\chi_C\right)$$

with $\chi_C \equiv \Theta_C / T_{par}$ and $\Theta_C = e\left(\Phi_\infty - V_C\right)$, where the subscript C denotes the value at the collector.

In this chapter, we considered three probe configurations that employ an electro-magnet to increase the local magnetic field. These probes exploit the magnetic mirror force in conjunction with the electric force that is provided by the classic Langmuir probe to determine the anisotropy in the electron distribution function in magnetized plasmas. Here, we summarize their *ideal* behavior, and, in particular, their $I-V$ characteristic for a bi-Maxwellian electron distribution function with $\beta \equiv T_\perp / T_{//}$.

In section **3.1**, we demonstrated that by placing a collector at the electromagnet throat, we produce a single hybrid (electric-magnetic) barrier that can readily yield the electron temperature anisotropy from the $I-V$ characteristic:

$$I_M = \left[1 - \frac{\alpha_0 \beta}{1+\alpha_0 \beta}\right] I_{s//} \exp\left(-\chi_C\right),$$

where $\alpha_0 = B_{em}/B_\infty$ with B_∞ equal to the field in the ambient. The temperature anisotropy is obtained from the *reduction* in the electron current with the local increase in the magnetic field, ΔI_M :

$$\beta = \frac{1}{\alpha_0}\frac{\Delta I_M}{I_M}$$

For $\alpha_0 \to 0$, this configuration can also readily give the average perpendicular energy of electrons with $U_{//}^{\infty} = \Theta_C$ via the operation

$$\left\langle U_{\perp}^{\infty} \right\rangle = \left. \frac{\partial I_M / \partial \alpha_0}{\partial I_M / \partial \Theta_C} \right|_{\alpha_0 = 0}.$$

Thus, the *M* probe is a rather simple extension of the Langmuir probe, which can deliver some detailed information about the distribution of the perpendicular energies.

In section **3.2**, we discussed the configuration described by a collector placed outside of the electro-magnet housing. This arrangement is referred to as the *EM* probe. We found that the *EM* probe produced a barrier with a magnetic and an electric segment. The dual-segmented barrier produced the following relation for the $I-V$ characteristic:

$$I_{EM} = \left[1 - \frac{\alpha_0 \beta}{1+\alpha_0 \beta} \exp\left(-\frac{\chi_C}{\alpha_0 \beta}\right)\right] I_{s//} \exp\left(-\chi_C\right),$$

which indicated that this configuration is unsuitable for the measurement of the temperature anisotropy. However, the EM configuration was able to readily unfold the current for the measurement of the distribution function:

$$F_{\infty}^{*} = \frac{\alpha_0^2}{\Theta_C} \frac{\partial^2 I_{EM}}{\partial \alpha_0 \partial \Theta_C}$$

evaluated at $\left(U_{//}^{*}, U_{\perp}^{*}\right) = \left(\Theta_C, \Theta_C / \alpha_0\right)$. The main drawback of this configuration was its inability to discriminate electrons with small pitch angle because the differentiation would require a large electromagnet current. Thus, the *EM* probe is unable to accurately measure the temperature anisotropy of an assumed bi-Maxwellian distribution function, and it can only measure a generic distribution function at large pitch angles.

We then demonstrated in section **3.3** that the placement of a *grid* electrode at the throat of the electromagnet in addition to a *collector* outside the electromagnet produced a configuration that reduced the burden on the electromagnet current. This arrangement is our *GEM* probe. We found that the *GEM* probe produced a barrier with two segments: one, which is electric, and one, which is a hybrid. The dual-segmented barrier produced the following relation for the $I-V$ characteristic:

$$I_C = \left[1 - \frac{\alpha_0 \beta}{1+\alpha_0 \beta} \exp\left(-\frac{\chi_C - \chi_G}{\alpha_0 \beta}\right)\right] I_{s//} \exp\left(-\chi_C\right),$$

where the subscript G denotes the value at the grid. In the regime where the collector absorbs all electrons that pass through the mesh, $V_C \geq V_G$ ($\chi_C \rightarrow \chi_G$), this configuration operates like the *M* probe and is thereby able to measure the temperature anisotropy. Whereas in the opposite regime, $V_C < V_G$, the GEM probe, like the EM probe, can readily unfold the current to measure a generic distribution function:

$$F_{\infty}^{*} = \alpha_0 \frac{\partial^2 I_C}{\partial \Theta_G \partial \Theta_C}$$

evaluated at $\left(U_{//}^{*}, U_{\perp}^{*}\right) = \left(\Theta_C, \left(\Theta_C - \Theta_G\right)/\alpha_0\right)$. Unlike the EM probe, the GEM probe is able to measure the distribution of electrons with *any* pitch angle.

The aforementioned relations are *ideal* because the barrier to the electrons is assumed to be free of the effects of space charge and of the grid's discrete structure. These effects are addressed in the next two chapters. For the *ideal* case, the relations are valid in the range

$$V_C < V_G \leq \Phi_{\infty}.$$

---

[i] Mechanics 3rd edition, L.D. Landau and E.M. Lifshitz, pp.159-162
[ii] Robert G. Littlejohn, J. Plasma physics (1983), vol. 29, part 1, pp. 111-125
[iii] R.J. Hastie, G.D. Hobbs, J.B. Taylor 3rd Int. Conf. On Plasma Phys. & Contr. Nuc. Fus. Research (1969)
[iv] D. Boyd, W. Carr, R. Jones and M. Seidl, Phys. Lett A **45**, p.421 (1973)
[v] C.D. Maldonado and H.N. Olsen, J. Opt. Soc. Am. **56**, p. 1305 (1966)
[vi] M .A. Hayes, M. R. Brown, M. A. Kasevich, and R. B. McCowan, Rev. Sci. Instrum. **55**, 928 (1984)
[vii] M.R. Brown, T.E. Sheridan, and M.A. Hayes, J. Appl. Phys. **70**, pp. 5306-5313 (1991)

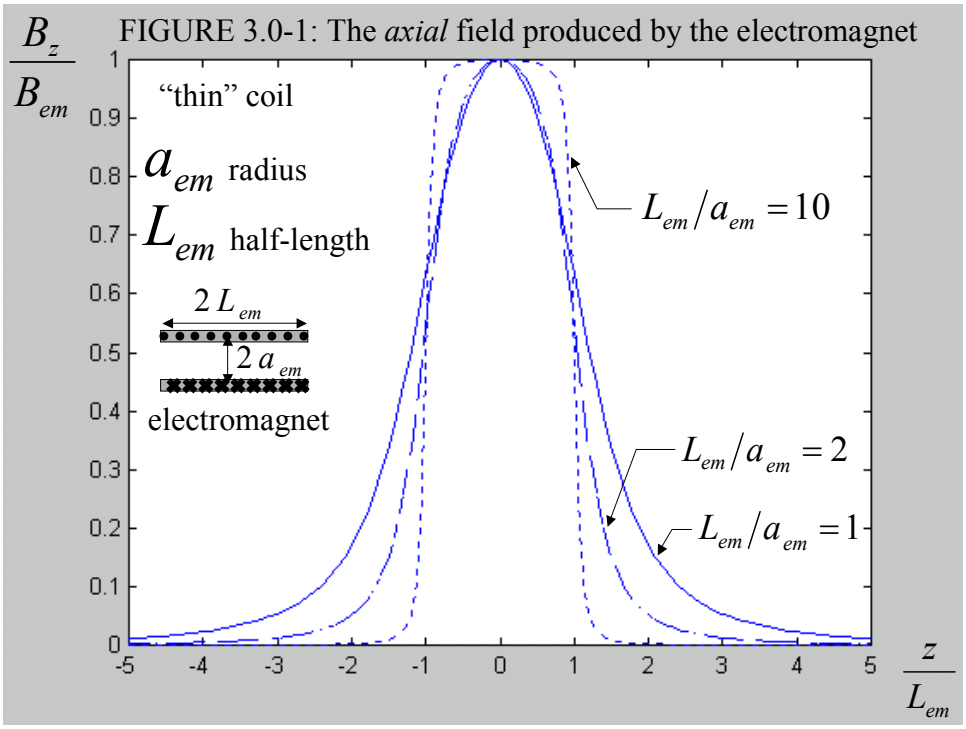

FIGURE 3.0-1: The *axial* field produced by the electromagnet

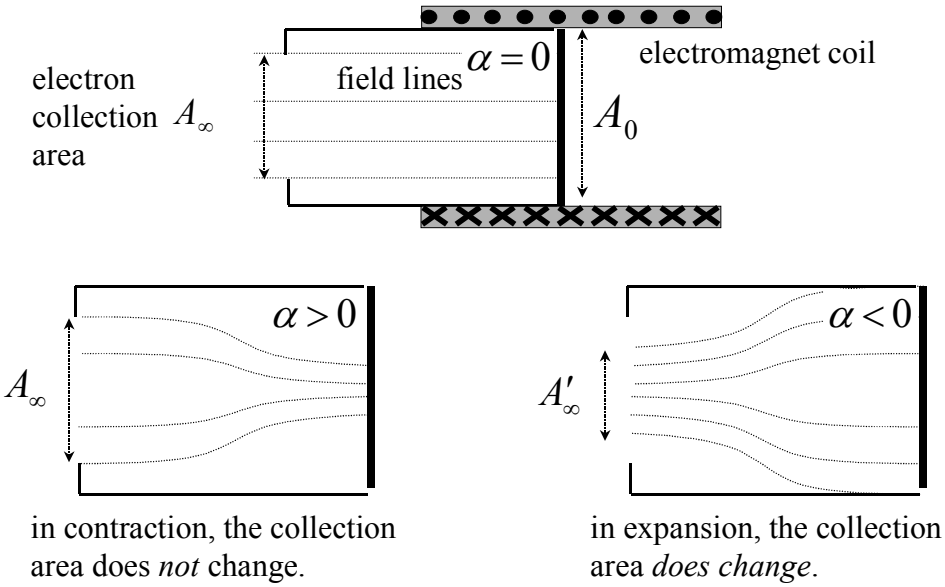

in contraction, the collection area does *not* change.

in expansion, the collection area *does change*.

FIGURE 3.0-2: The effect of the magnetic topology on the probe's projected (electron collection) area.

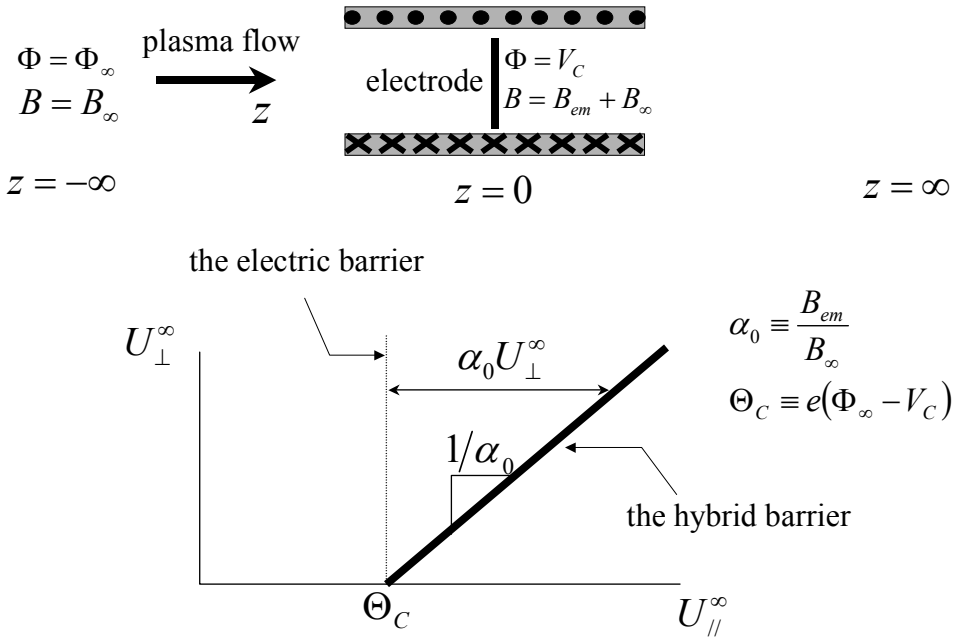

FIGURE 3.1-1: The *barrier* for the M probe

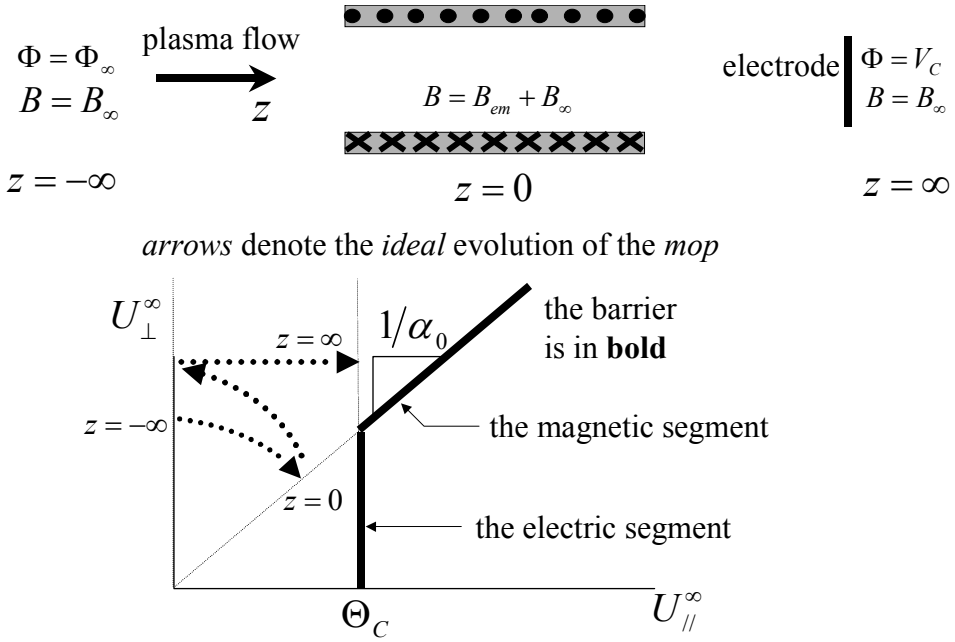

FIGURE 3.2-1: The *ideal barrier* for the EM probe

the variation in the current with the electrode voltage

the aforementioned variation for an incremental increase in the local magnetic field

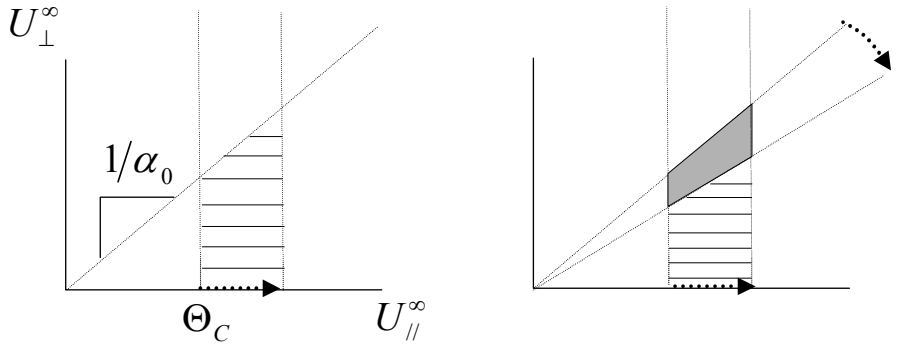

$$F_{\infty}^{*} = \frac{\alpha_0^2}{\Theta_C} \frac{\partial^2 I}{\partial \alpha_0 \partial \Theta_C}$$

FIGURE 3.2-2: The dissection of the energy space

cross-points allow for a measurement

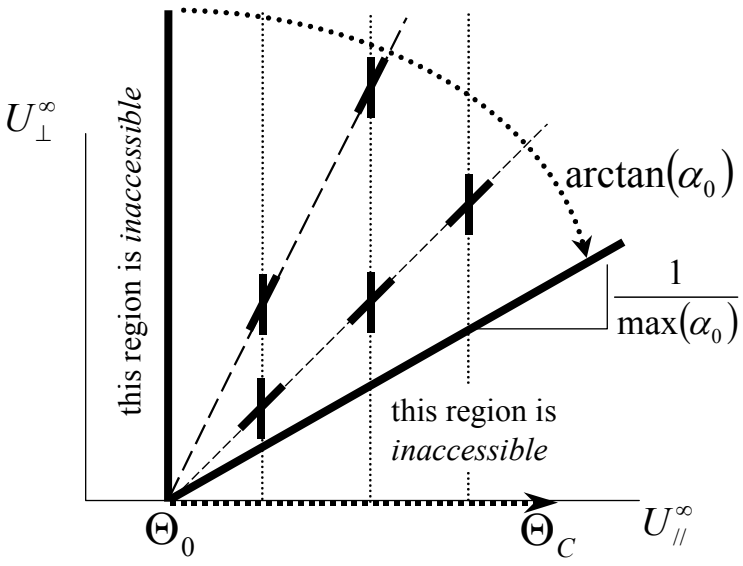

FIGURE 3.2-3: The region of accessibility for the EM probe

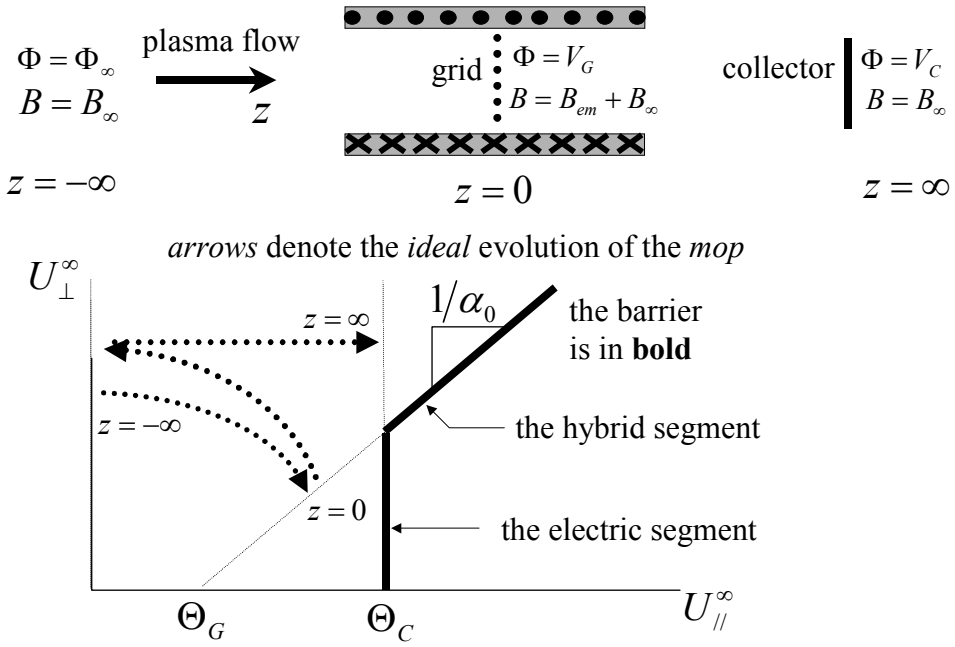

FIGURE 3.3-1: The *ideal barrier* for the GEM probe

the variation in the current with the collector voltage

the aforementioned variation for an incremental drop in the grid voltage

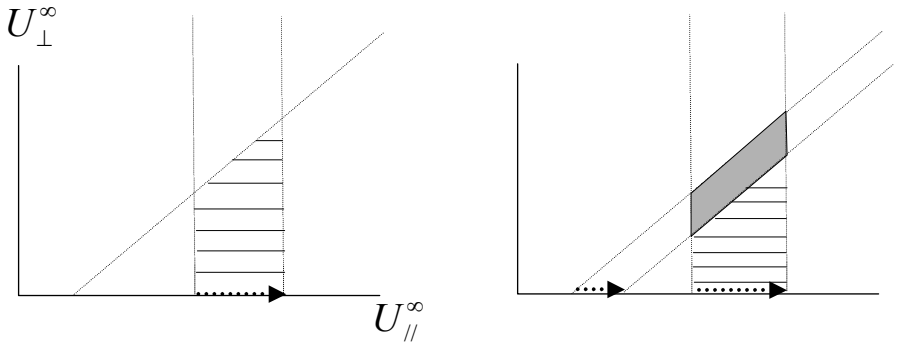

$$F_\infty^* = \alpha_0 \frac{\partial^2 I_C}{\partial \Theta_G \partial \Theta_C}$$

FIGURE 3.3-2: The dissection of the energy space

α_0 is reduced for measurements at large pitch angle

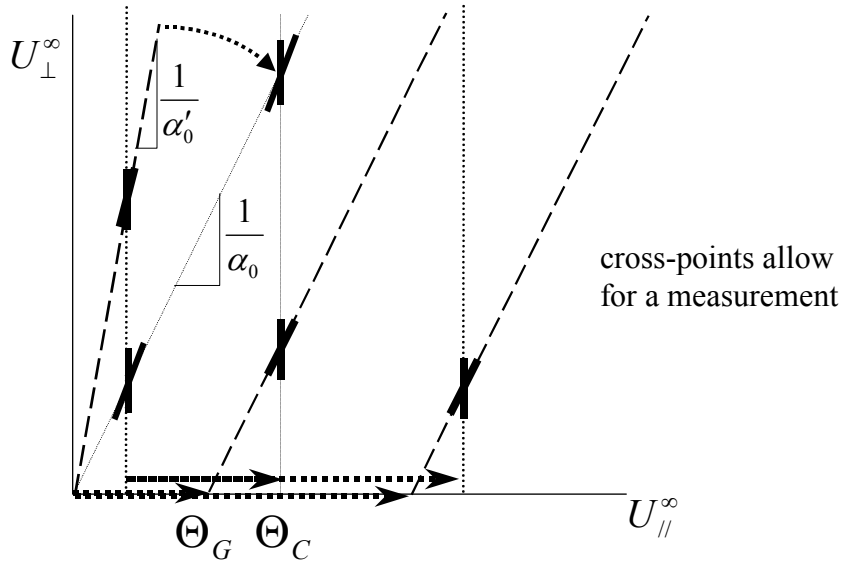

FIGURE 3.3-3: The grid renders the entire region accessible

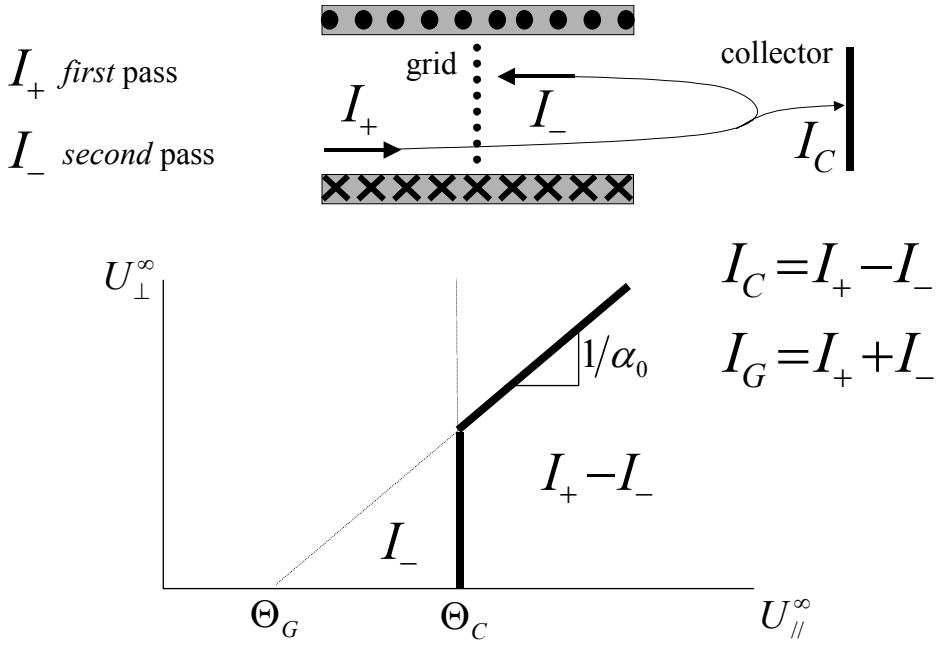

FIGURE 3.3-4: The duality between the grid and the collector currents

(This page left intentionally blank.)

CHAPTER 4

THE SPACE CHARGE DYNAMICS INSIDE THE GRID-COLLECTOR CAVITY AND ITS IMPACT ON THE COLLECTOR CURRENT

[4.0] Introduction

In the previous chapter, we discussed the ideal behavior of the electromagnet probes. This behavior assumes that the electrostatic energies at the electrodes *shape* the barrier. This assumption is valid for the M probe, but as a result of space charge effects, the assumption is violated for the EM probe and is valid only in a limited regime for the GEM probe.

For the configuration of the GEM probe, the effects of space charge reduce the electrostatic potential below the grid voltage over a *short* distance downstream from the grid-plane as the grid voltage is increased towards the plasma potential. This effect *modifies* the hybrid barrier at the grid-plane, which assumes that the grid voltage provides the maximum electrostatic energy in the region where the field of the electromagnet is significant.

To analyze this space charge effect, we exploit the plasma's drive to achieve a quasi-neutral state. This analysis is straightforward for the M probe and, in principle, for the EM probe because there is no physical structure to breakdown quasi-neutrality up to the collector. The analysis for the GEM probe, however, is complicated by the presence of the grid.

In this chapter, we focus on the impact of space charge effects on the collector current in the configuration of interest: the GEM probe. We perform the analysis in the

limit where the radius of the wires of the grid, r_w, is negligible in comparison to the wire spacing d and where the wire spacing is negligible in comparison to the Debye length; that is, in the limits where both r_w/d and d/λ_{De} go to *zero*. In these limits, the grid acts as a *transparent* medium that provides an *equipotential* grid-plane with a voltage of V_G. The discrete structure of the mesh is treated in the next chapter.

In the following subsections, we briefly discuss the previous treatments of the space charge dynamics in the region between a grid and a collector. We demonstrate that the assumptions employed in these treatments do not apply to the operation of the GEM probe and then discuss our own approach.

[4.0.1] The *fluid* treatment: cold ions, *no* electrons

Scientists have attempted to understand the impact of space charge in the region following a grid electrode to substantiate the use of the gridded-energy analyzer for the measurement of the ion distribution function. Hutchinson[i] presented a 1-D treatment of Poisson's equation that employs the density of *cold* ions (equation **2.1-3**) and neglects the electron contribution, which is adequate for $e(\Phi_\infty - V_G) >> T_e$. The *fluid* model yields the critical distance downstream from the grid-plane beyond which the potential forms a barrier to the ion flow (where $\Phi \geq \Phi_\infty$). This distance is approximately equal to

$$\Delta \approx \lambda_{De}\left[e(\Phi_\infty - V_G)/T_e\right]^{3/4}.$$

Experiments performed by Honzawa[ii] *et. al.* confirmed the above estimate via the observation of a drop in the current in the vicinity of this distance as measured by a collector.

The fluid model, however, is incomplete in that it cannot yield the variation in the ion current to the collector with the applied voltages and with the inter-electrode spacing z_{CG}, in the space charge limited regime: $\lambda_{De} << z_{CG}$. The space charge induced barrier that controls the ion current is determined by the solution to the potential in the entire grid-collector region; and the only solution allowed by the fluid model is one that gives *zero* ion current to the collector. The following argument demonstrates this claim.

If the potential is able to exceed the plasma potential, then the ion density abruptly vanishes because the fluid model assumes that the ions have no energy in the ambient ($T_i = 0$). As shown in figure **4.0-1**, the only solution for the potential profile in this case is one that reaches Φ_∞ with a slope that allows the ensuing linear (vacuum) profile to match a collector voltage that is greater than Φ_∞ (no solution exists for $V_C < \Phi_\infty$). On the other hand, if the potential remains below Φ_∞, the ion space charge produces a hump Φ^* in the potential profile. The dependence of the ion density on the potential in the region preceding and following the potential hump is identical because the fluid model assumes that the ions have positive energies for $\Phi < \Phi_\infty$; that is, it assumes that all ions overcome the potential hump. The densities' identical functional dependence with Φ in the two regions produces a symmetric potential profile about the hump location z^*. The potential then plummets on the scale of λ_{De} and thereby is unable to match the boundary condition at the collector, in general.

[4.0.2] The *kinetic* treatment: Maxwellian ions, *no* electrons

To determine the collector's $I-V$ characteristic in the space charge limited regime, we need a more sophisticated model for the ion energy distribution function, one with a finite spread of energies. Martin *et.al.*[iii] presented such a model in a 1-D kinetic treatment. They employed an ion distribution function that connects to a Maxwellian distribution in the quiescent region. They also neglected the electron density, which is an adequate approximation because they maintained the grid electrode electrically floating in their model. To determine $\Phi(z)$, they had to solve for the profiles that precede and follow the potential hump separately and then match the location and the potential at the hump (z^*, Φ^*) for the two profiles. The matching technique was necessary because the ion density is not completely defined *a priori*. This density is a function of the unknown Φ^* as well as Φ.

The derived dependence of the potential hump on the collector voltage allowed this group to relate the *apparent* ion temperature, derived from $edV_C / d\ln I_i$, to the *true* ion temperature, $T_i = ed\Phi^* / d\ln I_i$. Their experiment[iv] employed a gridded energy analyzer with a variable inter-electrode spacing. Overall, they illustrated the predicted trend for the temperature deviation with z_{CG}, with much better accuracy for large inter-electrode spacing: $z_{CG} >> \lambda_{De}$. Their results, however, are somewhat questionable because the experiments performed by Honzawa demonstrated a redistribution of the ion energies past the critical location; a phenomenon that must have stemmed from the enhanced probability for Coulomb collisions among the low-energy ions in the vicinity of the potential hump.

Regardless, the accuracy in their predictions for $z_{CG} >> \lambda_{De}$ does not necessarily reflect the strength of the matching technique because in this regime, the length of the region between z^* and z_C can be approximated by z_{CG}. In such a case, the matching is unnecessary because we can disregard the *width* of the region $z_G \le z < z^*$ and instead solve the following boundary value problem: $\Phi(z_G) = \Phi^*$, $E(z_G) = 0$, and $\Phi(z_C) = V_C$ with Φ^* to be determined.

[4.0.3] The inadequate assumptions of the kinetic treatment

The assumptions employed by Martin neither reflect the conditions in which we operate our diagnostic nor the operation itself. Firstly, the large aspect ratio of the grid-collector region renders our geometry two-dimensional, thereby bringing into play the voltage on the sidewall. Secondly, the multi-dimensional nature of the pre-sheath invalidates the 1-D connection of the ion distribution function at the grid to a Maxwellian distribution in the ambient. Not all of the electrostatic energy in the pre-sheath is translated to the ions' momentum in the direction normal to the grid-plane. The amount of energy that the ions gain in this direction is a variable. In fact, the resulting spread in the ions' *parallel* energies from this variability is generally greater than the initial spread in their ambient energies. As equation **4.0-1** will indicate, this result is true for magnetized ions as well.

Last, but not least, the operation of the probe requires that we ramp the grid voltage. As the grid barrier to the electrons diminishes, the finite electron density in conjunction with the reflection of a healthy fraction of the ions by the potential hump renders the electron and the ion densities beyond z^* comparable. Therefore, we cannot

generally neglect the electron contribution to the space charge inside the grid-collector cavity.

[4.0.4] Our approach: kinetic, *including* electrons

The purpose of our analysis is to understand how the presence of electrons inside the grid-collector cavity modifies the potential profile from the ideal: one that initially rises downstream from the grid to mirror the ions and then becomes *vacuum* like. This profile is shown schematically in figure **4.0-2**. The *vacuum* profile is one that reaches a plateau at the voltage on sidewall, V_{SW}. This voltage can be preset to maintain the potential *above* V_G in the region where the field of the electromagnet is significant. Then, the electrostatic energy at the grid would describe the hybrid barrier to the electrons as desired. However, what we find is that as the grid voltage rises, the increasing electron space charge eventually reduces the potential below the grid voltage in the region where the field of the electromagnet would be finite. We would like to estimate the grid voltage at which this transition occurs.

To determine the evolution of the potential inside the grid-collector cavity, we must solve Poisson's equation:

$$\nabla^2\Phi = e\left(n_e - n_i\right)/\varepsilon_0 .$$

This equation is difficult to solve for the 2-D cylindrical cavity. Instead, we solve for the potential in 1-D (assuming that the plasma has an infinite radial extent) and then discuss how the results can be interpreted for the geometry of interest. In addition, we limit the analysis to the case where $B_{em} = 0$. We will briefly address the impact of an inhomogeneous magnetic field inside the cavity at the end of section **4.2**.

The solution in 1-D with $B_{em} = 0$ is still intricate, but manageable. First, it requires models for how the potential affects the densities: the first moment of the parallel distribution function, $n = \int dv_{//} f_{//}$ (see next section). We model the electron density, n_e, to arise from a half-Maxwellian parallel distribution function in the ambient, $z_\infty \to -\infty$:

$$f_e\left[U_{//}^{\infty}\right] \equiv \frac{1}{2}\frac{n_\infty}{\sqrt{2\pi T_{//}/m_e}} \exp\left(-U_{//}^{\infty}/T_{//}\right),$$

which is then related to the distribution downstream via $f_e^+ = f_e\left[U_{//} + e\left(\Phi_\infty - \Phi\right)\right]$ (the distribution function is a constant of the total energy). The component of the electron density moving downstream, n_e^+, can then be expressed as a function of Φ, the potential at the location of interest z, and $\Phi_{\min}$, the minimum in the potential upstream, $z' \le z$. This potential determines the fraction of the low-energy electrons that have been mirrored. The density also has a component that is associated with the electrons that are mirrored downstream from z ($z' > z$), n_e^-. This component can be expressed as a function of Φ_{MIN}, the *global* minimum in the potential (the minimum in the entire interval $-\infty < z' \le z_C$). For example, if $\Phi_{MIN} = \Phi_{\min}$, then $n_e^- = 0$. Notice that the global minimum may not necessarily be given by either the grid or the collector voltage. In general then, the electron density is expressed as $n_e = n_e^+\left(\Phi, \Phi_{\min}\right) + n_e^-\left(\Phi, \Phi_{MIN}\right)$. This function is derived in section **4.1** and appendix **4.1x**.

To determine the ion density, we use the results of section **2.2**. There, we addressed the space charge dynamics in the pre-sheath leading up to a collector for the practical case of magnetized electrons. We found that in this regime, the ions enter the

flux tube that intersects the collector from its periphery. The source of ions then generates an electric field, which accelerates the ions. The balance between the ion source rate and the acceleration from the electric field then maintains $n_i = n_e$ (quasi-neutrality) up to the sheath of the collector, where

$$\Phi_s \cong \Phi_\infty - 0.85 T_{//}/e \,.$$

Our geometry, as shown in figure **4.0-2**, is somewhat different in that the ion source and, with it, the electric field diminish at the entrance to the housing to yield a potential profile that is constant in the region preceding the grid. The constant is equal to V_G for $V_G > \Phi_s$ and to Φ_s otherwise. Nevertheless, the analysis of appendix **2.2x** gives the ion parallel speed distribution at the *entrance*. Combining equations **2.2x-3** and **2.2x-5** and using the normalized potential $\chi = e\left(\Phi_\infty - \Phi\right)/T_{//}$, we obtain

$$f_i\left[U_{//}^E\right] \cong \frac{n_\infty}{\sqrt{T_{//}/m_i}} \frac{\sqrt{2}\left[1 - 2\chi' \exp\left(-2\chi'/3\right)\right]}{\pi\sqrt{\chi'}}, \qquad \{4.0-1\}$$

where $\chi' = \chi_E - U_{//}^E/T_{//}$ is equal to the value of χ where the ions are *born* inside the pre-sheath, and the letter E denotes the value at the entrance. The distribution inside the housing is then given by the relation, $f_i^{+\&-} = f_i\left[U_{//} - e\left(\Phi_\infty - \Phi\right)\right]$. The $+\,\&\,-$ denotes that ion distribution function derived has automatically incorporated the distribution moving upstream; that is, it is equal to the sum $f_i^+ + f_i^-$. The reason is explained in appendix **4.1x**. It has to do with the fact that f_i is derived from n_e. The expression for f_i, however, isn't quite complete because the derivation in appendix **2.2x** assumes that $n_e^- = n_e^+$ ($\Phi_{MIN} \to -\infty$). In general, the ion density, via its connection to n_e, is a function of Φ_{MIN}. It is also a function of $\Phi_{\max}$, the maximum potential upstream, in between z_E

and z. This potential determines the fraction of the low-energy ions that have been mirrored. The function $n_i\left(\Phi,\Phi_{\max},\Phi_{MIN}\right)$ is also derived in section **4.1** and appendix **4.1x**.

As a result of the densities' dependencies on quantities that are not known *a priori* ($\Phi_{\min}$, $\Phi_{\max}$, and Φ_{MIN}), the region between the grid and the collector, in general, has to be subdivided at locations at which the field is assumed to vanish. Poisson's equation has to then be solved in each section, and the boundary locations and the boundary potentials have to be matched subject to the constraints, $\Phi\left(z_G\right)=V_G$ and $\Phi\left(z_C\right)=V_C$. However, as we argue next, we do not need to solve this complicated boundary value problem for our purposes.

Figure **4.0-3** shows schematic drawings of potential profiles inside the grid-collector cavity for various ratios of the Debye-length, $\lambda_{De}\equiv\sqrt{\varepsilon_0 T_{//}/e^2 n_\infty}$, to the inter-electrode spacing z_{CG}. This parameter describes the degree to which the space charge modifies the potential profile from that in vacuum (which in1-D is a straight line connecting the voltages). The profiles are for the specific case, $V_C=V_G<\Phi_s$, where a sheath has formed upstream from the grid ($n_i>n_e$).

The figure illustrates that as λ_{De}/z_{CG} is reduced, the profile forms a hump, which eventually rises above the sheath potential Φ_s to mirror the low-energy ions. In this case, the ion current to the collector has become space charge limited. As λ_{De}/z_{CG} is reduced further, the hump removes enough ions to allow n_e to overtake n_i downstream from the hump location. For a critical value of λ_{De}/z_{CG}, this effect eventually produces

the condition, $d\Phi/dz = 0$, at the collector. For λ_{De}/z_{CG} less than the critical value, the potential forms a minimum below V_G, thereby making the electron current to the collector space charge limited.

This definition for the transition into space charge limited regime requires a solution to a relatively complicated boundary value problem. Moreover, this solution is sensitive to the 1-D geometry. The transverse dimension and the voltage on the sidewall govern the actual transition. Therefore, to find an overall definition that can be extended to the 2-D geometry, we first analyze the limiting case, $\lambda_{De} \to 0$, which gives (rather simple) solutions that is common to both the 1-D and the 2-D geometries.

In section **4.2**, we solve the initial value problem, $(\Phi, E)_{z_G} = (V_G, E_+)$, to obtain the long-range 1-D potential profiles in a grid-collector cavity of infinite size (radial and axial). Such solutions either attain a quasi-neutral state (a plateau) or settle into oscillations. In particular, we analyze the borderline case that separates the plateau and the oscillatory solutions. We refer to it as the *stationary* solution, which is also depicted schematically in figure **4.0-3**. This profile is characterized by two potentials, Φ^* and Φ^{**} (notice that $\Phi^{**} < V_G$), which describe the barriers to the ion and to the electron currents, respectively. We find that the drive for quasi-neutrality produces algebraic solutions for these potentials' dependencies with the grid voltage, which, in turn, give rather generic (and thereby robust) relations for the space charge limited currents to the collector. Furthermore, we estimate that the *sheath* describing the transition into the long-range behavior has an extent that is characterized by the enhanced Debye-length, $\lambda_G \equiv \exp(\chi_G/2)\lambda_{De}$: the Debye-length associated with the attenuated electron density.

The analysis of the long-range solutions then enables us to readily understand the role of the boundary condition at the collector for the 1-D geometry. A finite value for λ_{De}/z_{CG} is observed as a collector encroaching from $z \to +\infty$. As described in section **4.3**, the collector is, therefore, viewed as a boundary that truncates the long-range solution. In particular, if z_{CG} becomes of the order or less than λ_G, then the profile is truncated before it has had a change to settle into its long-range behavior. The early truncation is interpreted as the transition into the *vacuum* regime. This viewpoint can then be readily extended to estimate the transition in 2-D by simply replacing the inter-electrode spacing z_{CG} with the radial extent of the plasma beam inside the cavity, b.

From the numerical results, we estimate the desired *vacuum* regime to be described by the relation $\lambda_G > kb$ with $k \cong 0.1\exp(0.5)$. This form for the constant k allows the criterion on the grid voltage to be expressed conveniently as

$$V_G - \Phi_\infty < -\frac{T_{//}}{e}\left[1 + 2\ln\frac{b}{10\lambda_{De}}\right].$$

The radius of the entrance to the *GEM* probe, which gives the beam size b, is generally chosen to be much greater than the Debye-length in order to collect an appreciable amount of current. Hence, the measurement of the electron distribution function is practically limited to the high-energy population (those with $U_{//}^{\infty} > T_{//}$).

[4.1] The densities inside the probe housing

The electron and ion densities inside the probe housing are governed by the evolution of their distribution functions as described in section **2.0**. For a constant magnetic field, the perpendicular gyration speed is a constant of motion. This

simplification together with the separable form for our model distribution functions ($f = f_{par} f_{perp}$) allows us to readily integrate f over the perpendicular speeds, thereby reducing equation **2.0-3** for the densities inside the housing to

$$n = \int dv_{//} f_{//} = \frac{1}{\sqrt{2m}} \int \frac{dU_{//}}{\sqrt{U_{//}}} f_{//}$$

$$= \frac{1}{\sqrt{2m}} \int dU_{//}^{E} \frac{f_{//}\left(U_{//}^{E}\right)}{\sqrt{U_{//}^{E} + q\left[\Phi_{E} - \Phi(z)\right]}}. \qquad \{4.1-1\}$$

The electron parallel speed distribution is a constant of the total energy in the pre-sheath outside the housing as well. Therefore, we can represent its density in equation **4.1-1** as an integral over $U_{//}^{\infty}$ with Φ_E replaced by Φ_∞. We specify the bounds in the integration for each species in the following subsections.

[4.1.1] The electron density inside the housing

The electron parallel speed distribution in the ambient is assumed to be Maxwellian. Therefore, the electron energies at $z = -\infty$ range from *zero* to *infinity*. However, if the electrons are to contribute to the density inside the housing, they have to overcome the *maximum* electrostatic barrier between $-\infty$ and z. This requirement places the *lower* bound $\max\left[e\left(\Phi_\infty - \Phi(\zeta)\right)\right]$ in the integral in equation **4.1-1**, where the maximum is taken over the range $-\infty < \zeta \le z$.

The upper bound in the integral is infinite for the component of the electron distribution that is moving towards the collector. However, the component that has been mirrored is cut-off at high-energies because the collector absorbs a fraction of the electrons. In appendix **4.1x**, we calculate the density for the general case of partial

absorption of the electrons by the collector. However, here and through out the main body of the chapter, we approximate the electron density by neglecting the component that has been cut-off. The inclusion of this component would only serve to complicate the algebra without adding much insight.

Performing the integral of equation **4.1-1** then gives

$$n_e = n_\infty \exp(-\chi) erfc\sqrt{\chi_{\max} - \chi} \qquad \{4.1-2\}$$

with $\chi = e(\Phi_\infty - \Phi)/T_{//}$ and $\chi_{\max}$ equal to the maximum in χ (or equivalently, the *minimum* in Φ) in the range $-\infty < \zeta \le z$. The maximum *up to* the location of interest z, $\chi_{\max}$, is shown in figure **4.1-1a** for a potential profile that we study in the next section. The corresponding variation in the electron density is plotted in figure **4.1-1b** for the specific case of $\chi_G = 2$. These plots are described as follows.

In the region preceding the grid, $\chi_{\max} = \chi$ because the potential Φ is monotonically decreasing. Here, the electron density is described by its classic, (purely) exponential form as shown by the *A*-portion of the curve in figure **4.1-1b**:

$$n_e = n_e\big|_{\chi_{\max}=\chi} = n_\infty \exp(-\chi). \qquad \{4.1-2a\}$$

This dependence is a result of the mirroring of the low-energy population and the simultaneous compression in the density of the remaining high-energy population (because they slow down). Once the potential rises above V_G in the region following the grid, the barrier to the electrons remains fixed, equal to the difference between $e\Phi_\infty$ and eV_G. The density then continues to decrease as it expands from the acceleration of the remaining high-energy electrons as indicated by moving along curve *B*:

$$n_e = n_e\big|_{\chi_{\max}=\chi_G} = n_\infty \exp(-\chi) erfc\sqrt{\chi_G - \chi}\,, \qquad \{4.1-2b\}$$

which for $\chi_G - \chi >> 1$ gives $n_e \cong n_\infty \exp(-\chi_G)/\sqrt{\pi(\chi_G - \chi)}$. The density then retraces its steps once the potential attains the local maximum Φ^* and subsequently drops. The density continues to increase until Φ drops below V_G, at which point the density decreases exponentially once again along curve *C* as the electrostatic barrier reflects more electrons. Consequently, the electron density is again given by equation **4.2-1a**.

[4.1.2] The ion density inside the housing

The ion energies at the entrance z_E range from *zero* (the energy of ions born at the entrance) to the maximum energy $e(\Phi_\infty - \Phi_E)$, the energy gained in the pre-sheath outside the housing by ions born at $z = -\infty$. For the ions to contribute to the density inside the housing, their energies at the entrance have to overcome the maximum electrostatic barrier between z_E and z: $\max[e(\Phi - \Phi_E), 0]$. This criterion places a lower bound in the integral of equation **4.1-1**. The integral is performed in appendix **4.1x**. The result is the approximation

$$n_i \cong n_i^0(\chi, \chi_{\min}) \equiv n_\infty \frac{\exp(-\chi_{\min})}{\sqrt{1 + (\chi - \chi_{\min})/(k_{\min}^2 \chi_{\min})}} \qquad \{4.1-3\}$$

with $k_{\min} \equiv k(\chi_{\min}) \equiv (2/\pi)\exp(\chi_{\min}/3)$ and $\chi_{\min}$ equal to the minimum in χ (or equivalently, the *maximum* in Φ) in the range $z_E < \zeta \le z$. The minimum *up to* the location of interest z, $\chi_{\min}$, is described in figure **4.1-2a** for the same potential profile depicted in figure **4.1-1a**. The corresponding variation in the ion density is plotted in figure **4.1-2b**. These plots are described as follows.

In the region preceding the grid, the potential Φ inside the housing decreases below its value at the entrance, thereby making $\chi_{\min}$ equal to χ_E. In this case, the ion density is reduced as it expands from the acceleration of the ions as shown by curve *A* starting at z_E and for $\chi_E << 1$, we can see from equation **4.1-3** that

$$n_i \cong n_i^0(\chi, \chi_E) \cong n_\infty (2/\pi)\sqrt{\chi_E / \chi}\,. \qquad \{4.1-3a\}$$

The density then retraces its steps along curve *A* in the region following the grid as the potential rises above the minimum, V_G. Once the potential rises above Φ_E, $\chi_{\min}$ becomes equal to χ along the *B*-portion of the curve. In this region, the low-energy ions are mirrored, and the remaining ions are compressed. Here, the density regains the exponential dependence with χ it had in the pre-sheath outside the housing:

$$n_i \cong n_i^0(\chi, \chi) = n_\infty \exp(-\chi). \qquad \{4.1-3b\}$$

Once the potential attains the maximum Φ^* and subsequently drops, the ion density is reduced once again as it expands from the acceleration of the remaining ions as indicated by the curve *C*. The density drops more quickly from the expansion in this case because of the fewer remaining ions and for $\chi^* << 1$, we have

$$n_i \cong n_i^0(\chi, \chi^*) \sim n_\infty (2/\pi)\sqrt{\chi^* / \chi}\,. \qquad \{4.1-3c\}$$

Having determined the densities, we next solve Poisson's equation for the potential profile inside the housing.

[4.2] The potential profile inside a grid-collector cavity of *infinite* size

The operation of the GEM probe requires that we ramp the grid voltage. As V_G approaches Φ_∞, we will find that the rising electron density in the grid-collector region

contorts the potential to form an enhanced barrier to the electrons so that a quasi-neutral state is achieved. The resulting barrier is greater than the one applied at the grid, and its presence complicates the results of section **3.3**, where we derived the ideal relationship between the collector's $I-V$ characteristic and the electron distribution function. We would like to pinpoint the threshold value of the grid voltage, above which this enhanced barrier forms, so that we may avoid this regime in practice.

In this spirit, we first examine the dynamics in the regime where the potential is solely influenced by the plasma space charge and the grid voltage. We assume that the sidewall radius and the radial extent of the plasma are both *infinite*. We then characterize the potential in the region following the grid with the collector placed *far away*, $z_{CG} \to \infty$. The infinite size of the cavity and of the plasma allows us to study the space charge dynamics and its impact on the collector current without considering the constraints imposed by the boundary conditions at the sidewall and at the collector. We address the impact of the boundary conditions in the next section.

[4.2.1] The solution to the 1-D Poisson's equation

The infinite radial extent of the plasma and of the cavity reduces the dimensions of the problem to that describing the distance from the grid-plane, z, which we *normalize* to the electron Debye-length $\lambda_{De} = \sqrt{\varepsilon_0 T_{//} / e^2 n_\infty}$. To determine the 1-D profiles, we exploit *the analogy* in which $\chi = e\left(\Phi_\infty - \Phi\right)/T_{//}$ is viewed as the *position* of a *ball* with the *normalized* electric field E representing its *velocity*:

$$\mathrm{E} = d\chi/dz\,, \qquad \{4.2-1a\}$$

where the normalized distance z represents *time*. The *ball* is then viewed as being *accelerated* by the *driving force*, which is represented by the disparity between the ion and the electron densities:

$$d\mathrm{E}/dz = \delta n \qquad \{4.2-1b\}$$

with $\delta n = (n_i - n_e)/n_\infty$ determined by equations **4.1-2** and **4.1-3**. For a homogeneous magnetic field ($\alpha = 0$), the *force* is purely a function of the *ball's position*. Therefore, it can be expressed as the *gradient of a scalar potential*:

$$\delta n = -d\Pi/d\chi\,. \qquad \{4.2-1c\}$$

We exploit this relation to solve for the electric field by multiplying the *equation of motion*, equation **4.2-1b**, by the *velocity* and then by integrating the result to obtain the following conservation equation:

$$\mathrm{K} + \Pi = \text{constant} \qquad \{4.2-2\}$$

with

$$\mathrm{K} \equiv \mathrm{E}^2/2 \qquad \{4.2-2a\}$$

and

$$\Pi = -\int d\chi\,\delta n = \int d\chi\, n_e/n_\infty - \int d\chi\, n_i/n_\infty = \Pi_e - \Pi_i + \text{constant}\,, \qquad \{4.2-2b\}$$

where K and Π represent the *kinetic* and the *potential energies* of the *ball*, respectively. The integrals for Π_e and Π_i are performed in appendix **4.2x**.

We then solve for the *velocity* to obtain an implicit integral equation for the *position* of the *ball* as a function of *time*:

$$z = \left| \int^{\chi} \frac{d\chi'}{|\mathrm{E}|} \right| + \text{constant} \qquad \{4.2-3\}$$

with

$$|\mathrm{E}| = \sqrt{2(\text{constant} + \Pi_i - \Pi_e)}\,. \qquad \{4.2-3a\}$$

Notice that if $|\mathrm{E}|$ vanishes at a particular location, then the region has to be segmented at this *turning* point and equation **4.2-3** has to be applied separately to each region.

The analogy of a *ball rolling on a hill* is useful when we are not concerned with the boundary condition at the collector. Instead, we view equation **4.2-3** as a simulation, where we launch a *ball* at the *position* χ_G with a *velocity* E_+; the electric field at the grid associated with the *collector-side*. We then look for the *send-off velocity* E_+ that renders the *ball stationary* ($\mathrm{E}^{**} = 0$ and $\delta n^{**} = 0$) at some point in *time* $z^{**} > z_G$. That is, we look for the long-range quasi-neutral solution; a plateau, which carries the electrostatic potential all the way to the collector. Such a solution was not possible for the profiles derived by Martin *et. al.* because they *neglected* the electron density.

The quasi-neutral solution amounts to the solution of a few algebraic equations as we demonstrate in the next two subsections. The solutions to these equations give the fields emanating from the two sides of the mesh as a function of the grid voltage, which as we show in chapter **5**, influence the size of the electric perturbation about the grid. More importantly, the solutions give the dependence of the space charge induced barriers (to the electrons and to the ions) with V_G, which we use to derive the space charge limited currents to the collector. A comparison of the $I_C - V_G$ characteristics obtained from the probe with those derived from the following analysis would then indicate whether we are operating the probe in the appropriate regime.

[4.2.2] The *stationary* solution for $V_G > \Phi_s$

Normally, the long-range solutions require that the electrostatic potential form a barrier to the ions ($\mathrm{E}_+ < 0$) as discussed in section **4.0**. However, for small χ_G, the potential adopts a long-range solution with $\mathrm{E}_+ > 0$. The two solutions are illustrated in figure **4.2-1**.

The profile with $\mathrm{E}_+ > 0$ (the one depicted with the *solid* line) occurs if the pre-sheath outside the housing does *not* accumulate enough ions: $\chi_E = \chi_G < \chi_s$, where Φ_s is the potential below which a sheath forms[a] in the region preceding the grid. As a result, the profile remains quasi-neutral all the way up to the grid-plane ($\mathrm{E}_- = 0$); and in the region following the grid, the ion density is reduced below the density of the electrons as the potential drops below V_G. The resulting negative space charge then diminishes the initial field at the grid to form the stationary solution. The expressions for the densities in this case can be obtained from equation **4.1-2a** and from equation **4.1-3a** *with* χ_E replaced by χ_G.

The field E_+ that produces the *stationary* profile is derived from the solution to equation **4.2-2**, which gives $\mathrm{E}_+^2/2 + \Pi_G = \Pi^{**}$ since $\mathrm{E}^{**} \equiv 0$. The difference $\Pi^{**} - \Pi_G$ could be obtained from the integral $\int_{\chi_G}^{\chi^{**}} d\chi \left(n_e - n_i\right)/n_\infty$. However, we have already derived the expressions for Π at these locations (valid up to a constant) in appendix **4.2x**. Using equations **4.2x-3c** and **4.2x-3e** with $\chi_E = \chi_G$ gives $\Pi_G = 0$. Equations **4.2x-3d** and **4.2x-3e** (with the aid of equation **4.2x-4**) with $\chi_{\min} = \chi_G$ then give

---

[a] $\chi_s \cong 0.75$. A better approximation for the ion density would give $\chi_s \cong 0.85$.

$$\mathrm{E}_+^2/2 = \Pi^{**} \cong 1 - \left[2\chi^{**} + 1\right]\exp\left(-\chi^{**}\right) \qquad \{4.2-4a\}$$

for χ_G small. The plateau potential Φ^{**} is obtained from the relation of quasi-neutrality, equation **4.2x-4** with $\chi_{\min} = \chi_G$, which for χ_G small is reduced to

$$\exp\left(\chi^{**}\right) \cong \left(1/k_0\right)\sqrt{\chi^{**}/\chi_G}\,, \qquad \{4.2-4b\}$$

where $k_0 = 2/\pi$. Solving equation **4.2-4b** recursively for χ^{**} large then gives

$$\chi^{**} \cong 0.5\ln\left[-0.5\left(k_0^2\chi_G\right)^{-1}\ln\chi_G\right]. \qquad \{4.2-4c\}$$

[4.2.3] The *stationary* solution for $V_G < \Phi_s$

If $\chi_G > \chi_s$, then χ_E becomes pinned to χ_s, and a sheath forms in the region preceding the grid ($\mathrm{E}_- > 0$). In this case, the pre-sheath outside the housing has accumulated enough ions to maintain $n_i > n_e$ in the region following the grid if the potential drops below V_G. Therefore, a positive electric field at the grid would *not* be able to yield a stationary solution because the positive δn would accelerate the potential drop. The potential then has to increase from its value at the grid ($\mathrm{E}_+ < 0$) to repel a fraction of the ions as illustrated by the profile with the dotted line in figure **4.2-1**. The requirement on E_+ to produce a *stationary* solution in this case is more complex.

To understand the evolution of the potential from the sheath about the grid to the region of quasi-neutrality, we examine the behavior of the space charge. Initially, as the potential rises above the grid voltage, the ion density is compressed from the deceleration of its population (which had accelerated in the sheath preceding the grid). This density is given by equation **4.1-3a**. Once the potential rises above $\Phi_s = \Phi_E$, the electric field

mirrors the low-energy ions, and the ion density regains the exponential dependence it had outside the housing as described by equation **4.1-3b**. Even though, the electrostatic barrier is filtering the ions, the ion density increases to its ambient value n_∞ as $\chi \to 0$ because its remaining population slows down. Concurrently, the electron density is reduced below its value at the grid as a result of the acceleration of its remaining population. The expression for n_e in this case is given by equation **4.1-2b**.

The positive space charge eventually diminishes the field to form the hump Φ^* ($\mathrm{E}^* \equiv 0$). With the low-energy ions removed by the hump, the ion density plummets in the subsequent evolution from the acceleration of its remaining population. This variation is described by the *C*-portion of figure **4.1-2b**; equation **4.1-3c**. The electron density then overtakes the ion density as it retraces its steps to regain its value at the grid as the potential drops to V_G. Once the potential drops further, however, the electrostatic barrier filters more electrons, and the electron density is reduced exponentially once again as described by equation **4.1-2a**. The exponential drop in the electron density allows for δn to vanish. Furthermore, the reversal of sign in the space charge during the evolution beyond z^* enables the field to vanish as well, thereby producing the conditions for the *stationary* solution.

The field E_+ that produces the stationary solution is obtained in two steps. The first is the application of equation **4.2-2** in the region between the grid and the location of the potential hump (the *turning* point), and the second is the application of this equation in the region following the potential hump in conjunction with the requirement of quasi-neutrality at the plateau.

The application of equation **4.2-2** in the region between the grid location z_G and the *turning point* z^* gives

$$\mathrm{E}_+^2/2 = \Pi^* - \Pi_G \,. \qquad \{4.2-5a\}$$

The difference $\Pi^* - \Pi_G$ could be obtained by integrating the disparity in the densities, $\int_{\chi_G}^{\chi^*} d\chi \left(n_e - n_i\right)/n_\infty$, with n_e given by equation **4.1-2b** and with n_i given by equations **4.1-3a** and **4.1-3b** for the regions separated by $\chi = \chi_E = \chi_s$. The difference can also be obtained from equations **4.2x-3b** and **4.2x-3c** (with $\chi_E = \chi_s$), which yield

$$\Pi^* \cong 1 - \left(\pi\chi_G\right)^{-1/2}\left(2\chi_G + 1\right)\exp\left(-\chi_G\right) \qquad \{4.2-5b\}$$

and (with $k_s^2\chi_s \cong 0.5$)

$$\exp\left(\chi_s\right)\Pi_G \cong 1 - 2\left(1+\sqrt{1+2\chi_{Gs}}\right)^{-1}\chi_{Gs} - \exp\left(-\chi_{Gs}\right) \qquad \{4.2-5c\}$$

with $\chi_{Gs} \equiv \chi_G - \chi_s$ for $\chi_G > \chi_s$ and *zero* otherwise. For χ_G large, we find

$$\mathrm{E}_+^2/2 = 1 + \exp\left(-\chi_s\right)\left[2\left(1+\sqrt{1+2\chi_{Gs}}\right)^{-1}\chi_{Gs} - 1\right]. \qquad \{4.2-5d\}$$

As indicated by equation **4.2-5d**, the value of E_+ is to a good approximation independent of χ^* and thereby insensitive to the dynamics following the hump location.

The plateau potential is derived from the application of equation **4.2-2** in the region between z^* and z^{**} (where $\mathrm{K}^* = \mathrm{K}^{**} = 0$),

$$0 = \Pi^{**} - \Pi^* \qquad \{4.2-5e\}$$

with the *potential energies* approximated by the expressions in equation **4.2-4a** and **4.2-5b**. Solving equation **4.2-5e** recursively for $\left(\chi^{**} - \chi_G\right)/\chi_G$ small (which implies χ_G large) gives

$$\chi^{**} \cong \chi_G + 0.5(1+1/\chi_G)\ln(\pi\chi_G). \qquad \{4.2-5f\}$$

The potential hump Φ^* is then derived from quasi-neutrality, equation **4.2x-4** with $\chi_{\min} = \chi^*$, which for $\chi^* << 1$ gives equation **4.2-4b** with χ_G replaced by χ^*:

$$\chi^* \cong k_0^{-2}\chi^{**}\exp(-2\chi^{**}). \qquad \{4.2-5g\}$$

Lastly, the electric field E_-, which forms in the sheath *preceding* the grid, is found by applying equation **4.2-2** in the region $z_E \le z \le z_G$:

$$\mathrm{E}_-^2/2 = \Pi_E - \Pi_G. \qquad \{4.2-5h\}$$

The difference $\Pi_E - \Pi_G$ can be found by using $\Pi_E = 0$ (see equation **4.2x-3a**) and equation **4.2-5c** for Π_G. For χ_G large, we can also use equation **4.2-5a** to show that

$$\mathrm{E}_-^2 \cong \mathrm{E}_+^2 - 2. \qquad \{4.2-5i\}$$

The numerical results for the potentials and for the fields characterizing the *plateau* solution are plotted in figures **4.2-2a** and **4.2-2b**, respectively. They are calculated for the two limiting cases of χ_{MAX}, the *global* maximum: one describing our approximations, which assumes the complete reflection of the electrons ($\chi_{MAX} \to \infty$), and the other describing the *true* stationary solution, where the potential maintains its plateau ($\chi_{MAX} = \chi^{**}$). In this latter case, the electrons are partially absorbed by the collector.

[4.2.4] The general solutions

So far, we have not considered the value of the collector voltage in the analysis. As indicated by the plots of figure **4.2-3**, the plateau solution *cannot*, in general, yield a profile that matches the value of this voltage. The plateau solution can only match the

collector voltage if $V_C \le \Phi^{**}$. In this voltage range, the potential plateaus, remaining quasi-neutral up to within a few *enhanced* Debye lengths λ^{**} of the collector, where $\lambda^{**} \equiv \lambda_{De} \exp\left(\chi^{**}/2\right)$ is the Debye length associated with the *remaining* density beyond the plateau region: $n_e \cong n_\infty \exp\left(-\chi^{**}\right)$. In order for the potential to drop below Φ^{**}, the field E_+ must be slightly greater (less negative) than the one calculated for the plateau solution. The modification produces a potential hump that is slightly below Φ^*, thereby removing fewer ions. The excess ion density then yields an electric field in the plateau region (where $n_i \cong n_e$) that remains slightly positive, thereby allowing the potential to eventually drop to the collector voltage.

On the other hand, the solution for $V_C > \Phi^{**}$ requires that the field E_+ be more negative than the one for the *stationary* solution. For such a field, the potential hump rises above Φ^*, thereby removing additional ions. The shortage of ions in the region following the hump location then prevents the formation of a quasi-neutral plateau. Instead, the potential attains a minimum at a value $\Phi_{\min} > \Phi^{**}$, for which $n_i < n_e$. As the potential rises above the minimum, the ion density increases (retracing its steps), whereas the electron density is reduced further from the acceleration of its population. The opposing variations in the densities allow n_i to eventually overcome n_e. The positive δn then eventually diminishes the electric field to produce a local maximum in the potential. As the potential drops, *both* densities retrace their steps to diminish the electric field once again at $\Phi_{\min}$. The potential then rises and the cycle resumes, thereby producing the oscillations shown in figure **4.2-3**. Hence, the potential *cannot* adopt a long-range quasi-neutral solution in the regime $V_C > \Phi^{**}$. For a given pair of grid and

collector voltages then, one can use figure **4.2-2a** to determine whether the long-range behavior of the potential will be that of a plateau or of oscillations by simply comparing V_C with $\Phi^{**}(V_G)$ for the *stationary* solution: the solid line for χ^{**}.

[4.2.5] The $I-V$ characteristics

In the space charge limited regime, where the potential settles into its long-range behavior (whether it be a plateau or oscillations), the ion current that reaches the collector is not necessarily equal to that accumulated in the pre-sheath outside the housing, and the electron current that reaches the collector is less than what is allowed to pass through the grid.

The space charge limited electron current for a Maxwellian distribution is given by

$$I_C^e = I_{s//} \exp\left(-\chi^{**}\right). \qquad \{4.2-6a\}$$

When the collector is biased to absorb the electrons ($V_C > \Phi^{**}$), χ^{**} is ill defined, owing to the myriad of oscillatory solutions that could yield the same collector voltage. Hence, the best we can do is to place bounds on I_C^e:

$$I_{s//} \exp\left(-\chi^{**}\right) < I_C^e \le I_{s//} \exp\left(-\chi_G\right). \qquad \{4.2-6b\}$$

The lower bound occurs because the minimum in the potential for the oscillations is always above Φ^{**}. On the other hand, the upper bound exists because the current cannot be any greater than what the grid allows to pass through. Using the approximations for χ^{**}, equations **4.2-4c** and **4.2-5f**, we find that the lower bound in the

electron current has the asymptotic variations $I_{s//}\sqrt{-8\chi_G/\pi\ln\chi_G}$ and $I_{s//}\exp(-\chi_G)/\sqrt{\pi\chi_G}$ in the limits $\chi_G \to 0$ and $\chi_G \to \infty$, respectively.

The ion current on the other hand is given by the fraction of the current accumulated in the pre-sheath that reaches the collector. The current accumulated can be obtained from equations **2.2x-6**, **2.2-3**, and **2.2-1** with $\chi = \chi_E$. The fraction of this current that reaches the collector is then obtained by replacing χ_E with χ^*:

$$I_C^i \cong I_{si}\exp(-2\chi^*/3)\sqrt{32\chi^*}/\pi \cong I_{si}\sqrt{32\chi^*}/\pi, \qquad \{4.2-7a\}$$

where we have used the fact that χ^* is generally much less than *one*. For χ_G small ($E_+ > 0$), the space charge effects do not produce a barrier to the ions. Instead, the grid voltage controls the ion current entering the housing. In this case, χ^* is set equal to χ_G, and $I_C^i \propto \sqrt{\chi_G}$. On the other hand, for χ_G large ($E_+ < 0$), the ion current entering the housing is fixed ($\chi_E = \chi_s$), and the effects of space charge produce a barrier to the ions. Inserting the value of χ^* from equation **4.2-5g** into equation **4.2-7a** gives

$$I_C^i \cong 2\sqrt{2}\sqrt{\chi^{**}}\exp(-\chi^{**})I_{si} \qquad \{4.2-7b\}$$

for the current of ions that are able to overcome the barrier χ^*. By using the value of χ^{**} from equation **4.2-5f**, we find $I_C^i \propto \exp(-\chi_G)$. Once the collector voltage increases above Φ^{**}, the solution becomes oscillatory, and the potential hump becomes ill defined. In this case, I_C^i serves as an upper bound on the ion current because the potential hump has to remove additional ions to produce the oscillations.

The space charge limited characteristics are depicted in figure **4.2-4**. It is worth noting that the asymptotic variations in the ion current are *universal* owing to their insensitivity to the details of the ion distribution function. The square-root variation for small χ_G is a result of the drive for quasi-neutrality outside the housing, whereas the exponential variation for χ_G large stems from the drive for quasi-neutrality in the region downstream from the grid-plane together with the rather generic variation, $n_i \propto I_C^i / \sqrt{\chi}$.

[4.2.6] The effect of a locally varying magnetic field

Once the local magnetic field is varied, the space charge induced barriers to the electron and to the ion currents become uncertain for all values of the collector voltage because the local variation in the magnetic field produces oscillations in the potential profile. The oscillations occur regardless of the collector voltage because the conditions for quasi-neutrality are rigid and thereby cannot accommodate a varying magnetic field, which has a different impact on the electron and on the ion densities.

Given that we will have to vary the magnetic field to operate the GEM probe, then to interpret the $I-V$ characteristics with confidence, we must avoid the regime in which the space charge contorts the potential to form a barrier to the electrons. For a finite size grid-collector cavity, we will find that this regime is limited to small χ_G. We establish this regime and conversely the regime for the proper operation of the GEM probe in the next section.

[4.3] The potential profile inside a grid-collector cavity of *finite* size

In the previous section, we demonstrated that the space charge induces a barrier to the electron current in the limit $\lambda_{De} \to 0$. Moreover, we argued that the variation in this barrier with the local magnetic field is somewhat intractable and thereby concluded that we must avoid operating the GEM probe in such a regime. This regime has a limited range for the realistic geometry of a finite size grid-collector cavity. To determine this range, we must solve for the potential profile in a bounded volume. We solve this boundary value problem in two steps. We first incorporate the boundary condition at the collector, $\Phi(z_C) = V_C$, while maintaining the radial extent of the cavity and of the plasma infinite. We then consider a cavity with a radius $r = a$ that contains plasma with a beam size $r = b \le a$.

[4.3.1] The transition *out* of the space charge limited regime in 1-D

As was the case for the problem analyzed by Martin (see section **4.0**), the boundary values V_G and V_C do not readily yield the 1-D potential profile because they do not fully define Π in general. The *potential energy* is derived from the densities, which are not only functions of the local value of χ, but also functions of the lower and the upper bounds in the range covered by χ. Therefore, to solve the boundary value problem in general, we would have to employ the technique used by Martin: namely, we would have to partition the region $z_G \le z \le z_C$ at locations at which E is assumed to vanish, solve equation **4.2-3** in each region, and then match the solutions at the boundaries.

However, we are not concerned with the exact solutions in 1-D. We are only looking to determine the regime where the space charge effects produce a barrier to the electrons. In this space charge limited regime, the potential *settles* into a plateau or into oscillations, depending on the collector voltage. This evolution occurs within a few λ_G's downstream of the grid-plane, where $\lambda_G = \lambda_{De}\exp(\chi_G/2)$ characterizes the Debye-length associated with the electron density just past the grid-plane. If the inter-electrode spacing is of the order or less than λ_G, then the boundary at the collector truncates the profile before it has had a chance to settle into its long-range behavior. The truncation relieves the potential hump from having to remove the necessary amount of ions to produce the long-range solution. This effect weakens the connection between the potential hump and the grid voltage, and more importantly, it eliminates the space charge induced barrier to the electrons. We refer to this condition as the *vacuum* regime.

The changeover from the space charge limited to the *vacuum* regime is shown in figure **4.3-1**, where we have illustrated the 1-D potential profiles for various ratios of λ_{De}/z_{CG}. These profiles were obtained from solutions to equation **4.2-3** by guessing the value of E_+ to obtain the particular value of the collector voltage.

The profile for $\lambda_{De} << z_{CG}$ is shown to be space charge limited; that is, the potential is shown to plateau at Φ^{**} as described by the analysis of section **4.2**. As λ_{De} increases, the profile deforms to repel most of the ions as before, but the enhanced Debye-length λ_G allows for a *vacuum* solution beyond the potential hump. This solution is a linear profile *in 1-D* with an effective grid-voltage that is approximately equal to $\Phi^* \cong \Phi_\infty$ ($\chi^* \cong 0$). As the Debye-length increases further, such that $\lambda_{De} \approx z_{CG}$, the

potential profile attains the true vacuum profile, which, in 1-D, is a straight line connecting the electrode voltages.

In practice, the ratio of λ_{De}/z_{CG} is fixed, and the transition from the space charge limited to the *vacuum* regime occurs as an increasing electrostatic barrier at the grid reduces the electron density inside the grid-collector cavity. To avoid the space charge limited regime then, we must maintain V_G well below Φ_∞ so that the enhanced Debye-length λ_G, which is associated with the residual electron density, remains *comparable* to the inter-electrode spacing. From plots like figure **4.3-1**, we estimate the transition to occur about $\lambda_G/z_{CG} \sim 0.15 \cong 0.1\exp 0.5$. The *vacuum* regime can then be described approximately as

$$\chi_G = e\left(\Phi_\infty - V_G\right)/T_{//} > 1 + 2\ln\frac{z_{CG}}{10\lambda_{De}}. \qquad \{4.3-1\}$$

[4.3.2] The transition *out* of the space charge limited regime in 2-D

The result of the 1-D analysis is adequate for a grid-collector cavity with a small aspect ratio: $z_{CG}/b << 1$, where b is the radius of the plasma beam. However, the cavity for the *GEM* probe satisfies $z_{CG}/b >> 1$, owing to the large electromagnet aspect ratio. For this geometry, the size of the plasma beam b takes on the role of the inter-electrode spacing, and the sidewall bias Φ_a influences the *vacuum* potential profile. In fact, the sidewall bias completely shapes the true vacuum profile. This profile is obtained via the technique of *separation of variables* applied to Laplace's equation. It is illustrated in figure **4.3-2** for a sidewall bias that is positive with respect to the electrode voltages. The

figure shows that the potential transforms from its values at the electrodes to a plateau at the potential of the sidewall, outside of a radius a from the electrodes, where $\partial\Phi/\partial z \cong 0$.

In the presence of space charge, the profile adopts two distinct components: the profile inside the beam, $r < b$, and the one outside the beam, $b < r < a$. The latter profile will transform from the potential at the electrodes to the potential on the sidewall in the same manner as the vacuum profile depicted in figure **4.3-2**. For $\lambda_G/b << 1$, the potential inside the beam evolves axially from V_G to Φ^{**} on the scale of λ_G, leaving the burden of matching the plateau (or the oscillations) and the profile outside the beam ($r > b$) to the sheath that forms at the beam's edge.

We can describe the matching of these two profiles in the plateau region where $\partial\chi/\partial z \cong 0$ (for $V_C \le \Phi^{**}$) via the solution to $\chi'' + \chi'/r = \delta n$ (with the *prime* denoting the differentiation with respect to r). This solution can be performed numerically via an ODE solver by adjusting both the potential hump (which controls the ion density in this region) and the value of the plateau at $r = 0$ so that the potential reaches the desired value at the sidewall.

The outcome of the numerical solution is the following. For χ_G small, the potential remains constant, equal to Φ^{**}, up to within a few λ_G's from the beam's edge. The space charge at the edge then provides the necessary field to propel Φ^{**} to the potential on the sidewall. As χ_G increases and the enhance Debye-length becomes comparable to b, the condition of quasi-neutrality is relaxed. The plasma beam in this case is able to sustain a finite amount of space charge over a greater extent, and the penetration of the electric field allows the sidewall potential to influence a greater portion

of the profile inside the beam. As χ_G increases further, the plateau stabilizes at Φ_a, and the solution beyond the hump location z^* resembles the vacuum profile of figure **4.3-2** with the electrode voltage at the grid replaced by the value of the potential hump.

The numerical results indicate that we may estimate the transition out of the space charge limited regime in 2-D by using the criterion of equation **4.3-1** with the inter-electrode spacing z_{CG} replaced by the plasma beam radius, b:

$$\chi_G > \chi_\lambda \cong 1 + 2\ln\frac{b}{10\lambda_{De}}. \qquad \{4.3-2\}$$

[4.4] Conclusion

In this chapter, we have addressed the dynamics of the electron and of the ion space charge inside a region that is sandwiched by a grid and a collector. We found that the space charge, in general, not only produces a barrier to the ions, but that it also produces a barrier to the electrons; one that is greater than that applied at the grid. These barriers modify the collector's $I-V$ characteristics from that predicted in sections **2.2** and **3.3**.

The space charge limited electron current to the collector for $B_{em}=0$ is given by $I_C^e = I_{s//}\exp\left(-\chi^{**}\right)$, where $\chi = e\left(\Phi_\infty - \Phi\right)/T_{//}$ and χ^{**} is described by equations **4.2-4c** and **4.2-5f** in the opposing limits $\chi_G \to 0$ and $\chi_G \to \infty$, respectively. With the aid of the numerical results, the asymptotic variations for the two limits are spliced to produce the *Pade* approximation,

$$\chi^{**} \cong \chi_G + 0.5\left[1+\left(1+\chi_G^2\right)^{-1}\chi_G\right]\ln\left[1+\pi\chi_G-\left(\pi^2/8\right)\chi_G^{-1}\ln\chi_G\right].$$

The ion current to the collector in this regime is strongly dependent on the electron space charge in the grid-collector cavity and is virtually insensitive to the ambient ion distribution function. This current varies as

$$I_C^i \cong 2\sqrt{2}\sqrt{\chi^{**}}\exp\left(-\chi^{**}\right)I_{si},$$

which gives $I_C^i \sim \sqrt{\chi_G} I_{si}$ and $I_C^i \sim \exp\left(-\chi_G\right)I_{si}$ in the opposing limits $\chi_G \to 0$ and $\chi_G \to \infty$, respectively.

These relations were derived with the assumption that the potential attains a quasi-neutral state downstream from the grid-plane. However, we demonstrated that such a state is not possible when the collector voltage is increased above Φ^{**}. Furthermore, we argued that a variation in the local magnetic field eliminates the possibility of a quasi-neutral solution regardless of the voltage on the collector.

We then gauged the extent of the regime where the electron current is space charge limited by incorporating the boundary conditions at the collector and at the sidewall. We estimated that the space charge limited regime remains in effect until the grid removes enough electrons to make the Debye-length that is associated with the remaining density a respectable fraction of the radial extent of the plasma beam inside the housing; that is until $V_G = \Phi_\lambda$ where

$$\Phi_\lambda \cong \Phi_\infty - \frac{T_{//}}{e}\left[1 + 2\ln\frac{b}{10\lambda_{De}}\right] \qquad \{4.4-1\}$$

with b equal to the radius of the plasma beam.

As the grid voltage is reduced below Φ_λ, the potential profile becomes that in *vacuum* a few λ_{De}'s downstream from the grid with the value of the grid voltage replaced

by the potential hump $\Phi^* \cong \Phi_\infty$. This profile attains a plateau at the potential of the sidewall, a voltage that can be preset to allow the electrodes to control the electron current. Given that this control is desired in practice, the *operation* of the GEM probe is restricted to

$$V_C \leq V_G < \Phi_\lambda .$$

In practice, one can use the ion current to the collector as a means to check whether the probe is operating in the *vacuum* regime. In this regime, I_C^i should be *insensitive* to the grid voltage because the potential hump does not have to remove the necessary amount of ions to provide a quasi-neutral state in the region following the hump location.

---

[i] I. H. Hutchinson, Principles of Plasma Diagnostics, p. 82
[ii] T. Honzawa, T. Sekizawa, Y. Mityauchi and T. Nagasawa, Jpn. J. Appl. Phys. **32**, pp. 5748-5753 (1993)
[iii] P. Martin and G. Donoso, Phys. Fluids B **1** (1), p. 247 (1989)
[iv] P. Martin and G. Donoso, Rev. Sci. Instrum. **61**, p. 3381 (1990)

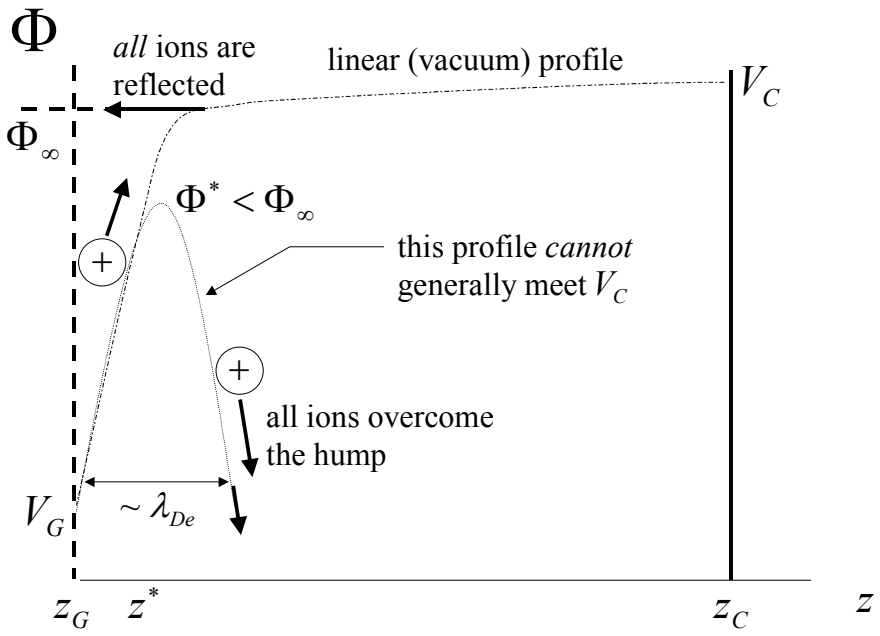

FIGURE 4.0-1: The 1-D solutions to the potential for *cold* ions

FIGURE 4.0-2: The geometry for the analysis of space charge effects

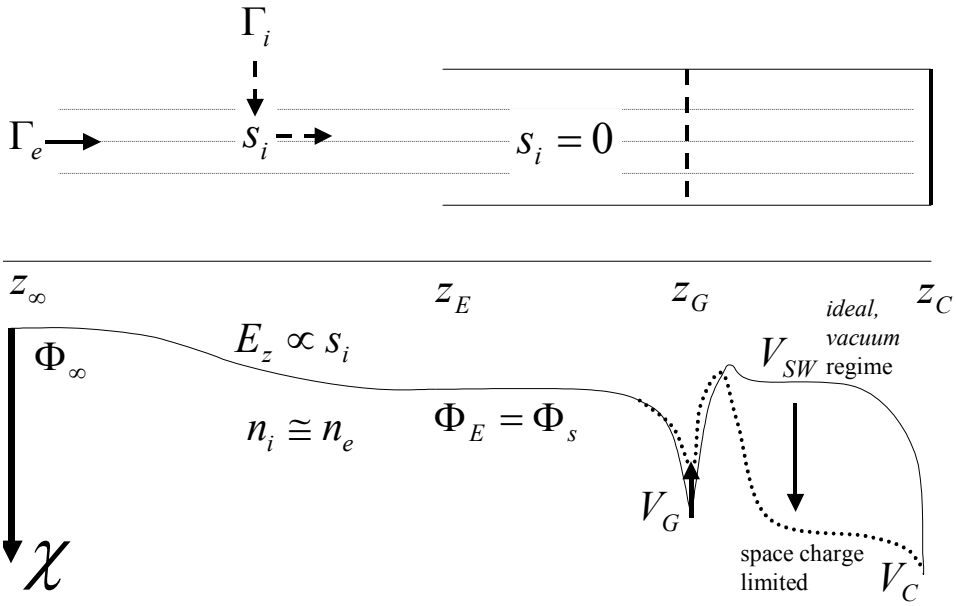

FIGURE 4.0-3: The two viewpoints for solving the 1-D Poisson's equation inside the grid-collector cavity.

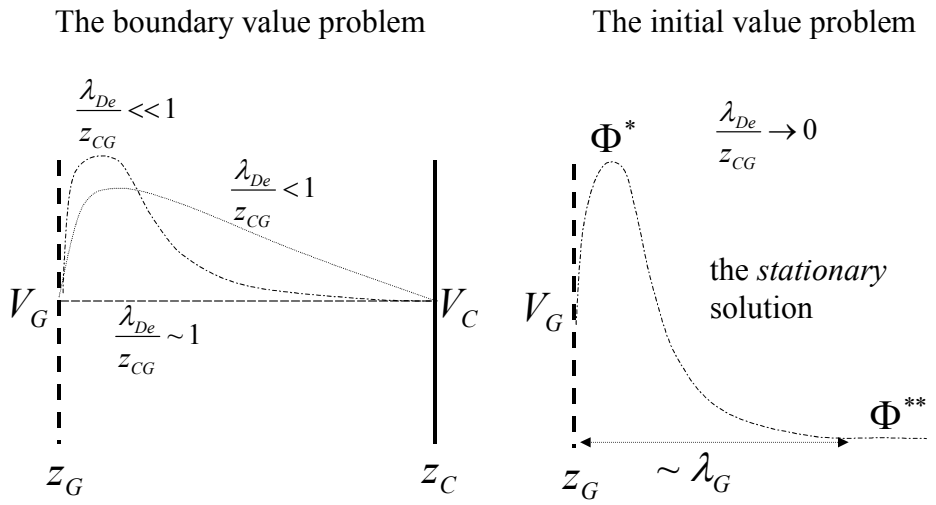

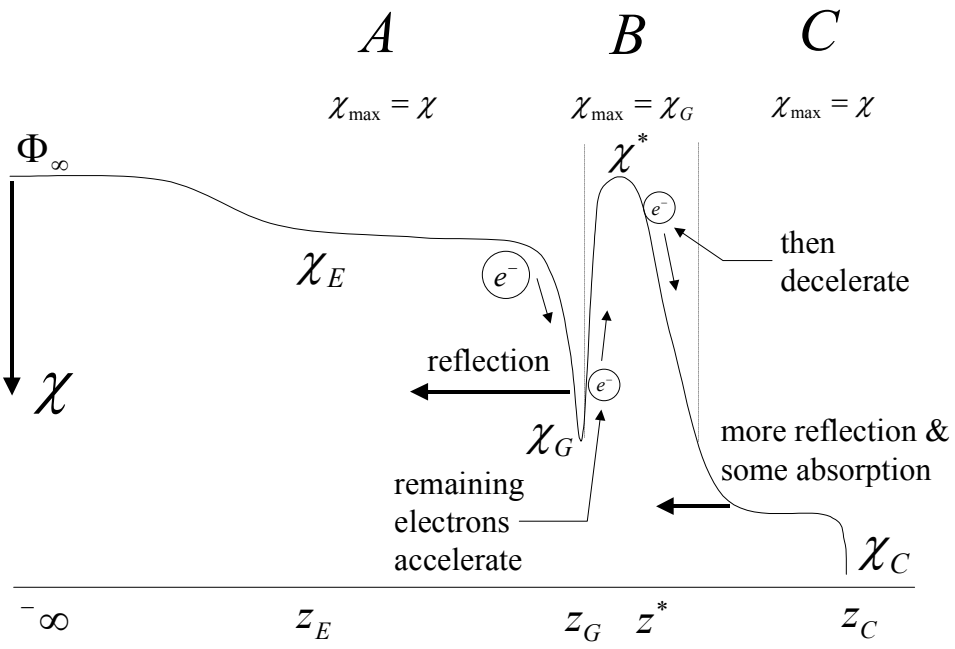

FIGURE 4.1-1a: The impact of the electric field on the electrons

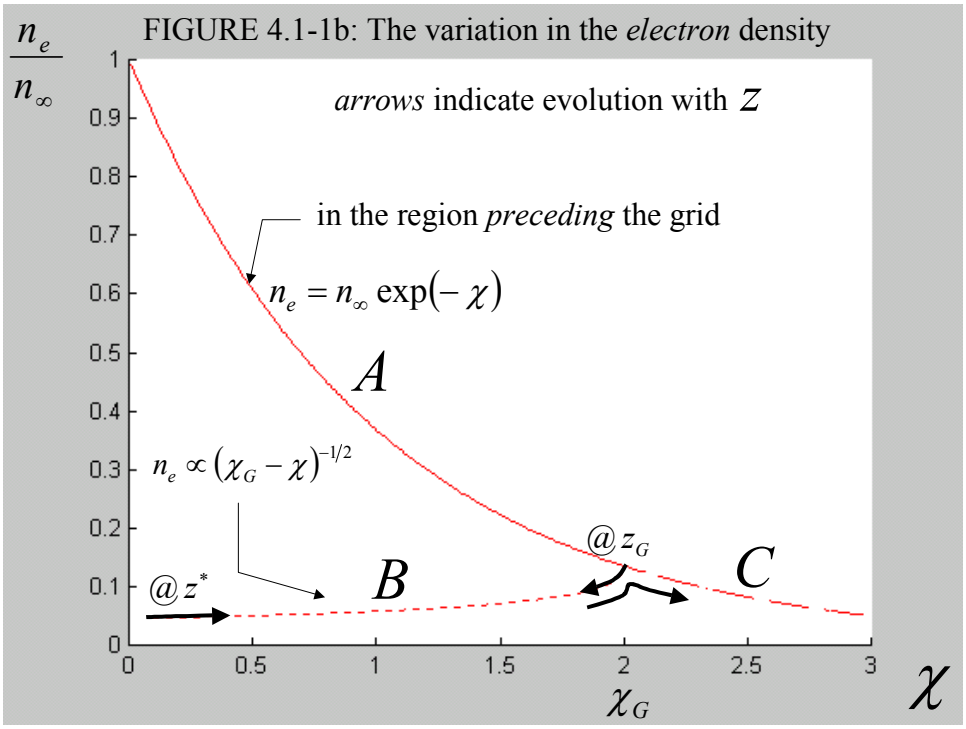

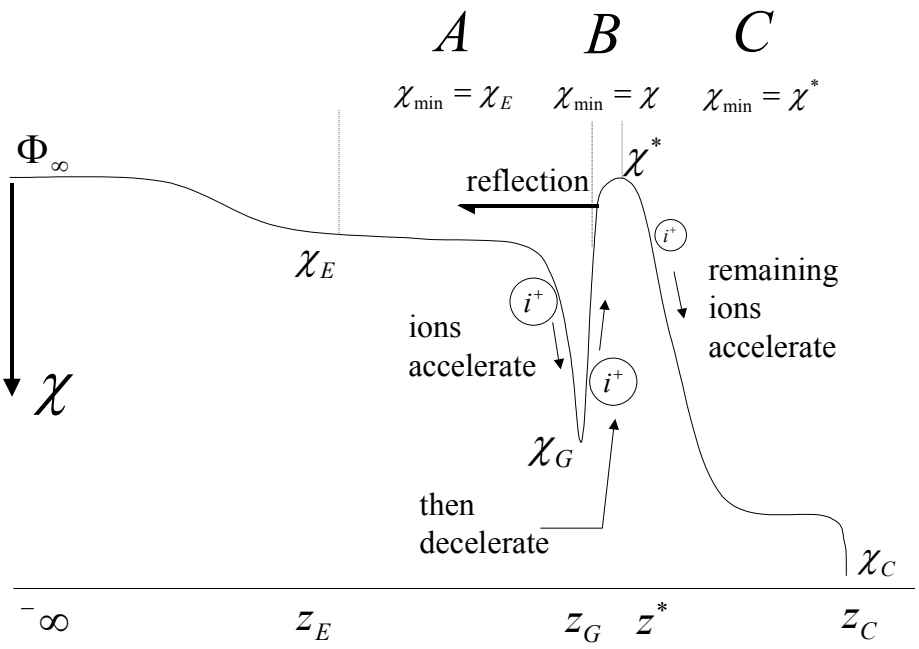

FIGURE 4.1-2a: The impact of the electric field on the ions

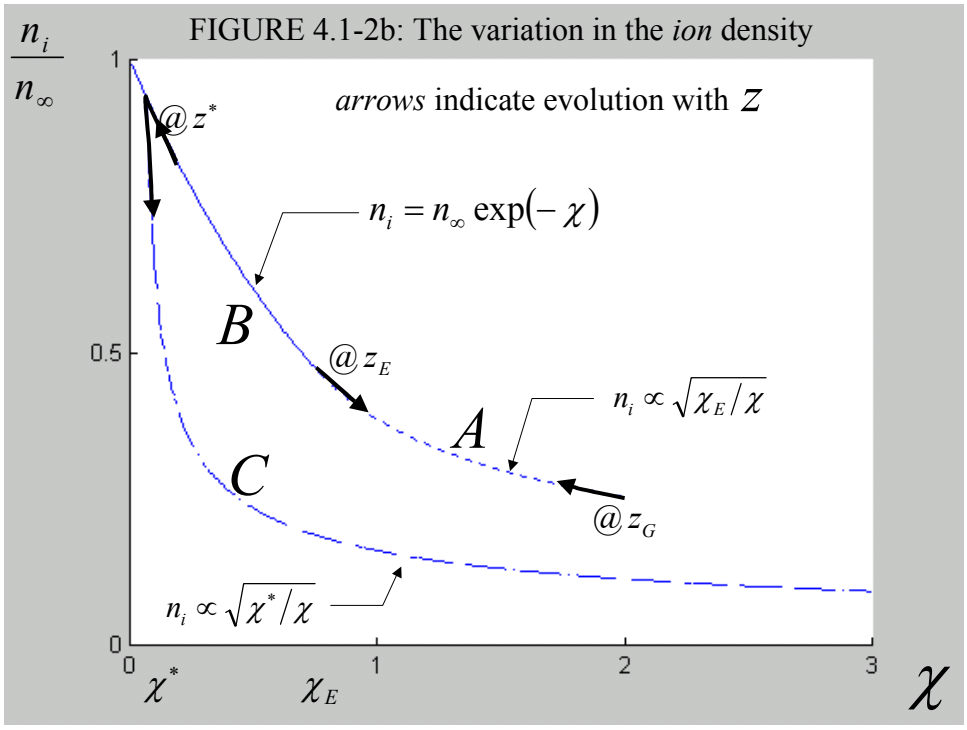
$\frac{n_i}{n_\infty}$
FIGURE 4.1-2b: The variation in the *ion* density
arrows indicate evolution with Z
$@\, z^*$
$n_i = n_\infty \exp(-\chi)$
B
$@\, z_E$
$n_i \propto \sqrt{\chi_E / \chi}$
A
C
$@\, z_G$
$n_i \propto \sqrt{\chi^* / \chi}$
1
0.5
0
0
1
2
3
χ^*
χ_E
χ

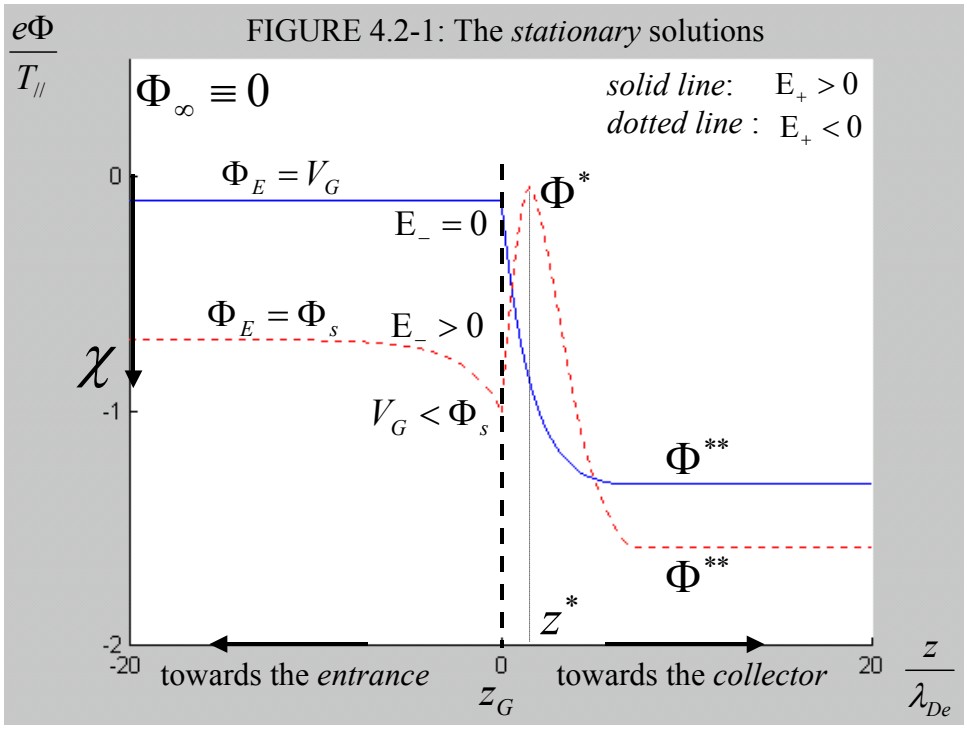
$\frac{e\Phi}{T_{//}}$
FIGURE 4.2-1: The *stationary* solutions
$\Phi_\infty \equiv 0$
solid line: $E_+ > 0$
dotted line : $E_+ < 0$
$\Phi_E = V_G$
$E_- = 0$
Φ^*
$\Phi_E = \Phi_s$
$E_- > 0$
$V_G < \Phi_s$
Φ^{**}
Φ^{**}
z^*
0
-1
-2
-20
0
20
towards the *entrance*
towards the *collector*
z_G
$\frac{z}{\lambda_{De}}$
χ

FIGURE 4.2-2a: The *potentials* characterizing the *plateau* solution

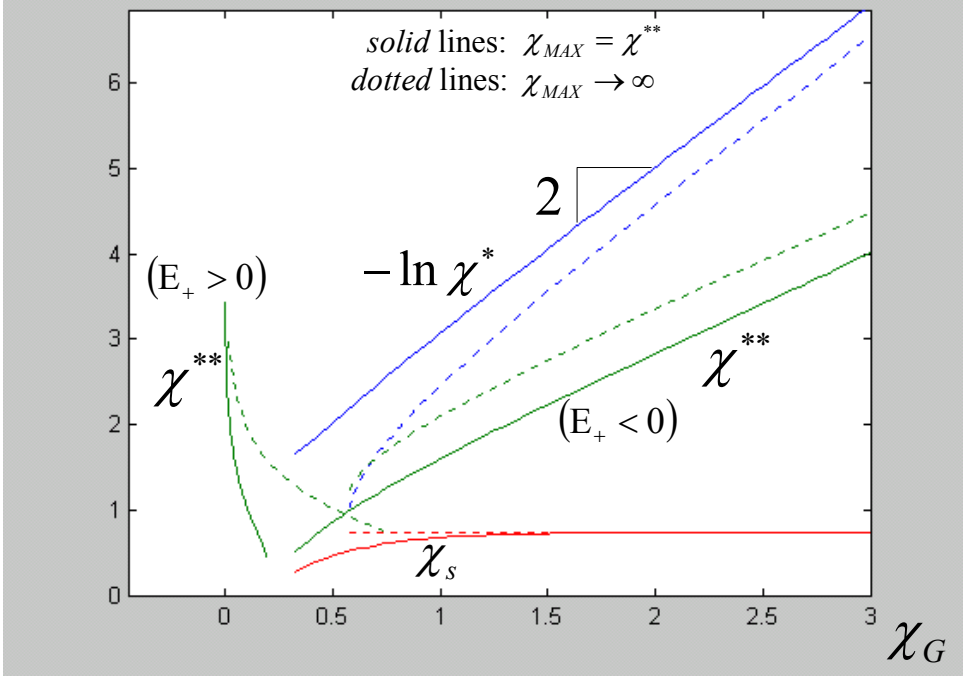

FIGURE 4.2-2b: The *fields* characterizing the *plateau* solution

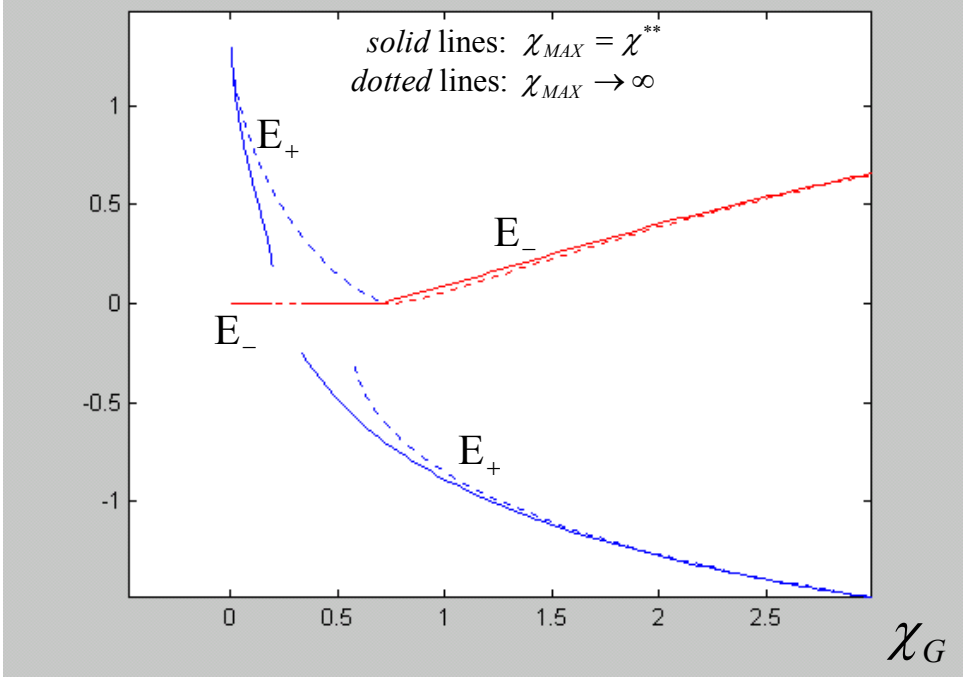

FIGURE 4.2-3: The general solutions when space charge limited

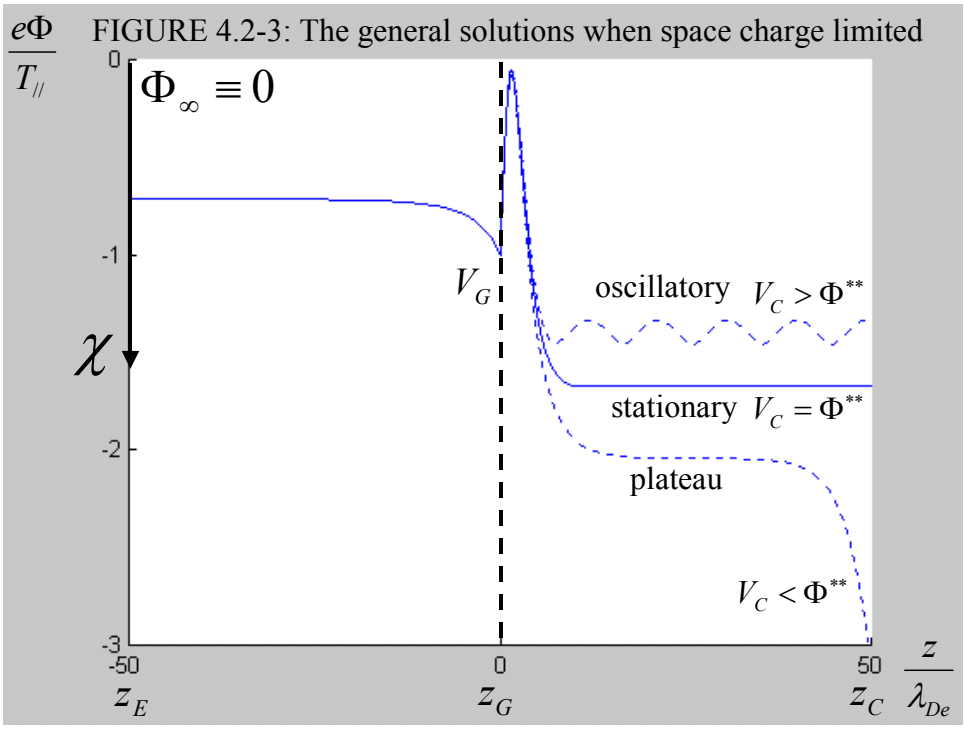

FIGURE 4.2-4: The space charge limited currents to the collector

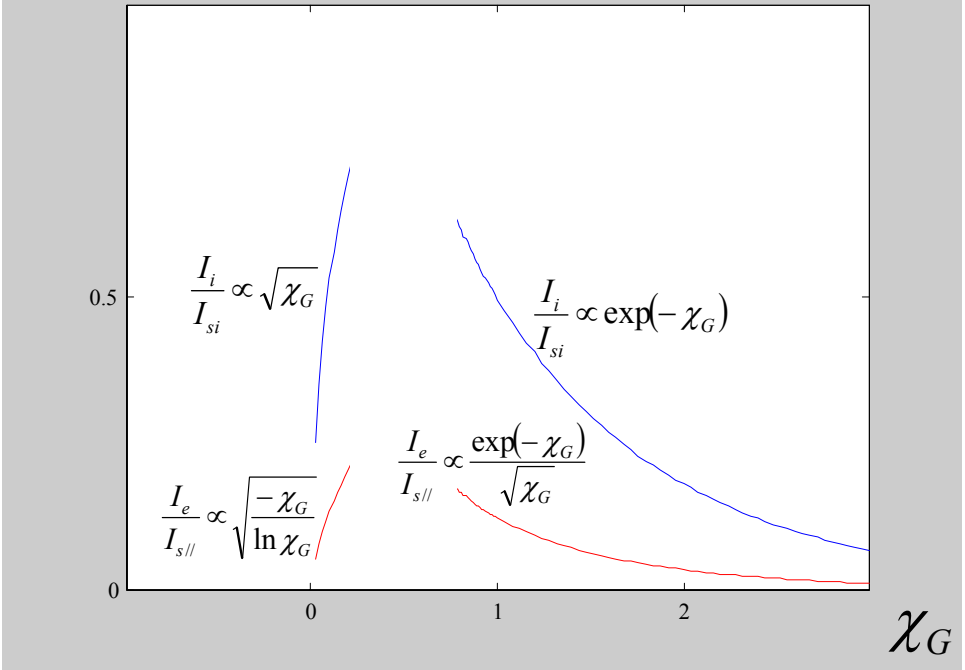

FIGURE 4.3-1: The *evolution* of the potential profile

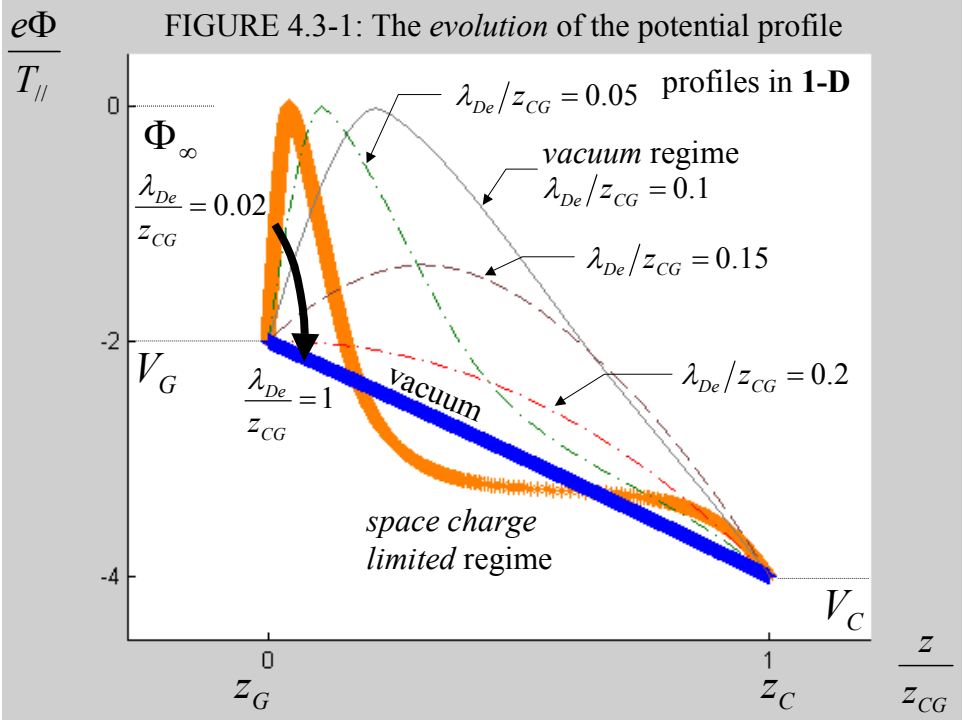

FIGURE 4.3-2: The potential in vacuum in the grid-collector cavity

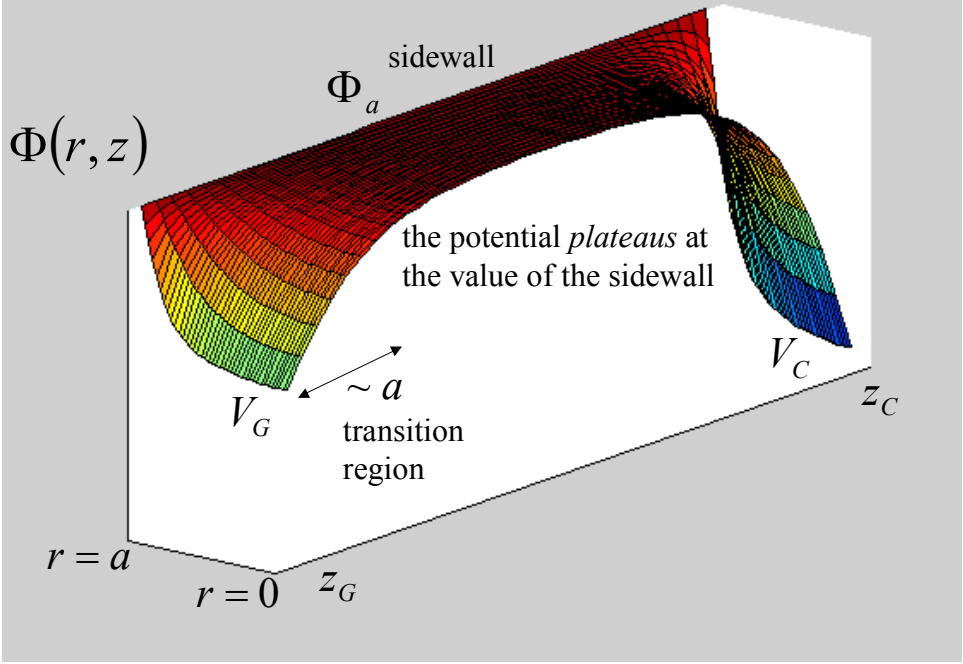

(This page left intentionally blank.)

CHAPTER 5

THE ELECTRICAL AND PHYSICAL STRUCTURE OF THE MESH AND ITS IMPACT ON THE MEASURED ELECTRON DISTRIBUTION FUNCTION

[5.0] Introduction

In chapter **3**, we concluded that a grid creates a dual-barrier configuration with the barrier at the electromagnet throat comprising an electric and a magnetic component. The electric component serves as a powerful aid because it allows the discrimination of electrons with small pitch angle. However, the provision of this aid comes with limitations in addition to those pertaining to space charge effects. There are also limitations that stem from the grid's discrete physical structure.

[5.0.1] The impact of the grid's electric field structure

A schematic drawing of a mesh is illustrated in figure **5.0-1**. The discrete, periodic structure of the mesh produces an electric perturbation. The field that emanates from the wires of the mesh is only partly directed normal to its plane. Therefore, the work done by the field on the electron's parallel energy is less than $\Theta_G = e\left(\Phi_\infty - V_G\right)$. The magnitude of the actual barrier depends on both the applied grid voltage and on the electron trajectory in the vicinity of the mesh. The average potential energy gained by an electron at the grid is actually given by $\Theta_0 = e\left(\Phi_\infty - \Phi_0\right)$, where the potential Φ_0 is the average of Φ over the patch cross-section.

Figure **5.0-2** illustrates the effect of the perturbation in vacuum for a grid sandwiched by two opaque electrodes. The electric hole in the mesh, $\Phi_0 - V_G$, depends

on the average *far* field emanating from the two sides of the mesh, where by "far" we mean the region outside of one wire spacing from the mesh, $|z| > d$. Here, the perturbation $\tilde{\Phi} \propto \exp(-2\pi|z|/d)$ has decayed to an insignificant level. For the geometry shown in figure **5.0-2**, the far field in vacuum on either side is equal to $(\Phi_0 - V)/l$, where V is the voltage on the electrode and l is the inter-electrode spacing. In practice, however, the sheaths that form about the grid determine the far field.

In addition to the electric hole, the path dependence for the exchange of energy with the field of the perturbation introduces an uncertainty in the grid barrier about its average value. The smear in the barrier degrades our ability to resolve the energies for the measurement of F_∞. Furthermore, the field perturbation produces an exchange between the electron's perpendicular and parallel energies as the electrons pass through the mesh. Unlike the exchange produced by the variation in the magnetic field, this one is somewhat unpredictable because its extent is also path dependent. This effective pitch angle scattering diffuses the electron energies, thereby altering the distribution function in the grid-collector cavity.

To assess the impact of the field perturbation on the relation between the collector current and the ambient distribution function, we first solve for the vacuum potential profile about a mesh of high transparency (the case in practice). The profile in the vicinity of the wires is difficult to model, owing to the topology of the corners where the wires cross. However, we demonstrate in section **5.1** that for a mesh of high transparency, we can determine the potential accurately without considering its exact structure about the wire.

For a *single vertical array of wires* of spacing d (figure **5.0-1** *without* the *horizontal* wires), we can calculate the potential profile exactly either by Fourier decomposing the variation of the surface charge about the wire's perimeter or by employing a conformal mapping technique. Martin and Donoso[i] utilized this latter technique to determine the potential of a grid with a 1-D array of wires sandwiched by two plates: one plate mimicking an entrance grid modeled as an equipotential plane and the other representing a collector. They used the vacuum solution to determine the *ion* $I_C - V_G$ characteristic for a Maxwellian distribution. They found that the characteristic shifted and stretched as compared to the one derived from an ideal grid (a grid mimicking an equipotential plane). The distortion in the characteristic stemmed from the dependence of the perturbation on the *far* field. Their findings correlated with their experiment[ii] in the regime where the space charge modifications were negligible (inter-electrode spacing less than or of the order of λ_{De}) and where the ions did not experience a significant deflection by the field perturbation (the deflection was not modeled).

The *advantage* of Martin and Donoso's vacuum solution is that it is valid for a mesh with any transparency as well as for any ratio of the wire spacing to the inter-electrode distance. However, these advantages are not relevant for the mesh in the *GEM* probe because our mesh has a high transparency and its wire spacing is minute relative to the distance between the grid and the collector. The *advantage of our derivation* is that it applies to both a one-dimensional and a two-dimensional array of wires. The addition of a second array of wires (to form a mesh) renders the grid more like an opaque plate, which in turn depresses the magnitude of the perturbation, thereby enhancing the performance of the grid as an electric barrier.

The application of the vacuum solution to the potential profile in plasma is addressed in section **5.2**. The solution in plasma comprises the matching of the electric field that emanates from the mesh to the field produced by the sheaths about the grid. This solution *neglects* the space charge in the vicinity of the wires, which is an adequate approximation when $d << \lambda_{De}$. For $d \sim \lambda_{De}$, the vacuum and the plasma sheath solutions coalesce, thereby requiring that we account for the space charge within the region that is subject to the influence of the field emanating from each wire individually. In other words, in this regime, we cannot employ the vacuum solution. We have not solved for the potential in the regime $d \sim \lambda_{De}$ because it is not of practical interest. In this case, the applied voltage at the wires is shielded by the plasma space charge.

With our model for the field perturbation, we next assess the distortion in the grid barrier and the dispersion of the *electron* energies. We evaluate these quantities in section **5.3** by calculating the work done by the field on the electrons along the fictitious path of the unperturbed gyro-orbit. The effect of the field perturbation is to shift and to distort the barrier as a result of the path sensitivity. That is, the effective electrostatic energy gained by the electrons at the grid is now $\Theta = \Theta_G - \Delta_0 \pm \delta_0$ with

$$\Delta_0 \sim \frac{1}{2\pi} \ln\left(\frac{d}{2\pi r_w}\right) \frac{d}{\lambda_{De}} T_{//}$$

and $\delta_0 \sim (d/2\pi\lambda_{De}) T_{//}$, where r_w is the wire radius.

We find that the electric *hole* imparts a correction of order d/λ_{De} to the parallel temperature as measured via the relation $edV_G / d \ln I_C$ (see section **2.3**). In addition, we show that the correction to the temperature anisotropy β as measured by the technique of

the *M* probe (section **3.1**) arises from the distortion in the grid barrier and is thereby higher order in d/λ_{De} : $\delta\beta/\beta \sim \left(d/2\pi\lambda_{De}\right)^{5/2} << 1$.

We also find that the electric *hole* modifies the relation for the distribution function F_∞ as described by equation **3.3-3** as well as the location of the perpendicular energy at which the distribution is evaluated. In addition, the distortion in the barrier limits our ability to resolve the perpendicular energies for the measurement of F_∞, and the diffusion of the electron energies produces an uncertainty in F_∞.

We conclude then that to assume the ideal behavior as described in section **3.3**, we must have $d/\lambda_{De} \le 0.1$, which for typical lab-plasmas translates to $d \sim 10\mu m$.

[5.0.2] The impact of the grid's physical structure

The *face* of the wires, which is associated with the grid's optical opacity O_w, reduces the current to the collector by the factor $1-\mathrm{O}_w = \left(1-w/d\right)^2$ due to the *width* of the wires, w. This effect, however, is benign in that it only modifies the coefficient in equation **3.3-3** for the distribution function by a constant, known factor. The adverse effect is associated with the depth of the wires, t, in the direction normal to the grid plane. The thickness preferentially absorbs electrons with large pitch angle. These electrons traverse a larger distance across the field lines as they pass through the mesh. Therefore, they are more likely to impact the *sides* of the wires.

In section **5.4**, we determine the variable mesh opacity associated with the wire thickness by calculating the fraction of electrons with given energies that impact the boundary of a mesh opening or "patch". We first use our result to determine the

amplification of the grid current from that computed by the optical opacity alone. In the limit $d/\lambda_{De} \to 0$, the amplification factor for a bi-Maxwellian electron distribution is found to be $A = 1 + (t/w)\sqrt{\beta}$, where we have taken $w << d$. This factor produces *another* means for measuring β (aside from equation **3.1-4**) via a comparison of the grid and the collector currents: $I_G / I_C = \mathrm{O}_w A$.

We then show that the operation $\partial^2 I_C / \partial V_G \partial V_C$ actually produces a convolution between F_∞ and the variable opacity, which complicates the inversion process for obtaining the distribution function. We find that the modification to equation **3.3-3** can be expressed as

$$F_\infty^* \cong \underbrace{\alpha_0 \frac{\partial^2 I_C}{\partial \Theta_G \partial \Theta_C}}_{F_\infty^*|_{t=0}} + \frac{4t}{\pi d}\sqrt{\frac{1+\alpha_0}{\alpha_0}}\int_0^1 \frac{du}{\sqrt{1-u}}\frac{\partial}{\partial u}\left[\sqrt{u}F_\infty\left(U_{//}^*, U_\perp^* u\right)\right],$$

which we can solve recursively for $t/d << 1$. The requirement on the wire thickness for such a solution, when coupled to the criterion on the wire spacing, gives $t \sim 1\mu m$.

[5.1] The potential structure of a mesh in vacuum

In this section, we solve for the potential about the mesh in vacuum. In doing so, we determine the extent and the magnitude of the electric perturbation produced by the discrete, periodic structure of the mesh. For the relevant case, where the grid is immersed in plasma, the vacuum solution yields an approximation to the potential with the accuracy depending on the ratio of the scale length characterizing the mesh (d) to that characterizing the plasma (λ_{De}).

[5.1.1] The "thin" wire approximation

As mentioned in section **5.0**, the GEM probe employs a mesh with a high transparency. As we demonstrate in the following argument, the resulting geometry allows us to neglect the variation of the surface charge about the wire's perimeter. The surface charge non-uniformity about the perimeter of a wire is associated with the wire's shape as well as the interaction of the wire's charge with the charge of the adjacent wires. The surface charge's *azimuthal* variation is determined by the cancellation of the electric field impinging the wire: $\sigma(\theta) = \varepsilon_0 \vec{E}_w \cdot \hat{n}$, where σ is the surface charge density, $\hat{n}$ is the surface-normal unit vector, $\vec{E}_w$ is the electric field at the wire, and the azimuthal angle θ describes the movement about the perimeter. The field at the wire is a sum of the fields impinging the mesh from $|z| \to \infty$ (associated with the plasma space charge) and the ones emanating from the adjacent wires.

The periodicity in θ allows the surface charge density to be represented as a sum over the Fourier coefficients $\sigma_k \equiv \oint d\theta \exp(-ik\theta)\sigma(\theta)$. The cancellation of the field from the adjacent wires generates coefficients with $|k| \geq 2$, which are small relative to the average surface charge σ_0 when $r_w/d << 1$, where r_w is the wire radius. This claim can be verified by examining the sum of the *opposing* fields at the edge of a wire ($\varepsilon_0 E \sim \sigma_0 r_w/r$) emanating from the wires to the *right*, $r = d - r_w$, and to the *left*, $r = d + r_w$: $\sigma_2 \sim \varepsilon_0 \delta E \sim \sigma_0 (r_w/d)^2$. The cancellation of the fields impinging from $z \to \pm\infty$, on the other hand, contributes to σ_1, which could possibly render $|\sigma_1|$ comparable to $|\sigma_0|$ if there is a significant disparity between the two fields. The

deviation of the wire's shape from that of a circle will also contribute to these Fourier coefficients.

Regardless of the magnitude of the $\sigma_{|k|\geq 1}$'s, however, their contributions to the field diminish faster than that from a dipole with the distance r from a wire, $E \propto (w/r)^{|k|+1}$, and thereby are small by the ratio of $(w/r)^{|k|}$ relative to the contribution from the average surface charge. The *neglect* of the surface charge irregularity about the wire perimeter then produces errors of the order r_w/d, which are negligible.

[5.1.2] Exploiting the periodic structure of the mesh

The surface charge also has a periodic variation along the wire, which is associated with the wires' crossover. The charge near the intersection point between two wires is reduced drastically from the mutual repulsion. This variation maintains the potential on the wire's surface constant over its extent, and unlike the variation about the wire's perimeter, it cannot be neglected.

We Fourier decompose the periodic variation of the charge on the wires so that we may express the potential as a sum of its average value at a given distance from the grid-plane $|z|$ and its perturbation:

$$\Phi = \overline{\Phi}(|z|) + \widetilde{\Phi}(x, y, |z|) \qquad \{5.1-1\},$$

with

$$\overline{\Phi} = \Phi_0 - (q_0/\varepsilon_0)|z|/d \qquad \{5.1-1a\},$$

$$\widetilde{\Phi} = \sum_{k,l\neq 0,0} \exp[2\pi i (kx + ly)/d]\Phi_{k,l}(|z|) \qquad \{5.1-1b\},$$

and $k,l \neq 0,0$ denoting that the sum *excludes* the term with $k = l = 0$. The quantity Φ_0 is equal to the average value of the potential at the grid, which is to be determined.

As we demonstrate in appendix **5.1x**, the potential's Fourier coefficients are given by

$$\Phi_{k,l} = \frac{q_k + q_l}{4\pi\varepsilon_0 |k,l|} \exp\left(-2\pi |k,l||z|/d\right) \qquad \{5.1-1c\},$$

where $|k,l| \equiv \sqrt{k^2 + l^2}$ and $q_k \equiv \int_0^d (dx/d) q(x) \exp\left(-2\pi i k\, x/d\right)$. Here, $q(x) = \oint d\theta r_w(\theta) \sigma(x,\theta)$ is the charge per *unit length* with x equal to the distance along the wire. The $q_{k\neq 0}$'s are determined by imposing the condition that the potential remain constant on the wire surface over its extent. We will find in subsection **5.1x.1** that these Fourier coefficients are proportional to the average charge per unit length q_0; a quantity that is determined by the average field emanating from the two sides of the mesh. This field is

$$\overline{E} = 0.5\left(E_+ - E_-\right) \qquad \{5.1-2a\},$$

with the subscripts $\pm$ denoting the two sides of the mesh and $E = -d\Phi/dz$. There are *four* wires surrounding each mesh opening or "patch", and each wire contributes a *quarter* of its charge to the average field emanating from either side of a patch. Therefore, the charge associated with a patch is $4 \times \left(q_0 d/4\right)$ giving $\varepsilon_0 \overline{E} d^2 = q_0 d$ or

$$q_0/\varepsilon_0 = \overline{E} d \qquad \{5.1-2b\}.$$

The quantity $\overline{E}$ is *determined* by the sheaths about the grid; the topic of section **5.2**.

Lastly, we note that the potential that we have constructed is symmetric about the grid-plane. The neglect of the *azimuthal* variation in the surface charge, however, allows us to readily generalize the solution by adding on the 1-D vacuum potential:

$$\Phi = \Phi_0 - 0.5\left[\left(E_+ - E_-\right)|z| + \left(E_+ + E_-\right)z\right] + \widetilde{\Phi} \qquad \{5.1-2c\}.$$

Notice that if $E_+ = E_-$, then q_0 and, with it, $\widetilde{\Phi}$ diminish, thereby rendering the potential blind to the presence of the mesh (up to the order r_w/d).

[5.1.3] The field perturbation associated with a 1-D array of wires

Before we analyze the electric perturbation of a mesh, we backtrack to describe the perturbation of a single array of wires, which is similar to that of a mesh but simpler to analyze. The solution for a single array is a subset of the solution for the mesh. It can be obtained by setting $q_l = 0$ for all l (because we only have a single array) and by setting $q_k = 0$ for all $k \neq 0$ (because for a single array, the surface charge does not vary over the wire's extent). What remains is a sum over the Fourier coefficients that describe the potential's periodic variation across the patch in the x-direction:

$\Phi_{1D}\left(x,|z|\right) = \overline{\Phi}_{1D}\left(|z|\right) + \widetilde{\Phi}_{1D}\left(x,|z|\right)$ with $\overline{\Phi}_{1D} = \Phi_0 - \left(q_0/2\varepsilon_0\right)|z|/d$ and

$\widetilde{\Phi}_{1D} = 2\,\mathrm{Re}\sum_{k\geq 1}\exp\left(2\pi i k\, x/d\right)\Phi_{k,0}\left(|z|\right)$.

The sum over k can be done readily if we first sum over $d\Phi_{k,0}/d|z|$. Taking the derivative allows us to exploit the solution for the sum over a power series, $\sum_{k\geq 1} a^k = a/(1-a)$, with $a = \exp\left[2\pi\left(ix - |z|\right)/d\right]$. Integrating the result then gives

$$\Phi_{1D} = \Phi_0 - \frac{q_0}{4\pi\varepsilon_0}\ln\left[4\sinh^2\left(\pi|z|/d\right)+4\sin^2\left(\pi x/d\right)\right] \qquad \{5.1-3\}.$$

For a *single array of wires*, there are only two wires per patch. Therefore, these wires need twice as much charge as the wires in a 2-D array in order to balance the average *far* field $\overline{E}$: $q_0/\varepsilon_0\big|_{1D} = 2\overline{E}d$.

A contour plot of the potential profile for a single array of wires is shown in figure **5.1-1**. The figure illustrates that the perturbation rapidly diminishes with distance from the grid plane, $\widetilde{\Phi}_{1D} \propto \cos(2\pi x/d)\exp(-2\pi|z|/d)$, and what remains is an equipotential plane that varies linearly with $|z|$: $\Phi_{1D} \propto |z|$. On the other hand, when $x^2 + z^2 << d^2$, the profile becomes that associated with a single wire: $\Phi_{1D} \propto \ln r$, where $r^2 = x^2 + z^2$. These behaviors are also valid for the mesh except for near the corners of the patch, where the $q_{k\neq 0}$'s contribute significantly.

Although the expression for $\Phi_{k,0}$ is strictly defined in the region $|z| \geq t/2$, equation **5.1-3** remains valid so long as we evaluate the potential *outside* the wire *radius* r_w. The magnitude of this radius for $w = t$ is simply $w/2$. To determine r_w in general, we compare the above solution to that for the case with $t \to 0$, which is performed via a conformal mapping technique described in subsection **5.1x.2**. A comparison of $\widetilde{\Phi}_{1D}$ at the wire, which can be found from equation **5.1-3** via the operation $\left[\Phi_{1D} - \Phi_0\right]_{z=0,x=r_w}$, with its counterpart for a mesh of wires with no depth, equation **5.1x-9**, indicates that we may define the wire surface to be at the location $r_w = (w+t)/4$.

[5.1.4] The field perturbation associated with a mesh (a 2-D array) of wires

The surface charge for the mesh is no longer uniform over the extent of the wires. Figure **5.1-2a** and **5.1-2b** illustrate the surface charge variation and the Fourier coefficients q_k, respectively, for various ratios of r_w/d. The surface plots of the perturbation $\widetilde{\Phi}$ are illustrated in figures **5.1-3a** and **5.1-3b**. The magnitude of the perturbation is normalized to $V_G - \Phi_0$, the difference between the voltage on the wires and the average potential at the mesh plane. This difference is essentially due to the average charge on the wire. Therefore, its value is approximately *half* that for the single array of wires:

$$V_G - \Phi_0 \cong 0.5\widetilde{\Phi}_{1D}\Big|_{r_w} \cong \frac{\overline{E}d}{2\pi}\ln\left[d/2\pi r_w\right] \qquad \{5.1-4a\}.$$

The $q_{k\neq 0}$'s produce corrections to $V_G - \Phi_0$ that scale as $\left[\ln\left(d/r_w\right)\right]^{-2}$. *Away from the patch corners*, we can neglect the contribution from the $q_{k\neq 0}$'s and thereby approximate the potential by $\Phi \cong 0.5\left[\Phi_{1D}\left(x,|z|\right)+\Phi_{1D}\left(y,|z|\right)\right]$, which yields

$$\Phi_m - \Phi_0 \cong \widetilde{\Phi}_{1D}\left(d/2,0\right) \cong -\overline{E}d\ln\left(2\right)/\pi \qquad \{5.1-4b\}$$

for the magnitude of the perturbation at the *patch midpoint*.

Having determined the structure of the perturbation in vacuum, we next apply the vacuum solution to the perturbation in plasma.

[5.2] The electrostatic perturbation of a mesh immersed in plasma

In this section, we find a solution for the potential profile about a mesh immersed in plasma in order to determine the size of $\widetilde{\Phi}$ in the practical regime $d/\lambda_{De} << 1$. We use

the result in the next section to assess the impact of the perturbation on the electron energies and on their energy distribution.

When solving for the perturbation in plasma, we cannot simply sum the contribution from the space charge along with the charge on the wires because the space charge is a function of the potential itself. Instead, we solve for the potential using Poisson's equation:

$$\partial^2 \chi / \partial z'^2 = \left(d/\lambda_{De}\right)^2 \delta n - \nabla'^2_{\perp} \chi ,$$

where $\chi = e\left(\Phi_\infty - \Phi\right)/T_{//}$, $\nabla'_{\perp}$ is the gradient operator in the x - y plane, the *prime* denotes *normalization* to the distance d, and $\delta n = \left(n_i - n_e\right)/n_\infty$. Even though the periodicity of the mesh reduces the analysis to one grid-patch, Poisson's equation remains difficult to solve because of the space charge's nonlinear dependence with a potential that varies in three dimensions. We can limit the analysis to two dimensions by analyzing the perturbation of a single array of wires. The 2-D geometry would allow us to exploit the conformal mapping technique described in subsection **5.1x.2** if we model the wires to have no thickness. The map would then simplify the boundary condition for a numerical solution. We have not attempted such a technique, however, because in the limit of practical interest, there exists an analytic solution as shown in the next subsection.

[5.2.1] The separation of the *vacuum* and the plasma sheath solutions

If the wire spacing is much less than the Debye-length, then the potential about the mesh will be governed by its physical structure. In other words, it will be dominated by the contribution from the charge on the wires as opposed to that from the plasma space

charge. In such a limit, the term $\nabla_{\perp}'^{\,2}\chi$ dominates $(d/\lambda_{De})^2\delta n$, and the potential profile in the vicinity of the mesh ($|z| << \lambda_{De}$) is well characterized by the vacuum solution. The contribution from the plasma space charge eventually overcomes that from $\nabla_{\perp}'^{\,2}\chi$ as the perturbation subsides with distance from the grid-plane, $\tilde{\Phi} \propto \exp(-2\pi|z|/d)$, to yield the plasma sheath solution.

If we *neglect* the space charge in the region that is subject to the field of the individual wires, $|z| < d/\pi$, then the solution to the potential reduces to the matching of the *far* fields E_+ and E_- produced by the surface charge on the mesh with the fields in the sheaths about the mesh as illustrated in figure **5.2-1**. Using equation **5.1-4a**, the matching gives the following estimate for the *size of the electric hole* $\Delta_0 = -e(V_G - \Phi_0) = \Theta_G - \Theta_0$:

$$\Delta_0 = -\frac{1}{2\pi}\ln\left(\frac{d}{2\pi r_w}\right)\frac{d}{\lambda_{De}}\overline{\mathrm{E}}(\chi_0)T_{//} \sim \frac{1}{2\pi}\ln\left(\frac{d}{2\pi r_w}\right)\frac{d}{\lambda_{De}}T_{//}, \qquad \{5.2-1\}$$

where $\overline{\mathrm{E}} \equiv e\overline{E}\lambda_{De}/T_{par}$ and $\chi = \Theta/T_{//}$. The average *normalized* field $\overline{\mathrm{E}} = (\mathrm{E}_+ - \mathrm{E}_-)/2$ is described accurately by the results of section **4.2** even in the *vacuum* regime because these fields are insensitive to the value of the potential hump that forms downstream from the grid-plane. Using equations **4.2-5d** and **4.2-5i**, we find that for χ_G large,

$\overline{\mathrm{E}} \cong 0.5\left(\mathrm{E}_+ - \sqrt{\mathrm{E}_+^2 - 2}\right)$ with

$$\mathrm{E}_+ \cong -\sqrt{2 + 2\exp(-\chi_s)\left[\frac{2\chi_{Gs}}{1+\sqrt{1+2\chi_{Gs}}} - 1\right]}, \qquad \{5.2-2\}$$

where $\chi_{Gs} = \chi_G - \chi_s$ and $\chi_s \cong 0.85$.

The validity of equation **5.2-1** hinges on a weak contribution from the space charge $\delta\tilde{n}$ in the region $|z| < d/\pi$ relative to the contribution from the space charge in the sheaths, $|z| > d/\pi$, where the fields emanating from the wires act collectively. The primary impact of $\delta\tilde{n}$ is to augment the surface charge on the wires, which enhances the (normalized) field at the wires by an amount that is of the order $|\delta\tilde{n}|\, d/\lambda_{De}$. The resulting correction to the potential drop is second order in d/λ_{De}. This claim can be demonstrated via a comparison of the profile about a wire in vacuum with that about a wire surrounded by plasma of constant density $\delta\tilde{n}$, with both profiles subject to the boundary condition $E(r \approx d) = \overline{E}$.

Having established the size of the electric *hole* in the grid barrier, we next examine its impact on the electron current.

[5.3] The impact of the field perturbation on the electrons

In this section, we relate the ambient electron distribution function to the current of electrons that have encountered the electric perturbation about the mesh; the ones that eventually contribute to the collector current. These electrons feel a barrier that is *path* and thereby energy *dependent* with a magnitude that is different from what is applied at the wires of the mesh. Therefore, they have a finite probability of reaching the grid plane with an initial parallel energy $U_{//}^{\infty}$ that is (generally) less than what is required to overcome the *ideal* hybrid barrier. Recall that the *ideal* barrier is a *step* function at

$$U_{//}^{G} = U_{//}^{\infty} - P_G \qquad \{5.3-1a\}$$

with $P_G = \alpha_0 U_\perp^\infty + \Theta_G$ given by equation **3.0-3** evaluated at the grid, where the relative change in the magnetic field is $\alpha_0 = B_{em}/B_\infty$. In addition to modifying the grid barrier, the field perturbation redistributes the electron energies along lines of constant total energy as the electrons pass through the mesh. That is, the perturbation induces an exchange between the parallel and the perpendicular energies. Therefore, the perpendicular energy at the grid is altered from what is assumed by the conservation of $\mu = U_\perp/B$ alone, which is

$$U_\perp^G = (1+\alpha_0)U_\perp^\infty. \qquad \{5.3-1b\}$$

The path dependent scattering of the energies along with the *hole* and the distortion in the grid barrier modify the relationship between the collector current I_C and the distribution function F_∞, as assumed by the ideal behavior described in section **3.3**. We want to understand these modifications so that we can gauge the errors that they impart to the results of section **3.3** as well as to the measurements of the parallel and perpendicular temperatures. To this end, we first estimate the magnitude of the energy scattering and establish a criterion for overcoming the variable grid barrier, which require that we isolate the impact of the perturbation on the electron's kinetic energy.

[5.3.1] The energies in the vicinity of the mesh

The magnetic field in the region where the potential and path perturbations occur is virtually constant, equal to α_0. The homogeneity of α in this region allows us to disassociate the effect of μ conservation from the effect of these perturbations. As a result, the kinetic energy $U = U_{//} + U_\perp$ about the mesh can be represented as the sum

$\overline{U}+\widetilde{U}$, where the *bar* and the *tilda* denote the average value and the perturbation, respectively. The quantity $\overline{U}=K-\overline{\Theta}$, where $K=U_{//}^{\infty}+U_{\perp}^{\infty}$ is the total energy ($\Theta_{\infty}\equiv 0$), would describe the electron's kinetic energy if the electric potential were uniform (in the $x-y$ plane) and equal to its average value over the patch cross-section, $\overline{\Phi}$. *At* $z=0$, where $\overline{\Phi}=\Phi_0$, the average energies become $\overline{U}_{//}\rightarrow\overline{U}_{//}^{0}$ and $\overline{U}_{\perp}\rightarrow\overline{U}_{\perp}^{0}$ with

$$\overline{U}_{//}^{0}=U_{//}^{\infty}-\left(\alpha_0 U_{\perp}^{\infty}+\Theta_0\right)=U_{//}^{G}+\Delta_0, \qquad \{5.3-1c\}$$

$\overline{U}_{\perp}^{0}=U_{\perp}^{G}$, and $\Theta_G=\Theta_0+\Delta_0$. The remainder $\widetilde{U}$ describes the interaction with the field perturbation. That is,

$$\widetilde{U}_{//}=-\widetilde{\delta}\equiv -e\int_{-\infty}^{z}dz'\widetilde{E}_z\left(x',y',z'\right) \qquad \{5.3-2\}$$

and using the conservation of total energy ($\widetilde{K}=0$), $\widetilde{U}_{\perp}=-\left(\widetilde{\Theta}+\widetilde{U}_{//}\right)$, where $\widetilde{\Theta}=-e\widetilde{\Phi}$. The symbol of ∞ in the integration limit describes a distance from the mesh-plane, where the perturbation has diminished, *but* where α is still approximately α_0. The criterion for overcoming the barrier at the grid-plane is then described as $\overline{U}_{//}^{0}+\widetilde{U}_{//}^{0}=\overline{U}_{//}^{0}-\widetilde{\delta}_0\geq 0$, where $\widetilde{\delta}_0$ is $\widetilde{\delta}$ evaluated at $z=0$. In addition, using $\widetilde{K}=0$ and $\widetilde{\Theta}\big|_{z\rightarrow+\infty}\rightarrow 0$, the scattering of the perpendicular energy across the mesh can be described as $\widetilde{\delta}_{+}$, where $\widetilde{\delta}_{+}$ is $\widetilde{\delta}$ evaluated at $z\rightarrow\infty$.

The field $\widetilde{E}_z$ in equation **5.3-2** is given by $-\partial\widetilde{\Phi}/\partial z=-s\partial\widetilde{\Phi}/\partial|z|$ with $s\equiv sign(z)$ and with $\widetilde{\Phi}$ defined by equation **5.1-1b**:

$$\widetilde{E}_z=s\sum_{k,l\neq 0,0}\left(2\pi|k,l|/d\right)\Phi_{k,l}^{w}\exp\left[2\pi i\left(kx+ly\right)/d\right]\exp\left(-2\pi|k,l||z|/d\right), \qquad \{5.3-2a\}$$

where $\Phi^{w}_{k,l} \equiv \Phi_{k,l}(r_w)$ is given by equation **5.1-1c** with $|z| = r_w$. Here, we have *artificially* inserted the term $\exp(-2\pi|k,l|r_w/d)$ to obtain $\Phi_{k,l}(r_w)$ as opposed to $\Phi_{k,l}(0)$ so that the sum converges at $|z| = 0$ (as it would if we had Fourier decomposed the exact expression for the perturbation from a mesh of wires). The resulting errors produced by this term are of the order r_w/d and thereby negligible.

The integral in equation **5.3-2** is along the electron path, which we take to be its unperturbed gyro-orbit. That is, we take $x' \cong x_g + \rho_\perp \cos(\omega_{ce} z'/v_{//} + \phi)$ and $y' \cong y_g + \rho_\perp \sin(z'\omega_{ce}/v_{//} + \phi)$, where $\rho_\perp = v_\perp/\omega_{ce}$, and $v_\perp$ and $v_{//}$ are equal to the perpendicular and parallel speeds associated with the average energies at the mesh-plane. The use of the unperturbed orbit is appropriate because we are interested in the regime in which the electrostatic energy of the perturbation is small in comparison to the electron temperature. Furthermore, to reduce the algebraic complexity of the calculation, we also assume that the electron does not gyrate much as it passes through the region where the perturbation is significant. That is, we take $v_{//}/\omega_{ce}$ to be of the order or greater than d, which is satisfied by most electrons in the practical limit $\lambda_{De} >> d$, given that $v_{//}/\omega_{ce} \sim \rho_e \sim \lambda_{De}$. Then, as a result of the exponential drop in the field perturbation with distance from the mesh, we can obtain a good estimate for δ if we use the expression for the gyro-orbit in the limit $z'\omega_{ce}/v_{//} << 1$, which gives

$$(x', y') \cong (x_0, y_0) + (-\sin\phi, \cos\phi) z' v_\perp / v_{//} \qquad \{5.3-3\}$$

with $x_0 = x_g + \rho_\perp \cos\phi$ and $y_0 = y_g + \rho_\perp \sin\phi$. As suggested by equation **5.3-3**, the exchange of energy in this regime becomes a function of the pitch angle, insensitive to

effects of resonance between the electron's Larmor radius and the wavelength of the perturbation, d.

With the energies in the vicinity of the mesh defined, we next show how the quantities $\widetilde{\delta}_0$ and $\widetilde{\delta}_+$ describe the key effects on the electron distribution function downstream from the grid-plane. In the analysis to follow, we *neglect* the wire thickness, which preferentially absorbs electrons with large pitch angle. We also neglect the wire width, which is associated with the mesh optical opacity $\mathrm{O}_w = 1-(1-w/d)^2 \cong 2w/d << 1$. The wire opacity along with its impact on the electron current is the subject of the next section.

[5.3.2] Liouville's theorem for electrons passing through the mesh

For the ideal case treated in section **3.3**, the grid effectively cuts off the distribution function downstream from the grid-plane, F'_∞, at the line describing the hybrid barrier in energy space. That is, $F'_\infty \equiv TF_\infty$ with $T = Step\left[U_{//}^G\right]$. However, in reality, the transmission function T is complicated by the field perturbation about the mesh. The determination of F'_∞ for the general case is a rather daunting task, and we do not attempt to derive it exactly. However, we do want an estimate of F'_∞ that is credible. In this spirit, we provide the following formalism, which enables us to show where we are making approximations.

A realistic expression for F'_∞ can be derived by realizing that even though the electron energies redistribute, the current of electrons that overcome the grid barrier remains conserved. In other words, the current of electrons possessing given parallel and

perpendicular energies after having passed through the mesh, $\propto dU_{\perp}'^{\infty} dU_{//}'^{\infty} F_{\infty}'$, is precisely the sum of the current of electrons that, once pitch angle scattered, *enter* this particular energy range. To make this statement more precise, we introduce the more suitable variable,

$$2\mathrm{Y}_{\infty} \equiv U_{\perp}^{\infty} - U_{//}^{\infty} = 2U_{\perp}^{\infty} - \mathrm{K},$$

which describes the scattering along lines of constant total energy, and note the relations $dU_{\perp}^{\infty} dU_{//}^{\infty} = d\mathrm{K} d\mathrm{Y}_{\infty}$ and $d\mathrm{K}' = d\mathrm{K}$. Then, Liouville's theorem for electrons passing through the mesh can be expressed algebraically as

$$d\mathrm{Y}_{\infty}' F_{\infty}' = \left\langle d\mathrm{Y}_{\infty} \rho_0 F_{\infty}\big|_{\mathrm{Y}_{\infty}=\mathrm{Y}_{\infty}'-\delta\mathrm{Y}_{\infty}} \right\rangle.$$

The quantity ρ_0 is a probability density in the space of the guiding center position $\vec{r}_g \equiv \left(x_g, y_g\right)$ and gyro-phase ϕ. It is equal to *one* if the electron overcomes the grid barrier and *zero* otherwise. The incremental energy change $\delta\mathrm{Y}_{\infty} = \mathrm{Y}_{\infty}' - \mathrm{Y}_{\infty}$ represents the scatter in energy due to the field perturbation. It is equal to $\tilde{\delta}_{+} / \left(1 + \alpha_0\right)$, where the factor $1 + \alpha_0$ accounts for the measurement of the energy scattering (which occurs at the electromagnet throat) in the space of U_{perp}^{∞}. Lastly, the *bracket* represents

$$\langle Q \rangle \equiv \int_0^d \frac{dx_g}{d} \int_0^d \frac{dy_g}{d} \oint \frac{d\phi}{2\pi} Q,$$

which is the average over the various paths, where the path is defined by $\vec{r}_g$ and ϕ.

[5.3.3] The distribution function downstream from the grid-plane

To get an estimate for F'_∞, we neglect the dependence of $\widetilde{\delta}_+$ on the kinetic energy so that we can set $d\mathrm{Y}'_\infty = d\mathrm{Y}_\infty$. Then, by Taylor expanding F_∞, we can express the modified distribution function as $F'_\infty \cong \left\langle \rho_0 \left(1 - D + D^2/2\right)\right\rangle F_\infty$ with $D = \left[\widetilde{\delta}_+ / \left(1+\alpha_0\right)\right]\partial/\partial \mathrm{Y}_\infty$. Furthermore, if we approximate ρ_0 as a *step* function at the *average* barrier, $Step\left[\overline{U}^0_{//}\right]$, *when* it is coupled with the operator D and realize that $\left\langle \widetilde{\delta}_+ \right\rangle = 0$ (a claim that will become clear in the next subsection), then we obtain the two *main* distinct modifications to the distribution function:

$$F'_\infty \cong \left(T_0 + Step\left[\overline{U}^0_{//}\right]T_+\right)F_\infty, \qquad \{5.3-4\}$$

where

$$T_0 = \left\langle \rho_0 \right\rangle \equiv Step\left[\overline{U}^0_{//}\right] + \delta T_0 \qquad \{5.3-4a\}$$

describes the *average* barrier at the grid-plane and its path dependent *distortion* and

$$T_+ = \frac{1}{2}\frac{\left\langle \widetilde{\delta}^2_+ \right\rangle}{\left(1+\alpha_0\right)^2}\frac{\partial^2}{\partial \mathrm{Y}^2_\infty} \qquad \{5.3-4b\}$$

describes the *diffusion* of the energies induced by the field perturbation about the mesh.

The integral for the transmission function $T_0 = \left\langle \rho_0 \right\rangle$ amounts to the fraction of the paths that allows an electron with given energies to overcome the barrier at the grid-plane: $\overline{U}^0_{//} \geq \widetilde{\delta}_0$. This fraction varies from *zero* to *one* in the range $-e\left(\Phi_m - \Phi_0\right) < \overline{U}^0_{//} < -e\left(V_G - \Phi_0\right) = \Delta_0$, where we have assumed the practical case, $\overline{\mathrm{E}} < 0$, so that $\Phi_m > V_G$ as shown in figure **5.2-1**. The bounds on $\overline{U}^0_{//}$ describe the range in the energy of the perturbation at the grid-plane, and they are defined by equations **5.1-**

4[a,b]. Outside these bounds, the electron either has enough energy to reach the grid-plane regardless of its path, or it does not.

The electrons that are most sensitive to the distortion in the barrier are generally characterized by $\overline{U}_{//}^{0} << \overline{U}_{\perp}^{0}$. These electrons sample the electric field at various locations across the patch during their journey to the grid, making the work done on them insensitive to their path. Consequently, T_0 becomes a function that varies from *zero* to *one* about the location $\overline{U}_{//}^{0} = 0$, within a range $\delta\Theta_0$ that is characterized by the *square root* of $\left\langle \widetilde{\delta}_0^{\,2} \right\rangle$. Therefore, to gauge the impact of the barrier distortion, we *model* T_0 as a function that *ramps linearly* from *zero* to *one* within the range $-\delta\Theta_0 \le \overline{U}_{//}^{0} \le \delta\Theta_0$.

[5.3.4] The distortion in the grid barrier and the diffusion of the energies

We calculate the quantities $\left\langle \widetilde{\delta}_0^{\,2} \right\rangle$ and $\left\langle \widetilde{\delta}_+^{\,2} \right\rangle$ by inserting the approximation for the electron orbit, equation **5.3-3**, into the expression for the field, equation **5.3-2a**. We then integrate the result as prescribed by equation **5.3-2** to represent $\widetilde{\delta}$ as

$$\widetilde{\delta} = \sum_{k,l\neq 0,0} \exp\left(2\pi i \vec{k}\cdot\vec{r}_0/d\right)\widetilde{\delta}_{k,l}\,,$$

where $\vec{k}\cdot\vec{r}_0$ is the dot product of $\vec{r}_0 \equiv (x_0, y_0)$ with the vector $\vec{k} \equiv (k,l)$. The sum representation readily shows that $\left\langle \widetilde{\delta} \right\rangle = 0$ because $\widetilde{\delta}_{0,0}$ (which is the only term that would survive the operation) is not included in the sum. It also enables us to use the relation $\widetilde{\delta}_{-k,-l} = \widetilde{\delta}_{k,l}^{*}$ to express the variance $\left\langle \widetilde{\delta}^{\,2} \right\rangle$ as

$$\left\langle \widetilde{\delta}^{\,2} \right\rangle = \sum_{k,l\neq 0,0} \oint \frac{d\phi}{2\pi} \left|\widetilde{\delta}_{k,l}\right|^2 .$$

The variance in the loss of parallel energy to the grid-plane, $\left\langle \widetilde{\delta}_0^{\,2} \right\rangle$, and the variance in the exchange of energy, $\left\langle \widetilde{\delta}_+^{\,2} \right\rangle$, for electrons with a given pitch angle at the grid-plane are derived in subsection **5.3x.1**. They are

$$\left\langle \widetilde{\delta}_0^{\,2} \right\rangle = \delta_0^2 \frac{1}{\sqrt{1+\overline{U}_\perp^0/\overline{U}_{//}^0}} \qquad \{5.3-5a\}$$

and

$$\left\langle \widetilde{\delta}_+^{\,2} \right\rangle = 2\delta_0^2 \frac{\overline{U}_\perp^0/\overline{U}_{//}^0}{\left(1+\overline{U}_\perp^0/\overline{U}_{//}^0\right)^{3/2}} \qquad \{5.3-5b\}$$

with δ_0^2 equal to the *variance in the electrostatic energy at the grid plane*:

$$\delta_0^2 \cong \frac{1}{(2\pi)^2}\left[\frac{\pi^2}{6} - \frac{1}{\ln\left(d/2\pi r_w\right)}\right]\left(\frac{d}{\lambda_{De}}\right)^2 \overline{\mathrm{E}}^2 T_{//}^2 \sim \left(\frac{d}{2\pi\lambda_{De}}\right)^2 T_{//}^2 . \qquad \{5.3-5c\}$$

Using equation **5.3-5a**, we can then estimate the width $\delta\Theta_0$ for the transition in T_0 as $\sqrt{\left\langle \widetilde{\delta}_0^{\,2} \right\rangle}$ evaluated at $\overline{U}_{//}^0 = \delta_0$, which is the characteristic parallel energy at the grid for the electrons that are sensitive to the distortion in the grid barrier:

$$\delta\Theta_0 \cong \left(1+\overline{U}_\perp^0/\delta_0\right)^{-1/4}\delta_0 . \qquad \{5.3-5d\}$$

The parallel energy $\overline{U}_{//}^0 = \delta_0$ also characterizes the electrons that diffuse about the barrier cross-point (which contaminates the measurement of F_∞). Using equation **5.3-5b**, we estimate the variance $\left\langle \widetilde{\delta}_+^{\,2} \right\rangle$ for these electrons to be

$$\left\langle \widetilde{\delta}_+^{\,2} \right\rangle \cong 2\delta_0\left(1+\overline{U}_\perp^0/\delta_0\right)^{-3/2}\overline{U}_\perp^0 . \qquad \{5.3-5e\}$$

Notice that $\overline{U}_{//}^0 = \delta_0$ satisfies the initial assumption of the calculation:

$$\frac{v_{//}}{\omega_{ce} d} \sim \sqrt{\frac{d}{2\pi\lambda_{De}}} \frac{v_{te}}{\omega_{ce} d} = \sqrt{\frac{d}{2\pi\lambda_{De}}} \frac{\rho_e}{d} \sim \sqrt{\frac{d}{2\pi\lambda_{De}}} \frac{\lambda_{De}}{d} > 1 .$$

[5.3.5] The corrections to the measured temperatures

With our estimate of F'_∞, we can express the electron current *through the mesh* as

$$I_+ = \int dU_\perp^\infty dU_{//}^\infty T_0 F_\infty . \qquad \{5.3-6\}$$

Here, we have dropped the term T_+ because the diffusion in the energies beyond the grid location does not affect I_+. This term affects the current of electrons that are able to overcome the barrier at the collector. However, for the measurement of the temperatures, we operate the probe in the *M* regime (section **3.1**), where the collector is biased to absorb the electrons ($\Theta_C = 0$).

To determine the modifications to the measured parallel and perpendicular temperatures, we first transform the integration space of equation **5.3-6** to the coordinates $\left(\overline{U}_{//}^0, \overline{U}_\perp^0\right)$ using the Jacobian relation $(1+\alpha_0) dU_{//}^\infty dU_\perp^\infty = d\overline{U}_{//}^0 d\overline{U}_\perp^0$. We then set F_∞ equal to a bi-Maxwellian distribution function, equation **3.0-4**, which in the new energies is expressed as

$$F_M = I_{s//} \frac{1}{\beta T_{//}^2} \exp\left[-\frac{1}{T_{//}} \left(\overline{U}_{//}^0 + \Theta_0 + \overline{U}_\perp^0 / \beta_\alpha \right) \right] \qquad \{5.3-7\}$$

with

$$\beta_\alpha \equiv \frac{\beta + \alpha_0 \beta}{1 + \alpha_0 \beta} \qquad \{5.3-7a\}.$$

Next, we use the definition of equation **5.3-4a** for T_0, which enables us to represent the current as $I_+ = I_0 + \delta I_0$, where I_0 is given by equation **5.3-6** with $T \to Step\left[\overline{U}_{//}^0\right]$, and

δI_0 is given by equation **5.3-6** with $T \to \delta T_0 = T_0 - Step\left[\overline{U}_{//}^{0}\right]$, which is function that is localized about $\overline{U}_{//}^{0} = 0$ within the range $\pm \delta\Theta_0$. For $F_\infty = F_M$, the expression for I_0 becomes that of equation **3.1-2** with χ_C replaced by $\chi_0 = \Theta_0 / T_{//}$:

$$I_0 = I_{s//} \frac{\exp(-\chi_0)}{1+\alpha_0\beta} = I_{s//} \frac{\exp(-\chi_G)}{1+\alpha_0\beta} \exp(\Delta_0 / T_{//}). \qquad \{5.3-8\}$$

To evaluate δI_0, we take $\delta_0 / T_{//} << 1$ and Taylor expand F_M about $\overline{U}_{//}^{0} = 0$, which can be shown to give

$$\delta I_0 \sim \beta_\alpha^{-1/2} (\delta_0 / T_{//})^{5/2} I_0. \qquad \{5.3-8a\}$$

Equation **5.3-8** then yields the lowest order correction to the parallel temperature, due to the electric *hole*:

$$\frac{T'_{//}}{T_{//}} \cong \frac{d\Theta_G}{d\Theta_0} = 1 + \frac{d\Delta_0}{d\Theta_0} \cong 1 - \frac{1}{2\pi} \ln\left(\frac{d}{2\pi r_w}\right) \frac{d}{\lambda_{De}} \frac{d\overline{\mathrm{E}}}{d\chi_0}\bigg|_{\chi_0 \cong \chi_G}, \qquad \{5.3-9a\}$$

where $T'_{//} = -d\Theta_G / d\ln I_0$ is the *ideal* expression for the parallel temperature assuming that $\Delta_0 = 0$, $T_{//}$ is the *actual* parallel temperature, and $\overline{\mathrm{E}}$ is described in section **5.2**. The measurement of the temperature anisotropy, which is obtained from the change in the current with the local magnetic field, is *only* affected by the distortion in the barrier. The distortion imparts a *negligible* correction to β as determined by the operation of equation **3.1-4**:

$$\delta\beta / \beta \cong \alpha_0^{-1} \Delta(\delta I_0) / I_0 \sim (\delta_0 / T_{//})^{5/2}, \qquad \{5.3-9b\}$$

where $\beta \cong \alpha_0^{-1} \Delta I_0 / I_0$ and $\Delta I \equiv I_{\alpha=0} - I$.

[5.3.6] The corrections to the measured distribution function

The measurement of the distribution function requires that we dissect the collector current in energy space with the electrode voltages. As mentioned in the previous subsection, this process is affected by the diffusion of the electron energies as well as the distortion in the grid barrier. We can describe these effects concisely with the aid of figure **5.3-1**, which illustrates the regions about the barrier that are affected by the electric hole, by the distortion, and by the diffusion of the energies.

Firstly, the electric *hole* modifies equation **3.3-3** for F_∞^* to

$$F_\infty^* = \frac{T_{//}'}{T_{//}} \alpha_0 \frac{\partial^2 I_C}{\partial \Theta_G \partial \Theta_C} . \qquad \{5.3-10a\}$$

The factor $T_{//}'/T_{//}$ arises because the increment $d\Theta_G$ produces the increment $d\Theta_0$ in the movement of the *effective* barrier at the grid-plane. The electric hole also modifies the perpendicular energy at the barrier cross-point, where we measure the distribution function:

$$U_\perp^* = (\Theta_C - \Theta_0)/\alpha_0 = (\Theta_C - \Theta_G)/\alpha_0 + \Delta_0/\alpha_0 . \qquad \{5.3-10b\}$$

The effect of the distortion on the other hand is to limit the accuracy with which we can resolve the perpendicular energies. Evaluating equation **5.3-5d** at $\overline{U}_\perp^0 = (1+\alpha_0)U_\perp^* \sim T_\perp$ gives

$$\delta U_\perp^*/U_\perp^* \sim \delta\Theta_0/(\Theta_C - \Theta_0) \sim \alpha_0^{-1}(\delta_0/T_\perp)^{5/4} . \qquad \{5.3-10c\}$$

Lastly, the diffusion of the energies can be viewed as an effect that produces an inherent uncertainty in the measured distribution function: $\delta F_\infty \sim T_+ F_\infty$. Inserting

equation **5.3-5e** for $\left\langle \widetilde{\delta}_+^2 \right\rangle$ into the expression for T_+, equation **5.3-4b**, and estimating $\partial F_\infty / \partial \mathrm{Y}_\infty$ with $\partial F_M / \partial \mathrm{Y}_\infty = \left[(\beta - 1)/T_\perp \right] F_M$ gives

$$\delta F_\infty^* / F_\infty^* \sim T_+ \sim (\beta - 1)^2 (\delta_0 / T_\perp)^{5/2} . \qquad \{5.3-10d\}$$

These results then suggest that the corrections to the ideal behavior of the *GEM* probe can be made negligible if we choose a mesh with $d \sim 0.1 \lambda_{De}$. For typical lab-plasmas, this relation can be satisfied by a mesh with $d \sim 10 \mu m$. However, as we demonstrate in the next section, the complications from the mesh opacity require that $d > 10t$; and as a result of technological limitations and of concerns for the structural integrity of the mesh, the wire thickness t is practically limited to $t \sim 1 \mu m$.

[5.4] The grid's opacity for electrons

In this section, we demonstrate the need to maintain $d >> t$ for a practical measurement of the distribution function via the operation of equation **3.3-3**. This restriction stems from a variable mesh opacity for the electrons, as illustrated in figure **5.4-1**. The figure shows that while the range for the paths that strike the *face* of the wires is a constant (equal to the mesh optical opacity $\mathrm{O}_w \cong 2w/d$), the range for striking the *side* of the wires is greater for paths with $v_\perp >> v_{//}$. Therefore, the mesh opacity modifies the distribution function downstream from the grid-plane by preferentially absorbing electrons with large pitch angles.

To analyze this effect, we take the limit $d/\lambda_{De} \to 0$ so that we may focus on the grid's physical structure. Otherwise, we would have to address the complications from the average barrier to the wires of the mesh, which, unlike the average barrier to the

mesh-plane, varies with the electron energies. Here, it suffices to say that in order to make measurements with the grid current, it is essential to have $d/\lambda_{De} << 1$. In the prescribed limit then, the electric barrier to the wires of the mesh and to the mesh-plane are the same, equal to Θ_G.

[5.4.1] The opacity associated with the *depth* of the wires

We represent the *side* opacity as $O_t \equiv (1 - O_w)\hat{O}_t \cong \hat{O}_t$, where the first component (the optical transmission) is just the probability that the paths do *not* strike the *face* of the wires, which is approximated as *one*, $(1 - w/d)^2 \cong 1$. To calculate $\hat{O}_t$, we approximate the electron trajectory by its unperturbed straight-line orbit as shown in figure **5.4-2**. The approximation is excellent for $v_{//} > \omega_{ce} t$, which is satisfied by virtually all electrons (notice that t is the wire thickness, *not* time). The quantity $v_\perp t/v_{//}$ is the distance that the electron travels in the plane of the mesh during the time that it takes to move through the mesh the distance t. Therefore, if the electron enters the patch ($z = -t/2$) in the region outlined in *bold*, then it will strike the side of the mesh before passing through. The side opacity is then just the fraction of the area outlined in *bold* integrated over the range of angles $0 \le \arctan(v_y/v_x) \le \pi/2$, with which the electron enters the patch. For $r \equiv v_\perp t/v_{//} d \le 1$, which is also satisfied by virtually all electrons, the opacity is

$$\hat{O}_t = \frac{4}{\pi} r\left(1 - \frac{r}{4}\right) \cong \frac{4t}{\pi d}\sqrt{\frac{U_\perp^G}{U_{//}^G}} = \frac{4t}{\pi d}\sqrt{\frac{(1+\alpha_0)U_\perp^\infty}{\Theta_C - \Theta_G - \alpha_0 U_\perp^\infty}}, \qquad \{5.4-1\}$$

where the energies at the grid-plane are defined by equations **5.3-1[a,b]**.

Unlike the effects of the field perturbation, the variable opacity impacts the current of *all* electrons that reach the grid-plane, not just the current of the distribution in the vicinity of $U_{//}^{G} = 0$. This global impact will not only amplify the grid current beyond that calculated with the optical opacity alone, but it will also hamper our ability to localize the electron current in energy space for the measurement of the distribution function.

[5.4.2] The amplification of the grid current and its ramifications

The grid current for a *single* pass (collector biased to absorb the electrons) can be found by using $T \cong \left(\mathrm{O}_w + \mathrm{O}_t\right) Step\left[U_{//}^{G}\right]$ in the place of T_0 in equation **5.3-6**. Using the approximation for $\hat{\mathrm{O}}_t$, equation **5.4-1**, we find that for $F_\infty = F_M$,

$$I_G \cong I_{s//} \frac{2w}{d} \frac{1}{1+\alpha_0\beta} \exp\left(-\chi_G\right) \left[1 + \frac{t}{w}\sqrt{\frac{\beta+\alpha_0\beta}{1+\alpha_0\beta}}\right], \qquad \{5.4-2\}$$

For a typical mesh of wires with $t \cong w$, the grid current is then amplified by the factor $1+\sqrt{\beta_\alpha}$ from what is predicted by the optical opacity alone.

The corrections imparted by the side opacity to the measurement of the temperature anisotropy with the collector current scale as t/d and thereby are negligible. On the other hand, the corrections for the measurements with the grid current scale as t/w and cannot be ignored, in general. The *side* opacity modifies the change in the grid current with the magnetic field to

$$\frac{1}{\alpha_0}\frac{\Delta I_G}{I_G} \cong \beta\left(1 + \frac{t}{w}\frac{1}{1+\sqrt{\beta}\,t/w}\frac{\beta-1}{2\sqrt{\beta}}\right), \qquad \{5.4-2a\}$$

where we have approximated the second term by taking α_0 to be small. This expression indicates that the measurement of the temperature anisotropy would be complicated for the typical case, where $t \cong w$. The effect of the wire thickness can, however, be used to our *advantage*. If we compare the currents to the grid and to the collector with $\alpha_0 = 0$, we find that

$$I_G / I_C \cong \mathrm{O}_w \left(1 + \sqrt{\beta}\, t/w\right). \qquad \{5.4-3\}$$

Therefore, it is possible, in principle, to extract the temperature anisotropy from the ratio of these two currents *if* $d << \lambda_{De}$.

[5.4.3] The impact on the measurement of the distribution function

The impact of the side opacity on the collector current becomes substantial when we consider the change in this current with an increment in the grid voltage. The variation in the grid voltage modifies the electrons' parallel energies at the grid-plane and thereby the mesh opacity. The variation in the opacity, in turn, complicates the inversion process for F_∞.

To analyze the effect on the measured distribution function, we replace T_0 in equation **5.3-6** with the transmission function to the collector, $T \cong (1 - \mathrm{O}_t)\, Step\left[U_{//}^G\right] Step\left[U_{//}^\infty - \Theta_C\right]$, where we have neglected the optical opacity of the mesh. We then isolate the contribution to $\partial I_C / \partial \Theta_C$ to find

$$\frac{\partial I_C}{\partial \Theta_C} = -\int_0^{U_\perp^*} dU_\perp^\infty (1 - \mathrm{O}_t) F_\infty \left(\Theta_C, U_\perp^\infty\right), \qquad \{5.4-4a\}$$

where $U_\perp^* = (\Theta_C - \Theta_G)/\alpha_0$. The differential of equation **5.4-4a** for an incremental change in Θ_G can then be described as

$$d\left[\frac{\partial I_C}{\partial \Theta_C}\right] = \int_0^{U_\perp^*} dU_\perp^\infty (W_0 - W_t) F_\infty (\Theta_C, U_\perp^\infty), \qquad \{5.4-4b\}$$

where the *weight function* $W = W_0 - W_t$ is depicted in figure **5.4-3** for a finite increment in Θ_G. In the differential limit, the second partial derivative no longer just gives the distribution at the barrier cross-point. Instead, it gives

$$\alpha_0 \frac{\partial^2 I_C}{\partial \Theta_G \partial \Theta_C} = F_\infty^* - \frac{4t}{\pi d}\sqrt{\frac{1+\alpha_0}{\alpha_0}} \int_0^1 \frac{du}{\sqrt{1-u}} \frac{\partial}{\partial u}\left[\sqrt{u} F_\infty (\Theta_C, U_\perp^* u)\right], \qquad \{5.4-4c\}$$

where $u \equiv U_\perp^\infty / U_\perp^*$. This equation can be solved approximately for small t/d by replacing F_∞ inside the integral with the term on the left hand side.

In order to neglect the integral in equation **5.4-4c** all together, we must *localize* the weight of W. We gauge W's *global* (unwanted) contribution by examining the fraction of the area $\int_0^{U_\perp^*} dU_\perp^\infty W$ that lies in the region $U_\perp^\infty < U_\perp^* - d\Theta_G/\alpha_0$. This fraction is approximately

$$\Gamma \cong \frac{8t}{\pi d}\sqrt{\frac{1+\alpha_0}{\alpha_0}\frac{\Theta_C - \Theta_G}{d\Theta_G}};$$

valid for small Γ. Inverting this relation for the grid voltage then gives

$$\frac{dU_\perp^*}{U_\perp^*} = \frac{d\Theta_G}{\Theta_C - \Theta_G} \cong \frac{1+\alpha_0}{\alpha_0}\left(\frac{8t}{\pi d}\frac{1}{\Gamma}\right)^2. \qquad \{5.4-5\}$$

If we set the reasonable criterion, $\Gamma < 10\%$, then we must have $d/t \sim 100$ to obtain an acceptable resolution for the measurement of the perpendicular energy distribution. The

relation of equation **5.4-5** when coupled to the requirement on the wire spacing, $d \sim 10\mu m$, places a demand on technology that cannot be met at present. Hence, we must resort to the approximate solution to equation **5.4-4c**, which requires that we take yet another derivative of the collector current.

The criterion for measuring F_∞ with the grid current via the duality principle described in subsection **3.3-5** is even more severe. It is approximated by the relation of equation **5.4-5** with t/d divided by the mesh optical opacity, $2w/d$.

[5.5] Conclusion

In this chapter, we developed a formalism with which to understand the effects of the discrete structure of the mesh on the currents to the grid and to the collector. To study the impact of the field perturbation about the mesh, we first solved for the potential in vacuum about a mesh of wires with spacing d and radius r_w to find $\Phi = \overline{\Phi} + \widetilde{\Phi}$ with $\overline{\Phi}$ equal to the average potential at a location z normal to the grid-plane and $\widetilde{\Phi}$ equal to the perturbation, as described in subsection **5.1-2**. We matched the solution in vacuum to that in the sheaths about the mesh in the practical regime, $d << \lambda_{De}$, to determine the magnitude of the electric *hole* in the plane of the mesh. The size of the *hole* was found to be

$$\Delta_0 = \Theta_G - \Theta_0 = -\overline{\mathrm{E}}\frac{1}{2\pi}\ln\left(\frac{d}{2\pi r_w}\right)\frac{d}{\lambda_{De}}T_{//},$$

where Θ_0 is the average electrostatic energy at the grid-plane and $\overline{\mathrm{E}} = 0.5\left(\mathrm{E}_+ - \mathrm{E}_-\right)$ is the average *normalized* field *emanating* from the two sides of the mesh. For χ_G large, $\overline{\mathrm{E}} \cong 0.5\left(\mathrm{E}_+ - \sqrt{\mathrm{E}_+^2 - 2}\right)$ with E_+ given by equation **5.2-2**.

We then examined the impact of the field perturbation on the electron energies. We demonstrated that the path sensitivity for the exchange of kinetic energy with the perturbation distorts the grid barrier about its average value Θ_0 and scatters the energies of the electrons as they pass through the mesh. The magnitudes of the distortion in the barrier and the diffusion of the energies were found to be comparable to the standard deviation of the electrostatic energy in the plane of the mesh:

$$\delta_0 \cong \left|\overline{\mathrm{E}}\right| \frac{1}{2\pi} \frac{d}{\lambda_{De}} T_{//} .$$

The electric hole and the distortion in the barrier modify the current to the collector that is delivered by a bi-Maxwellian electron distribution function. In the range, $\Theta_C \geq \Theta_0$, this current is derived in the same manner as I_0 and δI_0 of equations **5.3-8** and **5.3-8a** with the *additional* criterion that the electrons overcome the barrier at the collector: $U_{//}^{\infty} = \Theta_C$ (see figure **5.3-1**). The result can be expressed as

$$I_C = I_{s//}\left[1 - \gamma_0 \exp\left(-\frac{\chi_C - \chi_0}{\alpha_0 \beta}\right)\right] \exp\left(-\chi_C\right) + \delta I_C ,$$

where $\chi = \Theta / T_{//}$, $\chi_0 = \chi_G - \Delta_0 / T_{//}$, $\gamma_0 = \alpha_0\beta / \left(1 + \alpha_0\beta\right)$ and $\delta I_C / I_C \propto \left(\delta_0 / T_{//}\right)^{5/2}$. For a comparison with the ideal expression, see the summary of section **3.4**.

The electric hole also modifies the parallel temperature as measured by the variation in the collector current with the grid voltage:

$$\frac{T'_{//}}{T_{//}} \cong 1 - \frac{1}{2\pi} \ln\left(\frac{d}{2\pi r_w}\right) \frac{d}{\lambda_{De}} \frac{d\overline{\mathrm{E}}}{d\chi_G},$$

where $T'_{//} = edV_G / d\ln I_C$ and $T_{//}$ is the *actual* temperature. However, it does *not* affect the measurement of the temperature anisotropy via the operation of equation **3.1-4**. This measurement is only affected by the distortion in the barrier, which imparts a higher order and thereby negligible correction that is of the order $\left(d/2\pi\lambda_{De}\right)^{5/2}$.

The imperfections of the grid barrier also affect the measurement of the distribution function. The electric hole not only modifies the relation between the collector current and the distribution function as described by equation **3.3-3**,

$$F_\infty^* \cong \frac{T'_{//}}{T_{//}} \underbrace{\alpha_0 \frac{\partial^2 I_C}{\partial\Theta_G \partial\Theta_C}}_{ideal},$$

but it also modifies the perpendicular energy at which the above equation is evaluated,

$$U_\perp^* = \underbrace{\left(\Theta_C - \Theta_G\right)/\alpha_0}_{ideal} + \Delta_0/\alpha_0 .$$

In contrast, the distortion in the barrier limits our ability to resolve the perpendicular energies,

$$\delta U_\perp^* / U_\perp^* \sim \alpha_0^{-1} \left(\delta_0 / T_\perp\right)^{5/4},$$

and the scattering of the energies produces an uncertainty in the magnitude of F_∞^*,

$$\delta F_\infty^* / F_\infty^* \sim \left(\beta - 1\right)^2 \left(\delta_0 / T_\perp\right)^{5/2}.$$

To assume the ideal behavior of section **3.3** then, we must use a mesh with $d \sim 0.1\lambda_{De}$, which for lab-plasmas translates to $d \sim 10\mu m$.

Having understood the effects of the field perturbation, we next focused on the effects of the physical structure of the mesh. We calculated the opacity of the mesh for the electrons. We found that the wire thickness t (the depth of the wires normal to the mesh plane) adds to the optical opacity $\mathrm{O}_w \cong 2w/d$ (where w is the width of the wires in the plane of the mesh), the function $\mathrm{O}_t \cong (4t/\pi d)v_\perp/v_{//}$ with the speeds equal to those at the grid. For $F_\infty = F_M$, the contribution from O_t amplifies the grid current from what is calculated by the optical opacity, which complicates the measurement of β via the method of section **3.1**. However (in the limit $d/\lambda_{De} \to 0$), it also produces another means for determining the temperature anisotropy via a comparison of the grid and the collector currents: $I_G/I_C \cong (2w/d)\left(1+\sqrt{\beta}\, t/w\right)$.

We then showed that the opacity O_t complicates the relationship between the distribution function and the second partial derivative of the collector current. The resulting modification to equation **3.3-3** for $t/d << 1$ can be approximated as

$$F_\infty^* \cong G(\Theta_C,\Theta_G) + \frac{4t}{\pi d}\sqrt{\frac{1+\alpha_0}{\alpha_0}}\int_{\Theta_G}^{\Theta_C}\frac{d\Theta}{\sqrt{\Theta-\Theta_G}}\frac{\partial}{\partial\Theta}\left[\sqrt{\Theta_C-\Theta}\,G(\Theta_C,\Theta)\right],$$

where $G(\Theta_C,\Theta_G) = F_\infty^*\big|_{t=0}$. A $t/d \sim 0.1$, when $d \sim 10\mu m$, then requires that $t \sim 1\mu m$.

[i] P. Martin and G. Donoso, Rev. Sci. Instrum. **57**, p. 1501 (1986)
[ii] P. Martin and G. Donoso, Rev. Sci. Instrum. **57**, p. 1507 (1986)

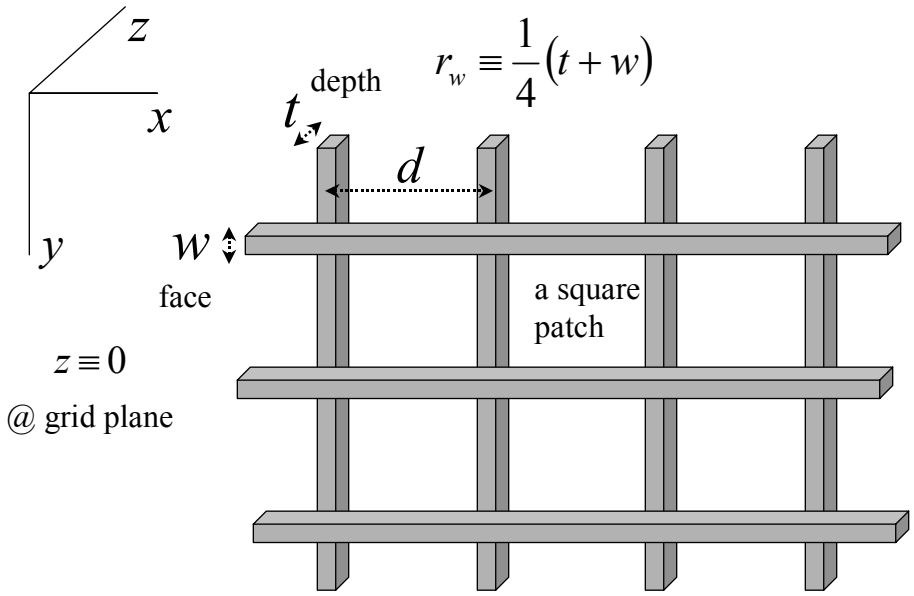

FIGURE 5.0-1: The geometry for a portion of a two-dimensional array of wires: a mesh

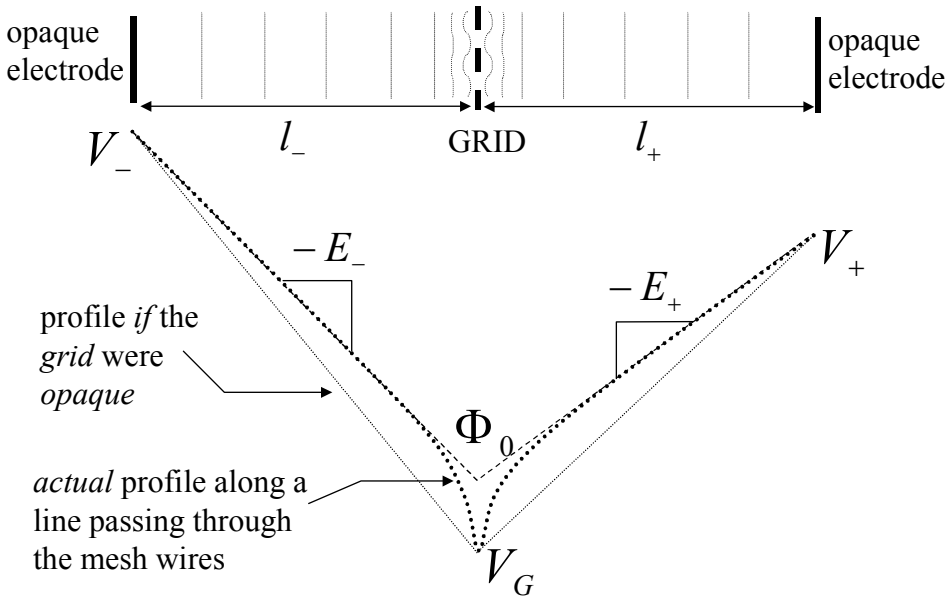

FIGURE 5.0-2: A schematic drawing of how a potential profile passing through a grid deviates from the ideal

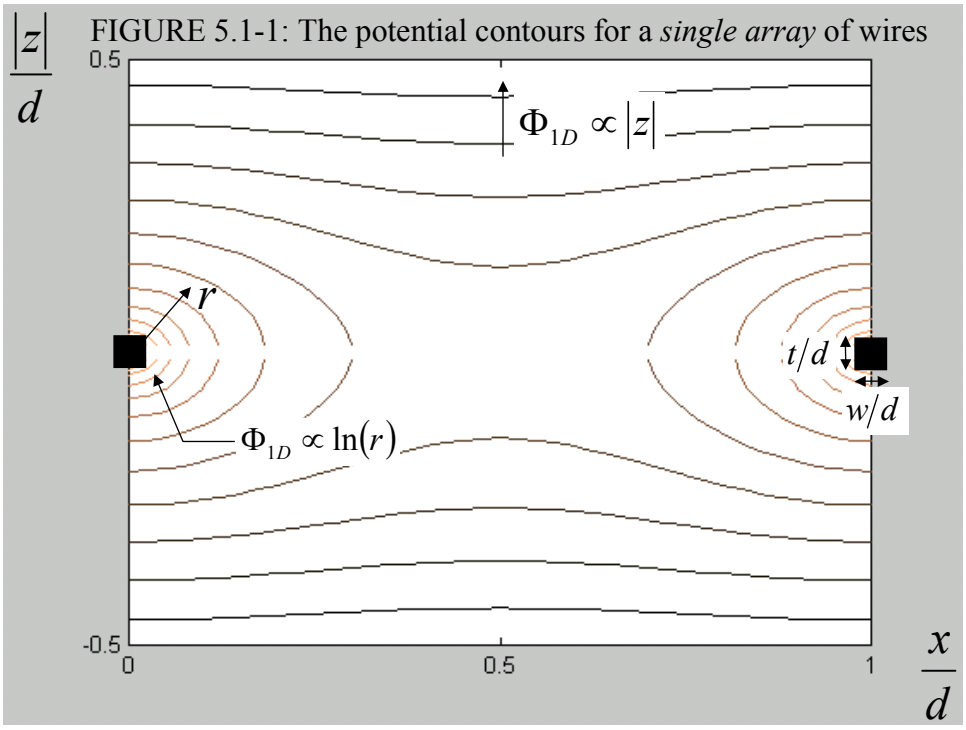

FIGURE 5.1-1: The potential contours for a *single array* of wires

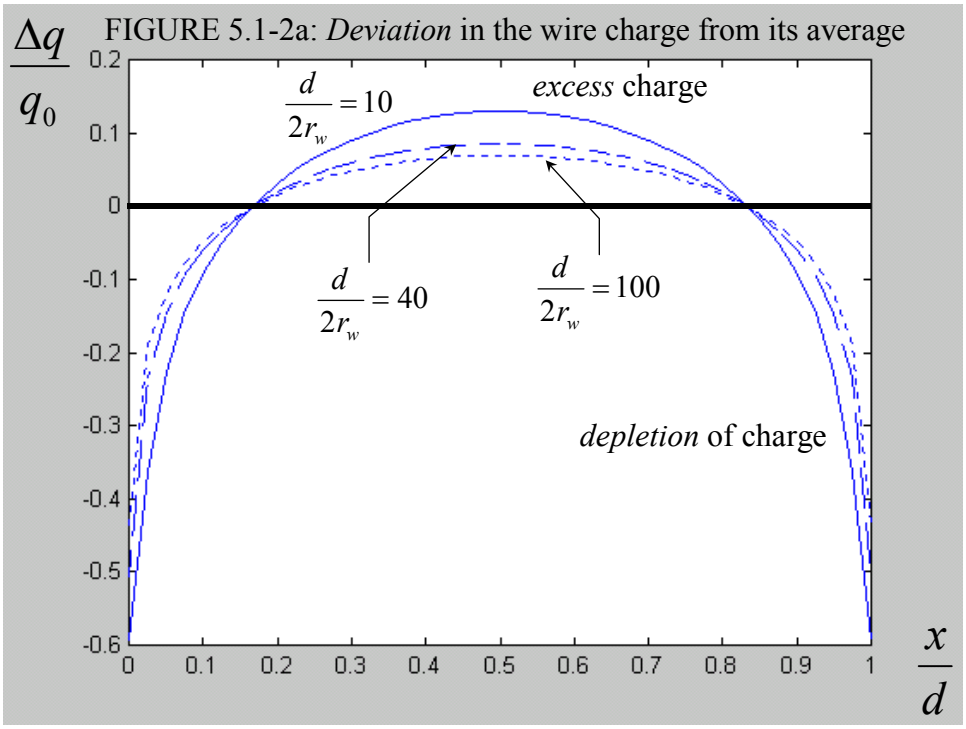

FIGURE 5.1-2a: *Deviation* in the wire charge from its average

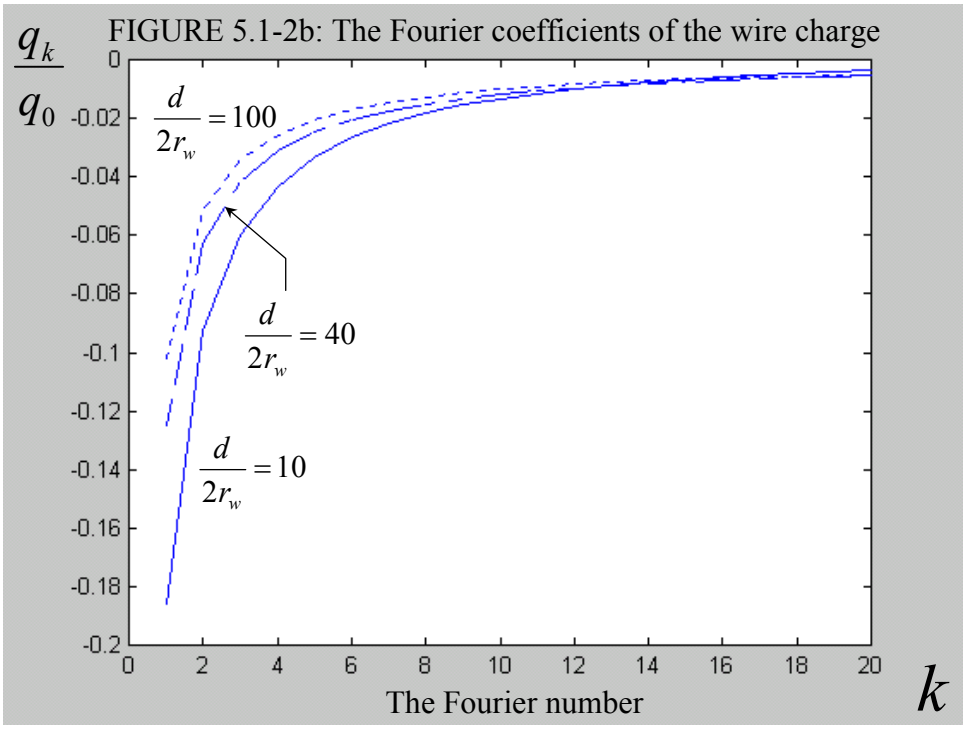
FIGURE 5.1-2b: The Fourier coefficients of the wire charge
$\frac{q_k}{q_0}$
$\frac{d}{2r_w} = 100$
$\frac{d}{2r_w} = 40$
$\frac{d}{2r_w} = 10$
0
-0.02
-0.04
-0.06
-0.08
-0.1
-0.12
-0.14
-0.16
-0.18
-0.2
0
2
4
6
8
10
12
14
16
18
20
The Fourier number
k

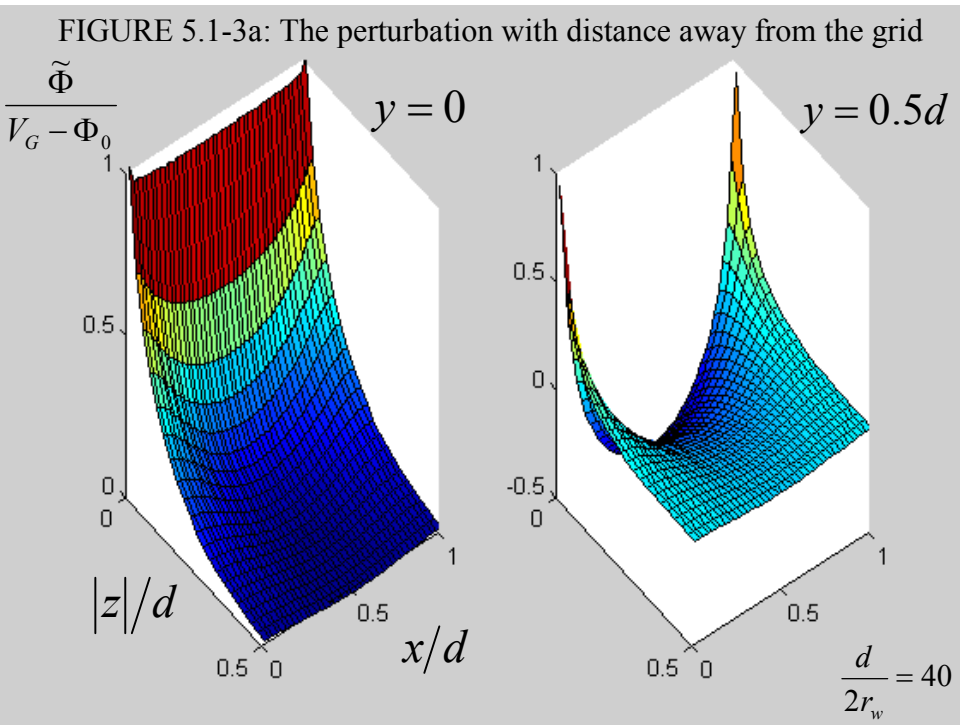
FIGURE 5.1-3a: The perturbation with distance away from the grid
$\frac{\tilde{\Phi}}{V_G - \Phi_0}$
$y = 0$
$y = 0.5d$
1
0.5
0
-0.5
$|z|/d$
x/d
$\frac{d}{2r_w} = 40$

FIGURE 5.1-3b: The perturbation at a given distance from the grid

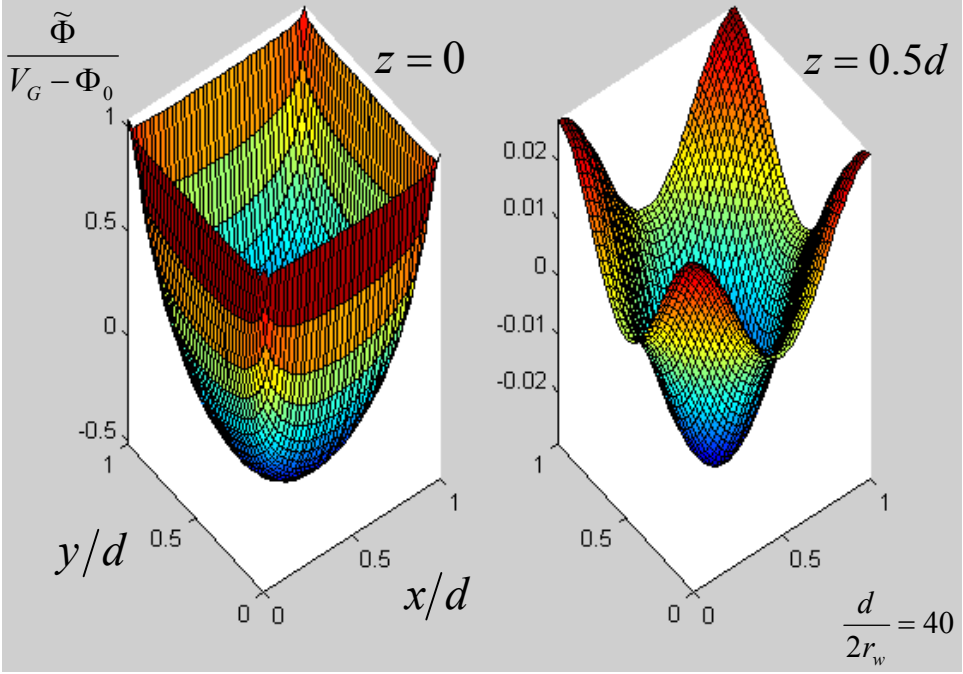

Φ

FIGURE 5.2-1: Matching the *far* field to that in the sheaths

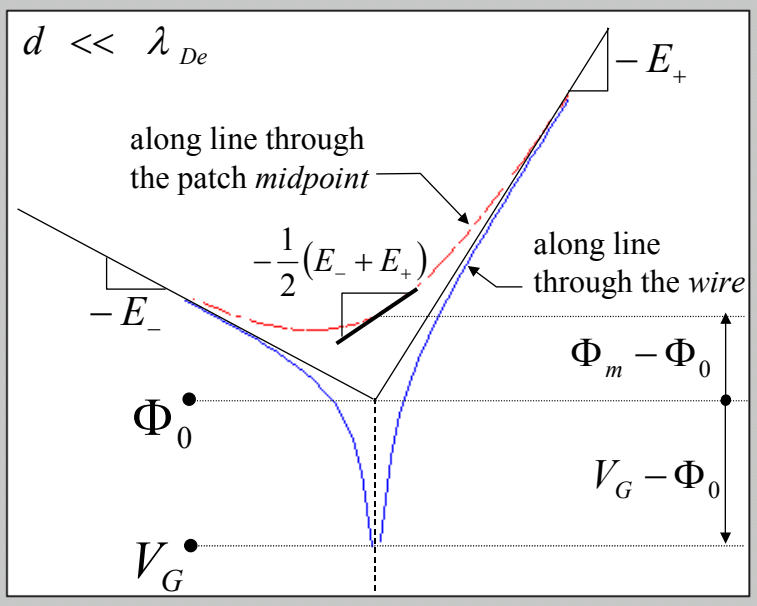

Z

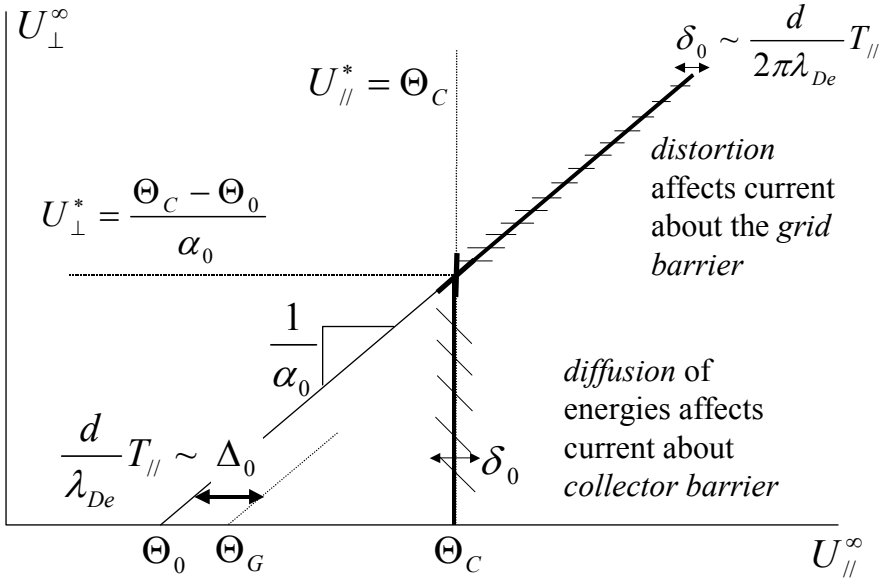

FIGURE 5.3-1: The regions about the barrier affected by the electrostatic hole, the distortion, and the diffusion

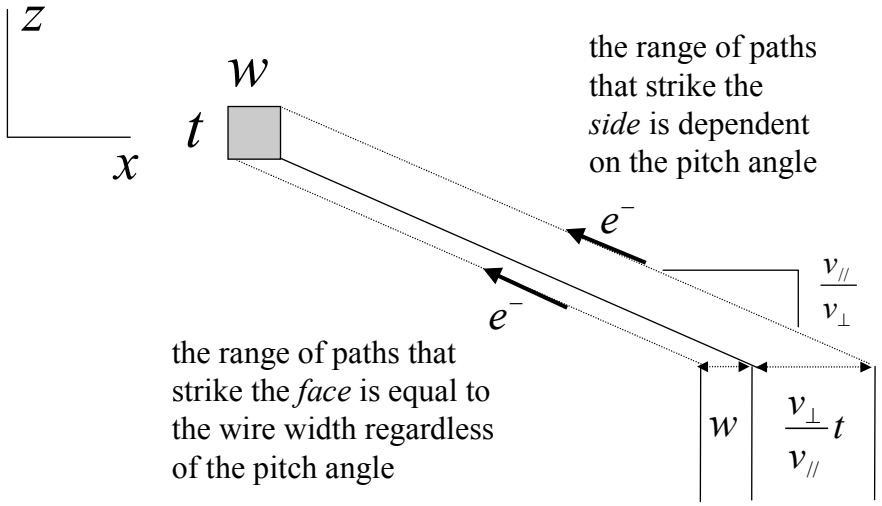

FIGURE 5.4-1: The opacity of the wires of the mesh for the electrons

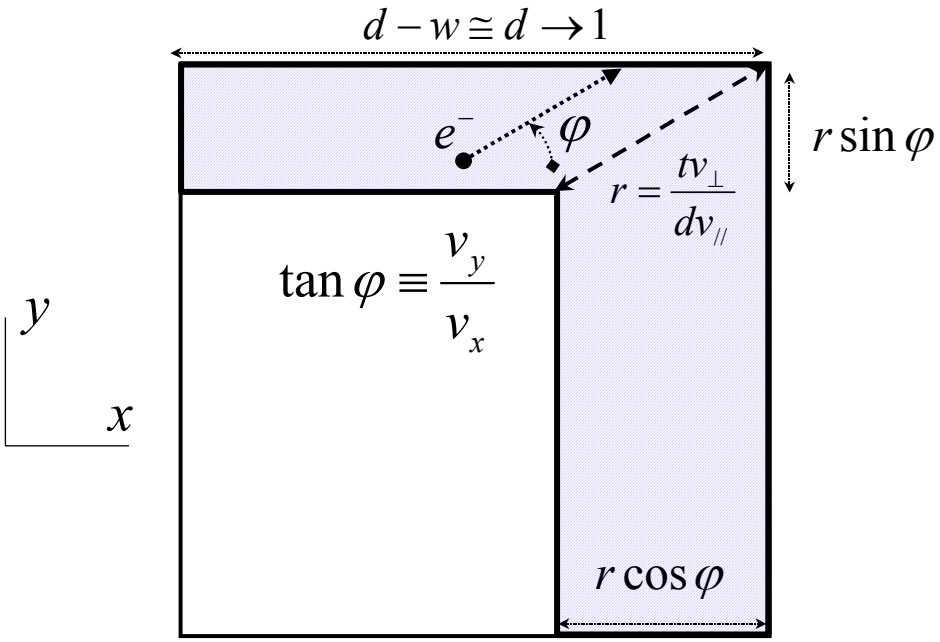

FIGURE 5.4-2: The geometry for the calculation of the *side* opacity

FIGURE 5.4-3: The *weight* function

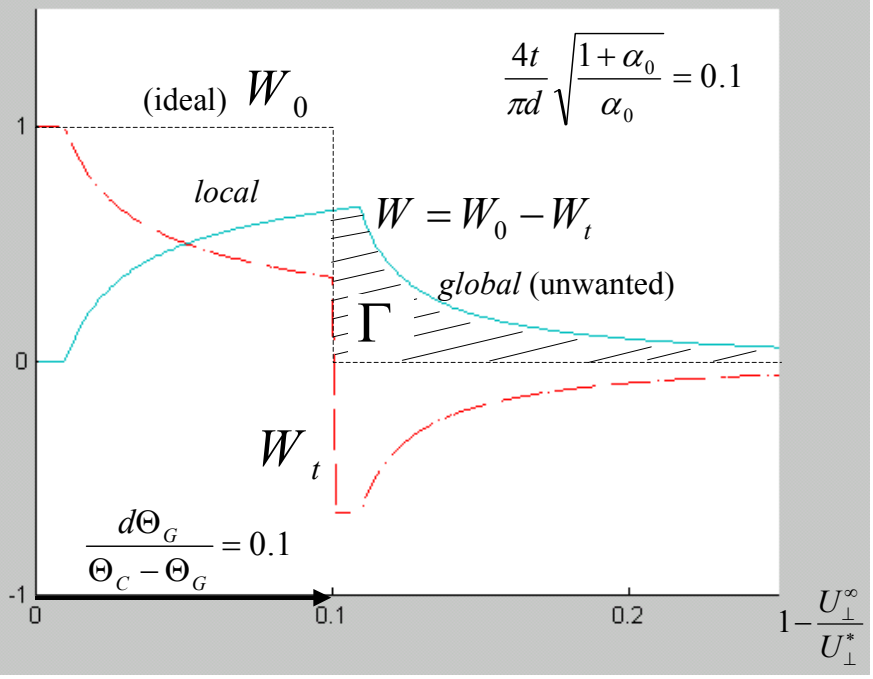

(This page left intentionally blank.)

CHAPTER 6

THE EXPERIMENT AND THE OPERATION OF THE GEM PROBE

[6.0] Introduction

In this chapter, we describe the experiment in which we used the GEM probe and apply the theoretical analysis of chapters **3** through **5** to the results of its operation. We begin in section **6.1**, where we describe the engineering of the probe, which includes the construction of the housing, the electromagnet coil, and the electrical and vacuum connections. We also describe the electronics hardware and software that were employed to measure the applied voltages and the collected currents. In section **6.2**, we examine the other component of the experiment: the plasma chamber. In particular, we address the problem regarding the alignment of the probe with the bulk magnetic field lines, which was a problem that we initially underestimated; one that consumed much of our time during the experiment.

In section **6.3**, we focus on the operation of the probe. We demonstrate the role of the electrodes at the entrance and at the sidewalls inside the housing with regard to drawing plasma to the collector by illustrating their $I-V$ characteristics. We conclude that the optimum bias configuration for these secondary electrodes is to leave the sidewalls electrically floating and to bias the entrance near the plasma potential.

We then analyze the $I-V$ characteristics from the primary electrodes, the grid and the collector, in section **6.4**. The $I-V$ characteristics of these electrodes, in principle, should give detailed information about the anisotropy in the electron energy distribution. However, we knew *a priori* that the parameters characterizing our

experiment were inadequate for this task. The signal-to-noise level in the data of less than *ten* was too low for the differentiation of the current in the space of the electrode voltages for the determination of F_∞. In addition, the experimental values of the wire spacing and the Debye-length produced a ratio of $d/\lambda_{De} \cong 2/3$, which made the barrier provided by the grid somewhat questionable.

Instead, our experiment turned into a feasibility study of the probe, where we established the probe's basic behavior as described in section **3.3**. This behavior speaks about the interaction between the hybrid barrier at the grid and the electric barrier at the collector. The interaction of the two barriers, in turn, revealed the size of the electric hole Δ_0. The size was found to be much bigger than what is estimated by equation **5.2-1**. The discrepancy is due to the shortcomings of our analysis in chapter **5**, which assumes that $d/\lambda_{De} << 1$. Using equation **5.2-1** in conjunction with the observed size in the electric hole, we derived an *effective* value for d/λ_{De} of about 1.5.

In addition to demonstrating the ideal behavior of the GEM probe, the $I-V$ characteristics revealed the effects of space charge in the grid-collector cavity as predicted by the analysis of chapter **4**. The characteristics also exhibited evidence that the electrically floating structures inside the housing affected the flow area for the low-energy electrons.

With all of the problems that plagued our experiment, we were still able to extract a value for the temperature anisotropy, $\beta \equiv T_\perp / T_{//}$, via the method of section **3.1** for the *M*-probe. We analyzed the collector current in the voltage range where the data was neither tainted by effects of space charge nor by effects of the floating structures. The electric *hole* in the mesh, of course, still affected the data. However, the analysis of

subsection **5.3-5** demonstrated that the measurement of β is only sensitive to the distortion in the grid barrier, which produces errors of the order $\sim (d/2\pi\lambda_{De})^{5/2}$. Using the *effective* value of $d/\lambda_{De} \cong 1.5$, we crudely estimate the error from the distortion to be $\delta\beta/\beta \sim 3\%$. The value of β itself was found to be 1.5 ± 0.25.

[6.1] The engineering of the GEM probe

Here, we describe the hardware and the software for the experiment. We begin with the description of the probe housing, whose schematic is shown in figure **6.1-1**. The housing is manufactured from a piece of high-grade alumina (a ceramic). With the exception of the grid, the electrodes in the probe were composed of sub-*mm* thick stainless steel sheet metal. The grid[a] was constructed from a mesh of gold-plated tungsten wires sandwiched by a stainless steel ring casing. The mesh was characterized by a wire thickness and spacing equal to $t = [5 \pm 0.5]\mu m$ (the minimum available) and $d = [200 \pm 20]\mu m$, respectively. The error in the wire spacing was determined via a measurement of the variability in the spacing between adjacent wires over a section of the grid with the aid of a microscope. The wire thickness, on the other hand, was observed to be uniform on the scale of the resolving power of the microscope ($0.5\mu m$).

We used an alumina spacer to insulate the grid from the electrode at the entrance-sidewall. We also used an alumina end-cap to seal the collector so that it would only receive current from the side facing the entrance. The figure does not show the sub-*mm* holes near the entrance, the grid, and the collector, which gave access to the copper wires used as the electrical connections. These wires were spot-welded onto the electrodes.

[a] Graceby Specac Inc. 301 Commerce Drive, Fairfield, CT 06430; (800) 447-2558

The entrance electrode's plasma-facing area was originally much larger: $ID = 8mm$ and $OD = 13mm$. The large area greatly perturbed the dynamics outside the housing as determined through the experimental observation of a reduction in the *grid's* electron saturation current with an increasing *entrance* voltage. This effect was an indication that the large electron sink to the entrance enabled this electrode to "pull" the plasma potential. The original size also enabled the finite curvature of the field lines in conjunction with any misalignment to direct some of the current that entered the housing to the ceramic spacer about the grid. The loss of current to the spacer made the current collection area dependent on the magnetic geometry. The modified size of the entrance electrode, $ID = 6mm$ and $OD = 8mm$, alleviated both of these problems to a great extent.

[6.1.1] The assembly

We attached the probe housing to a stainless steel tube with the aid of an aluminum brace shown in figure **6.1-2**. We used fiberglass sock to cushion the contact between the brace and the housing as well as to provide a tight fit to the stainless steel tube. The tube housed the copper wires for the electrodes and the electromagnet. It also formed the connection to the plasma chamber as shown in figure **6.1-3**. The figure does not show the three rods that were used to bolster the assembly or the electrical feed-throughs that mated with the tees to provide the power connections for the electromagnet and for the electrodes. It also does not show the 18″ long ceramic (alumina) jacket that was used to electrically insulate the stainless steel tube from the plasma. The jacket was held fixed by a setscrew that penetrated the tube.

[6.1.2] The electrical connections

We used sub-mm copper wires to provide the electrical connections to the electrodes and $1/8$ inch diameter copper rods to provide the connection to the electromagnet. The rods and wires were covered with fiberglass sock for electrical insulation and fed through the stainless steel tube. Two ceramic disks containing multiple holes were placed inside the ends of the tube to provide a straight-line form for the wires and the rods. The wires were soldered to the instrumentation feed-through, whereas the rods were screwed into $1/4$ inch diameter (drilled and tapped) copper feed-throughs.

The other ends of the wires were soldered to $Be-Cu$ power crimps, which provided the connection between these wires and the wires that were spot-welded onto the electrodes (these wires were pushed into the crimps). On the other hand, the other ends of the rods were connected to two small copper cylinders with an outer diameter of $1/4$ inch and length of $1/2$ inch, which formed the electrical connection between the rods and the electromagnet. The cylinders had an $1/8$ inch hole drilled on one side for the rods and a $2mm$ hole drilled on the other for electromagnet wire. We used setscrews to hold the rods and the electromagnet wire to the copper cylinders.

[6.1.3] The electromagnet

The electromagnet was constructed from copper wire with a wire diameter of $2mm$. The wire was wrapped along the length of the housing to effectively form a solenoid with two layers of approximately *ten* rings, spanning $4cm$ in length and $4mm$ in thickness. The finite helical twists of the wires in addition to the fiberglass sock that

formed the insulation expanded the length of the electromagnet by a factor of *two* from the ideal. The solenoid produced a modest field of $B_{em} \cong 100(I_{em}/18A)G$ at the throat, which for the ambient field of $B_{\infty} \cong 0.875kG$ yielded an $\alpha_0 = B_{em}/B_{\infty}$ of $(1/9)I_{em}/18A$. As we demonstrate shortly, the circuit that we used to drive the electromagnet limited I_{em} to less than $35A$. The resulting bound on $\alpha_0 < 2/9$ unnecessarily increased the duration of the experiment for the purpose of attaining the optimum signal-to-noise level, as demonstrated by an analysis of the Joule-heating of the electromagnet in appendix **6.1x**.

[6.1.4] The electronics

The data was obtained by pulsing the electromagnet and by ramping the voltage of an electrode while maintaining the remaining electrodes either at a constant voltage or electrically floating. To ramp a particular electrode, we used a function generator to drive a bipolar voltage source as shown schematically in figure **6.1-4**. The generator produced a variety of waveforms with a maximum amplitude of $2V$ in a range of frequencies that spanned $10^{-2}hz \rightarrow 10^{5}hz$. The signal was then amplified by the bipolar voltage source to sweep the voltage within the practical range of $\pm 50V$. We used an amplifier[b] circuit to step down this voltage by a factor of *twenty* so that it would fall within the recording range of the digitizer, which was $\pm 5V$. We also used a differential amplifier in conjunction with a sense resistor to measure the plasma current. The sense resistor was chosen as $R_{sense} = 200\Omega$ so that the product $I_C R_{sense} \sim 1mA \cdot 200\Omega$ would well exceed the bin resolution of the digitizer, which was $\Delta V_{bin} = 1mV$.

[b] Rev. Sci. Instrum., Vol. 57, No. 10, October 1986

The current to the electromagnet was controlled by the gate of a MOSFET powered by a function generator, as shown in figure **6.1-5**. The FET was capable of handling a drain-source voltage and current of $V_{DS} \cong 70V$ and $I_{DS} \cong 50A$. We added a power diode to prevent V_{DS} from exceeding its maximum tolerance (from the *inductive spike*) at times when the gate *opened* the drain-source channel. In addition, a finite amount of resistance $R \cong 2\Omega$ was added to the circuit because the source could not drive a stable square pulse through a *short*. The finite resistance limited the maximum current to $I_{em} \cong 70V/2\Omega \cong 35Amp$. The electromagnet current was measured with a differential amplifier in conjunction with a high-precision sense resistor of $100mV/A$ to produce an output within the recording range of the digitizer.

[6.1.5] Data acquisition

A typical data set for shots in which we ramped the grid voltage while maintaining the collector voltage at a constant value is shown in figure **6.1-6a**. A close up of the data is shown in figure **6.1-6b**. The x-axis in the figures represents the bin number, which corresponds to a time of $time = bin\#/f_{bin}$, where $f_{bin} = 40kHz$ is the frequency at which we sampled the data. We chose a triangular waveform with a sweep frequency of $f_V = 200\sec^{-1}$ to ramp the electrode voltage in between $\pm 30V$. The contamination from the capacitance between the wires, $C \sim 10pF$, for this frequency was insignificant: $I \sim 10pF \cdot 100V \cdot 100Hz = 0.1\mu A$.

To prevent the overheating of the electromagnet, the function generator was triggered at the beginning of the shot by the clock on the digitizer to provide 8 square

pulses at $50m\sec$ intervals with a 50% duty cycle. In addition, we limited I_{em} to about $18A$, which is about *half* the maximum tolerance of the FET driving the circuit. This current produced a field of $100G \pm 5\%$ at the electromagnet throat, where the error is dominated by the uncertainty in the measurement of the magnetic field inside the housing with a Hall probe. The field of the electromagnet, in turn, yielded an α_0 of about 12%.

The data presented in sections **6.3** and **6.4** was averaged over *five* to *ten* shots to enhance the signal-to-noise level within bins that spanned $1V$ in the voltage (being ramped) for the electromagnet *on* and *off*. There were typically of the order of *hundred* samples per shot for a given voltage bin.

[6.2] The plasma chamber

We inserted the probe into the chamber of the Versatile Toroidal Facility at MIT's Plasma Science and Fusion Center. The plasma chamber is a torus with dimensions depicted in its cross section view in figure **6.2-1**. This view happens to be at a toroidal location that possesses a side port. The chamber allows access to its interior from the side and from the top. Eighteen poloidally wrapped coils separated by twenty degrees in the toroidal direction provide the current that produces the toroidal magnetic field with a strength that is of the order $1kG$. An industrial microwave produced $1kW$ of power at a frequency of $2.45Ghz$, which ionized a hydrogen gas with a gas pressure of the order $10^{-5} torr$. The gas is ionized via the electron cyclotron resonance at $B \cong 875G$. The current that produces the toroidal field controls the resonance location ($B \propto I_{TF}/R$).

[6.2.1] The plasma characteristics at the operating point

We determined the plasma density and the parallel electron temperature from the $I-V$ characteristics of the entrance electrode as described in section **2.2** (figures **2.2-3[a,b]**). The area of the entrance electrode is approximately $A_E \cong 25mm^2$ with an uncertainty that produced a *systematic* error in the measured density of the order $\delta A/A \approx 10\%$. The results of the fit for n_e and $T_{//}$ for various toroidal field currents are plotted in figure **6.2-2**. The x-axis in the figure is actually the voltage of the sense resistor that measures I_{TF}. We did not have an accurate calibration for the ratio of B_∞ / I_{TF}. Hence, we estimated the ambient field at the probe, which was located at $R_0 \cong 1m$, as $B_\infty \cong \left[I_{TF}/I_{res}\right]\cdot 875G$, where I_{res} is the toroidal field current that maximized the plasma current detected. Using figure **6.2-2**, we find that the width of the resonance region is approximately $\Delta I_{TF}/I_{TF} \cong 5\%$. Therefore, we estimate that our operating point placed the probe to within 5% of the magnetic field at resonance. The electron density and temperature at this point are approximately $T_{//} \cong 7.5eV$ $(\pm 0.5eV)$ and $n_e \cong 5\cdot 10^9 cm^{-3}$, which gives $\lambda_{De} \cong 300\mu m$. Considerations for the signal-to-noise level prevented us from working with $n_e < 10^9 cm^{-3}$. Hence, we could not reduce the ratio of d/λ_{De} below $2/3$.

[6.2.2] The alignment of the probe with the magnetic field lines

We first inserted the probe from a side port as illustrated in figure **6.2-3**. The port, however, did not allow the probe to enter radially, which caused the surface-normal of the entrance electrode to be skewed relative to the bulk field lines. In addition, the

finite extent of the assembly placed the housing in a region where the field inhomogeneouty exacerbated the misalignment. To align the probe, we attempted to tilt the assembly. However, because of the limited range of motion of the stainless steel tube, the assembly could not be tilted enough.

As a result, we inserted the probe from the top of the chamber, which placed the probe in the center of the chamber where the field lines were essentially toroidal. To align the probe with the field lines, we twisted the assembly about its axis. The assembly was flexible enough to be torqued to zero the *initial* skew angle ϕ (upon insertion). The method with which we twisted the assembly was not elegant. We placed a metal bar in between the assembly's supporting rods and pinned the bar against a clamp. We then slipped a wedge of aluminum with a variable thickness between the bar and the clamp in order to rotate the bar. To achieve alignment, we maximized the grid and the collector currents for various degrees of rotation. The currents were averaged over a few shots with the electrodes biased to obtain the electron current. Although the collector current was space charge limited, we expected its variation to reflect the probe's degree of alignment with the field lines.

Even though the method for alignment was somewhat coarse, it was more than adequate. The analysis of the geometry for alignment in appendix **6.2x** shows that the current to the collector drops rapidly for a skew angle that is greater than *one* degree (see figure **6.2-4b**). The current's sensitivity to this angle virtually guaranteed that we had achieved near perfect alignment once we obtained an appreciable increase in the collector current with the rotation of the metal bar.

[6.2.3] The magnetic geometry and the electron collection area

The analysis of the alignment geometry is also important for determining the variation in the electron collection area A_{EGC} with the local magnetic field, as illustrated in figure **6.2-4a**. The figure indicates that for $\phi \neq 0$, there are field lines that initially don't penetrate the grid electrode when $\alpha_0 = 0$, but bend pass this electrode upon compression. Hence, it is possible for the collection area in our experiment to increase with α_0. This effect would *counter* the reduction in the current from the magnetic mirror force and thereby mask the measurement of the anisotropy in the electron distribution function.

For the case of perfect alignment, $\phi = 0$, we can eliminate the signal contamination from the effects of magnetic geometry by maintaining the radius of the grid aperture a_G greater than that of the entrance a_E by an amount equal to the radial displacement in the field lines from the entrance to the grid. This distance is approximately $\Delta r \cong (l/R_0)^2 R_0/2$, where R_0 is the radius of curvature of the field lines at the probe and l is the distance between the grid and the entrance. The criterion is satisfied in our experiment, where $a_G - a_E = 1mm$ and $\Delta r \cong 0.8mm$ ($l = 40mm$ and $R_0 \cong 1m$).

However, we cannot guarantee that we had achieved perfect alignment in our experiment. Therefore, in subsection **6.2x-1**, we calculate the magnetic projection of the entrance area onto the collector for different values of α_0 and ϕ. Figure **6.2-4b** illustrates the results of the calculation. It shows that there is a small window in the skew angle ($0.5^\circ < \phi < 1^\circ$) for which the projected area increases with increasing α_0 for the

experimental value of $a_G = 4mm$. The window is small because the field lines must satisfy *two* criteria to affect the collector current. First, they must remain outside of the grid aperture but strike the collector when $B_{em} = 0$; and second, they must squeeze pass the grid aperture upon compression. Figure **6.2-4b** indicates that the relative change in the collection area *could have been* as much as 4%, which is substantial when compared to the signal of interest: $\Delta I/I \sim \alpha_0 \beta$, where $\alpha_0 \cong 12\%$ and $\beta = T_\perp / T_{//} \sim 1$.

Furthermore, the contamination in the signal for the low-energy electrons could have been even greater. These electrons are subject to being reflected by the field that emanates from the electrically floating spacer about the grid. The sheath about the spacer penetrates a distance of $5\lambda_{De} \sim 1mm$, thereby effectively reducing the radius of the grid aperture. Now, the movement of the field lines does not directly alter the flow area through the grid because the potential is *tied* to the field lines. However, as a result of the separation of the field lines from the spacer, the compression of the magnetic field will reduce the electron current to the spacer, which will increase the spacer's floating potential. The rise in the floating potential will reduce the electric field, which will effectively increase the flow area for these electrons. If the effective change in a_G is of the order of the sheath thickness of $1mm$, then a comparison of the curves for $a_G = 4mm$ and $a_G = 3mm$ with $\alpha_0 = 0$ in figure **6.2-4b** illustrates that the relative change in the flow area can be as large as 20%; a value that is comparable to the signal associated with the magnetic mirror force.

To eliminate the unwanted effects of the magnetic geometry in the future, we should separate the electrically floating structures inside the housing from the plasma

beam. In addition, we should employ the configuration described in subsection **1.3.1**, in which the collector is placed at the throat and the grid is placed at the entrance. The configuration reduces the length of the probe by a factor of two, thereby increasing the tolerance for alignment. It also makes the plasma flow area relatively immune to changes in the magnetic geometry because most of the variation occurs near the throat, which is now the location of the opaque electrode.

[6.3] Drawing plasma to the collector

In this section, we examine the ability of the secondary electrodes (the ones at the sidewalls and at the entrance) to draw plasma into the housing, through the grid, and to the collector. The analysis reveals the strong influence of the sidewall bias on the current to the primary electrodes as well as the effects of the electrically floating structures inside the housing. The results suggest that for optimum performance, we should leave the sidewalls electrically floating and that we should bias the entrance electrode near the plasma potential.

[6.3.1] The impact of the *ion* current to the sidewall

Figure **6.3-1a** illustrates the effect of the bias on the entrance-sidewall (labeled as ESW) on the grid current with the voltage on the entrance left electrically floating (labeled as $\circ$). The grid voltage for the $I_G - V_{ESW}$ characteristics was set to $\pm 30V$ (labeled as $\pm$) to draw either electron or ion saturation current. These voltages were chosen in accord with the results of the $I_E - V_E$ characteristics of figures **2.2-3[a,b]**.

The sidewall's ability to control the grid current is a result of the radial mobility of the ions as demonstrated in figure **6.3-1b**, where we have plotted the $I_{ESW} - V_{ESW}$ characteristic. The ion current to the sidewall is shown to be of the order of the ion saturation current to the entrance, $200\mu A$ (see figure **2.2-3a**). Given that the area of the entrance electrode, $A_E \cong 25mm^2$, is approximately equal to that of the entrance aperture, $A \cong 28mm^2$, we conclude that the sidewall can attract virtually all of the ions.

The ions, unlike the electrons, are not confined radially when $V_{ESW} < \Phi_s$, where Φ_s is the plateau potential of the plasma beam in the region upstream from the grid. The initial magnetic mirror force on the ions, $\sim ev_{ti}B_0$, tends to be miniscule relative to the electric force near the edge of the beam. Hence, the ions initially accelerate to the sidewall until the two forces become comparable. By modeling the electric force generically as U/r, where $U/r \sim T_e/\lambda_{De}$ in the sheath at the edge and $U/r \sim (\Phi_s - V_{ESW})/(a_{ESW} - a_E)$ outside the sheath near the sidewall, we can approximate the ion speed at which the two forces balance as $v_i \sim v_{te}(\rho_e/r)(U/T_e) \sim v_{te}\,\rho_e/r$, which gives an effective ion Larmor radius of $\rho_i \sim (m_i/m_e)(\rho_e^2/r)$. Taking the larger value of r, $a_{ESW} - a_E \sim 1mm$, and using $\rho_e \sim 100\mu m$ and $m_i/m_e \cong 1833$, we find that ρ_i is at minimum of the order $1cm$, which is the characteristic size of the cavity in the housing.

The loss of ions to the sidewall leaves an electron space charge in the beam, which lowers the plateau potential below the value on the sidewall. The resulting electric barrier to the electron flow along the field line then enables V_{ESW} to control the electron current to the grid. As V_{ESW} is increased towards the plasma potential, the radial field

that attracts the ions to the sidewall diminishes, and more ions are able to reach the grid. Hence, V_{ESW} controls the current of both species. The voltage on the collector-sidewall is similarly able to control the current of both species to the collector, as illustrated in figures **6.3-2[a,b]**. Here, we chose a grid voltage of $15V$ because (as we demonstrate in the next section) it happens to maximize the current of both species.

A comparison of the $I-V$ characteristics from the sidewall electrodes in figures **6.3-[1,2]b** and the sidewall voltages at which the currents in figures **6.3-[1,2]a** *maximize* indicates that we should leave the sidewalls electrically *floating*.

[6.3.2] The impact of the *electron* current to the sidewall

Having determined the optimum bias for the sidewalls, we focus on the bias on the entrance electrode. Figure **6.3-3a** shows that the electron current to the entrance-sidewall is reduced when $V_E \cong \Phi_\infty$ as compared to the case when the entrance is left electrically floating. The reduction in I^e_{ESW} for $V_E \cong \Phi_\infty$ increases the floating potential on the sidewall as observed. We expect a similar effect for the floating potential of the ceramic spacer in front of the grid. These effects increase the area for flow through the grid aperture for the low-energy electrons as described in subsection **6.2.3**, thereby explaining the observed increase in the electron current to (and thereby through) the grid when $V_E \cong \Phi_\infty$.

In subsection **6.2.3**, we also argued that the flow area for the low-energy electrons will also increase with the compression of the magnetic field, thereby countering the effect of the magnetic mirror force. This claim is evident in figure **6.3-3b**, where it is shown that the signal for I^e_G with and without the compression of the field converges for

large V_{ESW}. The bias $V_E \cong \Phi_\infty$ *delays* the convergence of the two signals and is thereby *the bias of choice*. Hence, when operating the GEM probe, we will bias the entrance electrode near the plasma potential.

[6.4] The operation of the primary electrodes (the grid and the collector)

Having established the bias on the secondary electrodes, we focus on the operation of the primary electrodes: the grid and the collector. Here, we demonstrate the ideal behavior of the probe, as explained in section **3.3**, and reveal the non-ideal behavior associated with the effects of space charge, addressed in sections **4.2** and **4.3**, as well as the effects of the electric hole in the grid barrier, which was discussed in section **5.3**.

As explained in section **6.0**, the parameters characterizing our experiment did not allow for a measurement of the distribution function, itself. However, we were able to examine the data in a voltage range that was neither tainted by effects of space charge nor by effects of the floating structures in order to extract a value for the temperature anisotropy $\beta = T_\perp / T_{//}$. We found that $\beta \cong 1.5 \pm 0.25$, which is a plausible value for a plasma that is being heated via the electron cyclotron resonance.

We begin with a discussion of the systematic errors that were introduced as a result of the way in which we acquired the data.

[6.4.1] The systematic errors in the data

The ease in the analysis and in the real-time interpretation of the $I-V$ characteristics motivated the choice to maintain one of the two electrode voltages constant during each shot. We chose to maintain the collector voltage at a constant value.

We kept this voltage constant for *ten* shots (to increase the signal-to-noise) and then stepped it up by $1V$ for the next set of *ten* shots to span a voltage range of $\pm 30V$; the range for the grid voltage.

The choice to keep the collector voltage constant, however, introduced systematic errors in the $I - V_C$ characteristics as a result of the variability in the current for the toroidal magnetic field I_{TF} and in the microwave output power $P_{\mu wave}$ from shot to shot. We have no measure of the variation in $P_{\mu wave}$ during the period of the 600 shots for the experiment. However, we did measure the variation in I_{TF}, as shown in figure **6.4-1**. Here, the y-axis is proportional to the voltage drop across a sense resistor for the current in the coils for the toroidal field. The figure illustrates that the toroidal field remains within 1% of its nominal value of $875G$ at resonance, which is assumed be in the vicinity of $-0.35V$ (see figure **6.2-2**). Even though the variation is relatively small, it corresponds to about a $1cm$ shift in the location of resonance, which is substantial given that the diameter of the entrance aperture is $6mm$.

In fact, the jump in I_{TF} at $V_C = 24V$ produced a discernable jump in the electrode currents, which forced us to discard the set of data for $V_C \geq 24V$. The removal of this set, however, was not a great loss because, in this range, the collector is for the most part acting as a collector of electrons, and its voltage is superfluous. The data for $V_C < 24V$ still contained some unwanted variation from the variability in the experimental parameters. In the future, both electrodes should be ramped within each shot to eliminate such errors.

[6.4.2] The predictors for the $I-V$ characteristics

Before, we examine the characteristics from the primary electrodes, we estimate the size of the electric hole and the threshold grid voltage for the onset of the space charge limited regime so that we may compare our theoretical predictions with the experimental observations. Using equation **5.2-1** in conjunction with the experimental value of $d/r_w \cong 80$, where $r_w \cong t/2$, we find

$$\Delta_0 = e\left(\Phi_0 - V_G\right) = -e\overline{E}d\,\frac{1}{2\pi}\ln\frac{d}{2\pi r_w} \cong -0.4e\overline{E}d\left[eV\right],$$

where Φ_0 is equal to the average potential in the grid-plane. The plasma potential Φ_∞ was estimated in section **2.2** to be in between $25V$ to $30V$. The average field $\overline{E}$ is negative for the practical range $\Phi_\infty - V_G > T_{//}$ (where Φ_0 is greater than V_G). Its magnitude is estimated in section **5.2-2** to be of the order $T_{par}/e\lambda_{De}$, which for the experimental values of $T_{//} \cong 7.5eV$ and $d/\lambda_{De} \cong 2/3$ gives $\Delta_0 \sim 2eV$.

Noting that the space charge responds to the effective voltage at the grid-plane, the threshold voltage for the onset of a space charge induced barrier to the electron flow is given by the relation $\Phi_0 = \Phi_\lambda$, where $\Phi_\lambda \cong \Phi_\infty - T_{//}$, as estimated by equation **4.4-1** for the experimental value of plasma beam radius ($b \cong 3mm$). Using the relation $V_G = \Phi_0 - \Delta_0/e$ then, we predict that the electron current to the collector will become space charge limited for

$$V_G > V_\lambda \equiv \Phi_\lambda - \Delta_0/e \cong \Phi_\infty - 10V\,.$$

[6.4.3] The interaction between the two electric barriers

If the *GEM* probe is to have a future, it must demonstrate the interaction of the hybrid barrier at the grid-plane with the electric barrier at the collector as predicted in section **3.3**. To this end, we first demonstrate the interaction between the two electric barriers with $\alpha_0 = 0$. Figure **6.4-2** illustrates a contour plot of the electron current to the collector in the space of the grid and the collector voltages along with the curve describing the boundary $V_C = \Phi_0$ for various ratios of d/λ_{De}. Ideally, if the grid provided a *perfect* barrier, the boundary for exchange of control over the collector current would be given by $V_C = V_G$. However, the finite size of the electric *hole* shifts this boundary as depicted. The shift that is predicted by the experimental value of $d/\lambda_{De} \cong 2/3$, however, is less than what is shown in the figure. The actual boundary corresponds to a d/λ_{De} of about 1.5 ($\Delta_0 \sim 5eV$). The larger size for the *hole* in the grid barrier is believed to arise from the contribution of the space charge in the region where the perturbation is significant, $|z - z_G| < d$. This contribution was neglected in our derivation in section **5.2-2**, where we assumed that $d/\lambda_{De} << 1$.

Apart from this discrepancy, figure **6.4-2** demonstrates the exchange of power between the electric barrier at the collector and the average electric barrier at the grid. The remnant variation with the collector voltage in the region where the grid barrier is supposed to govern I_C^e is attributed mainly to a changing plasma parameter ($P_{\mu wave}$). The distortion in the grid barrier and the diffusion of the energies would not be able to

contribute to this anomalous variation for $e(V_C - \Phi_0) > \delta_0$, where the standard deviation in the grid barrier δ_0 is of the order $(d/2\pi\lambda_{De})T_{//} \sim 1eV$.

[6.4.4] The effects of space charge

Having demonstrated the interaction of the electric barriers at the grid and at the collector, we next examine the $I_C^e - V_G$ ($V_C = 23V$) and the $I_C^i - V_G$ ($V_C = -30V$) characteristics of figure **6.4-3**, which reveal the qualitative effects of space charge as summarized in section **4.4** and depicted in figure **4.2-4**. We forego a quantitative comparison of the theoretical and the experimental results because in the regime where the effects of space charge become important, our model for the electric hole in the grid barrier breaks down as a result of the large value for the ratio of d/λ_{De}.

Figure **6.4-3** shows a weak variation in the ion current for $V_G < 0V$. In this range, the electron density contributes weakly to the space charge inside the grid-collector cavity, and the potential hump that forms downstream from the grid-plane is not required to remove the necessary amount of ions to produce a quasi-neutral state in the region following the hump location. However, as the grid voltage increases towards the plasma potential, the ion current to the collector becomes tied to the presence of the electrons and thereby begins to rise exponentially with the grid voltage. This rise is then a precursor to the formation of a space charge induced barrier to the electrons, whose current is shown to saturate and eventually reduce as the grid voltage approaches the plasma potential. The onset for this regime more or less corresponds to what we have predicted: $V_G > V_\lambda$, where V_λ is in the vicinity of $15V$.

The magnitude of the electron current to the collector (before the saturation) is comparable to what is shown in figure **2.2-3a** for the electron current to the entrance electrode. On the other hand, the magnitude of the ion current to the collector at its peak is only about 25% of I_{si} estimated to enter the housing. The smaller value for I_C^i might be the result of the potential hump remaining *above* the value of the pre-sheath potential preceding the grid-plane. Another explanation could be the absorption of a fraction of the ions by the electrically floating structures inside the housing. One last explanation is the non-zero electron current for the $I_C^e - V_G$ characteristic at $V_G = -30V$, which suggests that (even with the electric *hole* in the grid barrier in mind) the bias of $V_C = -30V$ does not completely isolate the ion contribution for the $I_C^i - V_G$ characteristic. The contamination from the electron signal could be as large as $40\mu A$.

[6.4.5] Exploiting the grid current

The grid current can corroborate the evidence of a space charge barrier to the electron flow to the collector via the principle of duality, which states that the current reflected inside the grid-collector cavity produces a second pass contribution to the grid. To perform this task, we note that, in general, we can express I_G as the sum of $I_+ + I_-$ (times the mesh opacity), where the $\pm$ denote the *first* and *second* pass contributions. Therefore, when the collector is biased to reflect all the electrons ($V_C = -30V$), $I_G = I_G^a = 2I_+$ (Here, to simplify the argument, we have neglected the ion contribution). Now, if we subtract *half* of I_G^a from I_G for an arbitrary value of the collector voltage, then we obtain $I_G^b = I_G - 0.5I_G^a = I_-$.

Figure **6.4-4** shows the $I_G^a - V_G$ and $I_G^b - V_G$ characteristics with I_G^b evaluated at $V_C = 23V$, where the collector absorbs the impinging electrons. Now, if there were no space charge induced barrier to the electrons, we would expect I_G^b to be *zero*. However, the curve for I_G^b indicates that a barrier has formed inside the grid-collector cavity for $V_G > 10V$. This voltage range is consistent with the range for the saturation and subsequent drop in the electron current to the collector as depicted in figure **6.4-3**.

The initial drop in I_G^b with increasing grid voltage in the range $V_G < 0V$ stems from an increasing ion contribution, which is explained as follows. As the grid voltage increases, the field that accelerates the ions in the sheath upstream from the grid is reduced, and the field perturbation about the mesh bends the ion trajectories towards the wires. This deflection effectively increases the grid ion collection area. The resulting variation in the ion current is difficult to remove. Hence, it is essential to have $d << \lambda_{De}$ when extracting information about the electrons from the grid current.

[6.4.6] The variation in the flow area through the grid aperture

In addition to corroborating the evidence of space charge effects, the grid current can also be used to determine whether the signal for the change in the current with the compression of the magnetic field, ΔI, is contaminated by the variation in the flow area. Such a variation would counter the effect of the magnetic mirror force and thereby contaminate the signal of interest.

To gauge the variation in the flow area, we examine the ratio $\Delta I_G^e / I_G^e$, where the operator Δ is defined as the *reduction* in the electron current with α_0 and I_G^e is the

electron current with $\alpha_0 \neq 0$. We remove the ion contribution by approximating I_G^i crudely as $c_1 V_G + c_2$, where the constants are found from a fit to the $I_G - V_G$ characteristic in the range $V_G < -10V$. We then examine $\Delta I_G^e / I_G^e$ in the range $V_G > 0V$, where the uncertainty in I_G^i is insignificant. We average the signal over the set of shots described by $V_C < -10V$ (where the collector reflects virtually all electrons) in order to enhance the signal-to-noise level. The result is depicted in figure **6.4-5**.

If the signal stemmed purely from the magnetic mirror force, then it would be a constant, approximately equal to $\alpha_0 \beta \cong 0.12\beta$ (for a bi-Maxwellian distribution function). However, the signal is shown to drop with increasing grid voltage. This drop is consistent with the notion described in subsection **6.2.3** and substantiated in subsection **6.3.2**; namely, that the area for the flow of the low-energy electrons through the grid aperture increases with field compression. Hence, we expect that the signal from the magnetic mirror force contained in ΔI_C^e in the range $V_G > 5V$ will be degraded as well.

[6.4.7] The interaction between the hybrid and the electric barriers

Having examined the effects of space charge and the varying flow area through the grid aperture, we next look to establish the interaction between the hybrid barrier at the grid-plane with the electric barrier at the collector. Figure **6.4-6** shows the collector's equivalent to what is shown in figure **6.4-5** for the grid. Here, we have smoothed the data to enhance the image. In addition, we have added $25\mu A$ to I_C^e mainly to suppress the singularities in the region where the subtraction of the ion current gives $I_C^e = 0$. As explained at the end of subsection **6.4.4**, the addition of this current is not entirely

inappropriate given that the actual ion current that should be subtracted to obtain I_C^e is greater than what is shown in figure **6.4-3**.

The surface plot of $\Delta I_C^e / I_C^e$ illustrates a sharp transition from the region where the signal is finite and more or less constant to the region where the signal diminishes. The boundary for the transition is shown to be described adequately by the experimentally determined curve for $V_C = \Phi_0$ (see figure **6.4-2**). This profile is consistent with the theory of section **3.3**, which states the following. In the region where the grid barrier governs I_C^e ($V_C > \Phi_0$), the collector absorbs all electrons that overcome the hybrid barrier, and the variation in the magnetic field impacts the electron current collected. On the other hand, in the region with $V_C < \Phi_0$, the field compression has little impact because the collector barrier would have reflected most of the electrons that are being mirrored at the grid.

Using equation **3.3-2** (with χ_G replaced by χ_0), we find that for a bi-Maxwellian distribution function, the theory of section **3.3** gives

$$\frac{\Delta I_C^e}{I_C^e} = \alpha_0 \beta \frac{\varepsilon_{C0}}{1 + \alpha_0 \beta [1 - \varepsilon_{C0}]}$$

with

$$\varepsilon_{C0} \equiv \exp\left(- \frac{Step[\Phi_0 - V_C]}{\alpha_0 \beta T_{//}} \right),$$

a function that equals *one* for $V_C > \Phi_0$ and reduces exponentially as V_C is reduced below Φ_0. Hence, the magnitude of the signal in the region where the grid barrier dominates should be constant, equal to $\alpha_0 \beta$, where $\alpha_0 \cong 0.12$ for our experiment. The *early* drop

in the signal denoted in the figure (in the range $0V < V_G < 10V$) is attributed to the countering effect of the varying flow area for the low-energy electrons. On the other hand, the resurgence in the signal as the grid voltage approaches the plasma potential is ascribed to the effects of space charge, which reduce the potential below Φ_0 (and eventually below V_C) downstream from the grid.

Even though our main objective here was to establish the ideal behavior of the *GEM* probe, we have the information with which to estimate the temperature anisotropy. By examining $\Delta I_C^e / I_C^e$ in the region where $V_C > \Phi_0$ and $V_G < 0V$, we find that the signal lies approximately between the values of 0.15 to 0.20, thereby giving the estimate

$$1.25 < T_\perp / T_{//} < 1.7 .$$

The greater temperature for the perpendicular energy distribution is not surprising given that we heat the plasma via the coupling of the microwave energy to the electron's gyro-motion. The mean-free-path for collisions in our plasma is *tens* of *meters*, which is greater than the characteristic length of the circumference of the plasma chamber. Hence, we expect that the electrons will retain a healthy fraction of the energy in their gyro-motion.

[6.5] Conclusion

In this chapter, we described the construction of the gridded-electromagnet probe and its operation in a plasma that is heated via the electron cyclotron resonance. In section **6.2**, we addressed the difficulties in aligning the probe with the magnetic field and concluded that in the future, we should modify the configuration of the *GEM* probe to

that described in subsection **1.3.1**. We then turned to the operation of the various electrodes.

In section **6.3**, we discussed the role of the secondary electrodes, where we demonstrated that we should leave the sidewalls of the probe electrically floating and that we should bias the entrance to the probe near the plasma potential. We then focused on the $I-V$ characteristic of the primary electrodes in section **6.4**. We first established the interaction between the electric barriers at the grid and at the collector and found that the size of the electric hole in the mesh was bigger than what we had predicted from the results of chapter **5**. We argued that this discrepancy was plausible given the large value of $d/\lambda_{De} \cong 2/3$. We then showed evidence of space charge effects in both the grid and the collector $I-V$ characteristics. The effects were found to be consistent with the predictions of chapter **4**.

With a reasonable understanding of the physics of the probe, we examined the signal pertaining to the anisotropy in the electron distribution function. We established the interaction of the hybrid barrier at the grid-plane with the electric barrier at the collector as described in section **3.3**. The parameters characterizing our experiment did not allow for the measurement of F_{∞}. However, we were able to extract a value for the temperature anisotropy $\beta = T_{\perp}/T_{//}$. We found $\beta \cong 1.5 \pm 0.25$, which we argued to be a reasonable value for a plasma that is being heated via the electron cyclotron resonance.

Overall, the results suggest that the GEM probe should be able to deliver detailed information about the anisotropy in the electron distribution function with a mesh characterized by $t \sim 1\mu m$ and $d \sim 10\mu m$.

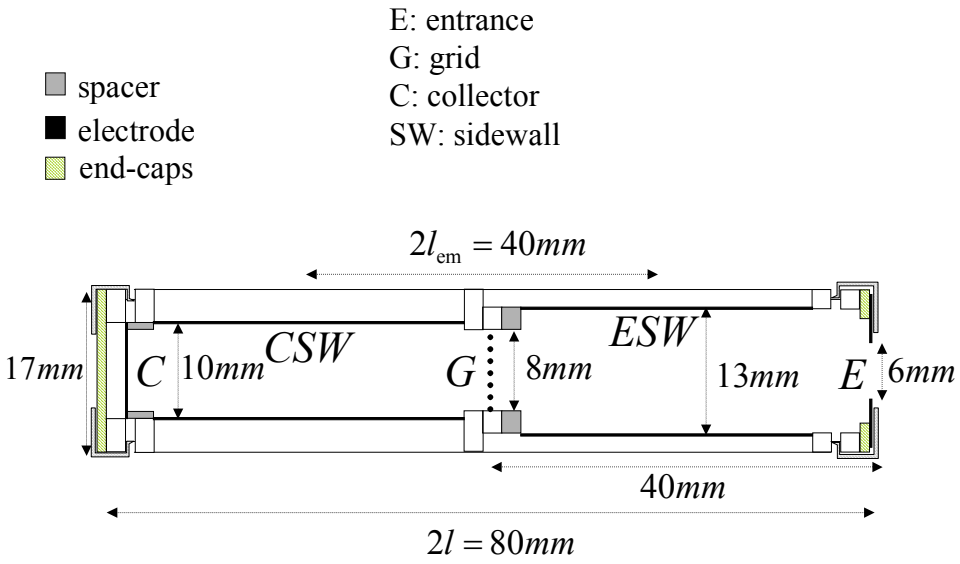

FIGURE 6.1-1: A schematic drawing of the probe cross section

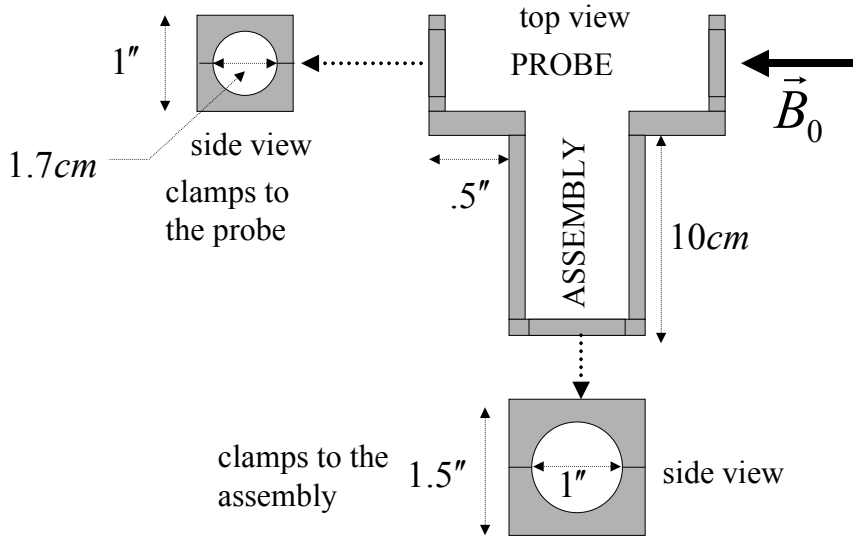

FIGURE 6.1-2: A schematic drawing of the aluminum brace that connects the housing to the assembly

FIGURE 6.1-3: A schematic drawing of the assembly

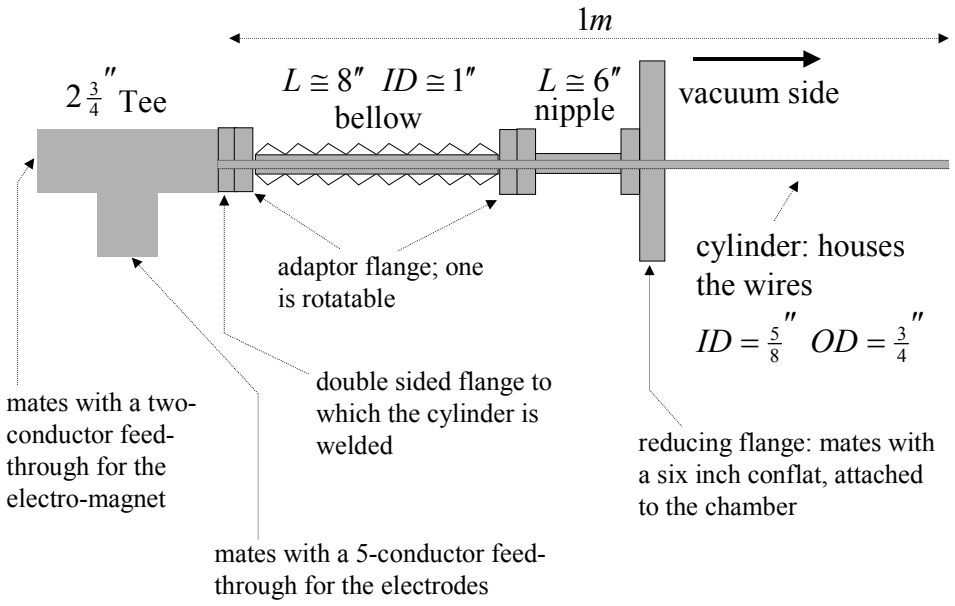

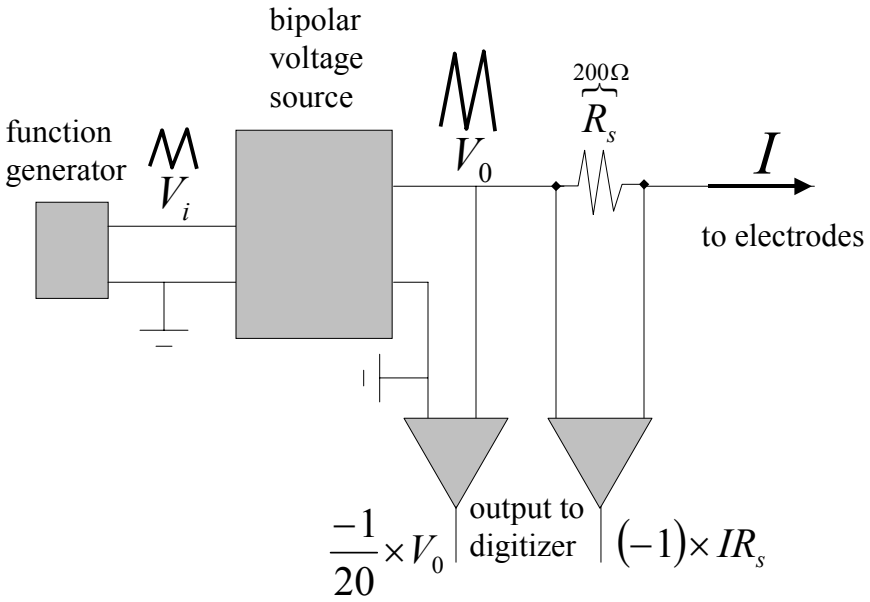

FIGURE 6.1-4: The circuit for measuring the plasma current

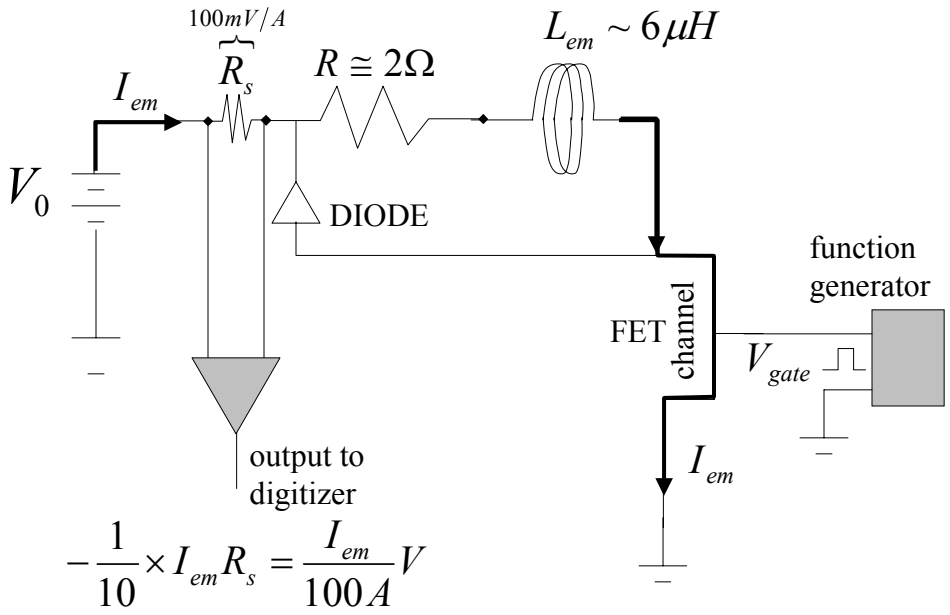

FIGURE 6.1-5: The circuit driving the electromagnet current

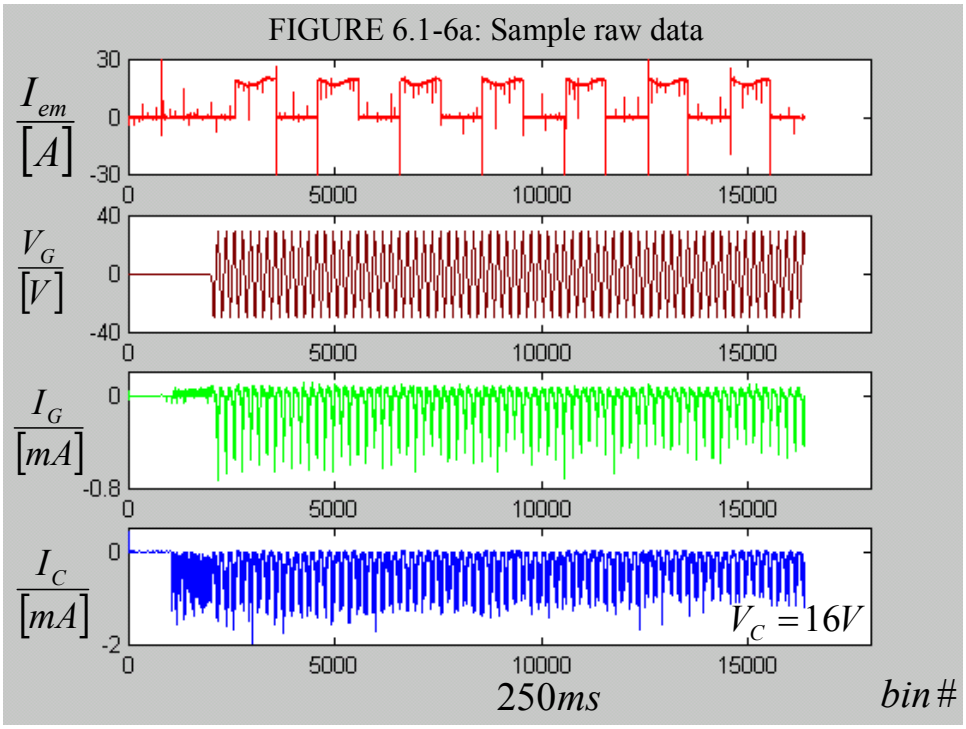

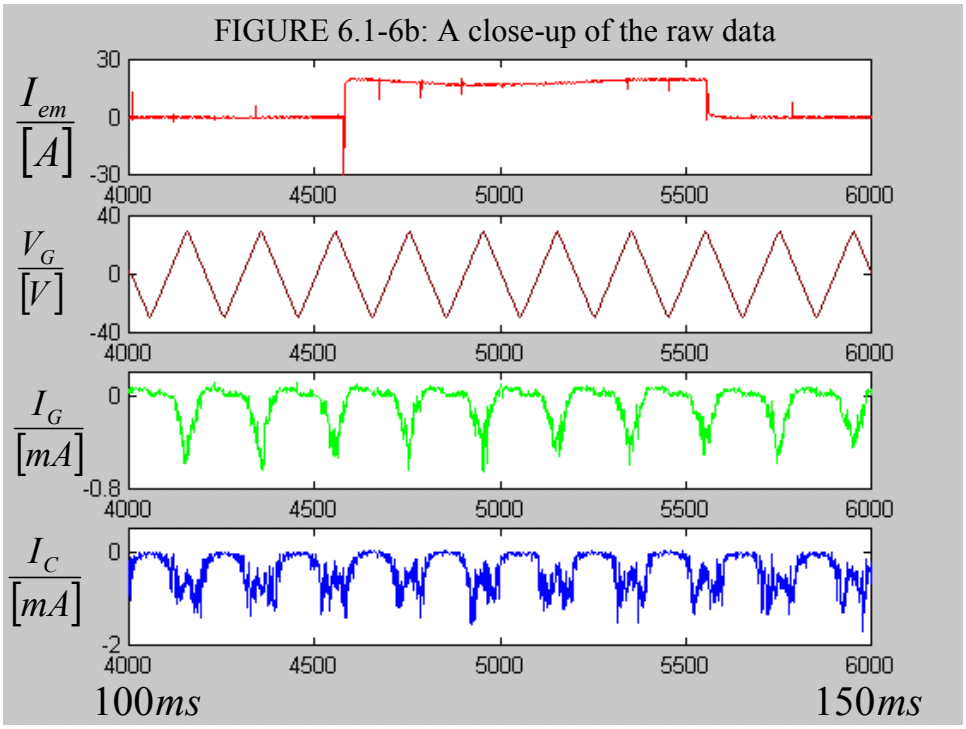

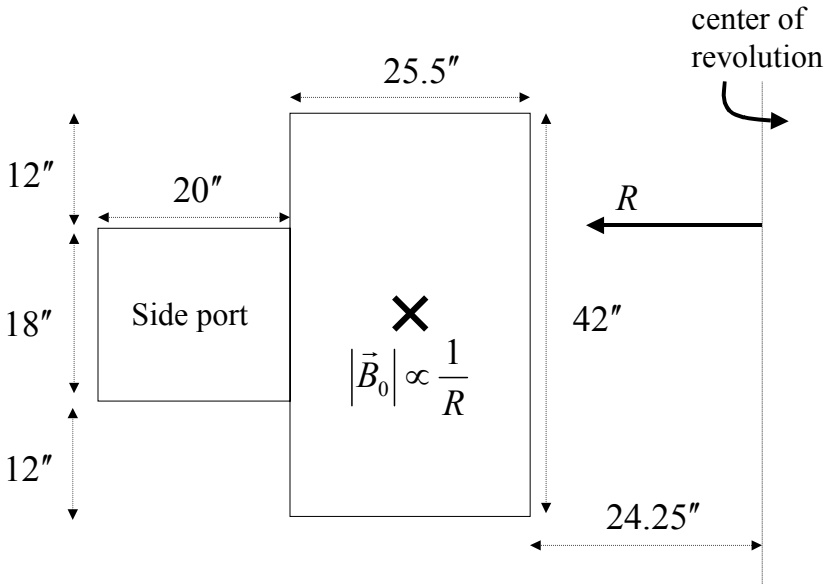

FIGURE 6.2-1: A cross section view of the plasma chamber

FIGURE 6.2-2: The electron density and temperature at the probe

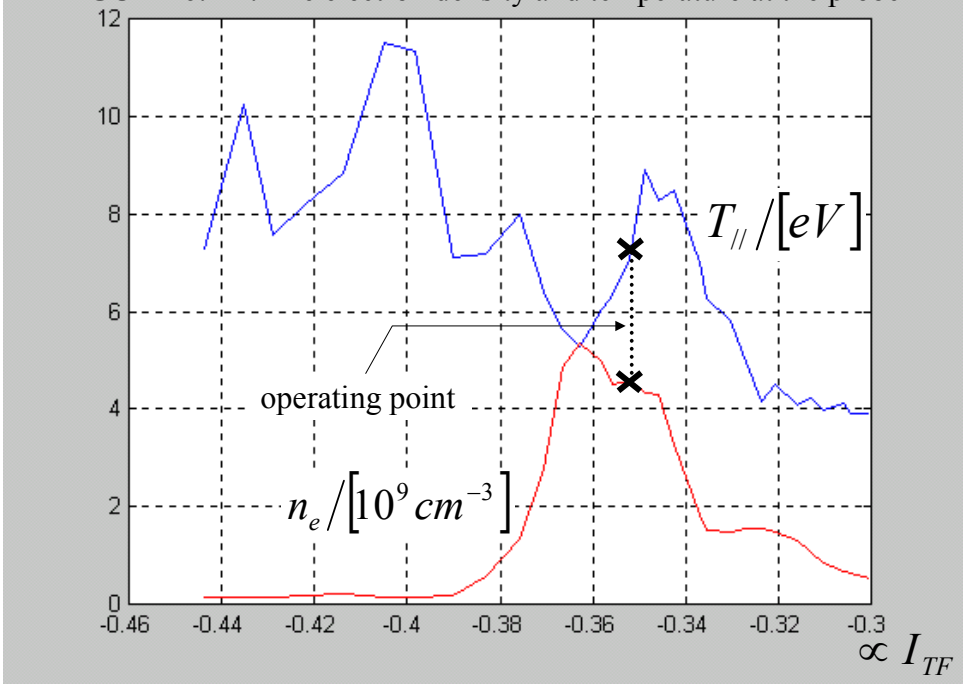

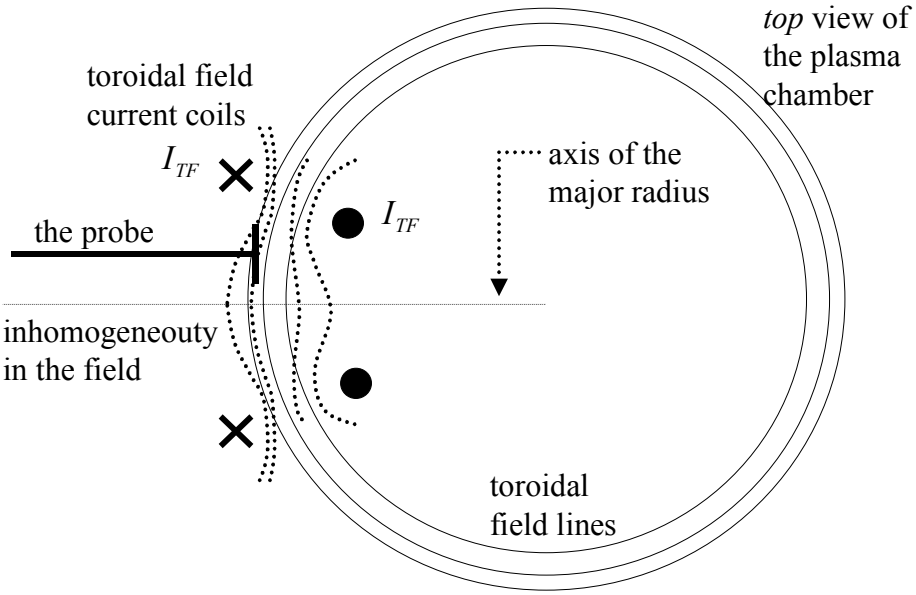

FIGURE 6.2-3: The alignment of the probe with the field lines when inserted via the side port

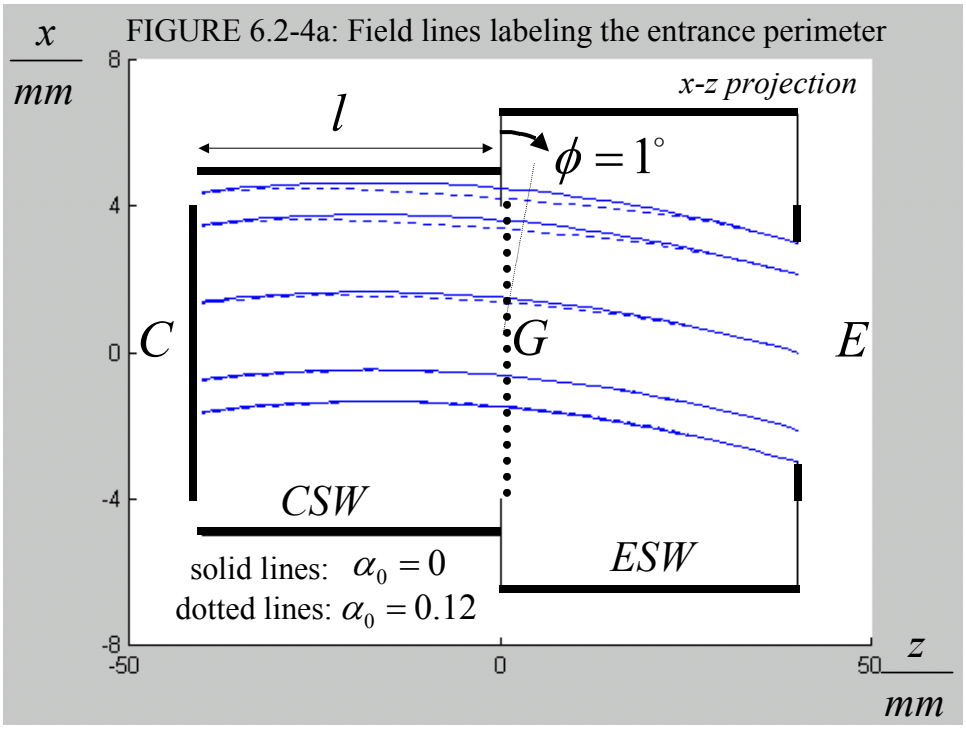

FIGURE 6.2-4a: Field lines labeling the entrance perimeter

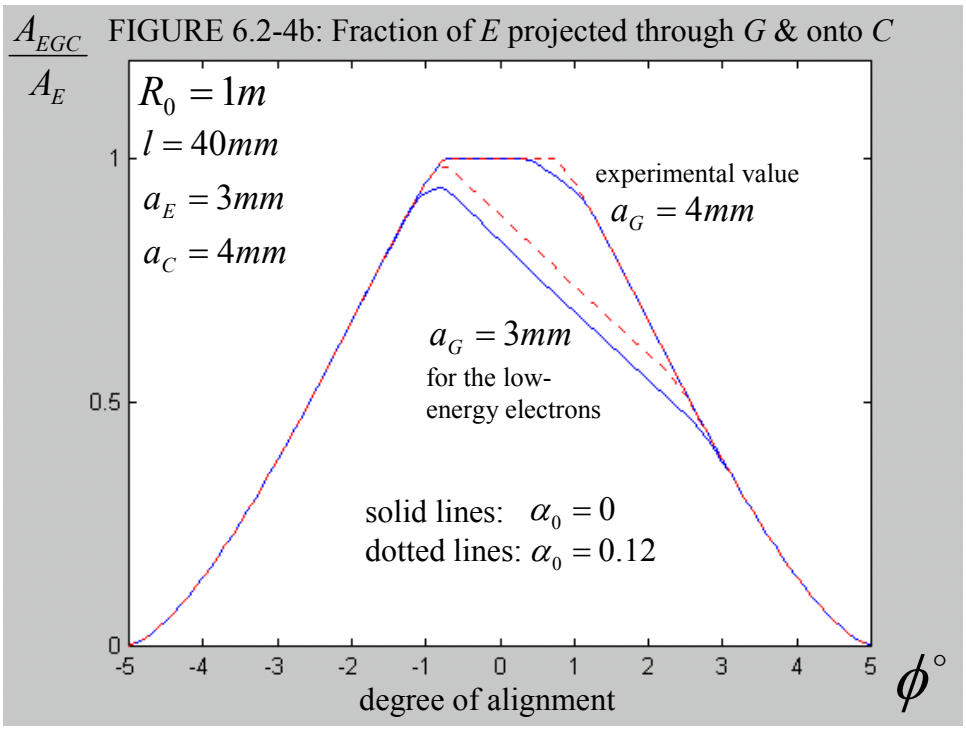

FIGURE 6.2-4b: Fraction of *E* projected through *G* & onto *C*

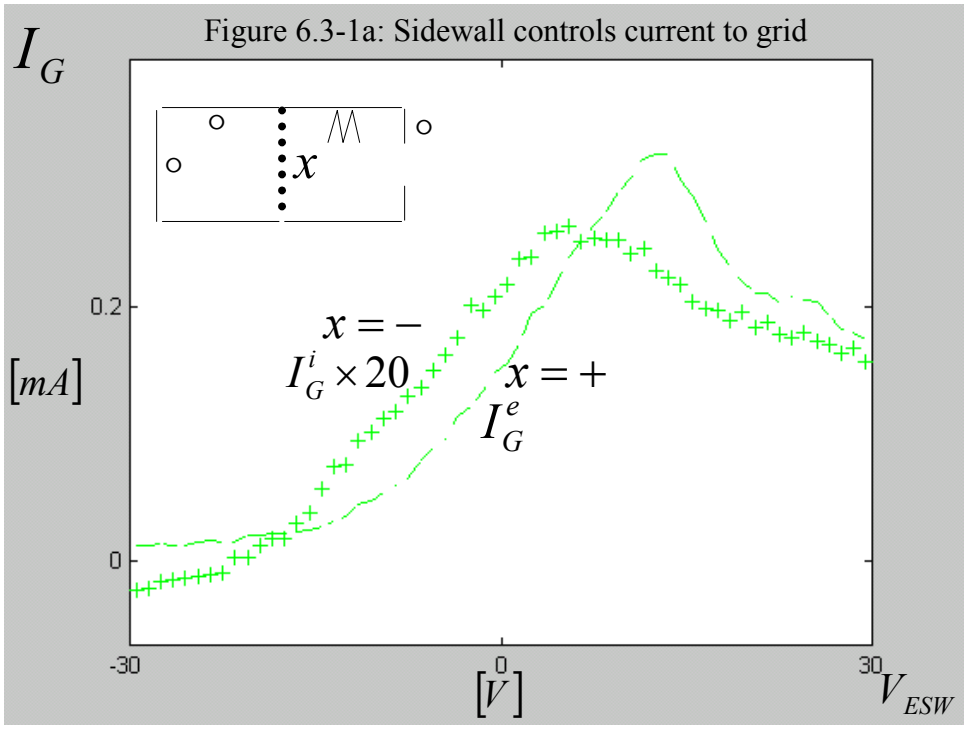
Figure 6.3-1a: Sidewall controls current to grid
I_G
x
0.2
$x = -$
$I_G^i \times 20$
$x = +$
I_G^e
$[mA]$
0
-30
0
30
$[V]$
V_{ESW}

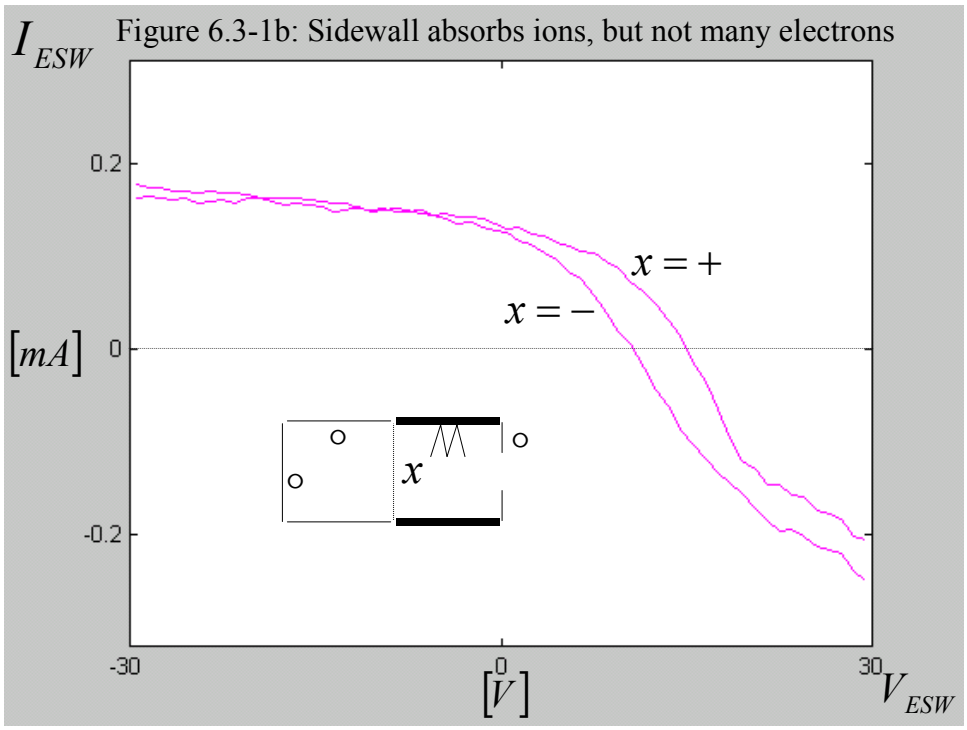
Figure 6.3-1b: Sidewall absorbs ions, but not many electrons
I_{ESW}
0.2
$x = +$
$x = -$
$[mA]$
0
x
-0.2
-30
0
30
$[V]$
V_{ESW}

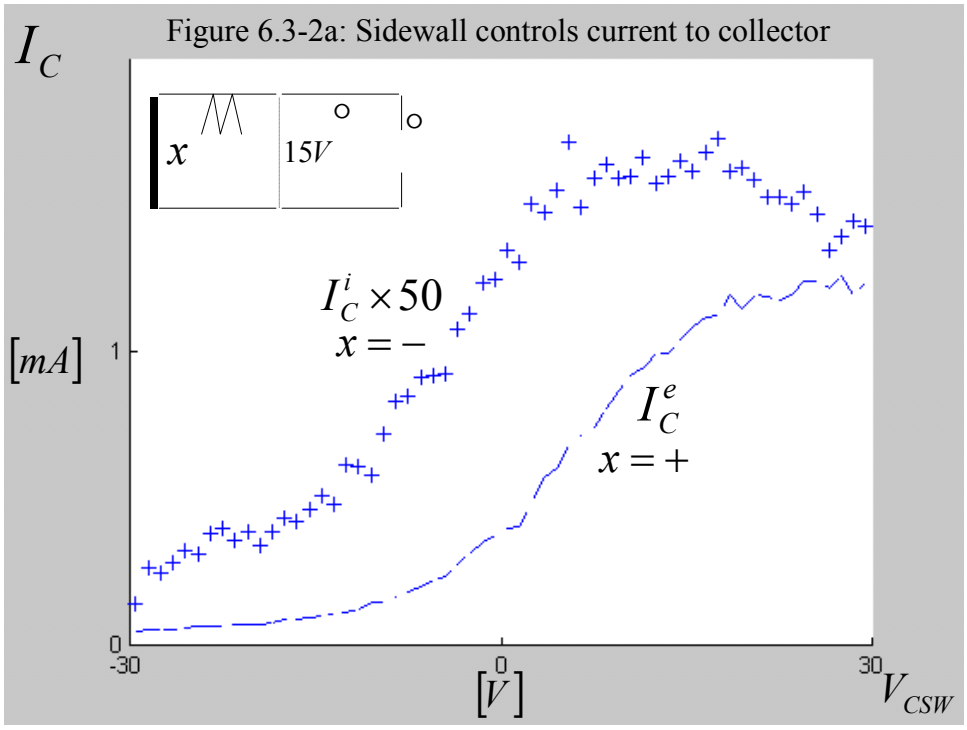

Figure 6.3-2a: Sidewall controls current to collector

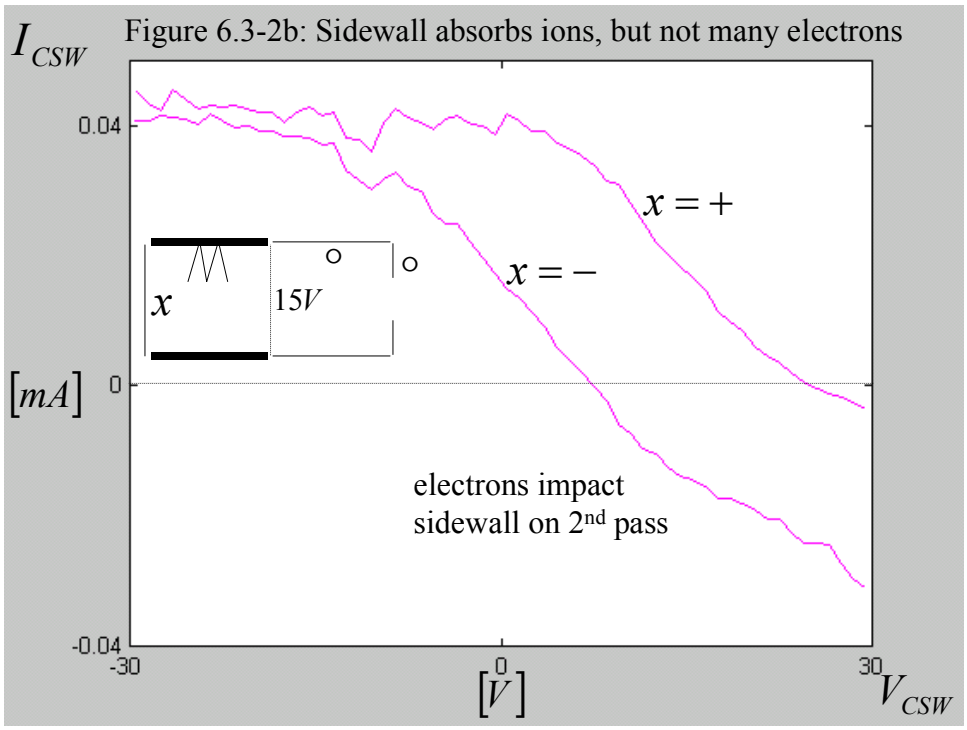

Figure 6.3-2b: Sidewall absorbs ions, but not many electrons

Figure 6.3-3a: The effect of the bias on the entrance electrode

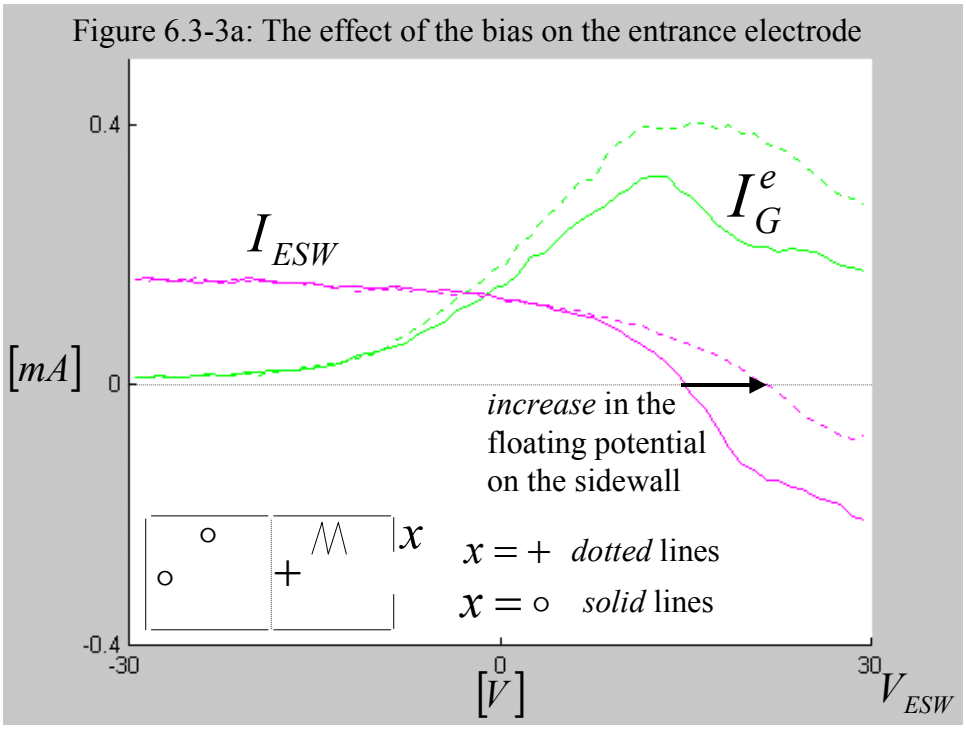

Figure 6.3-3b: The effect of the compression of the magnetic field

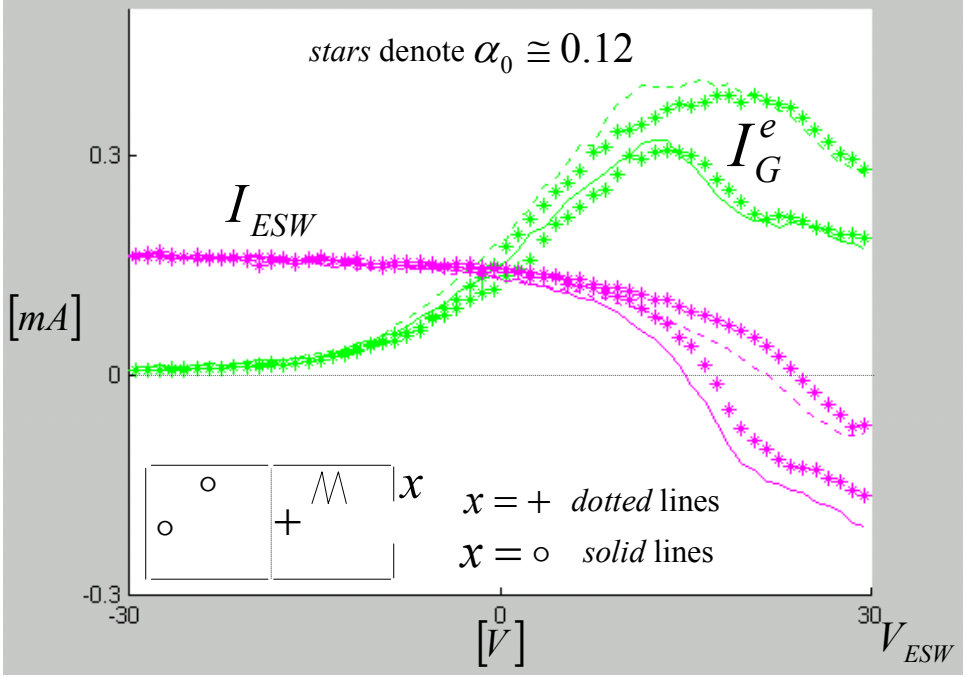

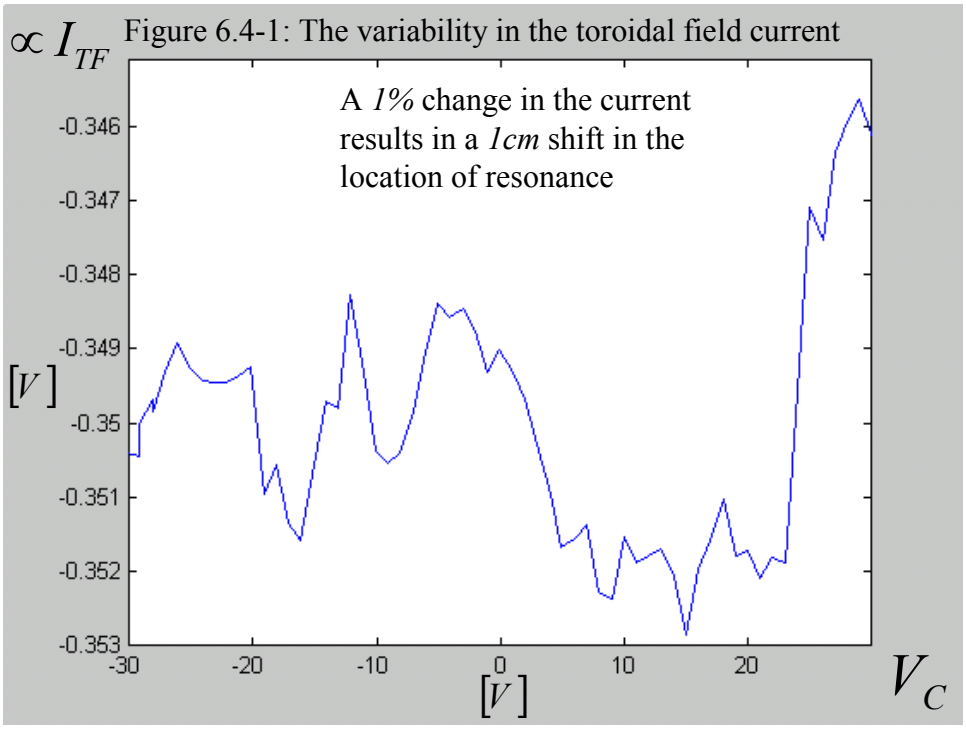
Figure 6.4-1: The variability in the toroidal field current
$\propto I_{TF}$
A *1%* change in the current results in a *1cm* shift in the location of resonance
-0.346
-0.347
-0.348
-0.349
-0.35
-0.351
-0.352
-0.353
$[V]$
-30
-20
-10
0
10
20
$[V]$
V_C

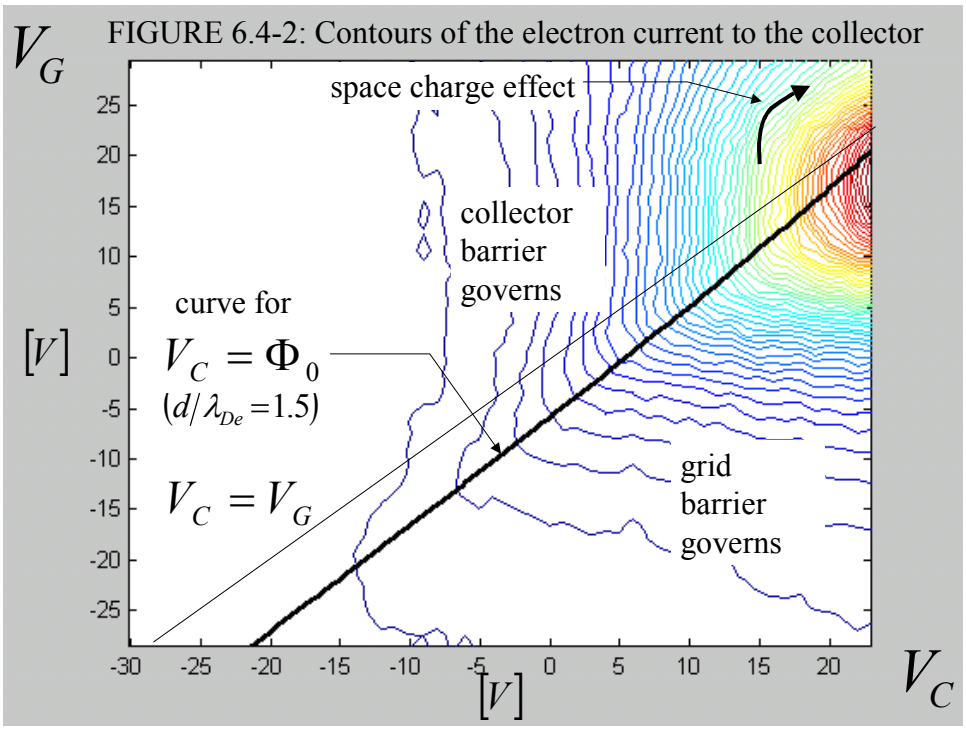
FIGURE 6.4-2: Contours of the electron current to the collector
V_G
space charge effect
collector barrier governs
curve for
$V_C = \Phi_0$
$(d/\lambda_{De} = 1.5)$
$V_C = V_G$
grid barrier governs
25
20
15
10
5
0
-5
-10
-15
-20
-25
$[V]$
-30
-25
-20
-15
-10
-5
0
5
10
15
20
$[V]$
V_C

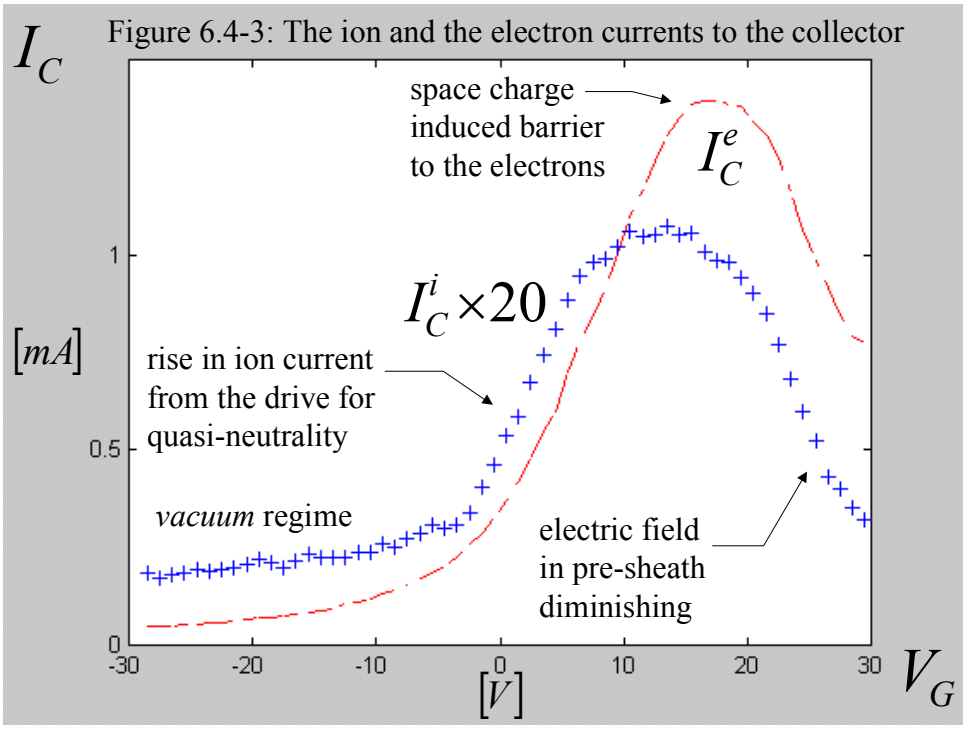

Figure 6.4-3: The ion and the electron currents to the collector

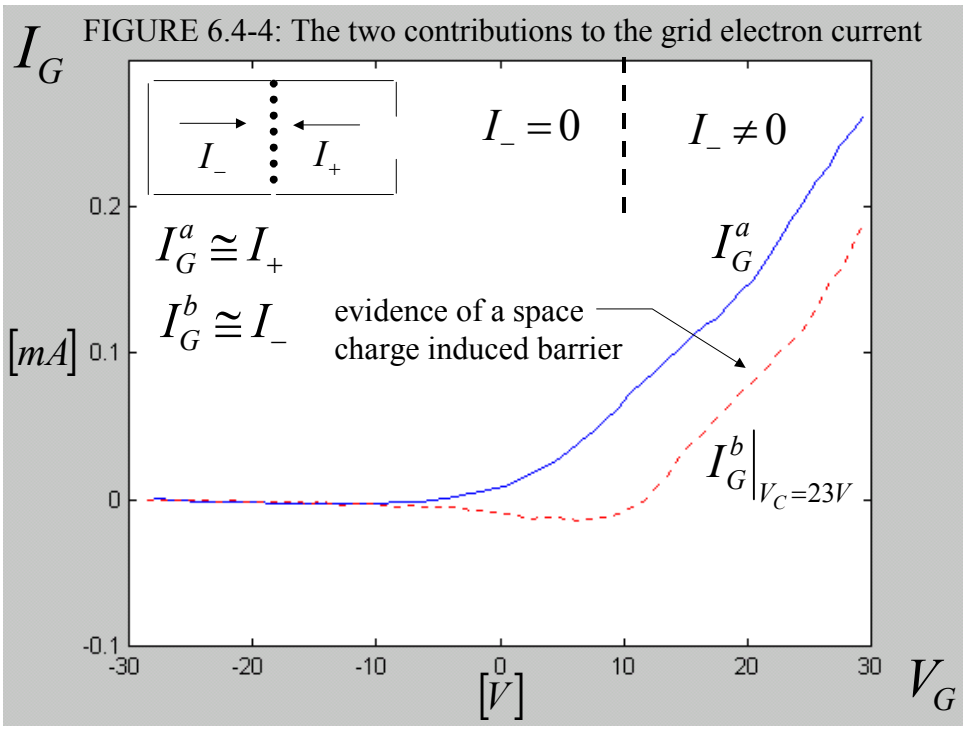

FIGURE 6.4-4: The two contributions to the grid electron current

FIGURE 6.4-5: The evidence of a varying flow area

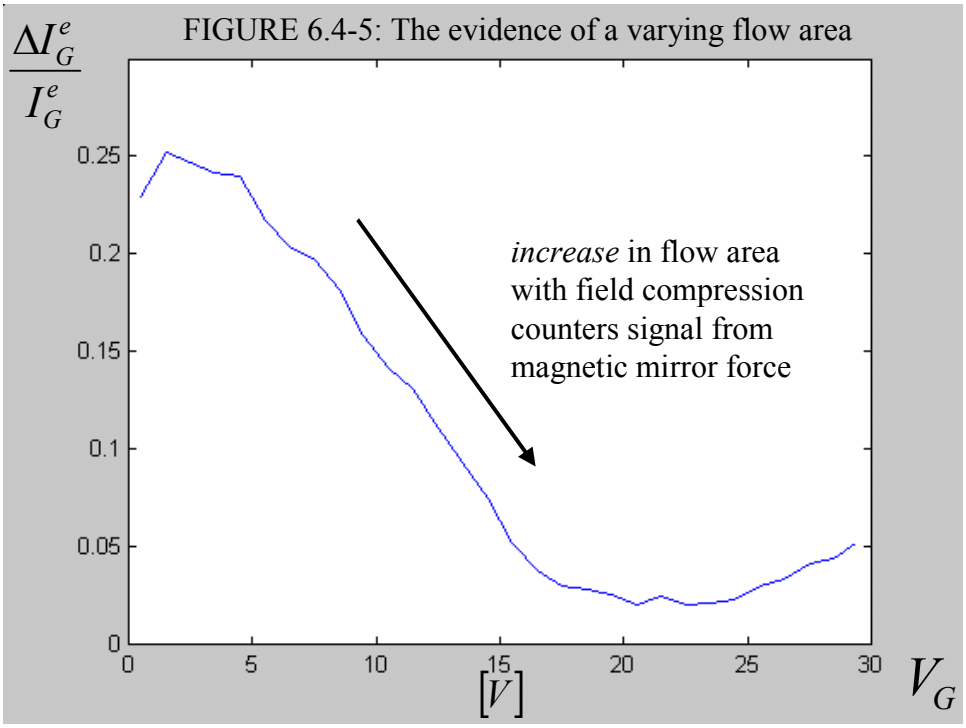

FIGURE 6.4-6: The change in the current with the magnetic field

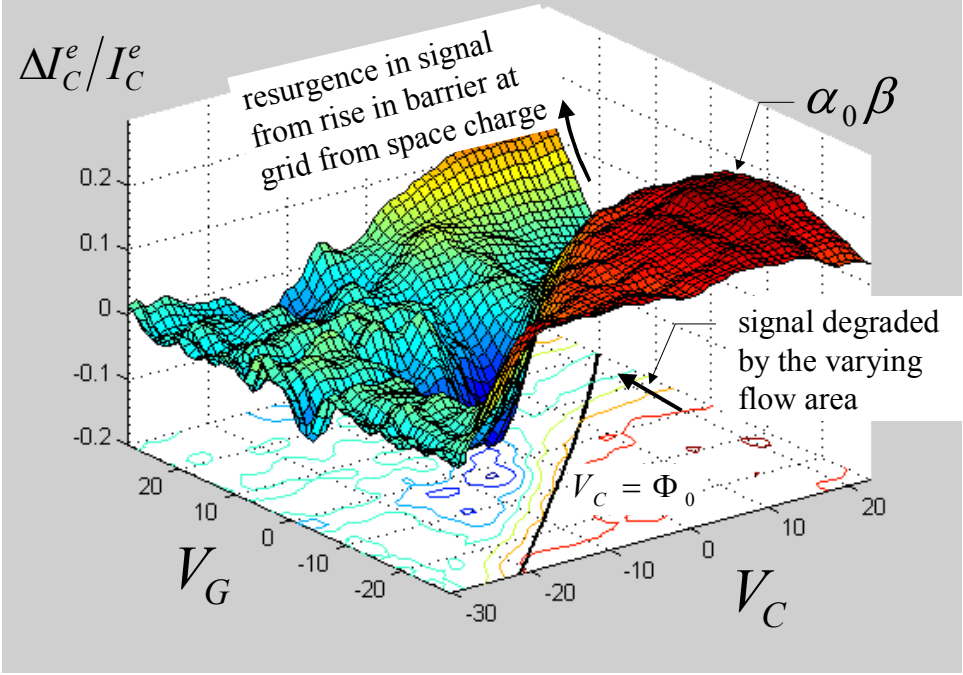

CHAPTER 7

THE FUTURE OF THE GEM PROBE

The GEM probe requires a mesh that is composed of micron size wires with wire spacing d of order *tens* of microns. This requirement can be relaxed somewhat if we choose an opaque mesh with *flat* wires; that is, wires characterized by $t << w \sim d$, where t is the wire depth normal to the mesh plane and w is the wire width in the plane of the mesh. The use of such flat wires would reduce the size of the electric hole as compared to that for a fine mesh with the same wire spacing. Until the time when a mesh with such dimensions becomes readily available, other experiments can be performed with a cavity composed of just a grid and a collector to further substantiate the reliability of the probe.

For example, we could isolate the effects of space charge by using a mesh with $d << \lambda_{De}$ and then examine the $I-V$ characteristics of the electrodes at the grid, at the collector, and at the sidewall for various plasma beam and sidewall radii. This analysis would give us a better understanding of the range for the grid voltage for the proper operation of the probe. On the other hand, we could isolate the effects of the electric hole in the mesh (Δ_0) by reducing the inter-electrode spacing to a value comparable to λ_{De} and then observe the grid and the collector $I-V$ characteristics for various values of d. An inspection of the contours of I_C in the space of the electrode voltages would then give the scaling of Δ_0 with d, which we can then compare with theory. A theoretical analysis of the field perturbation in the regime where $d \sim \lambda_{De}$ will also better our understanding of when the grid fails as an electric barrier.

We can also improve the configuration of the GEM probe by moving the collector to the electromagnet throat and the grid to the probe entrance, as shown in figure **7.0**.

The modification effectively interchanges the role of the grid and the collector: now, the collector provides the hybrid barrier. The reduced aspect ratio of the modified GEM probe increases the tolerance for alignment with the field lines. It also helps to eliminate the signal contamination from a varying flow area because the compression of the field lines now occurs in the vicinity of the opaque electrode.

Lastly, as discussed in appendix **6.1x**, the signal-to-noise level (*SNL*) is roughly proportional to the product $\sqrt{t_{em}} B_{em} / B_{\infty}$, where t_{em} is the duration of the electromagnet pulse. For an inertially cooled electromagnet, the Joule heating limits this product. To remove the bound on the *SNL* then, we should actively cool the electromagnet.

On a different note, the M probe is a simple configuration (a collector placed inside an electromagnet), which is able to make *global* measurements of the anisotropy in the distribution function. This probe has been overlooked in the past.

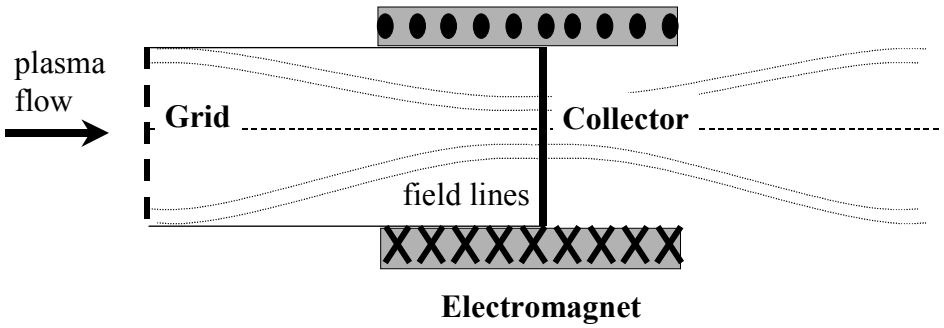

FIGURE 7.0: A schematic drawing of the *modified* GEM probe

APPENDIX TO CHAPTER 2

[2.2x] The pre-sheath potential profile in magnetized plasmas

The electron density in magnetized plasma maintains the exponential variation with the potential as described by equation **2.1-2**. The new feature is that the temperature for the variation is associated with the electrons' thermal motion along the field line, $T_{//}$. The electron's gyro-motion has no bearing on its ability to overcome the collector's electrostatic barrier.

The geometry of the 2-D potential contours in magnetized plasma complicates the variation in the ion density. To approximate the ion density, we assume that the ions diffuse across the magnetic field to enter the flux tube with virtually no energy and that once they enter the tube, they accelerate along the magnetic field line due to the electrostatic potential. These assumptions neglect the component of the electric field normal to the field lines, thereby effectively producing a 1-D geometry.

We assume that the cross-field ion flux Γ_i into the flux tube of perimeter p and incremental length dz behaves as a volume source rate s_i in the incremental volume $A_C dz$ defined by the area of the collector:

$$\Gamma_i p dz \equiv s_i A_C dz . \qquad \{2.2x-1\}$$

The ion density can then be determined by balancing the rate of *production* of *cold* ions inside the flux tube at a location z' with the ion parallel flux along the field line at the location z:

$$dv_{//} v_{//} f_{//}\left(z, U_{//}\right) = dz' s_i\left(z'\right) \qquad \{2.2x-2a\}$$

with z' denoting the birth location with $U'_{//} \cong 0$ so that

$$e\Phi(z') = U_{//} + e\Phi(z), \qquad \{2.2x-2b\}$$

where $v_{//}$ and $U_{//}$ are the ion parallel speed and energy, respectively. The differentials dz' and $dv_{//}$ are related by taking the differential of equation **2.2x-2b** at *constant* z:

$$edz' \frac{d\Phi(z')}{dz'} = dU_{//} \qquad \{2.2x-2c\}$$

with $|dU_{//}| = m_i v_{//} dv_{//}$.

The above relations state that the ions born within the differential volume $A_C dz'$ at the location z' contribute to the flux of ions in a particular energy range *downstream* at a location z. The energy of the ions is determined by the difference in the electrostatic potential at the two locations.

Using equation **2.2x-2c**, equation **2.2x-2a** can be expressed as

$$f_{//} = \frac{n_\infty}{\sqrt{T_{//}/m_i}} \frac{1}{\hat{E}'} \qquad \{2.2x-3\}$$

with

$$\hat{E}' \equiv \hat{E}(\chi') = L \frac{d\chi'}{dz'}, \qquad \{2.2x-3a\}$$

$$L \equiv \frac{n_\infty \sqrt{T_{//}/m_i}}{s_i} \qquad \{2.2x-3b\}$$

equal to the characteristic length of the pre-sheath, and $\chi = e(\Phi_\infty - \Phi)/T_{//}$. The ion parallel speed distribution is *evaluated* at $U_{//} = T_{//}(\chi - \chi')$ and the location z. Its magnitude is proportional to the *ratio* of the electric field to the ion source rate at the location z'.

The ion density is then represented as an integral over $\hat{E}$ in the region preceding the location of interest; that is,

$$n_i(z) = \int_0^{\sqrt{\frac{2e}{m_i}(\Phi_\infty - \Phi)}} dv_{//} f_{//} = n_\infty \int_0^\chi \frac{d\chi'}{\sqrt{2(\chi - \chi')}} \frac{1}{\hat{E}'}. \qquad \{2.2x-4\}$$

For $L >> \lambda_{De}$, the case in practice, the potential profile in the pre-sheath is determined via the imposition of quasi-neutrality. The equation $n_i = n_e \cong n_\infty \exp(-\chi)$ is then Abel-inverted (see ref. viii in chapter **2**) to yield an integral expression for $\hat{E}$. The integral in the expression is approximated by a power series for small χ. The result may be written conveniently as

$$\hat{E} \cong \frac{\pi\sqrt{\chi}}{\sqrt{2}\left[1 - 2\chi\exp(-2\chi/3)\right]} \qquad \{2.2x-5\}$$

by using the approximate relation $1 - 2\chi/3 + \chi^2/5 \cong \exp(-2\chi/3)$ to obtain this compact form. Equation **2.2x-5** can be integrated (again using the power series) to yield an implicit relation for the potential profile:

$$\hat{z} \equiv \int_{-\infty}^z \frac{dz'}{L'} = \int_0^\chi \frac{d\chi'}{\hat{E}'}.$$

The result is described by equation **2.2-1**. Notice that $\hat{z}$ is also proportional to the *accumulated* ion current inside the pre-sheath:

$$en_\infty \sqrt{T_{//}/m_i}\, A_C \hat{z} = e\int_{-\infty}^z dz' A_C s_i(z') = I_i(z). \qquad \{2.2x-6\}$$

APPENDIX TO CHAPTER 4

[4.1x] The general expression for the densities inside the housing

The general expression for the electron density requires that we account for the absorption of the high-energy electrons by the collector. The electrons that are absorbed are those with energies greater than $MAX\left[e\left(\Phi_\infty - \Phi(\zeta)\right)\right]$, where the *capital letters* denote the maximum taken over the *entire* range $-\infty < \zeta \le z_C$. If we artificially separate the contribution of the electrons that are moving towards the collector, n_e^+, from those that have been mirrored, n_e^-, then we can represent the electron density as

$n_e = 2n_e^+ - \left(n_e^+ - n_e^-\right)$, where $2n_e^+ = n_e^0\left(\chi, \chi_{\max}\right)$, $n_e^+ - n_e^- = 0.5 n_e^0\left(\chi, \chi_{MAX}\right)$,

$$n_e^0\left(\chi_a, \chi_b\right) \equiv \frac{n_\infty}{\sqrt{\pi T_{//}}} \int_{T_{//}\chi_b}^{\infty} dU_{//}^{\infty} \frac{\exp\left(-U_{//}^{\infty}/T_{//}\right)}{\sqrt{U_{//}^{\infty} - T_{//}\chi_a}}, \qquad \{4.1x-1\}$$

and $\chi = e\left(\Phi_\infty - \Phi\right)/T_{//}$. The quantities $\chi_{\max}$ and χ_{MAX} are the *local* and the *global* maximums in χ (or equivalently, the *minimums* in Φ) in the range $-\infty < \zeta \le z$ and $-\infty < \zeta \le z_C$, respectively. The function $n_e^0\left(\chi, \chi_{\max}\right)$ would equal the actual electron density if all of the electrons were reflected at some point during their journey to the collector (that is, if χ_{MAX} were infinite). Performing the integration for $n_e^0\left(\chi, \chi_{\max}\right)$ and using the above relations gives $n_e = n_e^0\left(\chi, \chi_{\max}\right) - 0.5 n_e^0\left(\chi, \chi_{MAX}\right)$ with

$n_e^0\left(\chi_a, \chi_b\right) = n_\infty \exp\left(-\chi_a\right) erfc\sqrt{\chi_b - \chi_a}$, or

$$n_e = n_\infty \exp\left(-\chi\right)\left[erfc\sqrt{\chi_{\max} - \chi} - 0.5\, erfc\sqrt{\chi_{MAX} - \chi}\right]. \qquad \{4.1x-2\}$$

The ion density, on the other hand, is determined by using the lower and upper limits, $\max\left[e\left(\Phi-\Phi_E\right),0\right]$ and $e\left(\Phi_\infty-\Phi_E\right)$, in the integral of equation **4.1-1** together with equation **4.0-1** for the ion parallel speed distribution. By letting $\chi'=\chi_E-U_{//}^E/T_{//}=\chi\sin^2(\theta)$, the integral can be expressed as

$$n_i=n_\infty(2/\pi)\int_0^{\arcsin\left(\sqrt{\chi_{\min}/\chi}\right)}d\theta g\left[\chi\sin^2(\theta)\right] \qquad \{4.1x-3\}$$

with $g[x]\equiv 1-2x\exp(-2x/3)$ and with $\chi_{\min}$ equal to the minimum in χ (or *equivalently*, the maximum in Φ) in the range $z_E<\zeta\le z$. The contribution from the ions that have been mirrored inside the housing is automatically incorporated in the expression for the ion density because the ion parallel speed distribution at the entrance is pre-determined by the electron density in the pre-sheath outside the housing via the demand of quasi-neutrality. Therefore, even though the fraction of ions that are mirrored by the electric field inside the housing may vary, the pre-sheath potential profile adjusts accordingly so that the *sum* of the contributions to the ion density from the ions moving towards (n_i^+) and away (n_i^-) from the collector remains equal to that given by the above integral.

At the entrance to the housing, the preceding integral approximates the ion density derived from quasi-neutrality: namely, $n_i\cong n_\infty\exp(-\chi)$. This claim can be verified by setting $\chi_{\min}=\chi$ and by using the approximation $g[x]\cong 1-2x+4x^2/3$ for small x. To obtain a general algebraic expression for the ion density, we splice the exponential form with an approximation to the integral in the limit $\chi_{\min}/\chi<<1$. The resulting *Pate* approximation is $n_i\cong n_i^0(\chi,\chi_{\min})$, which is described by equation **4.1-3**.

Lastly, we note that the ion parallel speed distribution at the entrance was derived with the assumption that $n_e \cong n_\infty \exp(-\chi)$ outside the housing. This approximation does not account for the absorption of the high-energy electrons by the collector. To correct equation **4.1-3** for electron absorption by the collector, we would ideally Abel-invert $n_i = n_e$ (section **2.2x**) with the more involved expression for n_e: equation **4.1x-2**. This calculation, however, is unnecessary because the correction essentially modifies the *magnitude* of the ion density inside the housing, but not its functional dependence with the potential. Consequently, we simply multiply equation **4.1-3** by a factor that *would* render the electron and the ion densities equal in the pre-sheath outside the housing where $\chi_{\max} = \chi$ for the electrons and $\chi_{\min}$ is set equal to χ for the ions:

$$n_i \cong [1 - 0.5\varepsilon_{\min}]\, n_i^0(\chi, \chi_{\min}) = n_\infty \frac{[1 - 0.5\varepsilon_{\min}]\exp(-\chi_{\min})}{\sqrt{1 + (\chi - \chi_{\min})/(k_{\min}^2 \chi_{\min})}} \qquad \{4.1x-4\}$$

with $k_{\min} \equiv k(\chi_{\min}) \equiv (2/\pi)\exp(\chi_{\min}/3)$ and $\varepsilon_{\min} = \varepsilon(\chi_{\min}) = erfc\sqrt{\chi_{MAX} - \chi_{\min}}$.

[4.2x] The *potential energy* for the electrostatic potential

We derive an expression for the indefinite integral $\Pi \equiv -\int^{\chi} d\chi' \delta n$, where $\delta n = (n_e - n_i)/n_\infty$, by separating its ion and electron contributions: $\Pi \equiv \Pi_e - \Pi_i$, where $\Pi_j \equiv \int^{\chi} d\chi'\, n_j'/n_\infty$. Here, to reduce the clutter in the resulting expressions, we only display the result for $\chi_{MAX} \to \infty$: complete reflection of the electrons. The densities for Π_j are then given by $n_e' = n_\infty \exp(-\chi') erfc\sqrt{\chi'_{\max} - \chi'}$ and $n_i' = n_i^0(\chi', \chi'_{\min})$ with n_i^0 defined by equation **4.1-3**.

The quantity of interest is the difference in Π at two locations separated by a region in which the field E *does not vanish*. In this region, there exist unique values for χ' at which the densities inside the integrals for the Π_j's switch functional form: the ion density changes form at $\chi' = \chi_{\min}$, whereas the electron density changes form at $\chi' = \chi_{\max}$.

The integral over the electron density is performed so that χ' approaches χ from above ($\chi' \geq \chi$), whereas the one for the ion density is performed in the opposite direction ($\chi' \leq \chi$). The opposing directions for the two integrals allow us to readily display the results by using the generic variables $\chi_{\min}(\chi)$ and $\chi_{\max}(\chi)$. Remember, these variables are defined so that $\chi_{\min} \leq \chi$ and $\chi_{MAX} \geq \chi_{\max} \geq \chi$.

We separate the integral for Π_e into $\int^{\chi_{\max}} + \int_{\chi_{\max}}^{\chi}$, where $\chi'_{\max} = \chi'$ for the integral $\int^{\chi_{\max}}$ (for which $\chi' > \chi_{\max}$) and $\chi'_{\max} = \chi_{\max}$ for the integral $\int_{\chi_{\max}}^{\chi}$ (for which $\chi' < \chi_{\max}$):

$$\Pi_e = \int^{\chi_{\max}} d\chi' \underbrace{n_e^0(\chi', \chi')/n_\infty}_{\exp(-\chi')} + \int_{\chi_{\max}}^{\chi} d\chi' \, n_e^0(\chi', \chi_{\max})/n_\infty = \Pi_e^0(\chi, \chi_{\max}) \qquad \{4.2x-1a\}$$

where

$$\Pi_e^0(\chi, \chi_{\max}) \equiv \int^{\chi} d\chi' \, n_e^0(\chi', \chi_{\max})/n_\infty = \int^{\chi} d\chi' \exp(-\chi') erfc\sqrt{\chi_{\max} - \chi'}$$

$$= \frac{1}{\sqrt{\pi}} \int^{\chi} d\chi' \int_0^{\infty} \frac{du}{\sqrt{u + \chi_{\max} - \chi'}} \exp[-(u + \chi_{\max})]$$

$$= -\exp(-\chi_{\max}) \frac{1}{\sqrt{\pi}} \int_0^{\infty} du \exp(-u) \int^{\chi_{\max} - \chi} \frac{dx}{\sqrt{u + x}}$$

$$= -\exp(-\chi_{\max}) \left[\frac{2}{\sqrt{\pi}} \sqrt{\chi_{\max} - \chi} + \exp(\chi_{\max} - \chi) erfc\sqrt{\chi_{\max} - \chi} \right]. \qquad \{4.2x-1b\}$$

In regions *A* and *C* of figure **4.1-1a**, where $\chi_{\max} = \chi$, $\Pi_e = -\exp(-\chi)$, while in region *B* of this figure, where $\chi_{\max} = \chi_G$, $\Pi_e = \Pi_e^0(\chi, \chi_G)$.

The integration for Π_i is performed analogously by separating it into $\int^{\chi_{\min}} + \int_{\chi_{\min}}^{\chi}$, where $\chi'_{\min} = \chi'$ for the integral $\int^{\chi_{\min}}$ (for which $\chi' < \chi_{\min}$) and $\chi'_{\min} = \chi_{\min}$ for the integral $\int_{\chi_{\min}}^{\chi}$ (for which $\chi' > \chi_{\min}$):

$$\Pi_i = \int^{\chi_{\min}} d\chi' \underbrace{n_i^0(\chi', \chi')/n_\infty}_{\exp(-\chi')} + \int_{\chi_{\min}}^{\chi} d\chi' \, n_i^0(\chi', \chi_{\min})/n_\infty$$

$$= -\exp(-\chi_{\min}) + \Delta\Pi_i^0(\chi, \chi_{\min}), \qquad \{4.2x-2a\}$$

where $\Delta\Pi_i^0(\chi, \chi_{\min}) = \Pi_i^0(\chi, \chi_{\min}) - \Pi_i^0(\chi_{\min}, \chi_{\min})$ and

$$\Pi_i^0(\chi, \chi_{\min}) \equiv \int^{\chi} d\chi' \, n_i^0(\chi', \chi_{\min})/n_\infty$$

$$= 2\exp(-\chi_{\min}) k_{\min}^2 \chi_{\min} \sqrt{1 + (\chi - \chi_{\min})/(k_{\min}^2 \chi_{\min})}$$

$$= \frac{2(\chi - \chi_{\min})}{1 + \sqrt{1 + (\chi - \chi_{\min})/(k_{\min}^2 \chi_{\min})}} \exp(-\chi_{\min}) + \Pi_i^0(\chi_{\min}, \chi_{\min}). \qquad \{4.2x-2b\}$$

In region *B* of figure **4.1-2a**, where $\chi_{\min} = \chi$, $\Pi_i = -\exp(-\chi)$, while in regions *A* and *C* of this figure, where $\chi_{\min}$ is either χ_E or χ^*, $\Pi_i = \Delta\Pi_i^0(\chi, \chi_{\min}) - \exp(-\chi_{\min})$.

[4.2x.1] The *potential energy* at locations of interest

The description of the two characteristic plateau solutions ($E_- = 0$ and $E_- > 0$) requires the evaluation of

$$\Pi = \Pi_e - \Pi_i$$

at the following locations:

1. z_E, where $\chi_{\min} = \chi_{\max} = \chi = \chi_E$ gives

$$\Pi_E = 0 \qquad \{4.2x-3a\}$$

2. z^* (for the solution with $\mathrm{E}_- > 0$), where $\chi_{\min} = \chi = \chi^*$ and $\chi_{\max} = \chi_G$ gives

$$\Pi^* = \exp(-\chi^*) erf\sqrt{\chi_G - \chi^*} - \frac{2}{\sqrt{\pi}}\exp(-\chi_G)\sqrt{\chi_G - \chi^*} \qquad \{4.2x-3b\}$$

3. z_G, where $\chi_{\min} = \chi_E$ (which for $\mathrm{E}_- = 0$ equals χ_G) and $\chi_{\max} = \chi = \chi_G$ gives

$$\Pi_G = \breve{\Pi}(\chi_E, \chi_G) \qquad \{4.2x-3c\}$$

4. z^{**}, where $\chi_{\max} = \chi = \chi^{**}$ gives

$$\Pi^{**} = \breve{\Pi}(\chi_{\min}, \chi^{**}) \qquad \{4.2x-3d\}$$

with $\chi_{\min} = \chi_G$ if $\mathrm{E}_- = 0$ and $\chi_{\min} = \chi^*$ if $\mathrm{E}_- > 0$, and

$$\breve{\Pi}(\chi_{\min}, \chi) = \exp(-\chi_{\min})\left\{1 - \frac{2(\chi - \chi_{\min})}{1 + \sqrt{1 + \dfrac{\chi - \chi_{\min}}{k_{\min}^2 \chi_{\min}}}}\right\} - \exp(-\chi) \qquad \{4.2x-3e\}$$

When manipulating the expression for Π^{**}, it is advantageous to use *quasi-neutrality* at $\chi = \chi^{**}$, which can be expressed conveniently as

$$\sqrt{1 + \frac{\chi^{**} - \chi_{\min}}{k_{\min}^2 \chi_{\min}}} = \exp(\chi^{**} - \chi_{\min}). \qquad \{4.2x-4\}$$

APPENDIX TO CHAPTER 5

[5.1x] Constructing the vacuum potential profile about a mesh

We build the potential by adding the contribution from each wire. We begin with a set of wires spaced a distance d apart in the x-direction and elongated in the y-direction. In the anticipation of adding another set aligned perpendicular to this one to form the mesh, we allow the charge per unit length to vary *periodically* along the wire. The potential for *a single array of wires* located at $z = 0$ can then be expressed as

$$\Phi_{1D}(x,y,z) = \frac{1}{4\pi\varepsilon_0}\sum_{n=-N}^{N}\int_{-L}^{L} d\lambda \frac{q(\lambda)}{\sqrt{(x-nd)^2+(y-\lambda)^2+z^2}}, \qquad \{5.1x-1\}$$

where we take the limit of an infinite set of wires, $N \to \infty$, possessing an infinite span, $L \to \infty$. The above expression is valid in the *entire* $x-y$ plane in the region $|z| \geq t/2$, where the wires do not occupy space.

The periodic structure of the array enables us to express the potential as a sum over the Fourier components $\Phi_{k,l}$:

$$\Phi_{1D} = \sum_{k,l} \exp\left(2\pi i \frac{kx+ly}{d}\right)\Phi_{k,l}^{1D}(|z|) \qquad \{5.1x-2a\}$$

with

$$\Phi_{k,l}^{1D} \equiv \frac{1}{d^2}\int_0^d\int_0^d dxdy \exp\left(-2\pi i \frac{kx+ly}{d}\right)\Phi_{1D} \qquad \{5.1x-2b\}$$

and Φ_{1D} given by equation **5.1x-1**. The sum over the Fourier coefficients will converge exponentially. More importantly, the Fourier decomposition of the potential and of the

charge per unit length, $q = \sum \exp(2\pi i\, l'\lambda'/d) q_{l'}$, will transform the boundary condition at the wire surface (Φ = constant) into an algebraic equation for the q_l's.

Letting $\lambda = \lambda' - y$ and using the Fourier decomposition of q in equation **5.1x-1** in conjunction with the relations

$$\frac{1}{d}\int_0^d dy \exp\left(-2\pi i(l'-l)\frac{y}{d}\right) = \delta_{l',l}$$

and

$$\sum_n \int_{-nd}^{(-n+1)d} dx = \int_{-\infty}^{\infty} dx$$

when manipulating equation **5.1x-2b**, we find

$$\Phi_{k,l}^{1D} = \frac{q_l}{4\pi\varepsilon_0}\frac{1}{d}\int_{-\infty}^{\infty} d\lambda \int_{-\infty}^{\infty} dx \frac{1}{\sqrt{x^2+\lambda^2+z^2}} \exp\left(2\pi i \frac{-kx+l\lambda}{d}\right).$$

We perform this integral by first realizing that $\Phi_{k,l}/q_l$ is a function of $|k,l| \equiv \sqrt{k^2+l^2}$. This claim is demonstrated via the transformation $-kx + l\lambda = |k,l| r\cos(\theta)$, where $r \equiv \sqrt{x^2+\lambda^2}$ and θ is the angle between the two vectors $(-k,l)$ and (x,λ). The dependence on only k^2+l^2 means that $\hat{\Phi}_{k,l} \equiv 4\pi\varepsilon_0 \Phi_{k,l}^{1D}/q_l$ can be expressed as

$$\hat{\Phi}_{k,l} = \hat{\Phi}_{0,|k,l|} \equiv \hat{\Phi}_{|k,l|}, \qquad \{5.1x-3a\}$$

which reduces our task to the determination of $\hat{\Phi}_{|l|} = \hat{\Phi}_{0,|l|}$. To this end, we express $\hat{\Phi}_{|l|}$ as $\int_{\infty}^{|z|} d|z|\, d\hat{\Phi}_{|l|}/d|z|$ and solve for $d\hat{\Phi}_{|l|}/d|z|$ instead because the integral of this function with respect to λ produces the expression

$$\frac{d\hat{\Phi}_{|l|}}{d|z|} = -2|z|\frac{1}{d}\int_{-\infty}^{\infty} dx \frac{\exp(2\pi i|l|x/d)}{x^2+z^2},$$

which can be integrated by extending the path of integration to the complex domain to obtain

$$\frac{d\hat{\Phi}_{|l|}}{d|z|} = -\frac{2\pi}{d}\exp\left(-2\pi|lz|/d\right).$$

The integral $\int_{\infty}^{|z|} d|z|\, d\hat{\Phi}_{|l|}/d|z|$ then gives $\hat{\Phi}_{|l|} = \exp\left(-2\pi|lz|/d\right)/|l|$, which by using equation **5.1x-3a** yields

$$\hat{\Phi}_{k,l} = \hat{\Phi}_{|k,l|} = \frac{\exp\left(-2\pi|k,l||z|/d\right)}{|k,l|}. \qquad \{5.1x-3b\}$$

Now, the potential of a 2-D array of wires is given by $\Phi_{1D}(x,y,z)+\Phi_{1D}(y,x,z)$. This relation along with equation **5.1x-2a** enables us to extend our results to model the potential of a mesh of wires by simply adding $\Phi_{l,k}^{1D}$ to $\Phi_{k,l}^{1D}$ to find

$$\Phi_{k,l} = \frac{q_k + q_l}{4\pi\varepsilon_0}\hat{\Phi}_{|k,l|}. \qquad \{5.1x-4\}$$

[5.1x.1] The Fourier coefficients of the charge per unit length

The q_l's are determined by the boundary condition that the potential at the wire surface remain constant along the wire: $\Phi(x,0,r_w) = \text{constant}$, where we have defined the wire surface to be at the location $|z| = r_w = (w+t)/4$ (see subsection **5.1-3**). Setting $0 = \partial\Phi/\partial x$ and using the definition $\hat{\Phi}_{|k,l|}^{w} \equiv \hat{\Phi}_{|k,l|}(r_w)$, we find

$$0 = \sum_{k,l}\exp(2\pi ikx)k(q_k + q_l)\hat{\Phi}_{|k,l|}^{w},$$

which requires that $0 = k\sum_{l}(q_k + q_l)\hat{\Phi}_{|k,l|}^{w}$ for each k. This criterion then gives

$$q_k \sum_l \hat{\Phi}^w_{|k,l|} + (q_k + q_{-k})\hat{\Phi}^w_{|k,k|} + q_0 \hat{\Phi}^w_{|k|} + \sum_{l\geq 1, l\neq|k|} (q_l + q_{-l})\hat{\Phi}^w_{|k,l|} = 0 \qquad \{5.1x-5\}$$

for $k \neq 0$. The field $\overline{E}$ determines the average charge per unit length q_0.

Realizing that q_{-l} is equal to the complex conjugate q_l^*, we find that the q_k's are real. Using this property then gives an equation for $\hat{q}_k \equiv q_k / q_0$, which we solve iteratively:

$$\hat{q}_k^{(n+1)} = \hat{q}_k^{(0)} \left[1 + 2 \sum_{l\geq 1, l\neq|k|} \hat{q}_l^{(n)} \frac{\hat{\Phi}^w_{|k,l|}}{\hat{\Phi}^w_{|k|}} \right] \qquad \{5.1x-5a\}$$

with

$$\hat{q}_k^{(0)} = -\left[1 + 2\frac{\hat{\Phi}^w_{|k,k|}}{\hat{\Phi}^w_{|k|}} + 2\sum_{l\geq 1} \frac{\hat{\Phi}^w_{|k,l|}}{\hat{\Phi}^w_{|k|}} \right]^{-1}, \qquad \{5.1x-5b\}$$

where $\hat{q}_k^{(n)}$ denotes the n'th iteration. The sum over l in equation **5.1x-5b** must be carried out to a value $L >> k$ to render the remaining contribution negligible. We have used $L = 5k$ and $K = 20$ Fourier coefficients $\hat{q}_k$ (iterated K times) to determine $\widetilde{\Phi}$.

We can estimate the contribution from the $\hat{q}_{|k|\neq 0}$'s by examining the magnitude of $\hat{q}_1^{(0)}$. If we approximate $\sqrt{1+l^2}$ with $|l|$ and $\hat{\Phi}_1 = \exp(-2\pi r_w / d)$ with *one* for the sum in equation **5.1x-5b**, then we obtain

$$\hat{q}_1^{(0)} \cong -\frac{1}{1 + \sqrt{2} + 2\sum_{l\geq 1} l^{-1} \exp(-2\pi l\, r_w / d)}.$$

The sum over l can then be expressed as

$$\int_{2\pi r_w/d}^{\infty} dz \sum_{l\geq 1} \exp(-lz) = \int_{2\pi r_w/d}^{\infty} dz \frac{\exp(-z)}{1-\exp(-z)} \cong \ln\left(\frac{d}{2\pi r_w}\right),$$

which gives

$$\hat{q}_1^{(0)} \cong -\frac{1}{1+\sqrt{2}+2\ln\left(d/2\pi r_w\right)} \cong \frac{1}{2\ln\left(d/2\pi r_w\right)}. \qquad \{5.1x-6\}$$

[5.1x.2] The *exact* solution for a 1-D array of wires with no *depth*

For the specific case of a profile that is symmetric about the grid plane, we can easily transform the 2-D region of a 1-D array of wires via a conformal map to a region with a simple boundary condition if we model the wires' cross-section as being infinitesimally thin, as shown in figure **5.1x-1**. The new space is a rectangle with *no* electric field emanating from two of its sides. The map preserves the Laplacian operator in Poisson's equation to within a factor equal to the square of the Jacobian of the transformation, which is irrelevant for the solution to Laplace's equation.

The mapping is a two-step process. Each step is a type of a Schwarts-Christoffel Transformation[a], which consists of "straightening" the corners ($v_0 = d/2$) of a rectangular region to form a straight line as shown in figure **5.1x-2**. The first step straightens the segment describing the line through the midpoint between two wires, $u_0 = 1$, and the second step (an inverse transform) bends the straight line at the ends of the wire, $u_0 = \sin\left(\pi w/2d\right)$.

The solution in the new space is simply $\Phi = V_G - \overline{E}Z$. The burden of determining the solution in the geometry of interest is then transferred to the map

$$\sin\left(\pi\frac{x+i|z|}{d}\right) = \sin\left(\frac{\pi}{2}\frac{w}{d}\right)\sin\left(\pi\frac{X+iZ}{d}\right). \qquad \{5.1x-7\}$$

[a] Mathematical Methods of Physics, J. Mathews & R. L. Walker (1964), p. 132

The manipulation of the above equation gives

$$Z/d = \frac{V_G - \Phi}{\overline{E}d} = \frac{1}{\pi}\sinh^{-1}\left[\frac{b+\sqrt{b^2+4ac}}{2a}\right]^{1/2} \qquad \{5.1x-8\}$$

with $a = \sin^2(\pi w/2d)$, $a+b = \sinh^2(\pi z/d)+\sin^2(\pi x/d)$, and $c = \cos^2(\pi x/d)\sinh^2(\pi z/d)$. The magnitude of the perturbation is then obtained via the operation

$$\widetilde{\Phi} = \left(\Phi + \overline{E}|z|\right) - \left(\Phi + \overline{E}|z|\right)_{|z|\to\infty},$$

which yields

$$\widetilde{\Phi}_w = \widetilde{\Phi}(x \le w/2, 0) = -\frac{\overline{E}d}{\pi}\ln\sqrt{a} \cong \frac{\overline{E}d}{\pi}\ln\frac{2d}{\pi w}. \qquad \{5.1x-9\}$$

[5.3x] The exchange of kinetic energy with the perturbation

To calculate $\widetilde{\delta}_0$ and $\widetilde{\delta}_+$, we use the definitions,

$$\left(\widetilde{U}_{//}^-, \widetilde{U}_{//}^+\right) \equiv -e\left(\int_{-\infty}^0 dz'\widetilde{E}_z, \int_0^\infty dz'\widetilde{E}_z\right),$$

which give $\widetilde{\delta}_0 = -\widetilde{U}_{//}^-$ and $\widetilde{\delta}_+ = -\left(\widetilde{U}_{//}^- + \widetilde{U}_{//}^+\right)$. The quantity $\widetilde{U}_{//}^s$ describes the *gain* of parallel energy from the field of the perturbation for an electron traveling *to* ($s \to -$) the grid-plane if $s < 0$ and for an electron traveling *away* ($s \to +$) from the grid-plane if $s > 0$. We evaluate $\widetilde{U}_{//}^s$ by inserting the approximation to the path of the unperturbed gyro-orbit, equation **5.3-3**, into the expression for the electric field, equation **5.3-2a**. We then use the relation

$$-k\sin\phi + l\cos\phi = |k,l|\cos\phi'$$

with[b] $\phi' = \phi + \pi/2 - \psi_{k,l}$, in the integrals for $\widetilde{U}^s_{//}$ to find the representation

$$\widetilde{U}^s_{//} = \sum_{k,l\neq 0,0} \exp\left(2\pi i\, \vec{k}\cdot\vec{r}_0/d\right)\widetilde{U}^s_{k,l} \qquad \{5.3x-1\}$$

with

$$\vec{k}\cdot\vec{r}_0 = (k,l)\cdot(x_0,y_0) = (k,l)\cdot\left(x_g + \rho_\perp\cos\phi, y_g + \rho_\perp\sin\phi\right)$$

and

$$\widetilde{U}^s_{k,l} = -se\Phi^w_{k,l}\left[1 - isp\cos\phi'\right]^{-1}, \qquad \{5.3x-1a\}$$

where $p = v_\perp/v_{//}$.

The average of the quantities $\widetilde{\delta}_0^2$ and $\widetilde{\delta}_+^2$ over the paths can then be written as

$$\left\langle \widetilde{\delta}_0^2, \widetilde{\delta}_+^2 \right\rangle = \sum_{k,l\neq 0,0} \oint \frac{d\phi}{2\pi}\left(\left|\widetilde{U}^-_{k,l}\right|^2, \left|\widetilde{U}^-_{k,l} + \widetilde{U}^+_{k,l}\right|^2\right) \qquad \{5.3x-2\}$$

with

$$\left(\left|\widetilde{U}^-_{k,l}\right|, \left|\widetilde{U}^-_{k,l} + \widetilde{U}^+_{k,l}\right|\right) = \left|e\Phi^w_{k,l}\right|\left(\frac{1}{\sqrt{1+p^2\cos^2\phi'}}, \frac{2\left|p\cos\phi'\right|}{1+p^2\cos^2\phi'}\right).$$

We gyro-average the quantity $\left|\widetilde{U}^-_{k,l}\right|^2$ by first letting $\zeta = \exp(i\phi')$ and then by integrating along the unit circle in the complex ζ-domain:

$$\oint \frac{d\phi'}{2\pi}\frac{1}{1+p^2\cos^2\phi'} = \frac{2}{p^2}\oint_{|\zeta|=1}\frac{d\zeta}{2\pi i}\frac{\zeta}{\left(\zeta^2-\zeta_+^2\right)\left(\zeta^2-\zeta_-^2\right)}$$

with $\zeta_\pm^2 = -\left(1+2p^{-2}\right) \pm \sqrt{\left(1+2p^{-2}\right)^2 - 1}$. Using Cauchy's theorem, we find that the contributions from the poles inside the unit circle, $\pm\zeta_+$, give $\left(1+p^2\right)^{-1/2}$, which in turn yields

[b] $\psi_{k,l} = \arctan(l/k) + \pi Step[-k]$

$$\left\langle \widetilde{\delta}_0^2 \right\rangle = \delta_0^2 \left(1 + p^2\right)^{-1/2}, \qquad \{5.3x-2a\}$$

where $\delta_0^2 = \sum_{k,l\neq 0,0} \left(e\Phi_{k,l}^w\right)^2$ is the variance in the electrostatic energy at the grid plane. The gyro-averaged value of $\left|\widetilde{U}_{k,l}^- + \widetilde{U}_{k,l}^+\right|^2$ is then found by realizing that it equals $-4p^2\left(d/dp^2\right)\left|\widetilde{U}_{k,l}^-\right|^2$, which gives

$$\left\langle \widetilde{\delta}_+^2 \right\rangle \cong 2\delta_0^2 \left(1 + p^2\right)^{-3/2} p^2. \qquad \{5.3x-2b\}$$

To determine δ_0^2, we first notice that $\Phi_{k,l}^w$ is even in the integers k and l and is invariant under the transformation $(k,l) \to (l,k)$. These properties then allow us alter the sum for δ_0^2 to $4\left[\sum_{k\geq 1,0} + \sum_{k\geq 1,l\geq 1}\right]$. We neglect the sum with k and l both greater than *zero* because its contribution is relatively small by the factor $\hat{q}_k \hat{q}_l$. What remains can be expressed as

$$\delta_0^2 \cong 4\sum_{k\geq 1}\left(e\Phi_{k,0}^w\right)^2 \cong 4\left(\frac{e\overline{E}d}{4\pi}\right)^2 \sum_{k\geq 1}\left(1 + 2\hat{q}_k\right)\frac{\exp\left(-4\pi k\, r_w/d\right)}{k^2}.$$

As a result of the fast drop of $1/k^2$, we neglect the exponential term as well as the terms with $\hat{q}_{k>1}$ to find

$$\delta_0^2 \cong \left(\frac{e\overline{E}d}{2\pi}\right)^2\left[\frac{\pi^2}{6} + 2\hat{q}_1\right] \cong \left(\frac{e\overline{E}d}{2\pi}\right)^2\left[\frac{\pi^2}{6} - \frac{1}{\ln d/2\pi r_w}\right], \qquad \{5.3x-3\}$$

where we have used the sum identity[c] $\sum_{k\geq 1} k^{-2} = \pi^2/6$ and equation **5.1x-6** for $\hat{q}_1$.

[c] M.R. Spiegel, Schaum's Outline Series Mathematical Handbook, 1968

APPENDIX TO CHAPTER 6

[6.1x] The Joule-heating of the electromagnet

We assume conservatively that the only means for heat removal is via conduction along the length of the wire. The governing equation for the wire temperature then just includes inertial cooling, resistive heating, and conductive heat loss:

$$\rho c_p \partial_t T = \eta J_w^2 + \kappa \partial_z^2 T ,$$

with $\mathrm{T} = (T - 50)/250^\circ K$, J_w equal to the current density, $\rho c_p \cong 3.5 \cdot 10^6 \, Joule/m^3{}^\circ K$, $\kappa \cong 400 \, watt/m^\circ K$, and $\eta \cong 2\mathrm{T}\mu\Omega \cdot cm$ (obtained from the CRC handbook[d]). We forego modeling the temperature's spatial dependence because the resistive heating dominates conductive heat loss over much of the length. Instead, we determine the "global" power balance by integrating the equation over *half* of the wire length l_w, $A\int dz$, and by approximating the heat loss at the boundary as $\kappa(T - 300)/l_\kappa$. Here, l_κ is equal to the characteristic length near the boundary where the heat loss from conduction, $250\kappa\mathrm{T}/l_\kappa$, competes with the resistive heating, $\eta J_w^2 l_\kappa$. The balance gives $l_\kappa \sim 1/J_w$ with l_κ in *units* of $1m$ and J_w in *units* of $1A/mm^2$.

The power balance then becomes $d_\tau \mathrm{T} = P\mathrm{T} - (\mathrm{T} - 1)$ with $P \sim l_w J$, $\tau = t/t_D$, and the characteristic time for diffusion $t_D \equiv (\rho c_p/\kappa) l_k l_w \sim 2.5 l_k l_w \, hrs$ with l_w also in units of $1m$. Using $\Delta\mathrm{T} \equiv \mathrm{T} - 1$, the wire temperature for a cycle during which the current is switched on (τ_h) and off (τ_c) can be expressed as $\Delta\mathrm{T}_{n+1} = a\Delta\mathrm{T}_n + b$, where the subscript

[d] CRC handbook of chemistry and physics, 73rd edition

n indicates the number of such cycles, $a \equiv \exp\left[\left(P-1-\tau_c/\tau_h\right)\tau_h\right]$, and $b \equiv \left(P/P-1\right)\exp\left(-\tau_c\right)\left\{\exp\left[\left(P-1\right)\tau_h\right]-1\right\}$. With $\Delta \mathrm{T}_0 \equiv 0$, the temperature after N cycles becomes $\Delta \mathrm{T}_N = b\left(1-a^N\right)/\left(1-a\right)$.

The period for this cycle in our experiment was approximately $t_h + t_c \approx 30\,\mathrm{sec}$, which is much less than t_D. Hence, $a \cong 1+\left(P-1-\tau_c/\tau_h\right)\tau_h$ and $b \cong P\tau_h$. If we assume conservatively that the cooling cycle is not able to stabilize the wire's temperature, $P > 1+\tau_c/\tau_h$, then

$$\Delta \mathrm{T}_N = \mathrm{T}_N - 1 \cong PN\tau_h .$$

To prevent melting the wire then, we must maintain $\Delta \mathrm{T}_N < 1$, which translates to

$$J_w^2 N t_h < 450$$

with t_h in units of $1\,\mathrm{min}$. This relation sets a bound on the field produced by the electromagnet, which we estimate to be that from a solenoid of infinite span l_{em} ($l_{em} >> a_{em}$) with a coil thickness equal to the electromagnet radius a_{em}: $B_{em} \cong 0.1 J_w a_{em} kG$, where a_{em} is in *units* of $1cm$. Using this expression, we find that

$$\alpha_0 \sqrt{N t_h} < 2.5\, a_{em}/B_0 ,$$

where $\alpha_0 = B_{em}/B_0$ and B_0 is in *units* of $1kG$.

Now, the signal of interest is proportional to the difference in the charge collected by the electrodes, $N t_h I$, when the electromagnet is on and off, which can be estimated as $N t_h \alpha_0 \beta I/\left(1+\alpha_0\beta\right)$. On the other hand, the noise in the plasma current is proportional to $\sqrt{INt_h}$. Given that $I \propto n_e \sqrt{T_e} A$ and $A \propto a_{em}^2$, we find that

$$SNL \propto a_{em}\sqrt{Nt_h}\,\alpha_0\beta/(1+\alpha_0\beta),$$

where SNL is the signal-to-noise level. For $\alpha_0 < 1/\beta$ then, the SNL is essentially a function of the product $\alpha_0\sqrt{Nt_h}$. Therefore, we may increase α_0 to about $1/\beta$ and reduce the sampling time (to prevent melting the probe) without sacrificing the quality of the signal.

[6.2x] The dependence of the collection area on the magnetic geometry

We analyze the magnetic geometry in the reference frame of the probe's housing as shown in figure **6.2x-1**, where the toroidal field takes on the form

$$\vec{B}_0 = \hat{\phi}B_0\,R_0/R$$

with

$$R\hat{\phi} = \vec{R}\times\hat{y} = -(R_0\sin\phi + z)\hat{x} + (R_0\cos\phi + x)\hat{z}.$$

Here, the alignment is described by the angle ϕ. The field produced by the electromagnet is approximated by its value on-axis, which we write generically as $B_0\alpha(z)$, with its radial component derived from $0 = \nabla.\vec{B}_{em}$:

$$\vec{B}_{em} = B_0(\alpha\hat{z} - \alpha'\vec{r}/2)$$

with $\vec{r} = x\hat{x} + y\hat{y}$ and the *prime* denoting the derivative with respect to z.

The requirement that the tangent to the field lines be parallel to the magnetic field vector determines the field line's spatial variation: $\vec{0} = (dx, dy, dz)\times\vec{B}$, which translates to

$$dx/B_x = dy/B_y = dz/B_z,$$

where $\vec{B} = \vec{B}_0 + \vec{B}_{em}$. Inside the housing, we can exploit the limits $l_{em}/R_0 << 1$ and $a_{em}/l_{em} << 1$, where a_{em} and l_{em} represent the radius and the half-length of the electromagnet. By using the orderings, $z/R_0 \sim \varepsilon$ and $x/R_0 \sim \varepsilon^2$, where $\varepsilon << 1$, we obtain $\phi \cong z/R_0 \sim \varepsilon$, which then enables us to approximate the spatial variation of the toroidal field as

$$\vec{B}_0/B_0 \cong \hat{z} - (z/R_0 + \phi)\hat{x}.$$

The governing equation for the toroidal field lines can then be approximated as $dx/dz \cong -(z/R_0 + \phi)$, which gives

$$x - x_0 \cong \frac{R_0}{2}\left[\phi^2 - (z/R_0 + \phi)^2\right] \qquad \{6.2x - 1\},$$

where $x_0 \equiv x(z = 0)$. The equation describes a parabola with a vertex located at $(x, z) = (x_0 + R_0\,\phi^2/2, -R_0\phi)$.

The addition of $\vec{B}_{em}$ modifies the aforementioned differential equation to

$$(1+\alpha)dx = -(1/2)\left[x d\alpha + d(z + R_0\phi)^2\right]$$

and produces a second differential equation, $(1+\alpha)dy \cong -d\alpha\, y/2$. The latter equation describes magnetic flux conservation,

$$y^2(1+\alpha) = y_0^2(1+\alpha_0),$$

where $y_0 \equiv y(z = 0)$ and $\alpha_0 \equiv \alpha(z = 0)$; whereas the former equation describes the coupling between the toroidal field and the field of the electromagnet. To solve this equation for x, we divide the region axially as follows.

In the region $l_{em} - a_{em}/2 < |z| < l_{em} + a_{em}/2$, where the gradient in the field is strong, we neglect the curvature of the field lines in comparison to the compression of the field. On the other hand, for $|z|$ outside this region, we neglect the field compression because $\alpha'/\alpha << 1$. These approximations then give

$$(1+\alpha)dx \cong -(x/2)d\alpha$$

for $\big||z| - l_{em}\big| < a_{em}/2$, and

$$(1+\alpha)dx \cong -(1/2)d(z + R_0\phi)^2$$

for $\big||z| - l_{em}\big| > a_{em}/2$ with α approximated by α_0 for $|z| < l_{em} - a_{em}/2$ and by *zero* for $|z| > l_{em} + a_{em}/2$.

We can then integrate these equations and match the boundary values for the three regions to obtain

$$x_+ - x_\infty \cong \frac{1}{2R_0}\left[(R_0\phi + 2l_{em})^2 - (R_0\phi + l_{em} + a_{em}/2)^2\right],$$

$$(1+\alpha_0)x_-^2 \cong x_+^2,$$

and

$$(1+\alpha_0)[x_0 - x_-] \cong \frac{1}{2R_0}\left[(R_0\phi + l_{em} - a_{em}/2)^2 - (R_0\phi)^2\right],$$

where the subscripts $\pm$ denote evaluation at $z = l_{em} \pm a_{em}/2$, respectively, and the subscript ∞ denotes the evaluation at $z = 2l_{em} \equiv l$. Neglecting the ratio $a_{em}/2l_{em}$, we find

$$x_\infty \cong \sqrt{1+\alpha_0}\,(x_0 - \Delta x_0) \qquad \{6.2x-2\}$$

with

$$\Delta x_0 = \frac{1}{2(1+\alpha_0)}\frac{l^2}{R_0}\left[\frac{R_0\phi}{l}\left(1+\sqrt{1+\alpha_0}\right)+\frac{1}{4}\left(1+3\sqrt{1+\alpha_0}\right)\right] \qquad \{6.2x-2a\},$$

which indicates that a circle at the throat projects to a circle at the entrance with a center that is shifted by $-\sqrt{1+\alpha_0}\Delta x_0$ and with a radius that is expanded by the factor $\sqrt{1+\alpha_0}$. The change in the x coordinate of the field lines from the entrance to the collector is unaffected by the electromagnet. It is found from the evolution of the toroidal field line as described by equation **6.2x-1**:

$$x_\infty - x_{-\infty} = \left(x_\infty - x_0\right) - \left(x_{-\infty} - x_0\right) \cong \frac{1}{2R_0}\left[\left(R_0\phi - l\right)^2 - \left(R_0\phi + l\right)^2\right] = -2l\phi \qquad \{6.2x-3\}.$$

[6.2x.1] The overlap area between the entrance, the grid, and the collector

We use equations **6.2x-2** and **6.2x-3** to determine the fraction of the entrance aperture that enables the electrons to strike the collector. This fraction is equivalent to the overlap area of the entrance aperture with the magnetic projections of the areas of the grid and the collector electrodes onto the entrance. We determine the overlap area among the three electrodes in two steps. We first write the expression for the overlap between two circles as depicted in figure **6.2x-2**:

$$A = \theta_< r_<^2 + \theta_> r_>^2 - \left|\Delta x\right| r_< \sin\left(\theta_<\right) \qquad \{6.2x-4\}$$

with $\Delta x = x_< - x_>$, $\theta_> = \arcsin\left[\left(r_</r_>\right)\sin\theta_<\right]$, and

$$\theta_< = \pi - \arccos\left[\left(r_<^2 + \Delta x^2 - r_>^2\right)/\left(2r_<\Delta x\right)\right].$$

Here, the subscripts $<$ and $>$ denote the *smaller* and the *bigger* circle, respectively. We then use equation **6.2x-4** to obtain the overlap area among the three circles, A_{123}, as follows. We first sort the three circles, $\left(C_1, C_2, C_3\right)$, by the magnitude of their radii; that

is, we require that $r_1 \le r_2 \le r_3$. We then apply the following recipe in the order presented:

0. We only entertain a statement if none of the statements before it are true.
1. If any two of the three circles do not overlap, then $A_{123} = 0$.
2. If C_2 encircles C_1, then $A_{123} = A_{13}$
3. If C_3 encircles C_1 or C_2, then $A_{123} = A_{12}$
4. If the centers of C_2 and C_3 are on the same side of C_1 [that is, if $\Delta_{12}x \cdot \Delta_{13}x > 0$, where $\Delta_{ij}x \equiv x_i - x_j$] and $\left|\Delta_{13}x\right| < \left|\Delta_{12}x\right|$, then $A_{123} = A_{12}$

If none of the above statements are true, then we consider where the circles C_2 and C_3 intersect. The intersection point of the two circles in the *reference frame* of C_1 is given by $r_{23} \equiv \sqrt{\left(\Delta_{12}x\right)^2 - 2r_2 \cos\theta_{<}\big|_{23} \Delta_{12}x + r_2^2}$. Using this formula, we entertain the following conditions:

a) If $\Delta_{12}x \cdot \Delta_{13}x > 0$ and the intersection between C_2 and C_3 occurs *inside* C_1 ($r_{23} < r_1$), then $A_{123} = A_{12} - A'_{23}$, where $A'_{23} \equiv A_2 - A_{23}$

b) If $\Delta_{12}x \cdot \Delta_{13}x > 0$ and $r_{23} > r_1$, then $A_{123} = A_{13}$

c) If $\Delta_{12}x \cdot \Delta_{13}x < 0$ and $r_{23} > r_1$, then $A_{123} = A_{12} - A'_{13}$

d) Else if $\Delta_{12}x \cdot \Delta_{13}x < 0$ and $r_{23} < r_1$, then $A_{123} = A_{23}$

We apply this recipe to find the overlap between the entrance aperture, $\left(x_E, r_E\right) = \left(0, a_E\right)$, with the projection of the grid and the collector apertures onto the entrance: $\left(x_G, r_G\right) = \left(-\sqrt{1+\alpha_0}\,\Delta x_0, \sqrt{1+\alpha_0}\,a_G\right)$ and $\left(x_C, r_C\right) = \left(-2l\phi, a_C\right)$.

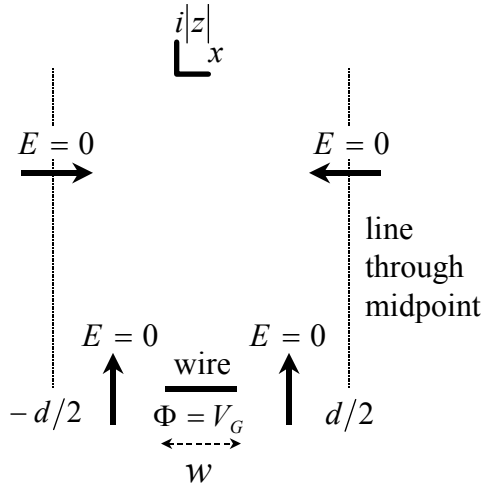

the geometry for the grid
(single array of wires)

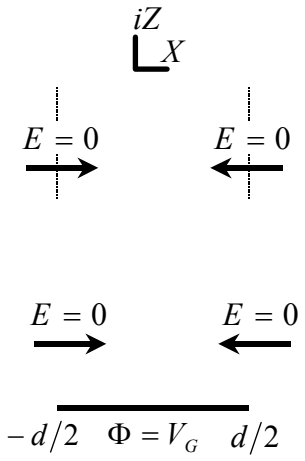

the geometry with the simple
boundary condition

Figure 5.1x-1: The map that simplifies the boundary condition

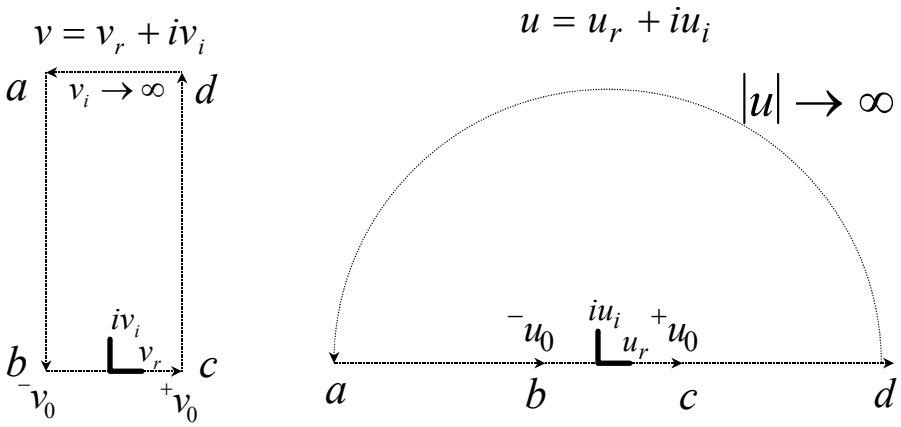

$$u = u_0 \sin\left(\frac{\pi}{2}\frac{v}{v_0}\right)$$

Figure 5.1x-2: General conformal map from a rectangle to a straight line

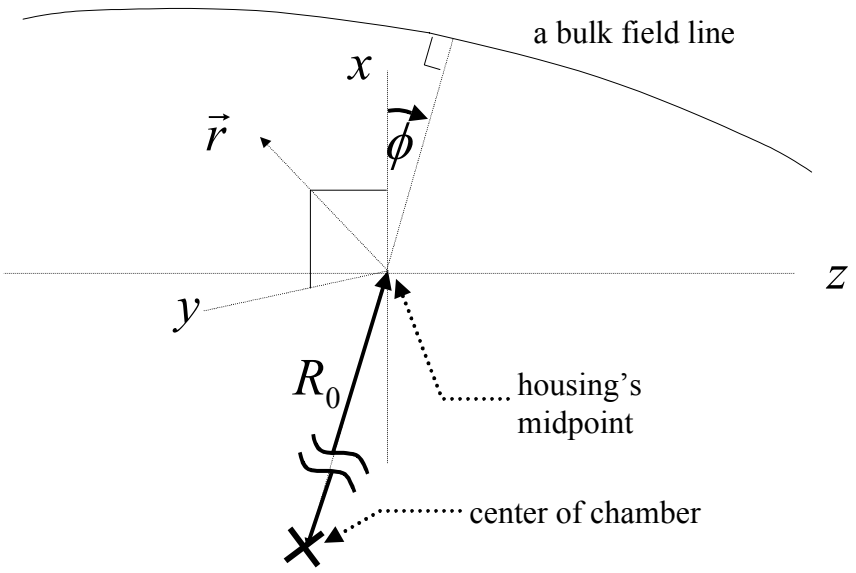

FIGURE 6.2x-1: The alignment geometry in the reference frame of the probe's housing.

$$A = r_<^2\theta_< + r_>^2\theta_> - |\Delta x| r_< \sin\theta_<$$

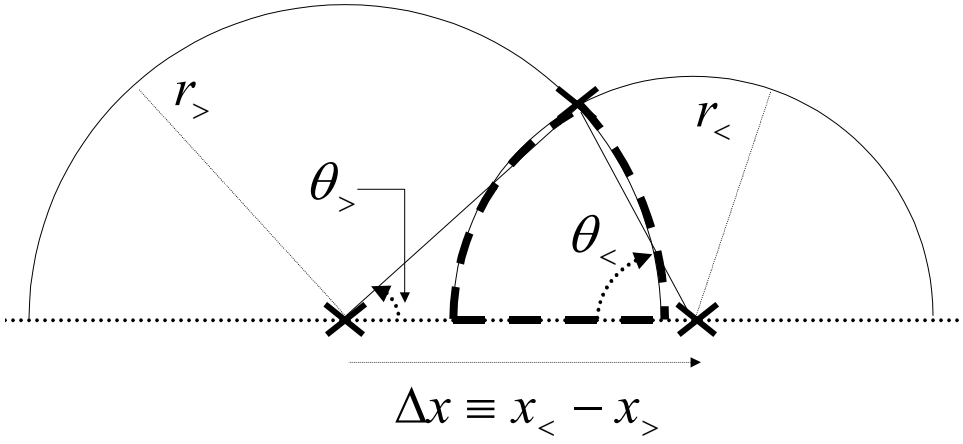

FIGURE 6.2x-2: The overlapping area between two circles.